A light scattering study of the kinetics of the sol-to-gel transition in particulate systems

by

Raiya Husein Ebini

B.S., Jordan University of Science and Technology, 2001
M.S., University of Arkansas, 2007

AN ABSTRACT OF A DISSERTATION

submitted in partial fulfillment of the requirements for the degree

DOCTOR OF PHILOSOPHY

Department of Physics
College of Arts and Sciences

KANSAS STATE UNIVERSITY
Manhattan, Kansas

2020

Abstract

We present investigations of the kinetics of the colloidal sol-to-gel transition by combining small angle static light scattering (SASLS), dynamic light scattering (DLS) techniques, and transmitivity measurement. Our choice of dilute monomer volume fraction allows for a full investigation of the gelation to obtain all possible kinetic regimes. Our data verify the predictions of a kinetic theory, the ideal gel point (IGP) theory, where three regimes of kinetics are expected. We observe the first regime, the well-known cluster-dilute regime, with a kinetic exponent of z = 1, a cluster-dense regime with an enhanced kinetics and z $\simeq$ 2, and finally, a gelation regime is observed where the aggregate growth slows and ceases to grow at the IGP predicted size, $R_{g,G}$.

The time from the onset of aggregation to the gelation point, the gel time t_{gel}, has also been investigated. The scaling behavior of t_{gel} with the initial monomer volume fraction, f_{vm}, and the stability ratio, W, was verified with the prediction provided by the kinetic description of gelation. It was important throughout this work to realize that the fractal dimension, D_f, of the aggregates that grow to form the gel is a function of W. For that we designed a procedure that proved viable in our analysis.

These results quantitatively verify the IGP theory and when combined with previous studies lead us to access the roles of thermodynamics, percolation and kinetics. We conclude that kinetics provides a complete theory of the gelation process from sol to percolated gel.

A light scattering study of the kientics of the colloidal sol-to-gel transition

by

Raiya Husien Ebini

B.S., Jordan University of Science and Technology, 2001
M.S., University of Arkansas, 2007

A DISSERTATION

submitted in partial fulfillment of the requirements for the degree

DOCTOR OF PHILOSOPHY

Department of Physics
College of Arts and Sciences

KANSAS STATE UNIVERSITY
Manhattan, Kansas

2020

Approved by:

Major Professor
Christopher Sorensen

Copyright

Abstract

We present investigations of the kinetics of the colloidal sol-to-gel transition by combining small angle static light scattering (SASLS), dynamic light scattering (DLS) techniques, and transmitivity measurement. Our choice of dilute monomer volume fraction allows for a full investigation of the gelation to obtain all possible kinetic regimes. Our data verify the predictions of a kinetic theory, the ideal gel point (IGP) theory, where three regimes of kinetics are expected. We observe the first regime, the well-known cluster-dilute regime, with a kinetic exponent of z = 1, a cluster-dense regime with an enhanced kinetics and z $\simeq$ 2, and finally, a gelation regime is observed where the aggregate growth slows and ceases to grow at the IGP predicted size, $R_{g,G}$.

The time from the onset of aggregation to the gelation point, the gel time t_{gel}, has also been investigated. The scaling behavior of t_{gel} with the initial monomer volume fraction, f_{vm}, and the stability ratio, W, was verified with the prediction provided by the kinetic description of gelation. It was important throughout this work to realize that the fractal dimension, D_f, of the aggregates that grow to form the gel is a function of W. For that we designed a procedure that proved viable in our analysis.

These results quantitatively verify the IGP theory and when combined with previous studies lead us to access the roles of thermodynamics, percolation and kinetics. We conclude that kinetics provides a complete theory of the gelation process from sol to percolated gel.

Table of Contents

List of Figures

(2) ($\boldsymbol{Rg-1,I0}$). (3) ($(\boldsymbol{2.3Rg})-\boldsymbol{1,I0}$). Both the black dashed & dotted black lines represents a slope of -1.82. (4) ($\boldsymbol{Rnn-1,I0}$), the solid red line gives a slope of -3..... 152

List of Tables

Acknowledgements

First, I would like to express my sincere gratitude to my advisor, Dr. Chris Sorensen, who has been patiently encouraging and guiding me since I joint his group. Words fail to express my gratidute to my advisor Dr. Sorensen.

I would like to thank Dr. Amit Chakrabarti, Dr. Jeremy Schmit, and Dr. Xiuzhi Sun for being my committee members and Dr. Jennifer Anthony for being the chairperson of my examination committee.

Last but not least, I am very grateful to have supportive friends and family. Especial thanks for Hamdi, for being a wonderful son and Dr. Durar for being a true friend.

Chapter 1 - Introduction to Dissertation

Colloids and aerosols are dispersion of small particles (~ submicrons) in a fluid medium. Common examples include milk, ink, paint, and smoke. Not only do they exist in nature, they are also relatively easy to manufacture. Colloids have many properties that make them important to a wide range of technological applications. One of their properties is that they are small enough to be controlled by thermal energy. Another important feature is that the particle interactions are easily tuned in a laboratory. This allows for the particles to assemble together. These primary particles, or monomers, act as building blocks to create new materials.

For example, non-coalescing colloidal particles, if allowed to aggregate, may form a gel. Gelation, which is equivalently named the sol-to-gel transition, has opened many avenues toward synthesis of new materials with special properties (Brinker and Scherer 2013; Dhaubhadel et al. 2007; H. Liu et al. 2004). Many descriptions have been around to explain such a complex but important process. The vast understanding of gelation evolved around three main descriptions, the kinetics, thermodynamic phase separation, and the percolation descriptions. Despite all of these efforts, no consensus has emerged and gelation is yet far from being well understood.

My work focuses on polystyrene spheres of radius a = 20nm dispersed in liquid. These particles are stable due to their repulsive interaction. I use salt to destabilize the particles and tune the interaction. This allows the monomers to aggregate and form fractal aggregates. If the initial monomer concentration is high enough, and the aggregation is uninterrupted, a gel will form. This gel is called fractal colloidal gel. To probe the gelation process, I merged three types of non-invasive techniques: dynamic and small angle static light scattering techniques in addition to the transmitivity measurement. This work combined with other work in our group shows that the sol-to-gel transition can be described by a kinetic theory, named the Ideal Gel Point (IGP) theory (IGP).

I will start my dissertation in Chapter 2 by introducing the light scattering principles behind the different techniques I used to probe the fractal colloidal gel. In Chapter 3, I will introduce the colloidal interactions and what we mean by tuning the interaction to start the aggregation process. In addition, I will provide an explanation of the three different descriptions of gelation. I slightly emphasize on the IGP theory within the kinetic description. In Chapter 4, I will discuss the experimental set up and calibration, along with some interesting observations during my work.

While in Chapter 5, I will discuss the procedure I developed in this work to achieve the right conclusions. This is an important contribution of this work. In the study of gels there are many parameters that are related to each other. We developed a procedure to be able to change one parameter at a time. This procedure is not practiced in literature. In Chapter 6, I will discuss the IGP theory and validate its kinetic predictions. In Chapter 7, I will discuss the proportionality of gel time as predicted by the IGP theory. In Chapter 8, I will discuss the anomalous diffusion observed with the DLS data for the gelling and non-gelling samples, and provide a physical picture of these observations. In Chapter 9, I will combine and integrate our results and understanding out of this work and other work in our group to come up with a single comprehensive understanding of the sol-to-gel transition based on the kinetic description.

Chapter 2 - Light scattering by fractal aggregates

Small particles, or monomers, may stick together to form aggregates. One type of aggregate is known as fractal aggregates. This type is common in nature as well as in practical situations. These aggregates when allowed may form a gel. The transition from a system of small particles, sols, to aggregates, to eventually a gel, hence the sol-to-gel transition, is the main interest of this work. Light scattering is a vital technique in studying this transition. It is a noninvasive technique, can be used to monitor the aggregation kinetics, and, with the proper light scattering technique, can determine the morphology of the aggregates as well.

In this chapter we will briefly introduce the main characteristics of fractal aggregates, followed by a brief description of the three different light scattering techniques used in this work; small angle static light scattering (SASLS), dynamic light scattering (DLS), and transmitivity measurements.

2.1 Fractals and fractal aggregates

Fractal objects (Mandelbrot 1977) are objects that can be described as scale invariant. This means that the object appears the same regardless of the different scale at which it is viewed. That is if you zoom in or zoom out, you still see the same geometry. Fractals are also self-similar objects. This means any portion of the object is structurally similar to the whole. In general, a self-similar fractal can be covered by N replicates of itself keeping an isotropic dilation of the linear size. This give fractal objects their unique mass to linear size scaling relation as follow

$$mass \sim (linear\ size)^{D_f} \tag{2.1}$$

where D_f is the scaling dimension. This scaling dimension is smaller than the spatial dimension, d, and it is referred to as the fractal dimension. It is this D_f that distinguishes the morphology of one fractal object from another. Figure 2.1 shows different examples of fractal geometries and their fractal dimensionalities. Even though these shapes, theoretically, may continue to infinite iterations, we show only up to the third iteration. Regardless of the number of iterations, the morphology will still have D_f = 1.585 & 1.465 for the top and bottom geometries, respectively.

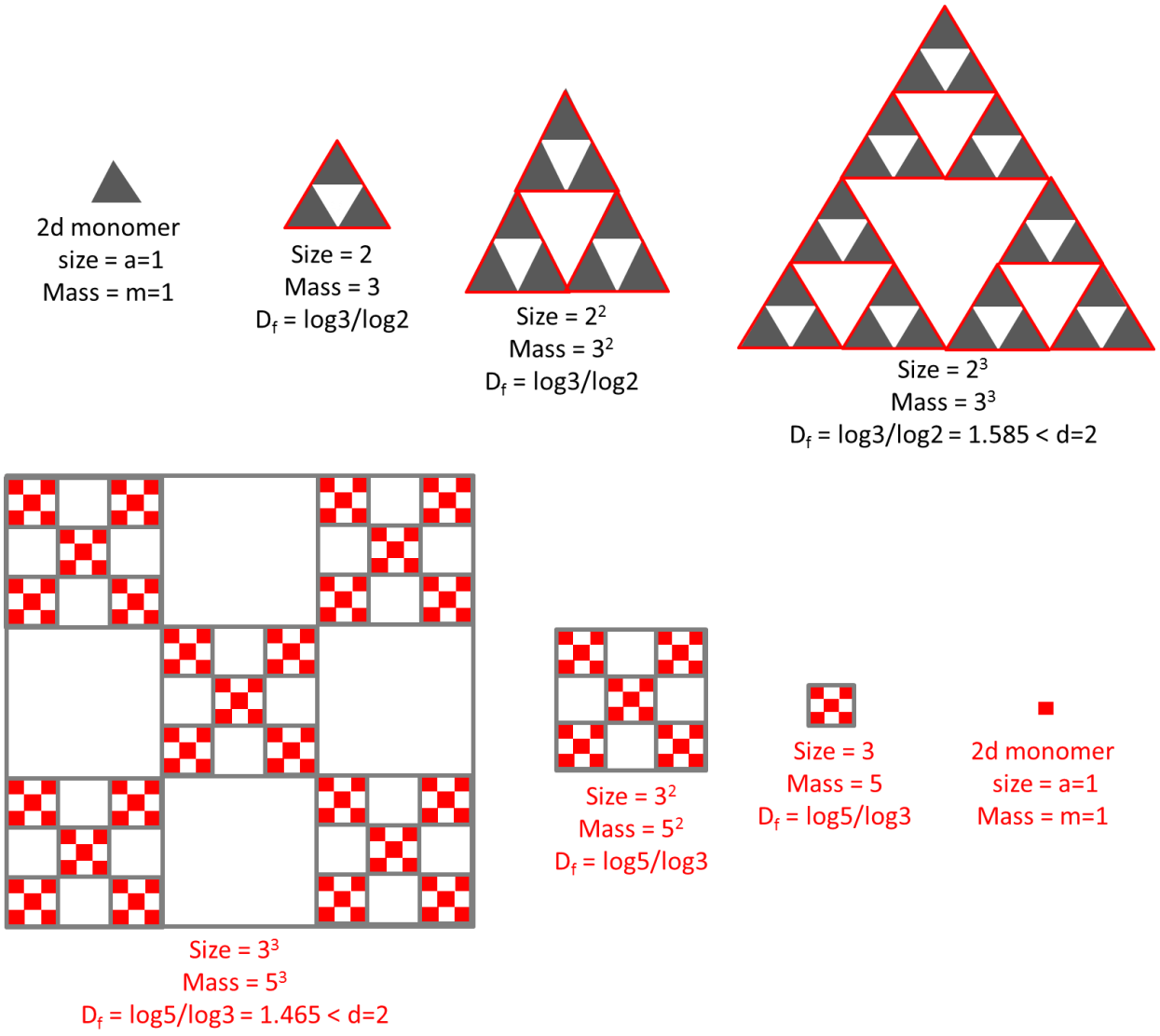

Figure 2.1 Examples of particles in two dimensional space with monomers of linear size, a, and mass, m, may join together to create different fractal geometries of D_f = 1.588 and 1.465 (top and bottom respectively) < d = 2. This figure shows three iterations of each example.

If non-coalescing particles are allowed to stick together, they may form ramified fractal aggregates. Fractal colloidal aggregates can be classified into two asymptotic models (Lin et al. 1989c; Weitz et al. 1985): diffusion limited cluster-cluster aggregation (DLCA) and reaction limited cluster-cluster aggregation (RLCA). In both models the clusters are allowed to diffuse, collide, and stick together to form larger clusters (Kolb, Botet, and Jullien 1983; Meakin 1987). The fundamental difference between these two limiting models is how many times the clusters need to collide before

they stick. This results in difference in their fractal dimensions, thus morphologies. Figure 2.2 shows the different morphologies for (a) DLCA & (b) RLCA aggregates.

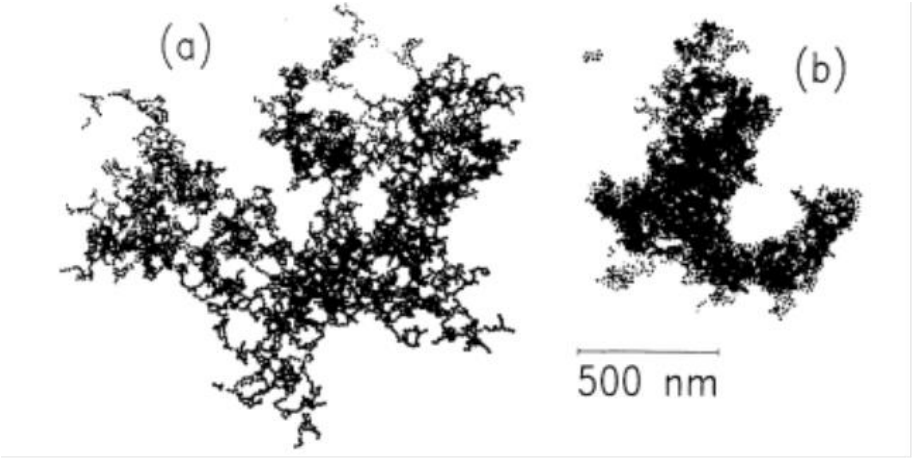

Figure 2.2 Transmission electron microscopy images of fractal aggregates. (a) DLCA model, (b) RLCA model. Image taken from (Weitz et al. 1985).

When dealing with aggregates, with indefinite boundaries, the radius of gyration R_g, also known as root mean square radius, is a useful measure of the linear size of an aggregate. R_g can be expressed as

$$R_g^2 = \frac{\int_0^R r^2 n(\vec{r}) d^3 r}{\int_0^R r^2 d^3 r} \tag{2.2}$$

where $n(\vec{r})$ is the mass density at position $\vec{r}$ of an object.

For a fractal aggregate, its mass, N, which is described by the number of monomers constitutes the aggregate, scales with its linear size, R_g, as

$$N = k_o \left(\frac{R_g}{a}\right)^{D_f} \tag{2.3}$$

Where k_o is the scaling prefactor and a is the monomer radius.

Fractal aggregates are self-similar over a particular range, because they are made of finite sized monomers and can grow up to a certain size. A successful method to understand the fractal aggregate morphology is by defining the monomer pair correlation function, G(r), which can be expressed as (W. R. Heinson, Sorensen, and Chakrabarti 2012)

$$G(r) = \Phi \frac{D_f}{4\pi a^{D_f}} r^{D_f - 3} \exp[-(r/\xi)^{\gamma}] \tag{2.4}$$

It is important to note, the monomer pair correlation function given in Eq. (2.4) depends on: the monomer size, a, the monomer packing fraction, ϕ, which describes the structure at the monomer level, and the aggregate's fractal dimension, D_f. In addition, the format of the monomer pair correlation function has a spatial power-law decay part, which will yield the fractal part in the structure of the aggregate between the monomer size and the aggregate size, and a stretched exponential part with the stretching exponent γ. This stretched exponential represents a cutoff for the spatial power law decay because, as mentioned above, fractal aggregates are fractals over a specific length scale. The exponent γ describes the boundary of the aggregate with the size specified by the correlation length, ξ. It was found that a Gaussian cut off function with $\gamma = 2$ is best to describe the light scattering data in experiments and simulations (C. M. Sorensen, Cai, and Lu 1992; W. R. Heinson, Sorensen, and Chakrabarti 2012; C. M. Sorensen 2001).

2.2 Principles of light scattering

Light scatters due to the heterogeneity of the scattering medium. If light passes through homogenous medium it will not scatter. Therefore, scattering is a result of local density fluctuations in the scattering medium. Fundamentally, the information is carried within the phase change between the incident and the scattered light due to the interaction between the incidents light with the scattering medium. In this discussion we are interested in elastic, single, and independent scattering. Elastic scattering means no shift of frequencies between the incident and scattered light. Single scattering means the total scattered light is due to the light scattered only once, in other words, there is no multiple scattering. Independent scattering means the particles are randomly located such that they scatter independently; hence there is no systematic relation among the phases of the waves scattered.

Consider a light wave incident with an angle θ on a small particle positioned at $\vec{r}$ as shown in Fig. 2.3. The direction of propagation for the incident wave is described by the incident wave vector $\vec{k_i}$. The incident field can be written as

$$E_i \sim E_0 \, e^{i\vec{k}_i \cdot \vec{r}} \tag{2.5}$$

The light scattered off the particle toward a detector at position $\vec{R}$ from the origin. The propagation of the scattered light is described by the scattered wave vector $\vec{k}_s$. Because the scattered photon by

the small particles is almost elastic then, for a good approximation, $k_i = k_s = k = 2\pi/\lambda$. The scattered electric field at the detector will take the form

$$E_s(\vec{R}, t) \sim E_i \, e^{i \vec{k}_s \cdot (\vec{R} - \vec{r})} = E_0 \, e^{i\vec{q}.\vec{r}(t)} \tag{2.6}$$

where $\vec{q}$ is the wave vector defined as

$$\vec{q} = \vec{k}_i - \vec{k}_s \tag{2.7}$$

with a magnitude of

$$q = 2\, k \sin(\theta/2) \tag{2.8}$$

The wave vector q has m^{-1} unit, then q^{-1} can be thought as a length parameter of the scattering experiment. One may think of q^{-1} as the resolution of the light scattering apparatus.

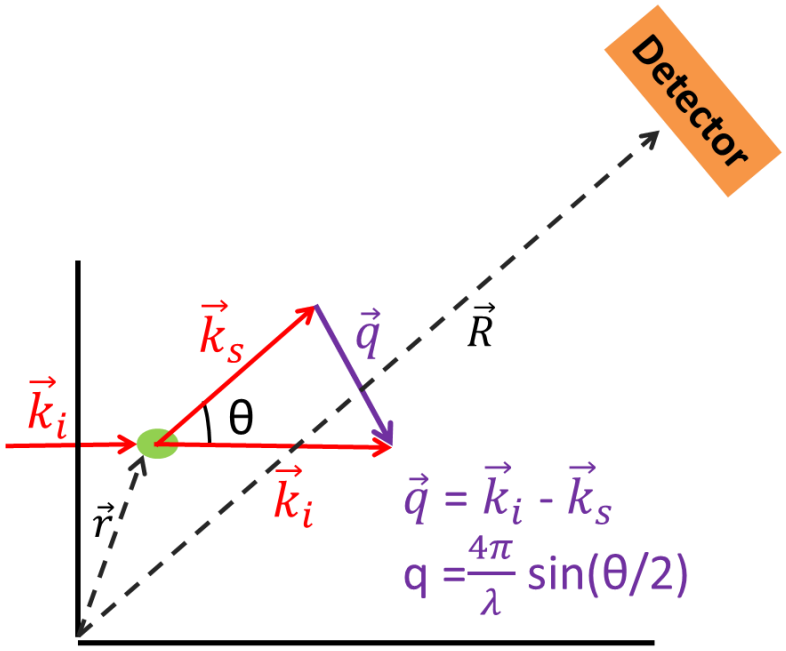

Figure 2.3 Incident beam is scattered from a small particle toward a detector at scattering angle θ. The difference of the wave vectors, $\vec{k}_i$ - $\vec{k}_s$, is the scattering wave vector, $\vec{q}$.

Generally, the scattered light depends on the wavelength, λ, of the incident light and its polarizability state, the size of the particle, a, the relative refractive index, m, of the material compared to the medium. The scattered intensity I_s is related to the incident intensity detected at distance r from the scattering position via the differential scattering cross section, dσ/dΩ

$$I_s = \frac{d\sigma}{d\Omega}\frac{I_o}{r^2} \tag{2.9}$$

Note that the unit of intensity is Watt/m^2. This means dσ/dΩ have to have a unit of m^2 to have the correct units. If the incident light is scattered off small particles compared to the wavelength of light such that it satisfies the following two conditions: ka, and mka <<1, then this scattering is called Rayleigh scattering with Rayleigh differential scattering cross section is $(d\sigma/d\Omega)_R$.

For Rayleigh particles, the phase of the incident field is uniform across the entire volume of the particle because a << λ. In addition, the phase irradiated from any portion within the particle volume will reach the detector in phase. Therefore, the total scattered field at the detector $E_{detector}$ ~ V_p, where V_p is the particle volume. Since intensity $I = E\,E^*$, then I ~ V_p^2. This implies $(d\sigma/d\Omega)_R$ ~ V_p^2, which gives an incorrect unit of m^6, which is not correct. To fix this we realize in this system there are two length scales the size of the particle, a, and the wavelength of light, λ. Unit analysis force the use of λ to obtain the correct unit for $(d\sigma/d\Omega)_R$, therefore, $(d\sigma/d\Omega)_R$ ~ V_p^2/λ^4. Hence $(d\sigma/d\Omega)_R$ can be written in terms of the wave-number, k, as

$$\left(\frac{d\sigma}{d\Omega}\right)_R = k^4 a^6\, F(m) \tag{2.10}$$

F(m) is called the Lorentz term and it involves the relative refractive index of the particle (C. M. Sorensen 2001).

We discussed the Rayleigh scattering, which assumes the phase of the incident field does not change a cross the particle because ka << 1. But what if the phase changes of an incident light a cross the particle is very small compared to the phase change of the surrounding medium? Then the Rayleigh scattering can be substituted by the Rayleigh- Debye-Gans (RDG) scattering. The conditions for RDG scattering are |m-1| < 1 , and ρ = 2ka |m-1| < 1 (C. M. Sorensen 2001). The parameter ρ is the phase shift parameter and represents the difference in phase between a wave that travels through the particle across its diameter and the wave that travels the same distance as the particle diameter but through the surrounding medium. At the time Rayleigh scattering works for any shape particle as long as it is small, the RDG can extend to any shape and any size particle (even big particles) as long as the relative refractive index of the particle, m, is close to unity.

In this work we used three different light scattering techniques, small angle static light scattering (SASLS), dynamic light scattering (DLS), and transmitivity measurement. We will discuss each

one separately. The fundamental difference between SASLS and DLS techniques originate from the part of the phase difference each technique is viewing. For SASLS, it is the spatial change in the phase that constitutes the static structure factor. On the other hand, for DLS technique it is the temporal change in the phase that produces the dynamic structure factor.

2.2.1 Static light scattering

In the example above we took a small particle and treated it as a point-like object which represents a single "scatterer". This scatterer will scatter isotopically. If we limit our discussion on phase changes due to propagation through space, which is the signature of static light scattering, then the scattered light field due to a point-like scatterer can take the form

$$E_s(R) \sim e^{i\vec{q}.\vec{r}} \tag{2.11}$$

Now if we generalize our particle into an extended object with a volume V_p, and divide this volume into N small sub-volumes, then each of the N sub-volumes can be treated as a point-like scatterer. With the assumption the scattered light reaching the detector is scattered only once from one sub-volume (no multiple scattering), and that these sub-volumes scatter independently from each other, then the total scattered field for a system of N scatterers can be written as

$$E_s \sim \sum_i^N e^{i\vec{q}.\vec{r}} \tag{2.12}$$

Using the definition of intensity, I = E E* one can write the scattering intensity as

$$I_s \sim \sum_i^N \sum_j^N e^{i\vec{q}.(\vec{r_i}-\vec{r_j})} \tag{2.13}$$

Now we can define the structure factor S(q) as

$$S(\vec{q}) = N^{-2} I_s = N^{-2} \sum_i^N \sum_j^N e^{i\vec{q}.(\vec{r_i}-\vec{r_j})} \tag{2.14}$$

Notice the N^{-2} normalization makes S(0) = 1. This normalization may differ in literature.

If we wish to change the sum into integral over the scattering volume, then Eq. (2.12) changes to

$$E_s(\vec{q}) \sim \int n(\vec{r})\ e^{i\vec{q}.\vec{r}}\ d\vec{r} \tag{2.15}$$

$n(\vec{r})$ is the number density of the scattering volume. This will yield an expression of $S(\vec{q})$ in the form (C. M. Sorensen 2001)

$$S(\vec{q}) = 4\pi \int G(\vec{r})\ e^{i\vec{q}.\vec{r}}\ d\vec{r} \tag{2.16}$$

The static structure factor is the Fourier transform of the monomer pair correlation function, $G(\vec{r})$. This is a very general result that works for any shaped particle or aggregate. The Rayleigh-Debye-Gans theory can be applied to obtain the structure factor for a fractal aggregate to give

$$S(q) = 1 \qquad for\ q \to 0 \qquad \text{Rayleigh regime} \qquad (2.17a)$$

$$S(q) = 1 - \frac{1}{3}\left(q\ R_g\right)^2 \qquad for\ q\ \leq\ R_g^{-1} \qquad \text{Guinier regime} \qquad (2.17b)$$

$$S(q) = C\left(q\ R_g\right)^{-D_f} \qquad for\ R_g^{-1} <\ q < a^{-1} \qquad \text{Power-law regime} \qquad (2.17c)$$

C is the coefficient that depends on the fractal dimension, D_f, and the stretched exponent, γ, in the monomer pair correlation function, see Eq. (2.4). The value of C ~ 1 (C. M. Sorensen 2001). Notice for Eq. (2.17c), the limits on q range is set by the monomers radius, a, because for $q > a^{-1}$ the structure factor of spherical particles of size, a, starts to appear. If the monomers size below the resolution of the light scattering apparatus then the structure factor for the monomers will not appear. Figure 2.4 shows a schematic diagram for the structure factor. The figure shows: for small q ($q << R_g^{-1}$), Rayleigh regime is apparent, for $q \sim R_g^{-1}$, the Guinier regime starts to show and at high q values ($q > R_g^{-1}$) the power law regime appears, which has a negative slope. If the initial concentration of the monomers are small, then the fractal dimension of the aggregate can be obtained directly from the slope of the power law regime in the I(q) vs q.

The average radius of gyration (R_g), can be determined using Guinier analysis (Guinier, Fournet, and Yudowitch 1955). The Guinier equation is

$$I(q) = I(0)(\ 1 - \frac{q^2 R_g^2}{3}\ ) \qquad (2.18)$$

At the limit of $qR_g \sim 1$, $I(q)/I(0) \sim 2/3$. When $qR_g << 1$ Eq. (2.18) can be written as

$$I(0) = I(q)(\ 1 + \frac{q^2 R_g^2}{3}\ ) \qquad (2.19)$$

Thus the slope of I(0)/I(q) vs. q^2 is $R_g^2/3$.

This above description is for a single aggregate. If we assume an ensemble of aggregates with polydispersity in its size distribution, then the structure factor can take the form (C. M. Sorensen 2001)

$$S(q) = 1 \qquad for\ q \to 0 \qquad \text{Rayleigh regime} \qquad (2.20a)$$

$$S(q) = 1 - \frac{1}{3}\left(q\,R_g\right)^2 \qquad for\ q \le R_g^{-1} \qquad \text{Guinier regime} \qquad (2.20b)$$

$$S(q) = C_p\,C\left(q\,R_g\right)^{-D_f} \qquad for\ R_g^{-1} < q < a^{-1} \qquad \text{Power-law regime} \qquad (2.20c)$$

C_p is the polydispersity factor for a given size distribution (C. M. Sorensen 2001; C. M. Sorensen and Wang 1999).

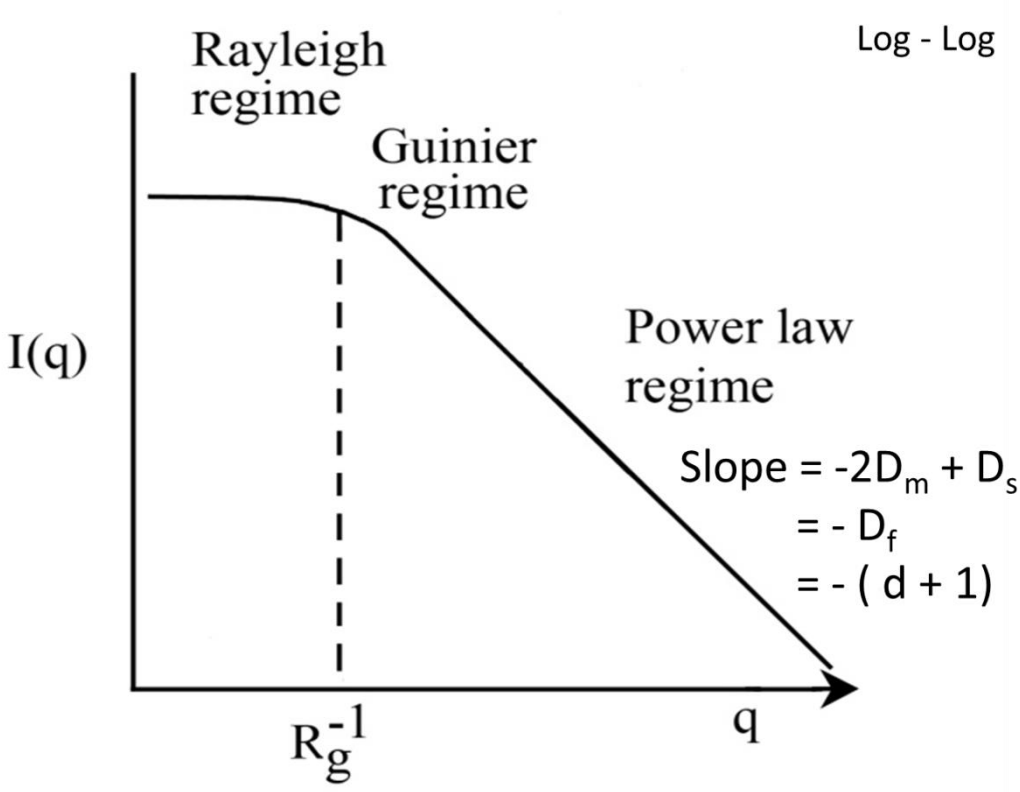

Figure 2.4 A schematic diagram of the scattered intensity I(q) vs. q.

An equivalent approach to obtain a general form of the structure factor is the scaling approach (C. M. Sorensen 2001; Oh and Sorensen 1999). Consider a system of N scatterers in a d-dimensional, spherical region of radius R and the scatterers are uniformly separated by 2a from each other. The scattered intensity, then, will vary depending on the length scale q^{-1} in which the system is observed, which can be summarized as follows (C. M. Sorensen 2001; Oh and Sorensen 1999)

$$I(q) \sim \begin{cases} N^2 & q < R^{-1} \quad (2.21a) \\ N^2(qR)^{-2D_m+D_s} & R^{-1} < q < a^{-1} \quad (2.21b) \\ N^2(R/a)^{-2D_m+D_s} & q > a^{-1} \quad (2.21c) \end{cases}$$

This most general approach works for arbitrary mass and surface dimensions, D_m and D_s, respectively. I will discuss two specific cases out of this most general format. One is the case of a solid sphere of radius R; the other is the case of fractal aggregates made of small spherical monomers.

I want to remind the readers that N which appears in the equations represents the number of point-like scatterers in the total scattering system. In the case of a compact solid sphere, N represents the number of sub-volumes that make up the total sphere. Each sub-volume is treated as a point scatterer. Then the scattered intensity in Eq. (2.21) for the solid sphere with spatial dimension, d = 3, can be modified with a → 0, D_m = d, and D_s = d – 1 to yield

$$I(q)_{solid\ sphere} \sim \begin{cases} N^2 \sim V_p^2 & q < R^{-1} \quad Rayleigh\ regime \\ N^2(qR)^{-(d+1)} \sim V_p^2(qR)^{-(d+1)} & q > R^{-1} \quad Power\ law\ regime \end{cases} \quad (2.22)$$

For fractal aggregates, the situation is different. It consists of N solid monomers, each monomer of radius a. Then the total scattered light of a fractal aggregate may be expressed as

$$I_{Total}(q) = I_{SC}(q)\ I_m(q) \quad (2.23)$$

Where I_{sc} is the scattered intensity of a single cluster made of N monomers. In this case, these N monomers are treated as N point-like scatterers. Then I_{sc} will follow the form of Eq. (2.21) with the exception that $D_m = D_s = D_f$ and that is because all monomers in a fractal are on the surface of the aggregate. I_m is the scattered intensity of one spherical monomer of size a. I_m will follow the format of Eq. (2.22) with replacing R by a and N = 1. Then the total light scatter of a fractal aggregate will yield

$$I_{Total}(q) \sim \begin{cases} N^2 & q < R^{-1} \quad (2.24a) \\ N^2(qR)^{-D_f} & R^{-1} < q < a^{-1} \quad (2.24b) \\ N^2(R/a)^{-D_f}(qa)^{-(d+1)} \sim N(qa)^{-(d+1)} & q > a^{-1} \quad (2.24c) \end{cases}$$

In Eq. (2.24c) we used the fractal mass-size scaling relation, Eq. (2.3). Figure 2.5 shows a schematic representation of Eqs. (2.24).

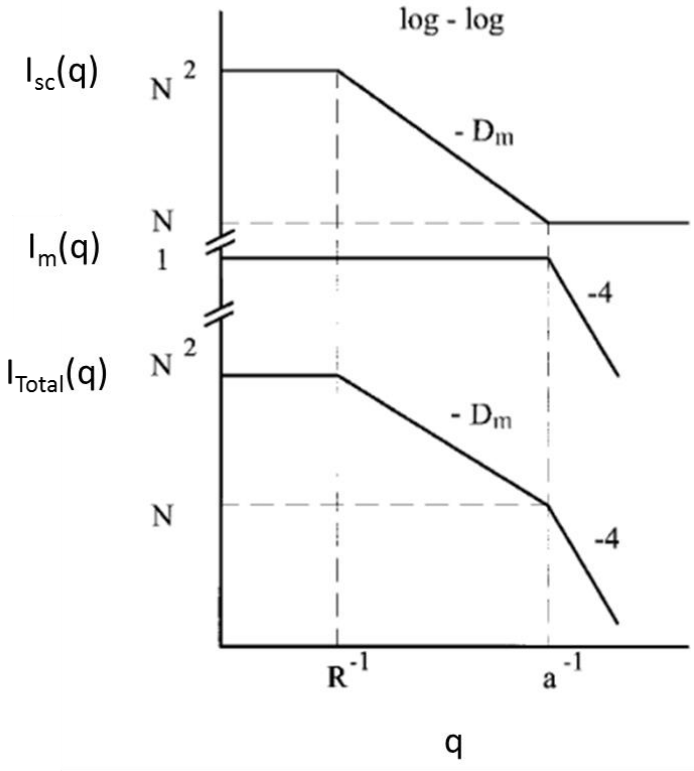

Figure 2.5 Prediction of Eq. (2.25) of a system consisting of one fractal aggregate of size R_g, consisting of N monomers of size a. The top curve shows the scattered intensity of a single cluster, $I_{sc}(q)$, made of N monomers taking its monomers as point scatterers. The second curve is the scattered intensity of a single spherical monomer, $I_m(q)$ with radius, a. The third curve is the product of the upper curves to yield the total scattered intensity, $I_{Total}(q)$, as Eqs. (2.24) predicts. This plot is taken from Oh and Sorensen, 1999 (Oh and Sorensen 1999).

In a real experiment there is an ensemble of aggregates in a scattering volume. We just found the scattering of a single cluster of radius, R, and composed of N monomers, each monomer of radius, a, produces two length scales, R and a, in the I_{Total} vs. q graph. Now if we consider the following: an ensemble of N_c clusters, each with radius R, and composed of N monomers, each monomer of radius a, the clusters are residing in a total scattering volume of length L, and are separated by a mean nearest neighbor separation, R_{nn}. This new scenario will bring additional length scales to the total scattered intensity $I_{Total}(q)$ vs. q depending on q value. The two obvious ones are the system length L, and the clusters nearest neighbor separation, R_{nn}.

An important assumption with the scaling approach discussed so far is that the scatterers are at a fixed distance apart from each other. It is like each scatterer is a point in a lattice. This means no

fluctuation in density within the volume of the system of scatterers. To bring the scaling approach closer to the real system, Oh and Sorensen (Oh and Sorensen 1999) considered randomizing the position of the scatterers relative to the fixed lattice position. This enables not only introducing fluctuations in the density, but also adding an additional length scale of the system. For an ensemble of fractal aggregates, the randomization of the aggregates was done by considering the average distance between aggregates ξR_{nn}, where ξ is the multiplicity factor which creates the randomization. The total structure factor of an ensemble of fractal aggregates is a product of individual structure factors as

$$I_{Total}(q) = I_{cc}(q)\, I_{sc}(q)\, I_m(q) \qquad (2.25)$$

where the new term $I_{cc}(q)$ is the scattered intensity of a system of clusters in the scattering volume of size, L, taking each cluster as a point. Figure 2.6 represent a schematic diagram of the total scattered intensity of an ensemble of aggregates as introduced by Oh and Sorensen (Oh and Sorensen 1999).

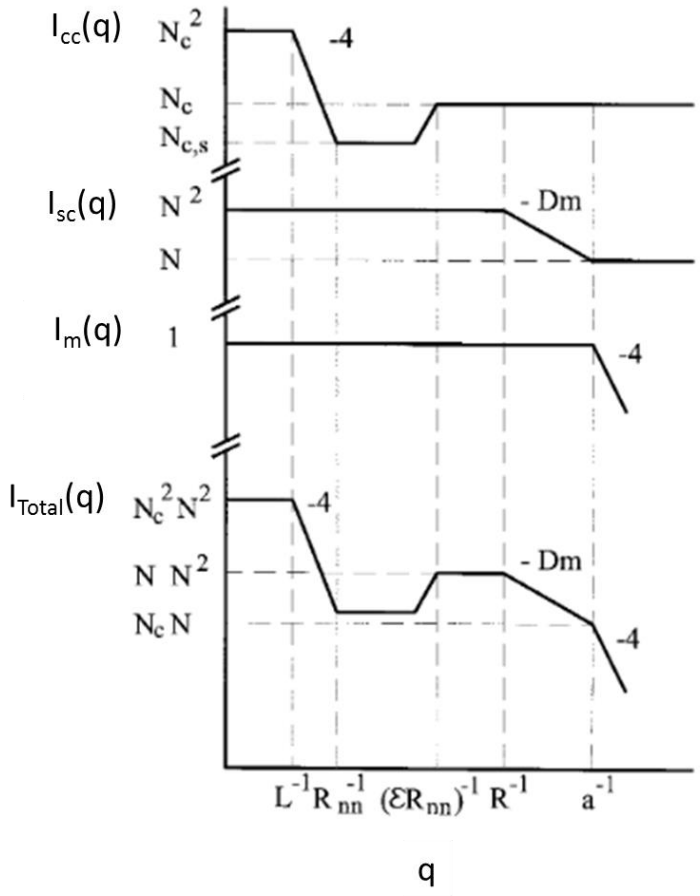

Figure 2.6 Prediction of Eq. (2.25) for a system consisting of N_c fractal aggregate of size R, of fractal dimension D_f and radius R composed of N spherical monomers of radius a. These aggregates reside in a scattering volume of size L, and have an average nearest neighbor separation R_{nn}. The upper curve is $I_{cc,}$ which represents the scattered intensity of a system of N_c clusters in the scattering volume, where each cluster is represented as a point. The second curve is the scattered intensity of a single cluster, $I_{sc}(q)$, made of N monomers taking its monomers as point. The third curve is the scattered intensity of a single spherical monomer, $I_m(q)$ with radius, a. The fourth curve is the product of the upper curves to yield the total scattered intensity, $I_{Total}(q)$. This plot is taken from Oh and Sorensen,1999 (Oh and Sorensen 1999).

2.2.2 Dynamic light scattering

If we consider Eq. 2.5 once again, but now we ask: how would the phase in the scattered field differ with time? One can imagine, initially, the phase shift due to the particle movement is very small, but with longer times, the phase difference gets bigger due to the relative motion the particles are making compared to the initial time. Hence, the electric field scattered from different particles that are moving is subject to variation in phases. So the interference pattern is fluctuating corresponding to particles' motion. Because the particle motion depends on its size and the medium properties, then the electric field phase fluctuation can give information about the particle (i.e. size) as well as the medium (i.e. viscosity). To understand the time scale of the fluctuations and characterize a random signal with itself after a delay time, t, one needs to define an electric field autocorrelation function $f_1(t)$ as

$$f_1(t) = \frac{<E_S^*(q,0)\, E_S(q,t)>}{<I(0)>} \tag{2.26a}$$

$$\sim \; < e^{i\vec{q}\,\cdot\,\vec{r}(t)} > \tag{2.26b}$$

To evaluate the average $< e^{i\vec{q}\,\cdot\,\vec{r}(t)} >$ one needs the information regarding the physical phenomena that generates fluctuations in the particle positions. This will provide the probability density P(r(t)). Then $f_1(t)$ gets the form

$$f_1(t) = \int P\big(r(t)\big)\, e^{i\vec{q}.\vec{r}(t)} d^3\vec{r}(t) \tag{2.27}$$

So $f_1(t)$ is simply the 3D Fourier transform (FT) of the probability density and is referred to as the dynamic structure factor. For example a Brownian particle with radius a has a probability density

$$P\big(r(t)\big) = \left[\frac{3}{2\pi<r^2>}\right]^{3/2} \; e^{-3r^2/2<r^2>} \tag{2.28}$$

where $< r^2 > = 6Dt$ for a Brownian particle. D denotes the translational diffusion coefficient for a particle of radius a suspended in a medium of viscosity, η, and takes the form

$$D = \frac{K_B T}{6\pi\eta a} \tag{2.29}$$

This is known as the Stokes-Einstein equation. Then, the FT of P(r) takes the form of

$$f_1(t) \sim e^{-q^2 <r^2>/6} = e^{-q^2 D\, t} = e^{-t/\tau} \tag{2.30}$$

This yields a characteristic decay time, τ, for the particle

$$\tau = (q^2\, D)^{-1} \tag{2.31}$$

In a DLS experiment we measure the intensity weighted time averaged autocorrelation function of the scattered intensity

$$g_2(t) = \frac{<I(q,0)I(q,t)>}{<I(q,0)>^2} \tag{2.32}$$

In the case of an ergodic sample, where the measured time averaged autocorrelation function is equal to the ensemble averaged autocorrelation function (Pusey and Van Megen 1989), the Siegert relation (Berne and Pecora 2000) connects the experimental measured quantity, $g_2(q,t)$, with the electric field autocorrelation function, $f_1(q,t)$ as

$$g_2(q,t) = 1 + \left| f_1(q,t) \right|^2 \tag{2.33}$$

2.2.3 Turbidity measurement

The Lambert-Beer law expresses the attenuation of a light beam with initial intensity of I_o to a new intensity I(x) while passing through a medium a distance x

$$I(x) = I_o e^{-\tau_x\, x} \tag{2.34}$$

Where τ_x is the turbidity factor that depends on the number of particles per volume, n, and the extension cross section, C_{ext}, i.e. $\tau_x = n\, C_{ext}$. The attenuated intensity now can be written as

$$I(x) = I_o e^{-n\, C_{ext}\, x} \tag{2.35}$$

Mokhtari et al. (Mokhtari, Sorensen, and Chakrabarti 2005) derived an expression for the Lambert-Beer law using the statistical approach. The assumptions were made: (1) photons act like classical

particles and (2) the photons are randomly encountering particles with a C_{ext} in the volume V. This random process has a Gaussian distribution. For such a process one can envision photons encountering a particle, but then continuing on along the same path to possibly encounter with another particle and so on before it passes the entire length x. Therefore, the possibility that a given photon has "s" encounters with particles during its travelling in the scattering volume of length x is giving by the Poisson distribution

$$P(s) = \frac{<s>^s}{s!} e^{-<s>} \tag{2.36}$$

Where <s> is the average number of scattering events, i.e. the average number of photon-particle encounters for an ensemble of photons. One can define the photon mean free path, l as the average distance traveled between scattering events

$$l = x/< s > \tag{2.37}$$

In a real turbid medium situation only the photons that have no encounter (i.e. s = 0) pass out of the far end of the scattering volume. Thus

$$P(0) = e^{-<s>} \tag{2.38}$$

Then the light intensity passing through the volume, I(x), is equal to this probability times the incident intensity, I(0), to yield

$$I(x) = I(0)e^{-<s>} \tag{3.39}$$

When Lambert-Beer law variables are compared to the statistical approach variables one may find

$$< s > = n\, C_{ext}\, x \tag{3.40}$$

with

$$l = x/(n\, C_{ext}) \tag{3.41}$$

Chapter 3 - Colloids, colloidal aggregation and gelation

3.1 Colloids and colloidal interaction

A colloidal system is a mixture consisting of at least one dispersed phase into a suspending medium. The size of the dispersed phase can range from few nanometers to few micrometers. Depending on the nature of the dispersed material and the suspending medium, we can categorize the colloids into different categories like suspension, emulsion, or soot. Common examples of colloids include milk, paint, ink, and smoke. Although they exist in nature, they are relatively easy to manufacture.

Colloidal systems have many properties that make them important to a wide range of technological applications. One of their properties is their size. For colloidal sizes up to ~ 500nm, the colloidal particle will move via Brownian motion throughout the volume. In other words, the thermal energy drives their dynamics. This makes colloidal systems very important in the field of statistical physics. For larger sized colloidal system gravitational force becomes significant and can cause sedimentation. Another reason the colloidal system is very interesting is that they provide the primary particles which we will call monomers as building blocks for more complex systems. These monomers are relatively easily prepared and stabilized, generally, by the Coulombic repulsive interaction. This type of colloidal system is called charge-stabilized colloids. This interaction can be controlled easily in the laboratory by changing the suspending medium properties. The new medium properties may induce aggregation. Changing the medium properties creates different types of interactions than the repulsive one. I will introduce the Derjaguin-Landau-Verwey-Overbeek (DLVO) interaction as it is the primary interaction that controlled the gel sample I prepared in the laboratory. In addition, I will introduce the depletion interaction which will become relevant when I discuss some of the other work in the literature, particularly the phase separation description.

3.1.1 DLVO interaction

Aggregation is induced in charge-stabilized colloids by adding a salt or by changing the pH of the solution. The interactions between charge colloids are, primarily, a result of long-ranged electrostatic repulsion, V_R, and short-ranged van der Waals attraction, V_A. Changing the ionic

strength of the solution acts to screen the electrostatic repulsion, allowing particles to come together and stick. These interactions are captured by a theory put forth by Derjaguin and Landau (Derjaguin and Landau 1941), and Verwey and Overbeek (Verwey, Overbeek, and Van Nes 1948) (DLVO). The DLVO potential is written as a sum of repulsive and attractive parts, at interparticle center-to-center separation r as

$$U_{DLVO}(r) = U_R(r) + U_A(r) \tag{3.1}$$

The screen electrostatic repulsion between two particles of diameter, σ, and a center-to-center distance separation r is given by (Victor and Hansen 1984)

$$U_R(r) = \pi\varepsilon_0\varepsilon\,\sigma\,\psi_0^2\,\frac{e^{-\kappa(x-1)}}{x} \tag{3.2}$$

where x = r/σ is the reduced distance between the centers of the two particles, ε_0 & ε are the permittivity of free space and the relative permittivity respectively, ψ_0 is the zeta potential, and κ = σ/λ_D is the reduced inverse Debye length, where λ_D is the Debye length, which for aqueous solution at 25°C, takes the following form (Israelachvili 2011)

$$\lambda_D(nm) = \begin{cases} \frac{0.304}{\sqrt{Cs}}\ , & for\ 1{:}1\ electrolyte\ like\ NaCl \quad (3.3a) \\ \frac{0.176}{\sqrt{Cs}}\ , & for\ 2{:}1\ or\ 1{:}2\ electrolytes,\ like\ MgCl_2\ and\ Na_2SO_4 \quad (3.3b) \\ \frac{0.152}{\sqrt{Cs}}\ , & for\ 2{:}2\ electrolytes\ like\ MgSO_4 \quad (3.3c) \end{cases}$$

where C_s is the salt concentration in units of molar, M.

The attraction induced by the van der Waals forces in terms of the reduced distance, x, can be expressed by

$$U_{vdW} = -\frac{A}{12}\left(\frac{1}{x^2-1} + \frac{1}{x^2} + 2\ln\left(1-\frac{1}{x^2}\right)\right) \tag{3.4}$$

The Hamaker constant, A, sets the energy scale. For polystyrene in water A = 3.16K_BT (Russel et al. 1991).

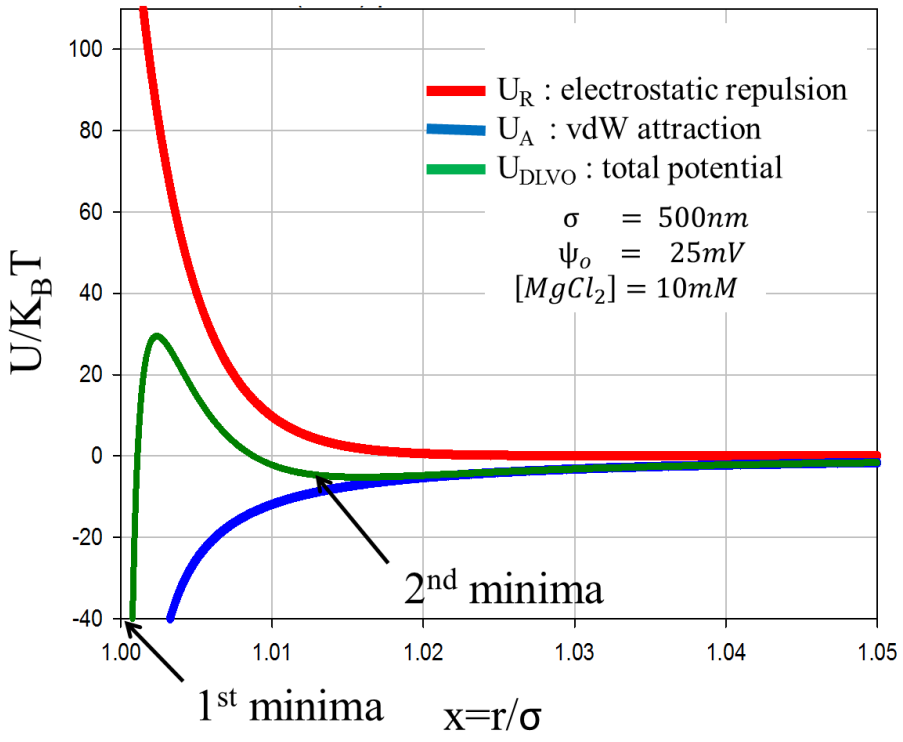

Figure 3.1 The repulsive electrostatic potential (U_R), the attractive van der Waals potential (U_A), and the total DLVO potential U_{DLVO} as a function of the reduced distance x=r/σ.

3.1.2 Depletion interaction

Depletion interaction causes instability of colloidal particle which occurs due to the presence of non-adsorbing polymer. This creates an attractive interaction between particles through polymer-induced depletion interaction. There is a depletion zone around each colloid of thickness equal to the polymer radius of gyration, from which the polymers are excluded between two nearby particles. The exclusion of the polymer creates an unbalanced osmotic pressure pushing the particles together. This results in an effective interparticle attractive interaction. The strength of this interaction can be controlled by the concentration of the non-adsorbing polymer and the ratio of the particle size to the polymer size (Asakura and Oosawa 1958),

$$\frac{U}{K_B T} = P(c_p) V_{overlap}(r) \qquad (3.5)$$

where $P(c_p)$ is the osmotic pressure of the polymer as a function of the polymer concentration c_p, and $V_{overlap}(r)$ is the volume of overlapping depletion zones as a function of particles' separation.

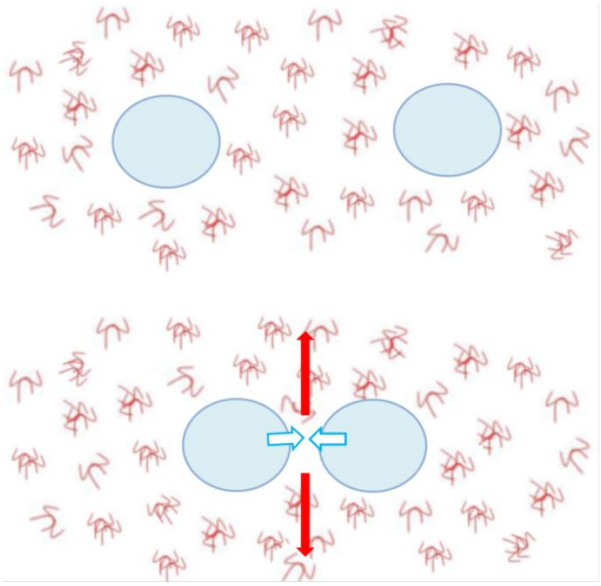

Figure 3.2 A schematic diagram for the depletion interaction.

3.2 Fractal colloidal aggregates

In Chapter 2, we discussed the characters of fractal aggregates. If non-coalescing colloidal particles are destabilized, they may form ramified fractal aggregates. Fractal aggregates have the unique property that their mass, N, scales with their average radius of gyration, R_g, with a scaling dimension: the fractal dimension D_f. D_f is smaller than the spatial dimension, d. The fractal mass-radius scaling law, as described in Eq. (2.3), is

$$N = k_o \left(\frac{R_g}{a}\right)^{D_f} \tag{3.6}$$

Traditionally, fractal colloidal aggregates can be classified into two asymptotic regimes (Lin et al. 1989c; Weitz et al. 1985): diffusion limited cluster-cluster aggregation (DLCA) and reaction limited cluster-cluster aggregation (RLCA). In both models the clusters are allowed to diffuse, collide, and stick together to form larger clusters (Kolb, Botet, and Jullien 1983; Meakin 1987). The fundamental difference between these two limiting models is how many times the clusters need to collide before they stick. This determines their sticking probability, P, which is governed by the interaction strength that was induced to destabilize the particles and start the aggregation

process. For the DLVO potential, for example, if the surface charge of the monomers is fully screened, then when monomers (or monomers in different clusters) come into contact with each other, they form bonds and stick at contact. This results in a fast aggregation, the DLCA aggregation, due to sticking probability P = 1. The salt concentration used to destabilize the colloid and results in P = 1 is called the critical coagulation concentration, ccc. This process is purely controlled by the mutual diffusion between the particles (or clusters) and results in an aggregate with a fractal dimension $D_f \sim 1.8$ (Asnaghi et al., 1994; Lin et al., 1989a; Weitz et al., 1985). On the other hand, for the RLCA model, the monomers, or monomers in different clusters, still follow the random walk (Brownian motion), but they don't successfully bond each time they come into contact. Instead, they continue in their maneuver and many collisions may be required before they form a joint cluster. This is the case when the surface charge of monomers is only partially screened. The sticking probability is controlled by the residual interaction energy barrier that the particles have to overcome in order to fill into the short range, strongly attractive potential well. This creates a slow aggregates, RLCA aggregates, where $P << 1$ and the resulting fractal dimension can vary between $D_f \sim 2.05$ (Lin et al. 1989c; Weitz et al. 1985) and $D_f \sim 2.14$ (Lin et al. 1989c). In between these two asymptotic regimes there is an intermediate regime where aggregates with $0 < P < 1$ resulting in different fractal dimensions. All aggregates with $P \neq 1$ are called slow aggregates. The value of the fractal dimension indicates the cluster morphology, and it is dependent on the sticking probability of the aggregates. This can be understood that for DLCA aggregates the clusters have open branches which results in smaller D_f values. This is because of the high probability of sticking between two monomers in two colliding clusters, such that the clusters don't have the chance to penetrate each other as a result a tenuous structure is formed with lower D_f value. On the other hand for RLCA, where the sticking probability is very low, the clusters have the chance to wander and penetrate into the interior of each other until they form a bond. This results in a denser aggregate with higher value of D_f than for the DLCA. That is why the D_f values are important to identify the morphology of the aggregates. In Chapter 2, Fig. 2.2 shows the different asymptotic types of aggregation models, and it shows the RLCA aggregate in (b) clearly denser than the DLCA one in (a).

The aggregation rate is controlled by the aggregation kernel K. For example; if two monomers come together and stick they form a doublet. The aggregation kernel for doublet formation is K_{11}. The aggregation process is often quantified in terms of the stability ratio W. Where W defined as

the ratio between the kernel of doublet formation for the fast aggregation, $K_{11,fast}$, to the kernel of doublet formation for the slow aggregation $K_{11,slow}$. This gives

$$W = K_{11,fast} / K_{11,slow} \quad (3.7a)$$

A lot of times the kernel subscript 11, which indicates doublet formation, is dropped to simply give

$$W = K_{fast} / K_{slow} \quad (3.7b)$$

The fast aggregation kernel, K_{fast}, is sometimes referred to as the Smoluchowski kernel, K_{SE}, which is a constant kernel, $K_{fast\ or\ SE} = 8K_B T/3\eta$, where K_B is the Boltzmann constant, T is the temperature in Kelvin, and η is the viscosity of the suspending medium. Further discussion of the aggregation kernel will follow in 3.3.1. The stability ratio can be understood as the inverse of collision efficiency, or the inverse sticking probability for two colliding particles to permanently stick together on contact. So for pure DLCA or fast aggregation W = 1, whereas for slow aggregation W > 1. The specific value of W is very sensitive to the initial conditions of the aggregation and it can provide evidence to what kind of aggregates the system is forming.

It is worth alerting the reader that despite the ability of the stability ratio to pin point the type of aggregates are forming, it is a common practice in the literature to refer to the fractal dimension, a less significant indicator, to determine the type of the aggregates. For example aggregates with D_f = 1.7 and 1.85 are both considered to be formed via the DLCA model (Asnaghi, Carpineti, and Giglio 1994b; Mokhtari et al. 2008), meanwhile D_f = 1.9 is considered to be in an intermediate regime between DLCA and RLCA (Cipelletti et al. 2000a). And for D_f = 2.05 and higher (Asnaghi, Carpineti, and Giglio 1994b) the system is considered to form via the RLCA model. These considerations are made solely on the D_f value regardless of the stability ratio, which is not always measured. Through this thesis, if W = 1, then I will refer to the system as in the pure DLCA aggregation or fast aggregation. Otherwise the system is formed via the slow aggregation. Slow aggregation can still be called DLCA if W > 1 (but not W >> 1) like the case of aggregates with D_f = 1.85. For W >> 1, I will refer to the system to be formed via the RLCA aggregation. There is no specific value in literature to define these limits. The practice of finding W turned out to be very critical in our analysis because the D_f values are a function of W. One of my goals in this work is to remind the researchers in this field of the importance of measuring W, which is often ignored.

3.3 Different descriptions of sol-to-gel transition

If aggregation is induced and allowed to proceed to form a ramified cluster that span the total system volume, then a gel is formed. The gel process is also referred to as gelation or the sol-to-gel transition. There are three major descriptions of the sol-to-gel transition: the kinetic description, the percolation description, and the thermodynamic phase separation description. Here I briefly present these three descriptions of gelation.

3.3.1 Kinetics description

The fundamental equation to describe the aggregation kinetics is the Smoluchowski equation (SE) (M. von Smoluchowski 1916), which is described as

$$\frac{dn_N}{dt} = \frac{1}{2}\sum_{i+j=N} K_{ij} n_i n_j - n_N \sum_{i=1} K_{iN} n_i \tag{3.8}$$

Where n_N is the number density of clusters with N monomers in a cluster, N-mers, and K_{ij} is the aggregation kernel. The aggregation kernel sets the collision rate between i-mer and j-mer clusters to form a new N-mer cluster, thus K_{ij} for a system sets the aggregation rate. The first term on the RHS of the equation represents the average rate at which N-mers are formed from i- & j-mers. The second term represents the rate at which N-mers disappear when binding with i-mers to form bigger cluster of size (N+i)-mers. In this representation fragmentation is not feasible. In addition the SE is based on a mean field theory which assumes no correlation between clusters. Even though finding the exact solution for SE is not always feasible, a scaling solution can be found because, for many physical situations, K_{ij} is a homogeneous function (Leyvraz and Tschudi 1982), defined as

$$K(ci, cj) = c^{\lambda} K(i, j) \tag{3.9}$$

where, c, is a constant and λ is the degree of homogeneity.

If we express the diffusion coefficient for an aggregate of i-mers using Stokes-Einstein relation, $D_i = K_B T / 6\pi\eta R_{h,i}$, where $R_{h,i}$ is the hydrodynamic radius, then the most general form of the

aggregation kernel is defined in the following format (Ball et al. 1987; Family, Meakin, and Vicsek 1985; Lattuada et al. 2003; Sandkühler et al. 2003)

$$K_{ij} = \frac{K_{fast}}{W} B_{ij}\, p_{ij} \tag{3.10}$$

Where $K_{fast} = 8\, K_B T/3\eta$ is the constant kernel and it accounts for the thermal energy of primary particles and clusters. The B_{ij} term incorporates the aggregates' collision radii R_c and the aggregates' hydrodynamic radius R_h in the following manner

$$B_{ij} = \frac{1}{4} (R_{c,i} + R_{c,j})(R_{h,i}^{-1} + R_{h,j}^{-1}) \tag{3.11}$$

If we assume spherical aggregates, with collision radius, hydrodynamic radius, and radius of gyration are all equal; then, using the mass-radius relation Eq. (3.6), the B_{ij} term can relate the aggregate structure and size via their dependence of the fractal dimension, D_f in the following manner

$$B_{ij} = \frac{1}{4} \left(i^{1/D_f} + j^{1/D_f}\right)\left(i^{-1/D_f} + j^{-1/D_f}\right) \tag{3.12}$$

The term $\left(i^{1/D_f} + j^{1/D_f}\right)$ represents the combined "cross-section" of an i-mer/j-mer collision, while $\left(i^{-1/D_f} + j^{-1/D_f}\right)$ expresses the size dependence of the mutual diffusion coefficient of the i-mer and j-mer. The product $K_{fast}B_{ij}$ is in fact the general kernel for pure DLCA fractal aggregation, or fast aggregation, without the assumption of equal sized aggregates. It should be noted that P and W terms are both equal to unity for pure DLCA aggregates. This corresponds to the maximum rate of aggregation achievable due to the fact that all collisions are successful in forming new aggregates. If we assumed for the pure DLCA model equal sized aggregates, then B_{ij} = 1, and K → $K_{fast\ or\ SE}$.

The stability ratio W discussed in Eq. (3.7), also known as Fuch stability ratio (Melis et al. 1999), applies mostly to primary particles, but not for aggregates. It has been verified experimentally that the reactivity of aggregates increases with their masses (Broide and Cohen 1990; Lin, Lindsay, Weitz, Ball, et al. 1990), and therefore, an additional factor, P_{ij}, has been introduced to the general form of any aggregation kernel other than the pure DLCA kernel. This P_{ij} term shows the dependence on the i-mer and the j-mer clusters. A physical picture one may come up with to justify this product P_{ij} is as follows: the attractive force in the DLVO potential – the van der Waals force – is a short range force. The screened electrostatic repulsion can also be considered as a short range

force (Israelachvili 2011). Due to the short range effect of these forces, one could assume to a first order approximation that the energy barrier to be overcome upon aggregation is determined only by the two primary particles in the two aggregates which are colliding. Meanwhile the neighboring particles play no role. In this case the collision between two aggregates can be described as a process controlled by the collision of the two primary particles belonging to the aggregates. Accordingly, the rate of aggregation of two clusters is proportional to the Fuch stability ratio of primary particles and to the product of the number of primary particles of the two clusters that can participate in the collision process. The latter is related to the mass and the structure of the clusters, and is therefore modelled in the P_{ij} term. The P_{ij} term is usually associated with the slow aggregates. This is because only a fraction of the collisions are successful in forming new clusters due to the incomplete screening of the repulsive forces between the particles. For pure DLCA aggregates, $P_{ij} = 1$.

There are many proposed formats for P_{ij} (Ball et al. 1987; Family, Meakin, and Vicsek 1985; Odriozola et al. 2001). It was found that the most acceptable expressions for the P_{ij} format that fits the experimental data (Lattuada et al. 2003; Sandkühler et al. 2003) was the product and Odriozola formats. The product format of P_{ij}, put forth by Family et al. (Family, Meakin, and Vicsek 1985), is expressed as

$$P_{ij} = (ij)^{\lambda} \tag{3.13}$$

The P_{ij} format put forth by Odriozola et al. (Odriozola et al. 2001) is expressed as

$$P_{ij} = \frac{(ij)^{\lambda}}{1+ W^{-1}((ij)^{\lambda}-1)} \tag{3.14}$$

Note that for $\lambda = 0$ both the product and Odriozola's format of $P_{ij} \rightarrow 1$, as expected for pure DLCA. Notice that Odriozola's P_{ij} goes to the product format if the limit of the stability ratio is sufficiently large and if the masses of the colliding clusters, i and j, are not very large. These conditions can be achieved experimentally for a system deep in the RLCA regime (such that W is sufficiently large) and if the system is in the early stages of aggregation such that clusters are not very large. According to Odriozola et al., their functionality of P_{ij} fits the complete aggregation regimes, the DLCA, the RLCA, and all the intermediate regimes, in a higher precision than the product kernel.

The stage of aggregation for a given system may be characterized by the cluster size distribution, $n = (n_1, n_2, \ldots . , n_N, \ldots)$ where n_N denotes the number of N-size clusters. The homogeneity of the

kernel, λ, determines the cluster size distribution, meanwhile the kinetics determine the cluster growth rate. Linking the size distribution of the aggregates with their kinetics is not necessarily realizable due to the complexity of the system. With the assumptions: all monomers are part of a cluster and aggregation produces equal sized clusters with same homogenous kernel, one can simplify the scaling approach and the SE becomes

$$\frac{dn_N}{dt} = -n_N^2\, K(N,N) \tag{3.15}$$

Using Eq. (3.9), one can rewrite Eq. (3.15) as

$$\frac{dn_N}{dt} = -n_N^2\ N^{\lambda} K(1,1) \tag{3.16}$$

The cluster size N changes with time, and the number density can be written as $n_N(t) = n_1(0)/N(t)$. Finding $dn_N(t)/dt$ and substituting it in Eq.(3.16) gives

$$N(t)^{-\lambda} dN = n_1(0)\, K(1,1)\, dt \tag{3.17}$$

Integrating gives

$$N(t) \sim (t + t_o)^z \tag{3.18}$$

Where z is the kinetic exponent $z = 1/(1-\lambda)$ (van Dongen and Ernst 1985). And $t_o = z/K(1,1)n_1(0)$, which is the time required for doublets formation. The kernel $K(1,1) = K_{11}$ is the kernel of forming doublets. This kernel represents the collision of sticking probability P = 1. This is due to the assumption that all monomers are eventually part of a cluster, which can be achieved experimentally only if the attractive interaction is strong, Thus, P = 1.

The homogeneity λ is a key parameter in the scaling distribution of the clusters and in the kinetics through the kinetics exponent z, which describes the asymptotic behavior of the cluster size. The cluster size increases with power law in time; $N(t) \sim t^z$. For the DLCA model (where P ~ 1) it is found that clusters grow in a power law format in time with z = 1 and λ = 0 (Kolb, Botet, and Jullien 1983; Kolb and Jullien 1984; J E Martin and Adolf 1991; Meakin 1987). On the other hand, for the RLCA aggregates the kinetics is very different than the DLCA aggregates. A solution of SE for RLCA model are best described as exponential, $\overline{N} \sim e^{At}$, where A is a constant depends on the sticking probability and the time between collisions. Light scattering experiments on colloids found an exponential growth of the cluster mass (Lin et al. 1989b; Weitz et al. 1985). The homogeneity value for RLCA is a

controversial value in the literature. It was found to take values from 0.4 - 1 (Ball et al. 1987; Family, Meakin, and Vicsek 1985; Lattuada et al. 2003; Lin, Lindsay, Weitz, Ball, et al. 1990; Lin et al. 1989b; Olivier and Sorensen 1990). It is important to mention that the z and λ values are always reported as a pair for the DLCA aggregates, with the standard values mentioned above for clusters that satisfy the SE. In the case of RLCA, the kinetic exponent z is not always reported like the case of the DLCA.

The less certain values of λ in literature for the RLCA model compared to the DLCA model might be due to the following reasons. First, aggregation phenomena itself is a complex process which does not always have an exact solution for the cluster distribution in SE. Second, the existing scaling solutions show that for DLCA the size distribution of the clusters is less polydispersed than the RLCA size distribution. One might think the narrow polydispersity in DLCA leads to a scaling approach with a closer representation of the average behavior of the system than the RLCA ones. The difference in polydispersity between the RLCA and DLCA models can be understood due to the sticking probability. With P = 1 the system aggregate fast, leaving less opportunities for the aggregates to create a wide size distribution of sizes like the case of P << 1 for RLCA. Third, even though the aggregation is described by the two asymptotic regimes, DLCA and RLCA, the pure DLCA boundary is sharply defined when the critical coagulation concentration of salt is used. This yield P exactly = 1, which is a unique and achievable P value experimentally. But for the RLCA, the situation is different as P << 1 is not sharply defined. How much is much less than one really is? As mentioned above there is an intermediate regime which may be sometimes mixed with the deep RLCA regime. Especially that the stability ratio is not always measured for the aggregation studies. Furthermore, there exist experimental data that suggest the crossover from RLCA kinetics to DLCA kinetics after some times in the aggregation process (Asnaghi, Carpineti, and Giglio 1994b; Olivier and Sorensen 1990; Wu, Xie, and Morbidelli 2013). So for the various λ values we reported above, were they measured before, while, or after the crossover? It is not clear.

The less certain values of homogeneity constant, λ, for RLCA compared to the DLCA in literature, with the above proposed reasons, suggest the need for systematic experimental and simulation work for a wide range of P values, or experimentally speaking, stability ratio values, i.e. W~1/P. The goal is to start from the pure DLCA regime and passing through the intermediate regime deep into the RLCA regime. This will test the hypothesis put by Olivier and Sorensen that there exist a

continuum values of λ (Olivier and Sorensen 1990). In addition, such a systematic study will resolve, or at least help resolving the crossover from RLCA to DLCA aggregation and answer some questions that I found valuable. Such as: what cluster size compared to the monomer size this crossover occurs? And how does z and λ change accordingly?

The relation of the kinetic exponent, z, and the size distribution homogeneity, λ, i.e. $z = 1/(1-\lambda)$ is, strictly speaking, for aggregates far away from each other, i.e. clusters are in a dilute regime. This satisfies the mean field SE condition of no correlation between clusters. But a quick look into why a system gel shows that clusters, if allowed to continue aggregation, are eventually entered into a dense regime before they form a gel. It is important to distinguish the fact that not all types of aggregation may form a gel. Gels are formed due to the fractal nature of non-coalescing fractal aggregates. This fractal nature provides the system with two independent length scales, the average radius of gyration, R_g, and the average nearest neighbor separation, R_{nn}. From Eq. (3.6) one can write $R_g \sim N^{1/D_f}$. Meanwhile, R_{nn} scales with the average number of the clusters, N_c, in a system of volume V by the spatial dimension, d, i.e. $R_{nn} \sim (V/N_c)^{1/d}$. In a closed system, the number of clusters is directly proportional to the total number of monomers, N_m. With the assumption that all clusters have the same size, one can write $N_c = N_m/N$ and $R_{nn} \sim N^{1/d}$. Since $d > D_f$ then R_g will increase faster than R_{nn} and eventually R_g will approach R_{nn}, and these two length scales become comparable to each other. The ratio R_{nn}/R_g will decrease with increasing cluster masses. We define the early stage of aggregation as the cluster-dilute regime, where clusters are far apart from each other i.e $R_{nn}/R_g >> 1$. But with time the clusters grow such that $R_{nn}/R_g \sim 10$ in which we say the system is in the cluster-dense regime. The clusters will continue to grow up to the point where $R_{nn}/R_g \sim 2$, which defines the point where the system starts to gel (Kolb, Botet, and Jullien 1983; Vicsek 1989). This physical picture is illustrated in Fig. 3.3. This picture is in contrast with coalescing particles, for example water droplets. The size of the droplets, R_g, and the nearest neighbor separation R_{nn} both are proportional to $N^{1/d}$. Thus, the ratios of these two length scales of the coalescing droplets will grow parallel at all times, and hence never gel.

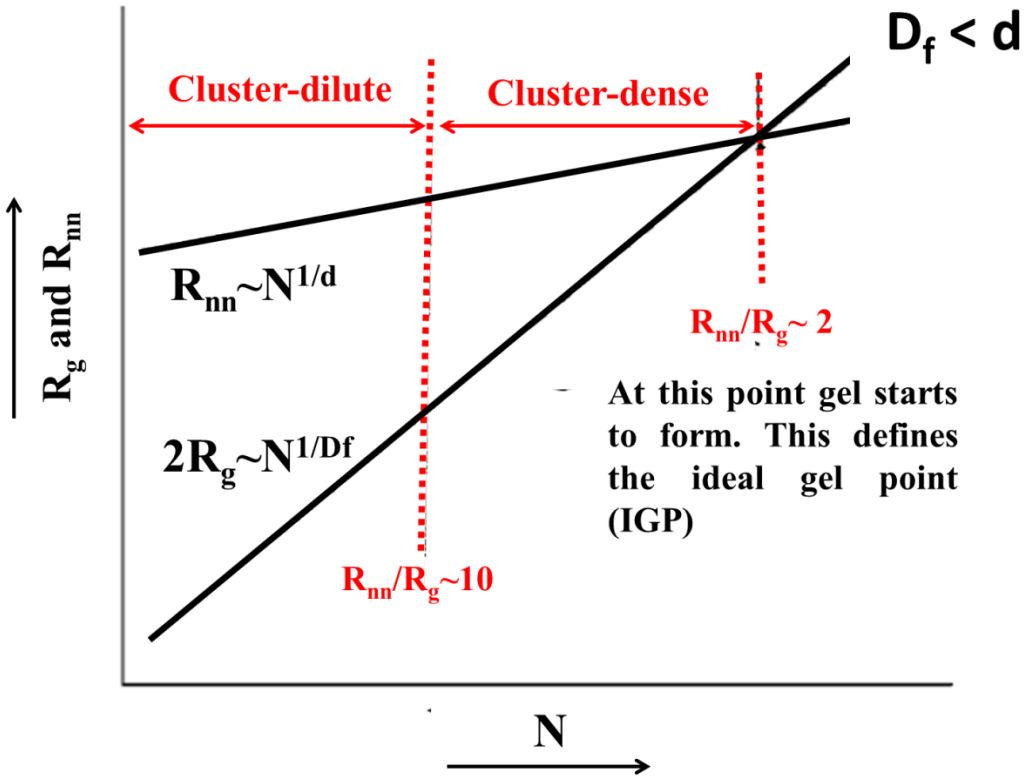

Figure 3.3 A schematic representation of the different growth rates of each of $2R_g$ and R_{nn} as a function of the average number of monomers per cluster N. The limiting cases for the cluster-dilute, the cluster-dense, and the starting of the gel point are illustrated. We will soon introduce the ideal gel point (IGP) at $R_{nn}/R_g \sim 2$. This figure is adapted from (Sorensen and Chakrabarti 2011).

The fractal aggregates evolution from the cluster-dilute to the cluster-dense regime has been strongly suggested in both simulations (Fry et al. 2002; Gimel, Nicolai, and Durand 1999; Gimel, Durand, and Nicolai 1995; Hasmy and Jullien 1995; Heine and Pratsinis 2007; Rottereau et al. 2004a; 2004b) and experiments (R. Dhaubhadel, Chakrabarti, and Sorensen 2009; R. Dhaubhadel et al. 2006; C. M. Sorensen et al. 1998; Wu et al. 2005; Wu, Xie, and Morbidelli 2013). At the time the kinetics in the cluster-dilute regime is well established especially for the DLCA model, this is not necessarily true for the cluster-dense regime, and to a lesser degree for the gelling regime. Furthermore, these simulations and experimental observations were not only limited to the change of the aggregation kinetics, but also for their morphologies (Fry et al. 2004; Gimel, Nicolai, and Durand 1999; Wongyo Kim et al. 2006; Mokhtari et al. 2008; Rottereau et al. 2004a; 2004b), and most recently their size distribution (P. Liu et al. 2019). Our group established a relatively new

theory rooted from the kinetic description of aggregation named the ideal gel point (IGP) theory. For the rest of this section I will introduce the IGP theory categorized by the three aspects I alluded to in this paragraph (i.e. the kinetics, morphology, and size distribution aspects) along with the explanations offered by the IGP theory.

3.3.1.1 Ideal Gel Point theory: The Kinetics Aspect

The IGP theory advocates for the importance of the two fundamental length scales, R_g and R_{nn}, in describing the kinetics of the sol-to-gel transition. The IGP specifies three distinct aggregation regimes depending on the ratio R_{nn}/R_g. First is the cluster-dilute regime where $R_{nn}/R_g \gg 1$ which has been well understood (Smoluchowski 1916) and yields z = 1 and λ = 0 for the DLCA model (Kolb, Botet, and Jullien 1983; Kolb and Jullien 1984; J E Martin and Adolf 1991; Meakin 1987). The system evolves from the cluster-dilute to the cluster-dense regime at $R_{nn}/R_g \lesssim 10$, with notably enhanced kinetics ((R. Dhaubhadel, Chakrabarti, and Sorensen 2009; Rajan Dhaubhadel et al. 2007; R. Dhaubhadel et al. 2006; Fry et al. 2004; 2002; Wongyo Kim et al. 2006; W. Kim, Sorensen, and Chakrabarti 2004). Fry et al. simulated the evolution of clusters from cluster-dilute to cluster-dense and finally formed a gel. They monitor the evolution of z in two ways as a function of the normalized free volume, Ω, (sometimes they alternate with $f_{v,c} = 1-\Omega$). They found the kinetic exponent through the kinetic scaling of $N \sim t^z$ and called z_{kin}. At the same time they obtained the homogeneity of the system from the size distribution of the clusters and they called λ_{sd}. From λ_{sd} they obtained z_{sd} using the mean field relation of $z = 1/(1-\lambda)$. Figure 3.4 shows the evolution of the kinetic exponent z as a function of clusters volume fraction, $f_{v,c}$, for different monomer volume fractions, $f_{v,m}$. This figure clearly shows that both z_{kin} and z_{sd} evolve from the initial value of ~1 for the cluster-dilute regime to enhanced values bigger than unity for the cluster-dense regime. The cluster-dense regime can be quantified when the cluster volume fraction, $f_{v,c}$~1-10%. The aggregates continue to grow up to the point where they fill the entire volume and neighboring clusters start to touch ($i.e\ R_{nn}/R_g \sim 2$) making $f_{v,c} \sim 1$ (Fry et al. 2002; C. M. Sorensen and Chakrabarti 2011). At this volume fraction of clusters, the IGP theory defines an ideal gel point (IGP). The maximum z value at the IGP ~ 2, which corresponds to λ = ½ as shown in the big circle in Fig. 3.4. The good agreement between z_{kin} and z_{sd} suggests that the mean field relation $z = 1/(1-\lambda)$ still holds even in the cluster-dense regime. For aggregates formed via

diffusion limited cluster aggregation (DLCA), the fractal dimension is $D_f = 1.8$, and $R_{nn}/R_g \sim 2.3$ (C. M. Sorensen and Chakrabarti 2011).

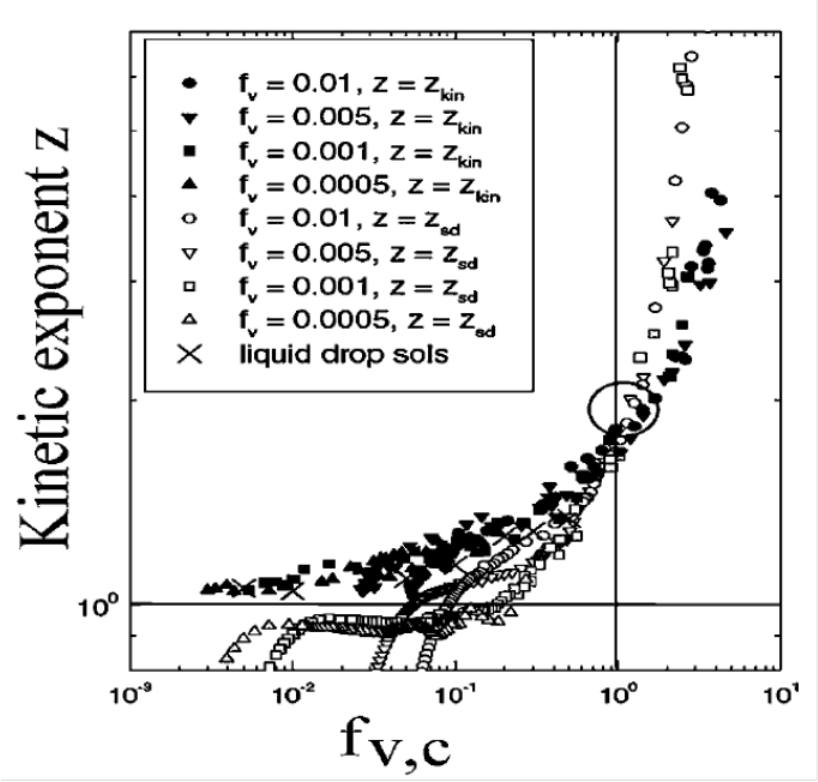

Figure 3.4 Shows the kinetic exponent z_{kin} obtained directly from the kinetics, and z_{sd} obtained from the size distribution homogeneity λ via the relation $z = 1/(1-\lambda)$. Both z_{kin} and z_{sd} graphed vs. $f_{v,c}$. The large open circle marks the ideal gel point (IGP) where $R_{nn} = 2R_g$. This figure obtained from (Fry et al. 2002).

There is a significant experimental literature that supports the description above. Enhanced kinetics have been observed during salt induced aggregation of spherical colloids (Carpineti and Giglio 1992; Wu, Xie, and Morbidelli 2013) and aqueous suspension of proteins (Wu, Xie, and Morbidelli 2005). In these works the enhanced kinetics was not fully explained. Enhanced aggregation kinetics was observed in a dense soot aerosol of a heavily sooting flame (C. M. Sorensen et al. 1998). Dhaubhadel et al. (R. Dhaubhadel et al. 2006) studied dense aerosol aggregation to find enhanced kinetics and z values as high as 2.3. Another scattering experiment on soot was done by the same group of Dhaubhadel et al. (R. Dhaubhadel, Chakrabarti, and Sorensen 2009). The particle size was 38nm. SASLS measurements were performed and temporal evolution of the structure factor was obtained. This provides a tool to measure R_g vs. t. For fractal aggregates $N \sim R_g^{Df}$, and from the kinetic theory $N \sim t^z$, this gives that $R_g \sim t^{z/Df}$. With a known D_f, the z value can

be found from the slope of R_g vs. t in a log-log scale. Figure 3.5 shows the experimental z values and the corresponding λ for different monomer volume fractions. The kinetic exponent increases from cluster-dilute (z = 1, λ = 0 for DLCA for small f_{vm}) to cluster- dense (z up to 1.7 and λ = 0.8 for higher f_{vm}). These results are consistent with the simulation work discussed above.

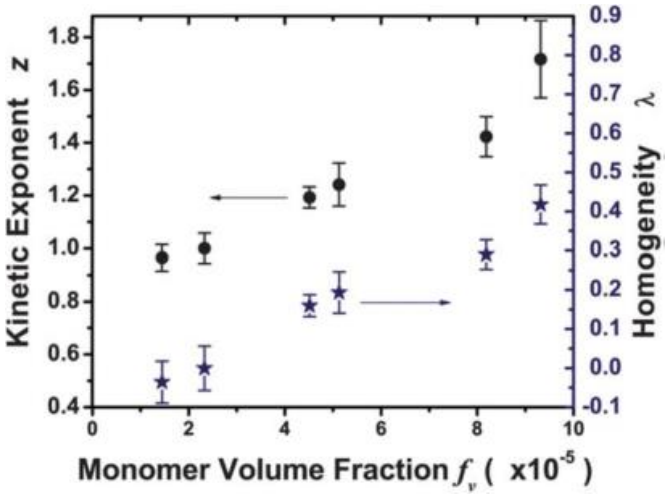

Figure 3.5 The experimental kinetic exponent z and the corresponding inferred kernel homogeneity λ graphed vs. different monomer volume fractions for gelling soot aerosols. This figure obtained from (R. Dhaubhadel, Chakrabarti, and Sorensen 2009).

A scaling argument can be used to find the functionality of the aggregation kernel, K, in the limiting cases, and hence determine the homogeneity, λ. (Fry et al. 2002; Kolb 1984) This scaling will further provide physical insights on the necessity of the existence of two length scales, R_g and R_{nn}, in the gelation process. The aggregation kernel, K, can be defined as the rate of collision between two clusters. Thus it depends on the cross-sectional area, A_c, of the clusters and their relative speed, v. Therefore, $K \sim A_c v$, gives the proper dimensions [L^3/t]. At the early stages of the aggregation, in the cluster-dilute regime, R_g is the main length scale. Clusters move through Brownian diffusion with $v \sim D/R_g$, where D is the diffusion coefficient. This gives $K \sim DR_g$, and this result was first derived rigorously by Smoluchowski (Smoluchowski 1916). But $D \sim 1/R_g$, thus K ~ 1, which gives λ = 0 the well-known results for the dilute case. As clusters keep growing, the volume fraction of the clusters will increase and the crowded state is inevitable. In the cluster-dense regime, the R_{nn} is the length that sets up the relative speed between clusters, such that $v \sim D/R_{nn}$. This yields $K \sim R_g/R_{nn} \sim N^{(1/Df-1/d)}$, and hence $\lambda = 1/D_f - 1/d$ = 0.23 for D_f = 1.8. Unlike

the dilute case, where clusters diffuse in an isotropic fashion, at the gel point the clusters move very short distances compared to their size before they collide. Thus, their motion is Ballistic-like. Here the relative speed is properly described by the energy equipartition, which gives $v \sim N^{-0.5}$. In such proximity, the clusters see branches and finger-like detail of the neighboring clusters. So the cross sectional area is properly replaced by the aggregate surface area, A_s. Additionally, for fractal aggregates, all the monomers constitute an aggregate are considered on the surface i.e. $A_s \sim N$. This will yield $K \sim N.N^{-0.5} \sim N^{0.5}$, with $\lambda = 0.5$, which corresponds to $z = 2$ as indicated by the simulations at the ideal gel point in Fig.3.5.

The situation, at which the aggregates fill the available volume and "touch," i.e. when the aggregate volume fraction equals unity, is expected to be a special point in the sol-to-gel transition. Although the exact definition of the volume fraction is somewhat arbitrary, to calculate it, we have chosen to assume that all the aggregates are the same size, a size given by their perimeter radius, $R_p = [(D_f+2)/D_f]^{1/2}R_g$, and that they have spherical symmetry. These conditions could vary, but the overall functionalities on R_g and D_f should be good. This definition worked very well in our simulations (Fry et al. 2004; C. M. Sorensen and Chakrabarti 2011). We shall call the point where this volume fraction equals unity the ideal gel point (IGP). With this definition and based on our previous work, the IGP theory identifies three regimes of aggregation kinetics (C. M. Sorensen and Chakrabarti 2011). Initially, if the monomer volume fraction is small, the destabilized sol (colloid or aerosol) will find $R_{nn} >> R_g$, the cluster-dilute regime (Meakin 1987; R. Jullien 1987; Kolb, Botet, and Jullien 1983; J E Martin and Adolf 1991) with two independent length scales, R_g and R_{nn}. As aggregation proceeds, R_g will grow faster than R_{nn} because $D_f < d$; eventually, these two length scales will become comparable to each other. Hence they act as one effective length scale and enter the cluster-dense regime (R. Dhaubhadel et al. 2006; Fry et al. 2002). Ultimately, with aggregation, the IGP is reached (C. M. Sorensen and Chakrabarti 2011). The condition that the aggregate volume fraction, as described above, equals unity at the IGP leads to the aggregate size at the IGP, $R_{g,G}$, as

$$R_{g,G} = a[\, f_{v,m}^{-1} k_o (D_f / (2+D_f))^{3/2}\,]^{1/(3-D_f)} \tag{3.19}$$

Where $f_{v,m}$ is the initial monomer volume fraction, which is conserved throughout the aggregation.

An important question in the aggregation kinetic is: when does the system gel? The gel time is not clearly defined in the literature. As there is the time at which the gel starts to form, i.e. $R_{nn} \sim 2R_g$ and this defines the IGP, and there is a final gel point (FGP) where the final gel state is already reached. In this discussion, we are dealing with the time at which the system starts gelling, i.e. the IGP. Here, I will present two methods of finding t_{gel}. One I will name it the KSU method, the other is the Bremer method. To do so we go back to SE with the assumption of a constant kernel and same sized aggregates, which simplifies SE to

$$\frac{dn}{dt} = -Kn^2 \tag{3.20}$$

With a solution of

$$n = (Kt)^{-1} \tag{3.21}$$

One may write n in terms of the aggregates size and initial monomer volume fraction by combining Eq. (3.6) with the fact that $n = N_c/V = N_m/(NV)$ to yeild

$$n = \frac{3}{4\pi} f_{vm}\, a^{-3} k_0^{-1} \left(\frac{R_g}{a}\right)^{-D_f} \tag{3.22}$$

Starting with the KSU method, one may substitute Eq. (3.22) into Eq. (3.21), with the use of the definition of $R_{g,G,}$ as described in Eq. (3.19), an expression for the gel time at IGP, t_{gel} can be reached

$$t_{gel} = \frac{4\pi}{3} k_o^{3/(3-D_f)} \left(\frac{D_f}{2+D_f}\right)^{3D_f/2(3-D_f)} {K_{fast}}^{-1} a^3 \, f_{vm}^{-3/(3-D_f)} \tag{3.23}$$

For the pure DLCA model, the aggregation kernel $K_{fast} = 8k_BT/3\eta$ with the assumption of spherical and equal sized clusters.

Experimentally, it is more common to deal with the stability ratio (W) than the kernel, where W is the ratio of the fast aggregation kernel to the slow aggregation kernel for doublet formation, $W = K_{fast}/K_{slow}$. For pure DLCA, W=1 and Eq. (3.23) can be written in the most general form as

$$t_{gel} = W.\ \frac{4\pi}{3} k_o^{3/(3-D_f)} \left(\frac{D_f}{2+D_f}\right)^{3D_f/2(3-D_f)} {K_{fast}}^{-1} a^3 \, f_{vm}^{-3/(3-D_f)} \tag{3.24}$$

The second attempt is the Bremer method (L. G. B. Bremer, Walstra, and van Vliet 1995). Starting from the SE, with the assumption of spherical and equal sized particles, they obtained the same

format of Eq. (3.20) above, except their representation of the aggregation kernel was different. Bremer's aggregation kernel, K_{Bremer}, takes the following format:

$$K_{Bremer} = \frac{8\,A\,K_B T}{3\eta} = A\,K_{fast} \tag{3.25}$$

Where A is a constant factor which is for pure DLCA takes the value of 1, and defined by Bremer as

$$A = \frac{BP}{4W} \tag{3.26}$$

When we compare K_{Bremer} with the general kernel, K_{ij}, of Eq. (3.10) we find A as introduced by Bremer represents

$$A = \frac{B_{ij}P_{ij}}{W} \tag{3.27}$$

With B/4 = Bij when comparing Eq. (3.27) with (3.26) and (3.11). This means B/4 → 1 under the assumption of spherical, equal sized aggregates. For fractal aggregates the hydrodynamic radius R_h is smaller than the collision radius which requires the factor A to increase by $B = R_c/R_h$. Bremer et al. estimated a value of B ~ 1.8. Bremer points out that this estimation of B ~ 1.8 is higher than the experimentally obtained value by conducting a permeability measurement on fractal gel which gave $B = 1.15 \pm 0.05$ for $D_f = 2.25$ (L. G. Bremer 1992). The factor A is also affected by the presence of polydispersity, which is measured by the polydispersity index P in the A factor. Initially during aggregation, the P value increases along the aggregation process, assuming a constant kernel. At some point of aggregation, the value of P starts to plateau due to the disappearing of the small aggregates. Another factor affecting A is the presence of a repulsive barrier that the small aggregates need to overcome before they become part of a bigger aggregate. This will slow the aggregation rate by a factor of the stability ratio W.

The SE works for aggregates in the dilute regime, meaning a small volume fraction of clusters. As the system gels, the cluster volume fraction increases and approaches unity at the gel point. Hence, a correction needs to be made. The correction Bremer et al. introduced is a correction for the kernel as the aggregation approaches gelation. The aggregation rate approaches infinity just before the gel point. Because the distance over which the clusters have to diffuse before they collide

approaches zero. The center-to-center distance between aggregates, i.e. R_{nn}, and that between their peripheries, X, are shown in Fig. 3.6, and can be defined by

$$(4/3)\pi\,(R + X/2)^3\, n = 1 \tag{3.28}$$

Substitute Eq. (3.22), with $k_o = 1$ and replace R_g by R (R is the average aggregates size, not R_g) as used by Bremer et al., into Eq. (3.28). An expression for the distance between the peripheries, X, and the aggregate's size, R, can be expressed as

$$X = 2f_{vm}^{-1/3}\ \mathrm{a}\ (R/a)^{D_f/3} - 2\mathrm{R} \tag{3.29}$$

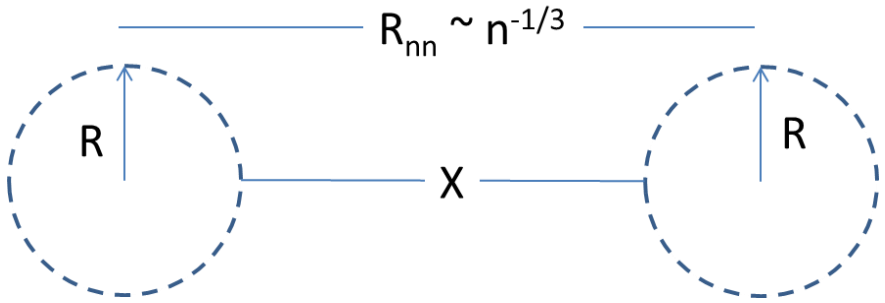

Figure 3.6 A schematic diagram showing the difference between the average distance between clusters when found as $R_{nn} = n^{-1/3}$ and the actual distance need to travel X before collision. In cluster-dilute regime R_{nn} may correctly considered equal to X, while in cluster-dense regime it is no longer correct. This is the basic idea of Bremer's correction to Eq. (3. 20).

Bremer's 1st order approximation to the correction of the aggregation rate of Eq. (3.20) was made by comparing the distances the aggregates need to diffuse without including their volumes, R_{nn}, to the actual distance X. In a diffusion process, $t \sim X^2$, then Eq. (3.20) can be written in the following manner

$$\frac{dn}{dt} \sim -\left(\frac{n^{-1/3}}{X}\right)^2 \frac{4K_B T n^2}{3\eta} \tag{3.30}$$

Differentiate Eq. (3.22) to obtain dn/dR and using Eq. (3.30) an expression for $dt/dR = (dn/dt)^{-1}\, dn/dR$ is obtained. Integrating this expression from monomer size, a, to the aggregate size at the gel time, R_{gel}, one can find an expression for the gel time in terms of R_{gel}. Substitute $R_{gel} = a\, f_{vm}^{1/(Df-3)}$ as used by Bremer into the gel time yield a final expression for t_{gel} as

$$t_{gel} = \left(1 - \left(\frac{6D_f}{2D_f+3}\right) + \left(\frac{3D_f}{D_f+6}\right)\right) K_{Bremer}^{-1}\, a^3\, {f_{vm}}^{-3/(3-D_f)} \quad (3.31)$$

3.3.1.2 Ideal Gel Point theory: The Morphology Aspect

It is well established that when noncoalescent particles come together, they form aggregates with fractal morphology. As we discussed before, the DLCA model adapts the morphology of aggregates with $D_f \sim 1.8$ while the RLCA adapts the morphology of aggregates with $D_f \sim 2.1$. These morphologies occur when the clusters are in the dilute regime. In this regime the aggregates follow Brownian motion, such that the collision of any two different clusters can occur in any direction. On the other hand, one can imagine in the cluster-dense regime a cluster cannot move far before it collides with a neighboring cluster. One might ask: how does the change in motion between clusters in the cluster-dilute regime and cluster-dense regime affect, if in any way, the morphology of the gel?

In a 3D simulation on fractal aggregates in the DLCA model, the scaling crossover on the mass radius relation, Eq. (3.6), of $D_f = 1.8$ for small sizes crosses over to $D_f = 2.5$ for large sizes (Gimel, Nicolai, and Durand 1999; Rottereau et al. 2004a; 2004b). The latter value is in excellent agreement with the predicted D_f value for the percolated cluster of 2.55.

Fry et al. (Fry et al. 2004) did a 3D simulation for DLCA and RLCA aggregates in reciprocal space. This allows them to resemble a light scattering experiment of a single cluster by calculating the scattered intensity, I(q), of these aggregates and graph I(q) vs. q. q is the wave vector and has a unit of inverse length, so q^{-1} represents a length scale of the system. I(q) for small monomers, represents the structure factor of the aggregates. As we discussed in Chapter 2, the structure factor (S(q) ~ I(q) for small monomers) has a q independent regime known as the Rayleigh regime at small q values. The q independent regime followed by a power law regime, where $I \sim q^{-Df}$, is known as the Porod regime. The transition between these two regimes is the Guinier regime, where $q^{-1} \sim R_g$. Figure 3.7(a) shows the evolution of the I(q) vs. qa for a single cluster, which is the biggest cluster in the system. Initially, when the number of monomers per cluster is small, the structure factor shows the power law regime at small q values with $D_f = 1.78$ to indicate the canonical DLCA aggregates. The increase of cluster size is indicated by the shift of the Guinier regime to the smaller q values. At later stages a second power law developed with a value of 2.6

at small q values, hence a large length scale. The crossover of the slopes occurs at a characteristic length scale of the system. Interestingly, it is found that this crossover occurs at the radius of gyration at the ideal gel point, $R_{g,G}$, described in Eq. (3.19). In addition, the second power law regime, at smaller q values, has a $D_f = 2.6$, which is very close to the D_f for percolated cluster of 2.55. Figure 3.7 (b) shows the structure factor of the entire system, in contrast with a single cluster as in (a). This better mimics the light scattering experiment. Again the canonical DLCA aggregates show in the larger q region in the I(q) vs. q graph. As the system evolves to a gel, a 2.6 power law appears. The dip in the structure factor is due to cluster-cluster anti-correlation (Oh and Sorensen 1999), which occurs in the cluster-dense regime when R_g and R_{nn} approach each other.

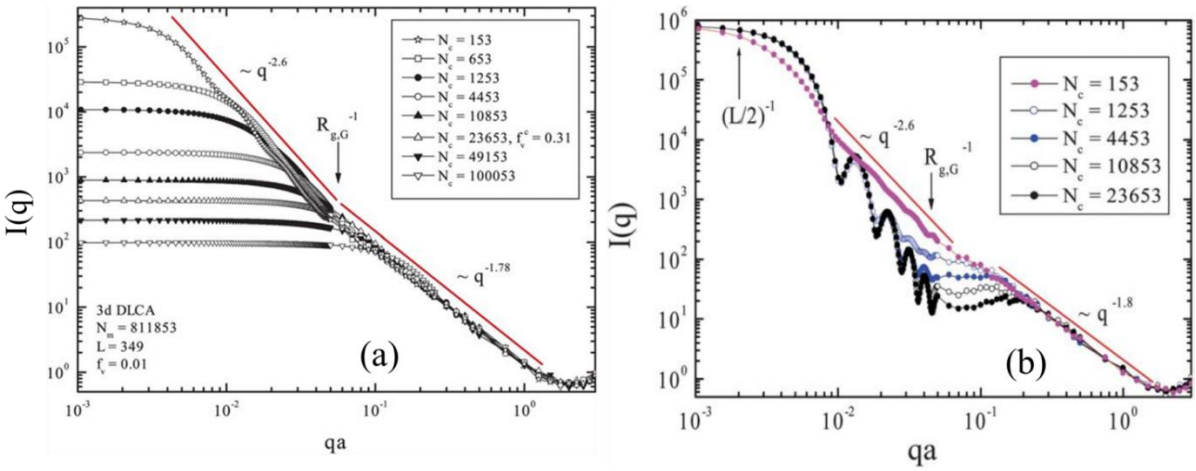

Figure 3.7 Temporal evolution of I(q) vs qa for (a) the biggest cluster in the system, and (b) the entire system. Both show the canonical DLCA aggregate for the large q values with D_f ~1.8, whereas at small q values a D_f ~2.6 is present. The crossover between the 1.8 to 2.6 occurs at $R_{g,G}$. N_c is the number of clusters in the system which is decreasing with time. The figure is taken from (Fry et al. 2004).

The interpretation of these two power law regimes is that at a relatively small length scale that is comparable to the cluster sizes (large q values), the aggregates have a DLCA morphology of $D_f \sim 1.8$. At larger length scale, a new morphology with $D_f \sim 2.6$ is formed. The morphology of the larger length scale is called the superaggregates. The monomers of these superaggregates are the DLCA aggregates of $D_f \sim 1.8$, hence, the name superaggregates. The crossover between these two morphologies is at a characteristic length scale of the system. This length scale is the radius of gyration at the ideal gel point, $R_{g,G}$. Therefore, the superaggregates morphology appears after the system starts gelling, hence after the IGP is reached. Figure 3.8 is a schematic diagram which represents the superaggregate with DLCA aggregates as monomers.

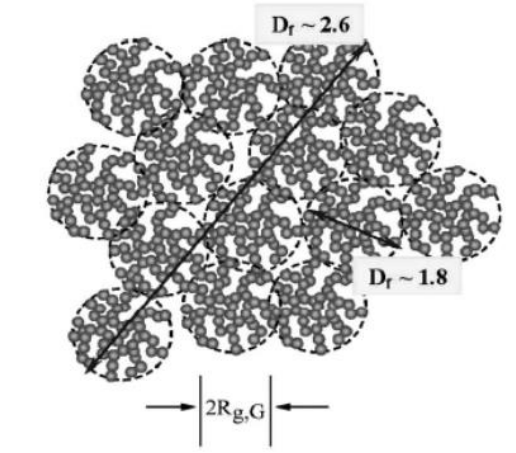

Figure 3.8 A conceptual representation of the superaggregate. Note they consist of DLCA aggregates as monomers. The figure is taken from (C. M. Sorensen and Chakrabarti 2011).

The presence of two power laws at different length scales shows that the superaggregates have hybrid morphology. This hybrid morphology has also been witnessed experimentally. Soot aerosols, just like colloidal sols, may form a gel (Rajan Dhaubhadel et al. 2007; Wongyo Kim et al. 2006; Christopher M. Sorensen et al. 2003; C. M. Sorensen et al. 1998; R. Dhaubhadel et al. 2006). Kim et al.(Wongyo Kim et al. 2006) did a light scattering experiment on soot forming particles in acetylene flame. Figure 3.9 shows I(q) vs. q for different heights above the burner. The height is designated by the symbol h. For small h values, which represent a short aggregation time for the soot, DLCA aggregates are formed with fractal dimension of 1.8. At further distances from the burner, which represent later aggregation times, a new feature starts to develop at smaller q values. At smaller q values a new morphology is detected with $D_f = 2.6$. This structure is very similar to what has been detected with simulations for superaggregates with a final fractal dimension of 2.6, which are constitute of smaller fractals of $D_f = 1.8$.

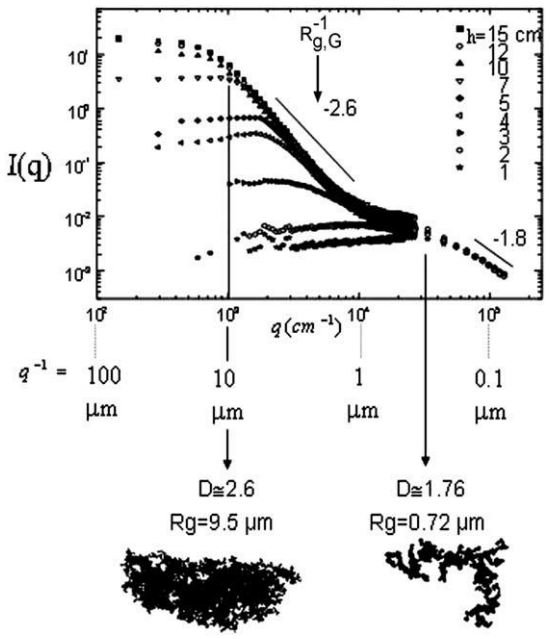

Figure 3.9 Experimental results of I(q) vs. q of soot aerosol for different heights, h, above the burner. Higher h means later in aggregation time. With increasing h, the hybrid morphology of 1.8/2.6 is present, hence superaggregates are formed. Below are the electron microscope images of the 1.8 aggregates and the 2.6 superaggregates. Figure is taken from (Wongyo Kim et al. 2006).

In colloidal systems the morphological changes in gelling colloids was observed under shear (Jung, Amal, and Raper 1996; Kikuchi et al. 2005; Mokhtari et al. 2008; Selomulya et al. 2002; Serra, Colomer, and Casamitjana 1997; Soos et al. 2008). The two mechanisms used to explain this behavior were fragmentation and restructuring. Fragmentation is viewed when aggregates are subject to shear and break the aggregates into smaller ones. In this case, either the fractal dimension is identical to the unsheared system (Torres, Russel, and Schowalter 1991) or the aggregates gets more compact as indicated by higher D_f values (Kikuchi et al. 2005; Serra, Colomer, and Casamitjana 1997; Soos et al. 2008). This mechanism does not show a hybrid of D_f. In contrast, restructuring due to shear can show hybrid in morphology. The magnitude of restructuring depends on the shear rate used. The higher shear rate created a higher fractal dimension at smaller q values. Similar to the fragmentation, restructuring shows a decrease in size (Jung, Amal, and Raper 1996; Lin, Klein, et al. 1990; Selomulya et al. 2002). All of the above studies used high shear rate such that the shear induced aggregation was dominant over the Brownian aggregation. This dimensionless ratio is quantified by the Peclet number (Pe) (Isaev et al. 2006; Swift and Friedlander 1964).

Mokhtari et al. studied the effect of shear in colloidal gelation using small angle light scattering technique. The aggregation process was initiated by adding $MgCl_2$. With the absence of shear, only the canonical DLCA aggregates of $D_f \sim 1.7$ were detected. To test for the effect of shear Mokhtari did a wide range of shear rates (~ 0.13-3.56 s^{-1}) which corresponds to Pe (~ 0.13-150). The applied shear initiated at different stages of the aggregation and continued for ~33sec. The results can be grouped into three different categories. (1) It was found if shear is applied at early aggregation stages the morphology of the aggregates will not differ than the no shear case. (2) If the shear is applied later in the aggregation with shear rates ranges from 1.6-2.6s^{-1}, a transient hybrid 1.8/2.6 morphology appears, but is soon washed out by the diffusion process, and the final value evolves to ~1.8 (similar to the unsheared value). (3) If the shear rate is applied deep in the aggregation process with a value as small as 0.48s^{-1}, a hybrid of 1.8/2.6 morphology appears and persists for long times. Figure 3.10 shows examples of hybrid morphologies appear in the case of (a) high shear rate of 3.56s^{-1} and (b) low shear rate of 0.48s^{-1}. In all the cases where hybrid morphology appeared either temporarily after terminating the shear or permanently, the radius of gyration was observed to significantly increase immediately after terminating the shear.

The increase of R_g was enough to rule out the fragmentation mechanism. Restructuring fails to explain not only the enhanced growth in R_g, but also the independence of fractal dimension at larger q values on the shear rate. The authors suggest the supper aggregates as an alternative explanation of these observations. The results here are very consistent with the superaggregates in soot and simulations we discussed earlier.

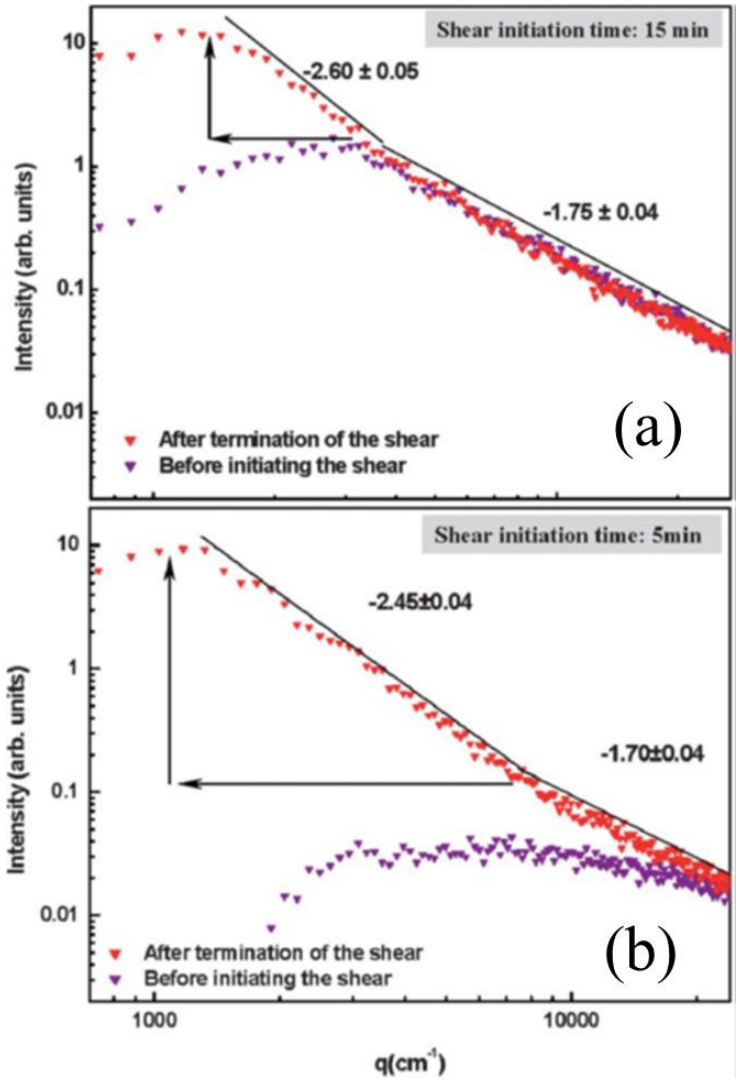

Figure 3.10 Scattered intensity I(q) v. q for aggregating colloid of 20nm diameter, and monomer volume fraction of 4.36×10^{-4} destabilized using $MgCl_2$. Shear rate value was (a) $3.56s^{-1}$ applied 15min after the initiation of aggregation and (b) $0.48s^{-1}$ applied 5min after initiation of aggregation. For both cases the duration of shear was 33sec. The hybrid morphology is clear in both cases. The superaggregates are formed and indicated by arrows in (a) and (b). Figure is taken from (Mokhtari et al. 2008).

Wu et al. (Wu et al. 2011; 2005; Wu, Xie, and Morbidelli 2013) used light scattering techniques to obtain the structure factor of aggregating fluorinated polymer (MFA) colloid. NaCl used to initiate the aggregation. The advantage of using this colloid is that it has a refractive index very close to that of water which minimizes the multiple scattering artifacts. This enables the study of gelation from high initial monomer volume fractions. Figure 3.11 (a) shows the temporal evolution of the structure factor of $f_{vm} = 0.04$. The structure factor at the latest time distinctly shows the different power laws at different length scales.(b) A repeat of the latest aggregation time in (a)

with the values of the slopes for the two power laws regimes as indicated in the graph. Authors repeated this experiment for different initial monomer volume fractions and represent their data in part (c). The authors presented, for different publication, similar experiment but with different monomer sizes. This is shown in part (d). It is important to note here that these experiments have no applied shear beyond the initial mixing required for sample preparation.

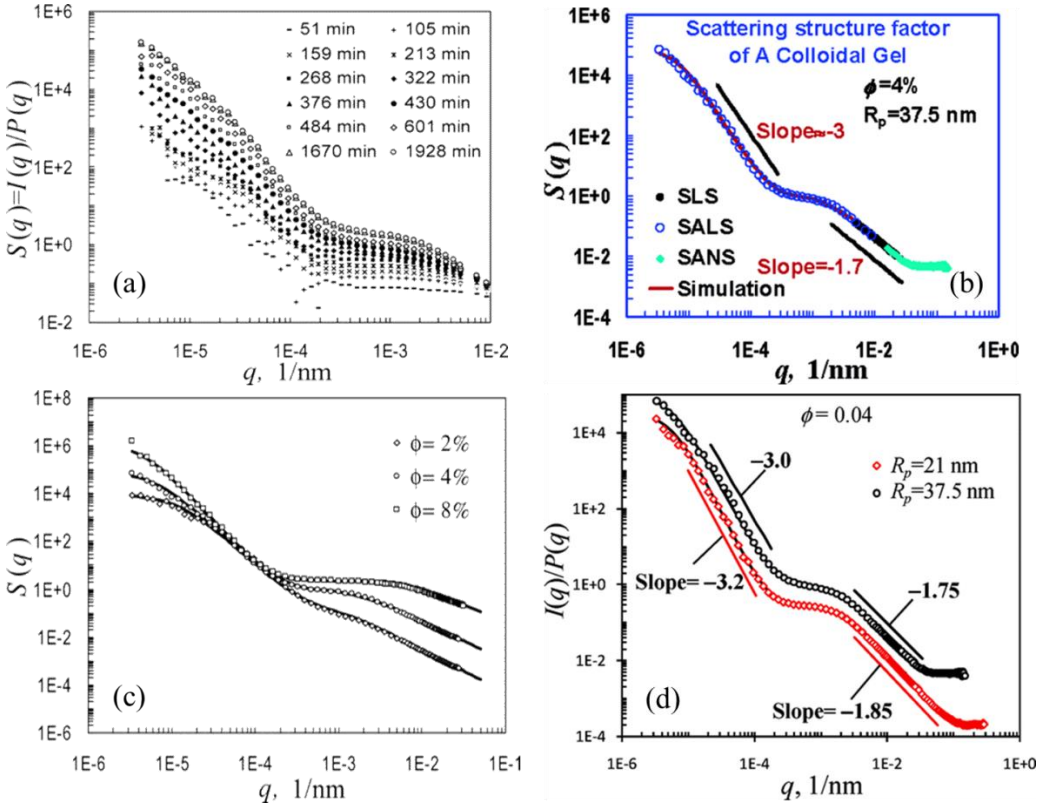

Figure 3.11 (a) temporal evolution of S(q) vs q for $f_{v,m}$=0.04. The latest structure factor of gelling colloid for (b) the latest time in (a) i.e. t=1928min, (c) three different volume fractions 0.02, 0.04, and 0.08, and (d) for different monomer sizes. In all these gelling structure factors the hybrid morphology is distinct. The arrows in (c) indicates the calculated $R_{g,G}$ from eq. 17 were added to the original graph. These graphs are taken from (a), (b), &(c) (Wu et al. 2005), (d) (Wu et al. 2011).

The authors used the structure factor put forth by Wong and Cao (Wong and Cao 1992) to explain the appearance of two different power laws in the structure factor at the two different length scales. According to the authors, at large q values, hence at smaller length scales that are comparable to the cluster sizes that constitute the gel, it is the mass fractal dimension (D_m) scaling that contributes to the negative slope. In other words $S(q) \sim q^{-Dm}$. For smaller q values, hence larger length scales than the cluster sizes, it is the surface fractal scaling (D_s) i.e. $S(q) \sim q^{-Ds}$. The authors justify the appearance of the surface fractal scaling at larger length scales because the scattering instrument

sees the clusters as spherical objects with rough surfaces. It is these rough surfaces that lead to the surface fractal dimension. It is important to note here that the graphs in Fig. 3.12 are all in the RLCA regime despite the fact that at small q regime the power law in the structure factor leads to D_m values smaller than what is anticipated for the RLCA, the anticipated value is ~ 2.1. The authors claim this reduction in D_m value is due to the nonfractal region of the aggregates (Wu et al. 2011; 2005). A study on dense aerosol gels showed that the mass fractal dimension and the surface fractal dimension are no longer equal in the region of higher fractal dimension for a hybrid morphology (William R. Heinson et al. 2018). In the two pictures introduced to explain the appearance of the two power laws in the structure factor, one is the rise of surface fractal dimension like the case of Wu et al., and the other is the superaggregates as in the case of Kim et al. and Mokhtari et al., these sets of experiments shows hybrid morphology of quite interesting similarities. One might claim that those observations are very similar and probably have the same origin. It is important to note the difference in the monomer volume fractions used in these studies. Wu et al. used $f_{vm} \sim 10^{-2}$, whereas Kim et al. and Mokhtari et al. used $f_{vm} \sim 10^{-4}$.

Other examples from literature that indicate the hybrid morphology at different length scales are the study of Cipelletti et al. (Cipelletti et al. 2000a) and Wu et.al. (Wu et al. 2012). Cipelletti et al. worked on the aging of fractal colloidal gels. Figure 3.12 (a) shows the temporal evolution of I(q) vs q for polystyrene colloids of radius a = 10.5nm and $f_{vm} = 4.8 \times 10^{-4}$. Aggregation was induced by adding $[MgCl_2]$ = 16mM. The time at which the peak in the I(q) vs. q is arrested and no more shifts toward smaller q values corresponds to the time at which the system starts to gel. Figure 3.12(a) shows that the peak of the structure factor arrested at about t = 1.4h with a measured D_f = 1.9 as shown in the insert (t = 1.4h ~ 5000sec). This indicates that the gel is starting to form. The dip in the data, at small q values, can be explained by cluster-cluster anticorrelation due to clusters being in the dense regime (Oh and Sorensen 1999).

An interesting behavior starts to show at about t = 4.1days. An enhanced scattering starts to appear at smaller q values and keep increasing, note the last I(q) vs. q data in Fig. 3.12(a) represents t = 13.7days. The authors suggest that the enhanced scattering at small q values is due to the development of inhomogeneities in the system due to gelling. According to the IGP this is suggestive of superaggregates formation in an unsheared colloidal system. One can imagine if their instrument can measure sizes bigger than 100μm, i.e. q values can go smaller than the $100cm^{-1}$, a structure factor of hybrid morphology might be detected. Wu et al. (Wu et al. 2012) studied the

gelation behavior of bovine serum albumin (BSA) filament destabilized by $CaCl_2$. Figure 3.12(b) shows the S(q) vs. qR_g. Graphing S(q) vs. qR_g forces the data at $qR_g>1$ to collapse into one graph as shown in the figure. The fractal dimension for the system is 2.1. At qR_g values smaller than unity, an enhanced scattering is observed. Authors did not acknowledge this behavior. But according to the IGP theory this behavior is an indication of superaggregates formation.

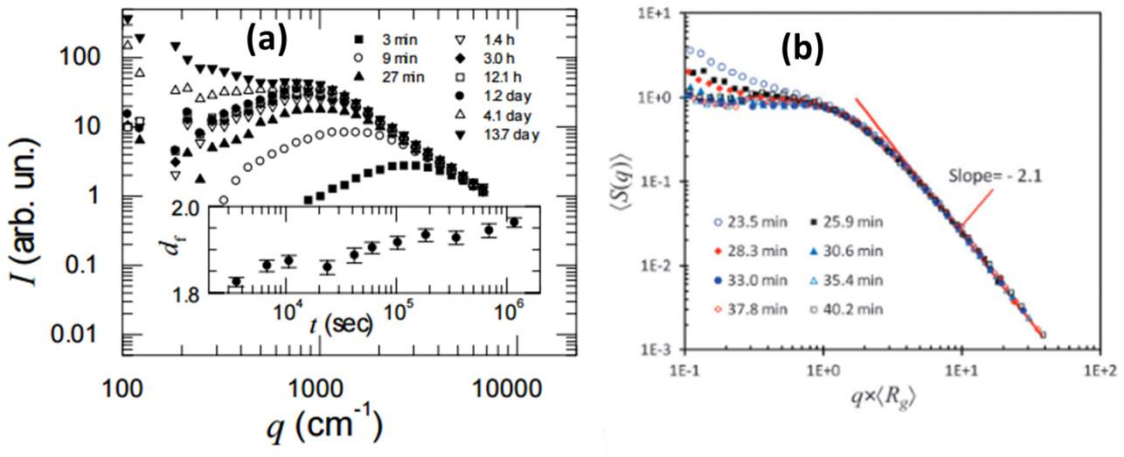

Figure 3.12 (a) the temporal evolution of I(q) vs q for polystyrene spheres of a=10.5nm, $f_{vm}=4.8x10^{-4}$ destabalilzed by 16mM $MgCl_2$. (b) The temporal evolution of S(q) vs qR_g for bovine serum albumin (BSA) filament of length 150nm and diameter of 8nm, the BSA concentration was 2g/L and destabilized by 0.01mol/L of $CaCl_2$. These graphs are taken from (a) (Cipelletti et al. 2000a), (b) (Wu et al. 2012).

3.3.1.3 IGP theory: the size distribution aspect

Recently Liu et al. (P. Liu et al. 2019) simulated the aggregation and gelation of irreversible particulate systems to study the sol-to-gel transition for the DLCA model for different initial monomer volume fractions, $f_{v,m}$. Their work provided the evolution of the cluster mass distribution presented by logN vs. t/ts as shown in Fig. 3.14 for different $f_{v,m}$. N is the number of monomers per cluster, t is the time from the initiation of aggregation, and t_s is the time interval during which the monomers move a root mean square distance equal to the monomers diameter, 2a. The red dashed line for each f_{vm} represents the average number of monomers per cluster, $N = k_o(R_g/a)^{Df}$. Whereas the solid red line represent the number of monomer per cluster at the IGP, $N_{IGP} = k_o(R_{g,G}/a)^{Df}$, where $R_{g,G}$ is the radius of gyration at the IGP as defined in Eq. (3.19).

In Fig. 3.13(a) the volume fraction was small enough that gelation never happened during the normalized waited time (t/ts). In contrast, Fig. 3.13(b)-(e) the volume fractions are high enough to enable gelation within the simulated t/ts time. The evolution of the N value reaches asymptotically the N_{IGP} for each of the systems from (b) to (e). The point at which the dashed curve crosses with the solid line, hence $N = N_{IGP}$, defines IGP. This time is referred to as t_{IGP} and is symbolized by the triangle shaped point. After the IGP is reached, two different distributions start to appear in the LogN vs. t/t_s graphs (b)-(e). This indicates that the gelation process creates a bimodal size distribution. The average sol cluster sizes remains relatively unchanged with a value ~ N_{IGP}. It is these sol clusters that move around and join the big cluster forming the gel. As a consequence, the bimodal size distribution becomes more distinguished at later times. The authors went beyond the IGP to study the aging of the gel. They defined a final gel point (FGP) when the number of monomers in the final gel is equal to the initial total number of monomers, N. The FGP is symbolized by the red circles.

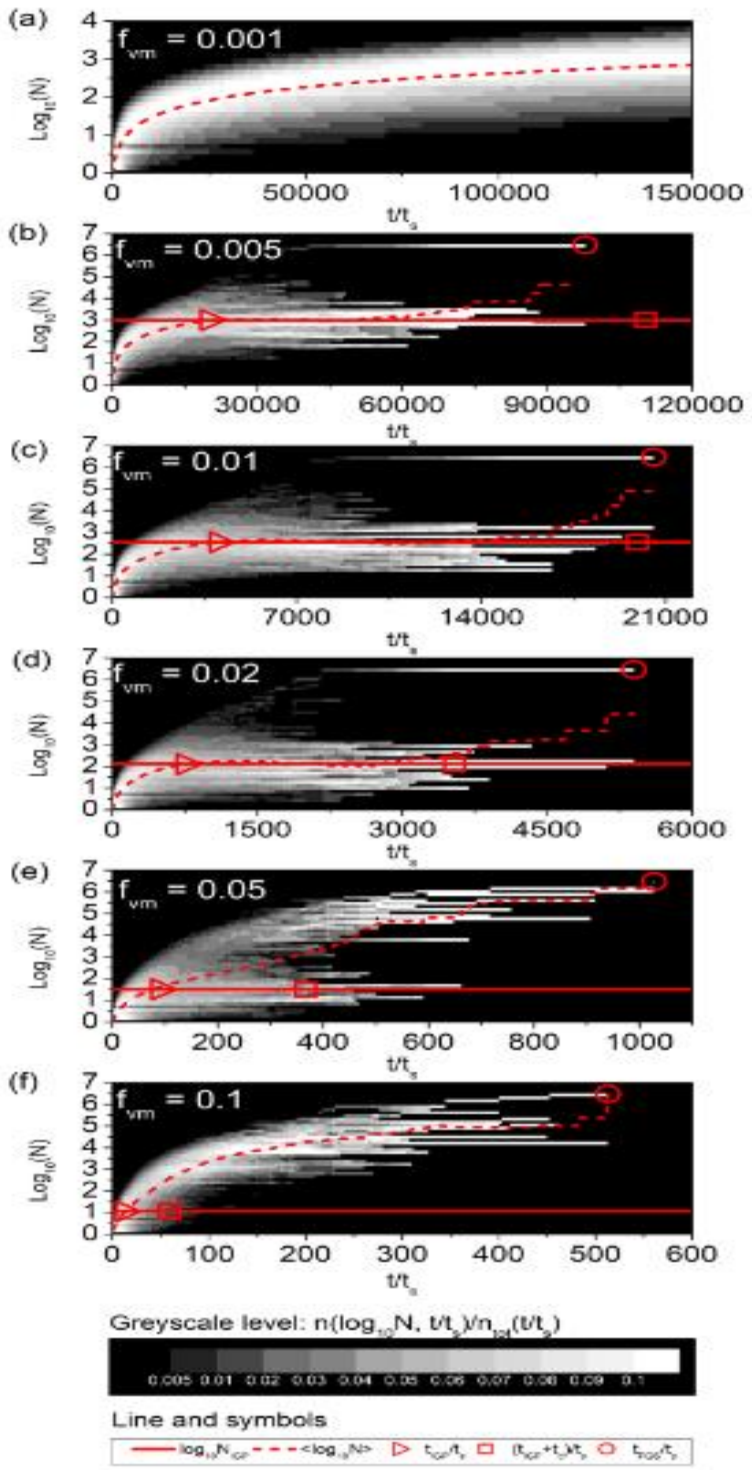

Figure 3.13 Temporal evolution of the cluster mass distribution, Log N vs. t/ts, N is the number of monomer per cluster, t is the time after the initiation of aggregation, and ts is the time for the monomers to move mean square distance equivalent to its size. This figure is taken from (P. Liu et al. 2019).

3.3.2 Percolation description

Stauffer (D. Stauffer 1976; Dietrich Stauffer, Coniglio, and Adam 1982) and others (De Gennes 1975) have laid a solid foundation for the percolation description of gelation. One version of the percolation model fills the available space with a point lattice. Then spherical monomers with a diameter equal to the lattice spacing are placed randomly on the lattice. If monomers occupying adjacent points (nearest neighbors) touch, then they are joined together and become part of the same aggregate. The percolation model predicts a critical probability of site percolation threshold, P_c, such that an infinite, space-filling aggregate will form. Hence a gel is created. It is found, according to the percolation theory, that the space-filling aggregate form with a fractal dimension of D_f = 1.9 in 2D aggregating system (Hasmy and Jullien 1996). On the other hand, for 3D aggregates, the gel is formed with a fractal dimension of D_f = 2.55.

Given that the monomers are placed on the lattice without regard to any time scale, the percolation model is a static model and hence does not describe the kinetics from sol-to-gel. Nevertheless, it successfully describes many critical-phenomena like, power law divergence of various physical properties as the concentration of monomers p approaches the critical concentration P_c. This implies that the structure of a 3D gel is that of a percolation aggregate with D_f = 2.55, not that of, for example, a diffusion limited cluster-cluster aggregate formed kinetically with D_f = 1.8.

3.3.3 Thermodynamics phase separation

Carpineti et al. (Carpineti and Giglio 1992) was the pioneer in advocating that particulate systems undergoing gelation display spinodal decomposition (SD) which is a well-known phase separation phenomenon. They recorded, along with others (Lu et al. 2008), two main features that strongly resembled the SD. The first feature is the observation of a peak at a finite q value in the structure factor that increases with time, and the peak position q_m is shifted to smaller and smaller q values with time as shown in Fig. 3.14. To them it was strongly reminiscent of the behavior exhibited by fluids that phases decompose according to spinodal decomposition dynamics.

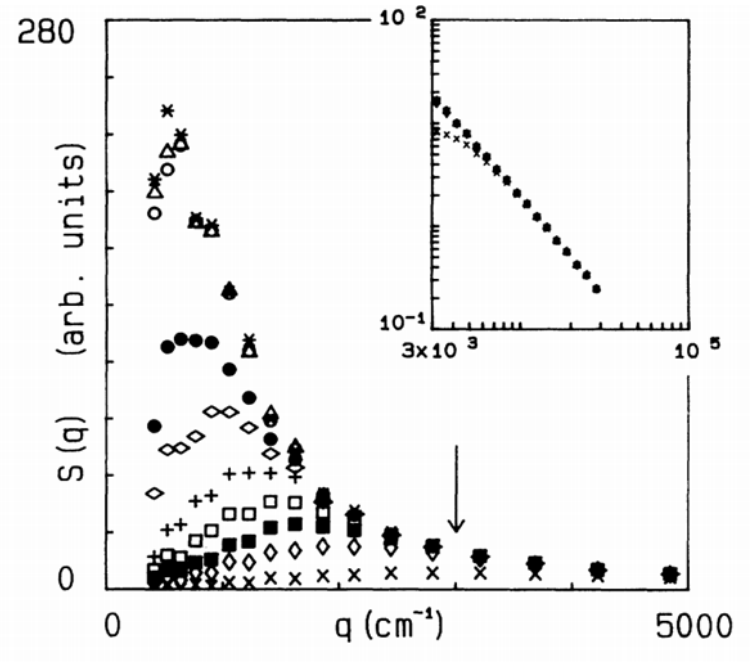

Figure 3.14 Temporal evolution of the structure factor of polystyrene spheres destabilized using $MgCl_2$. This Figure is taken from (Carpineti and Giglio 1992).

The second feature observed that mimics the SD is an optical structure factor with dynamical scaling behavior. This means that the position of the scattered wave vector peak q_m and the scaled structure factor $S(q/q_m, t)$ are related by the equation (Bates and Wiltzius 1989; Carpineti and Giglio 1992)

$$S(q/q_m, t) = q_m^{-d}(t)\, F(q/q_m) \tag{3.32}$$

where $F(q/q_m)$ is a time independent scaling function and d is a scaling exponent. For fluid systems the scaling exponent is the spatial dimension, d = 3. By replacing d with D_f in Eq. (3.32), they show that the scaling behavior was achieved for their colloidal aggregates at later stages of aggregation as shown in Fig. 3.15(a). On the other hand, they showed, for the same set of data, that at earlier stages of aggregation scaling was not successful, Fig. 3.15(b). The observation that the structure factor during late stage colloidal aggregation showed behavior described by Eq. (3.32) led them to conclude that particulate gelation is a phase separation.

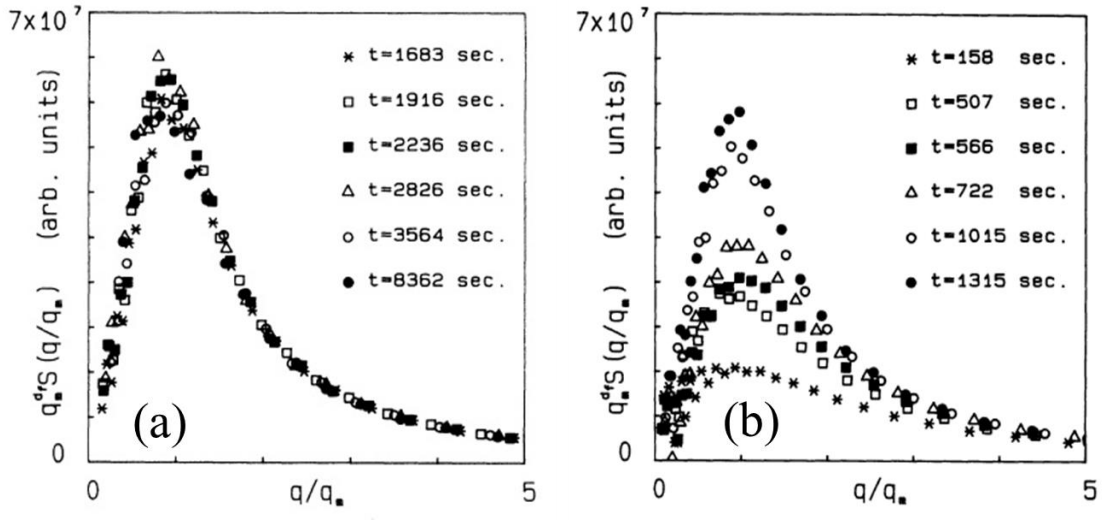

Figure 3.15 (a) Scaled data for the late stages of aggregation from data in Fig. 14 using eq.27(b) at early stages of aggregation scaling of the data does not work. Both of these figures are taken from (Carpineti and Giglio 1992).

Lu et al. (Lu et al. 2008) studied gelation of micron-scale colloidal particles made attractive with the addition of a non-adsorbing polymer depletant. The polymer concentration controlled the inter-particle interaction potential range and strength U relative to the thermal energy, U/k_BT. The onset of aggregation and subsequent gelation was sharply dependent on the polymer concentration, which suggests that the gel boundary occurs exactly at a phase separation. Once the critical polymer concentration was reached, aggregation ensued, and a clear peak appeared in the structure factor that was constructed using confocal microscopy images. This peak grew with time with its position (q_m) shifting to smaller q values, a behavior consistent with Eq. (3.32). The sharp phase-transition-like boundary for gelation and the spinodal-decomposition-like structure factor led Lu et al. to conclude that a thermodynamic instability is the driving force for all gelation processes.

A more recent approach to the sol-to-gel transition with connection to thermodynamics phase transition was put forth by Matsoukas (Matsoukas 2015; 2014). He developed the statistical thermodynamics of irreversible binary aggregation in discrete finite systems to obtain the partition function for the product kernel. He defined a cluster ensemble that contains a population of N_m monomers that form N_c clusters. He constructed the microcanonical ensemble of all possible distributions $n = (n_1, n_2, \ldots, n_i, \ldots)$ where n_i is the number of clusters with i-monomers. In the thermodynamics limit, when N_c and N_m are large, Matsoukas found that the populations may go through a "phase transition". It is important to clarify that a "phase", according to Matsoukas, refers to a distinct distribution. So "phase transition" means the transition from a distribution of

finite clusters to a distribution that contains a giant cluster, ultimately, this giant cluster will contain N_m individuals. The biggest cluster can have $i_{max} = N_m - N_c + 1$. If the biggest cluster in the system contains less than $i_{max}/2$, then this phase is called the sol phase, and if it contains $i_{max}/2$ or bigger, it is defined as the gel phase. Matsoukas predicted the gel will occur at a specific cluster number N_c^* which takes the value of 146.

Figure 3.16 shows a sample distribution of $N_m = 200$. Initially, when $N_c = 170 > N_c^*$, which represents early stages of aggregation, the distribution consists of a single sol, hence, a unimodal distribution. At $N_c = 75 < N_c^*$ the gel phase starts to occur and the distribution becomes bimodal. The gel phase moves to larger sizes as more of the smaller clusters from the sol region is crossing to the gel region, as shown for $N_c = 40$ and 5. The vertical sticks are the exact calculations for the most probable distributions. The circled symbols are the Monte Carlo simulations. The dashed line is the thermodynamics limit solution.

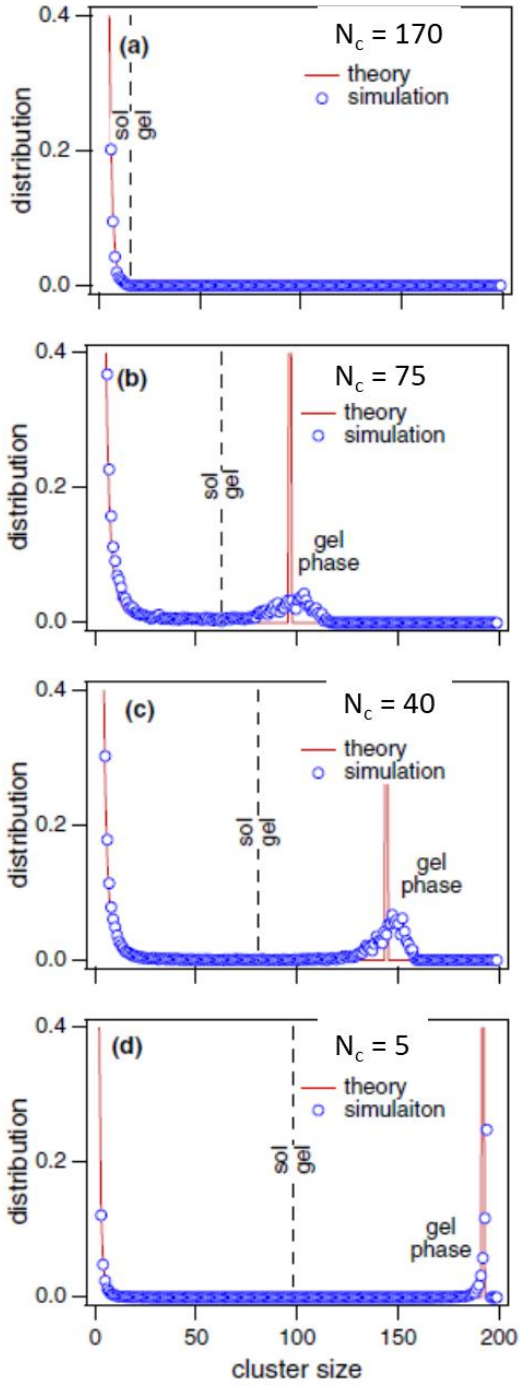

Figure 3.16 A sample distribution of N_m =200. The vertical sticks are the exact calculations for the most probable distributions. The circled symbols are the Monte Carlo simulations. The dashed line is the thermodynamics limit solution. This Figure is taken from Matsoukas (Matsoukas 2014).

Chapter 4 - Experimental setup and calibration

In this chapter the mixing and sample preparations are introduced. Small angle static (SASLS) and dynamic (DLS) light scattering setups used in this work are presented, along with the proper calibration methods. In addition, multiple scattering (MS) is quantified by finding the average numbers of scattering events, as described by Mokhtari et al. (Mokhtari, Sorensen, and Chakrabarti 2005), using the transmitivity measurement. A gelling experiment is shown for each of these three experiments individually. Next, the stability measurement is explained using DLS set up following the method of Holthoff et al. (Holthoff et al. 1996) with some modifications to suit the monomer concentrations used for the gelling samples used in this work. Finally, we present a combination of all the setups used in probing the gelation.

4.1 Mixing and sample preparation

Carboxyl modified latex (CML) nanoparticles (np) with an average radius of a = 20nm as measured by DLS were used. $MgCl_2$ (Sigma-Aldrich) was used to destabilize the particles. Different values of f_{vm} and [$MgCl_2$] were used in this work. The desired f_{vm} and [$MgCl_2$] are prepared in a density matching medium composed of H_2O/D_2O. The mixing procedure always consists of equal volumes of np and salt. For mixing, we used a double syringe system as shown in Fig. 4.1. The np and [$MgCl_2$] are ejected simultaneously into a quartz cuvette (fireflysci Inc.). The inner dimensions of the cuvette are 10mm x 5mm with the 5mm is the optical path length to minimize MS. Data was collected at different times after the onset of aggregation, a time that will be called the waiting time t_w. To minimize bubble formation, the exact volumes of prepared solution/dispersions into the syringes need to be pulled to avoid air.

Figure 4.1 Image of the double syringe system

4.2 Small Angle Static Light Scattering (SASLS) Set up and calibration

The SASLS set up is similar to that of Ferri (Ferri 1997). A 512 pixel photodiode array (PDA) (Hamamtsu, model S3902-512, each pixel is 50μm in length) was used for light detection. The actual detector and the data acquisition LabVIEW which is an interface program were put together by the Electronic Design Laboratory at KSU. The detectable range of the scattering angle in SASLS was ~ 0.1° – 14°, corresponding to a scattering wave vector q, $q = (4\pi/\lambda)\sin(\theta/2)$, ranging between 0.03 μm^{-1} to 3.8 μm^{-1}. A beam of λ = 532nm in *vacuo* (Laserglow, model R533001GX), vertically polarized passed through the sample. The light scattered by the sample is collected by lens L_1 (with focal length f_1 = 80mm). The Fourier image of the sample forms at a plane that includes the focal point of L_1. A second lens L_2 (f_2 =100mm) images the Fourier image of L_1 into the detector. Most of the light from the laser beam will go un-scattered. To eliminate the un-scattered light, a 45° mirror (0.6mm thickness) is placed in the focal plane of L_1. This small mirror acts like a beam stop. Fig. 4.2 shows a schematic diagram of the SASLS setup.

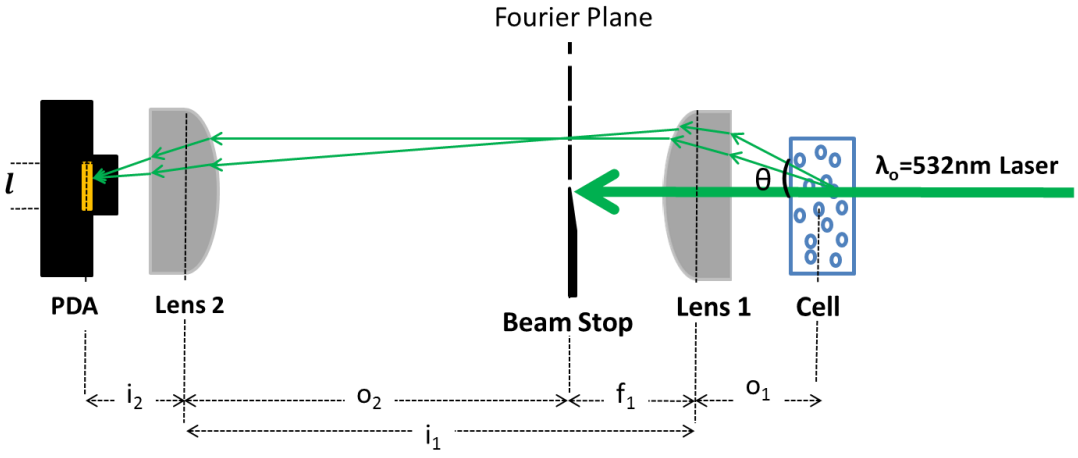

Figure 4.2 A schematic diagram of SASLS. The picture is not drawn to scale.

Using ray optics along with the definition of the wave vector, q, and small angle approximation, one can obtain the value of q in terms of the geometrical distances of the set up as

$$q = \frac{2\pi}{\lambda}\left(\frac{O_2\, l}{f_1 i_2}\right) \qquad (4.1)$$

where l is the length of the image on the detector, which can be written in terms of the photodiode array pixel size (50μm) and the pixel number as

$$l = 50\mu m \times pixel\ \# \tag{4.2}$$

The resolution of the SASLS is set by the choice of wavelength used, the detectable angles, hence the range of q values, as well as the optical arrangements of the set up as shown in Eq. (4.1). The optical arrangement sets the width of each pixel in the detector in terms of q, setting the resolution of the apparatus. In our set up, smallest size can be measured is ~ 260 nm which is much higher than the monomer radius, a = 20nm.

The proper alignment of any optical device is the key for obtaining a good calibration. Alignment means that the laser beam is parallel to the optical table surface before and after it passes through any optical component. First, the laser beam needs to be aligned with no optical component. This can be done using two irises of exact heights to set the reference point during the alignment procedure. Each optical component can be added one at a time and aligned before adding the following one. Let's say you start with L_1. To ensure that the laser beam is passing through the center of L_1, you need to place an iris before L_1 ($iris_1$) and another after L_1 ($iris_2$). A proper alignment of L_1 is when the backscattered light of L_1 passes through $iris_1$ and the un-scattered light still passes through $iris_2$.

The calibration was carried out by using a 10μm single slit (Thorlab). The slit was mounted on a slit holder. The holder was placed on a stage that allows for motion in x-, y-, and z- axes as well as rotational adjustment. The proper adjustments will allow the maximum intensity to be detected by the photo diode array (PDA). The scattered intensity was detected versus the pixel number. The background measurement should be determined for each experiment, and then subtracted from the collected light by the detector to give the desired scattered light. The scattered light I(q) vs q was then compared to the well-known far field diffraction theory (i.e. Fraunhofer diffraction) of a single slit

$$I(q) = I\ (0)\ (\frac{\sin(qw/2)}{(qw/2)})^2 \tag{4.3}$$

Where w is the single slit width (i.e. w = 10μm).

Figure 4.3 shows the result of the single slit calibration. The green data points are the experimental scattered intensity of the slit. The red line is the fit of Eq. (4.3) with theoretical fit of w = 10.1μm.

This is in excellent agreement with the measured w value of 10μm using optical microscope and as indicated by the manufacturer. The black line is the slope of the power law regime in the scattered intensity for a single slit. It takes the value of -2, which is typical for a single slit. As a reminder, the power law regime slope = – (1 + d), where d is the spatial dimension (d = 1 for a single slit).

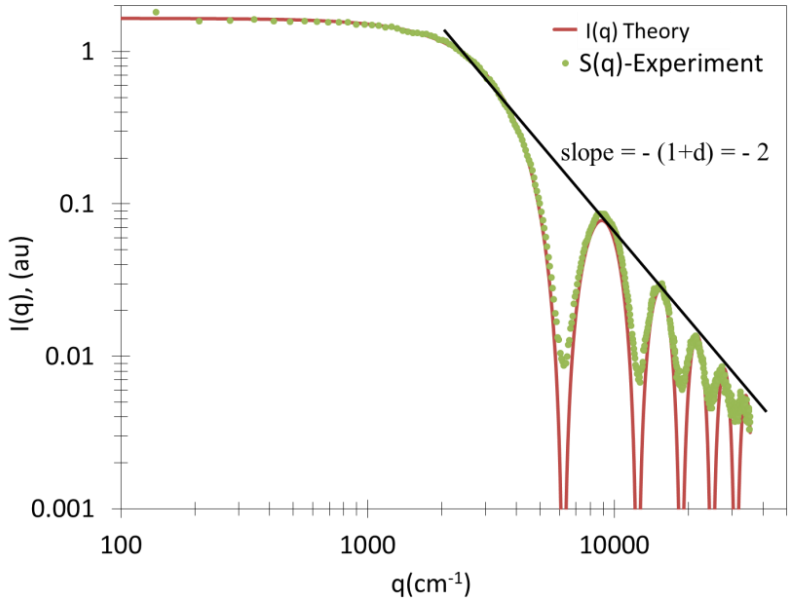

Figure 4.3 10μm single slit calibration for SASLS.

Gel experiment

After successfully calibrating the SASLS setup, the gelling experiments proceeded. Figure 4.4 shows an example of a gelling experiment using f_{vm} = 5x10^{-4} and [$MgCl_2$] = 10mM. Data was collected at different t_w. For fractal gels, with low initial monomers volume fractions, the slope of the power law regime is a direct measure of the aggregates fractal dimension. For this particular gel, $D_f = 1.8 \pm 0.04$. The region of small q values is the Rayleigh regime. For an ensemble of aggregates the scaling approach put forth by Oh and Sorensen (Oh and Sorensen 1999), and discussed in section 2.2.1, predicted a dip at small q values due to the cluster-cluster anticorrelation function when the clusters are in the proximity of each other's. In other word, when the clusters are crowded. Regardless of the dip, it is clear that the scattered intensity is increasing with longer waiting times, t_w. This is consistent with the increasing aggregates' average size (shifting q into smaller values). The transition from the Rayleigh regime to the power law regime is the Guinier

regime. The average radius of gyration, R_g, can be determined using Guinier analysis (Guinier, Fournet, and Yudowitch 1955) as introduced in section 2.2.1. For a sphere with radius of gyration R_g, the Guinier equation is

$$I(q) = I(0)(1 - \frac{q^2 R_g^2}{3}) \tag{4.5}$$

At the limit of $qR_g \sim 1$, $I(q)/I(0) \sim 2/3$. When $qR_g << 1$ Eq.(4.5) can be written as

$$I(0) = I(q)(1 + \frac{q^2 R_g^2}{3}) \tag{4.6}$$

Thus the slope of I(0)/I(q) vs q^2 is $R_g^2/3$. Originally, Guinier analysis is considered applicable when $qR_g \leq 1$, but it has been found that I(0)/I(q) versus q^2 remains linear up to I(0)/I(q) ~2 (C. M. Sorensen 2001), which was further supported in our data as shown in Fig. 4.5. In this figure, I(0)/I(q) vs q^2 for selected values of t_w from Fig. 4.4 are graphed. The corresponding R_g values are recoded in the graph. The temporal evolution of R_g is shown in Fig. 4.6.

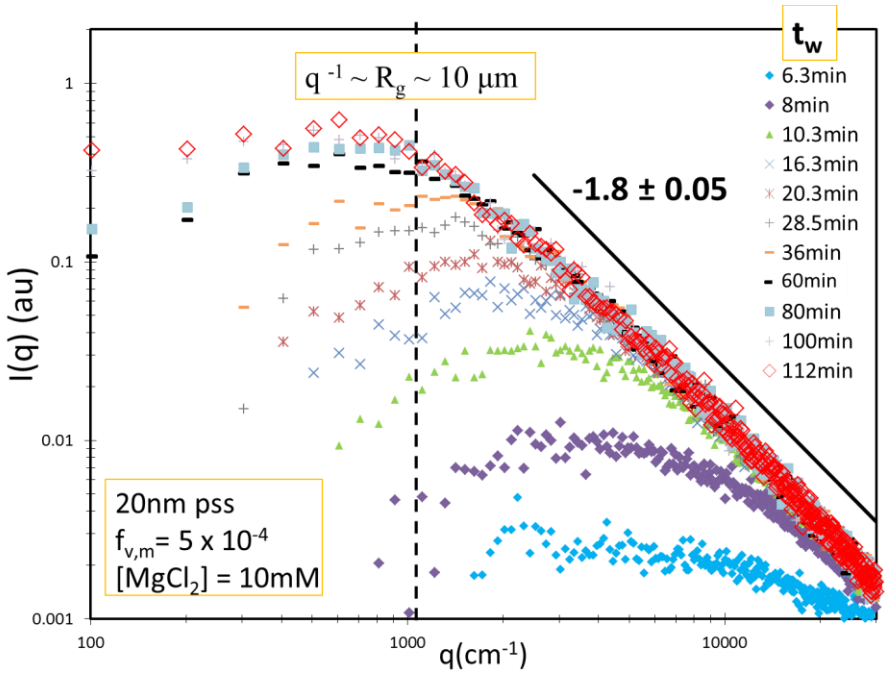

Figure 4.4 Static light scattering I(q) vs. q at different waiting times (t_w) after onset of aggregation for a gelling sample. The fractal dimension is 1.8 ± 0.04. In this experiment the optical arrangement created a pixel width of 101cm^{-1}.

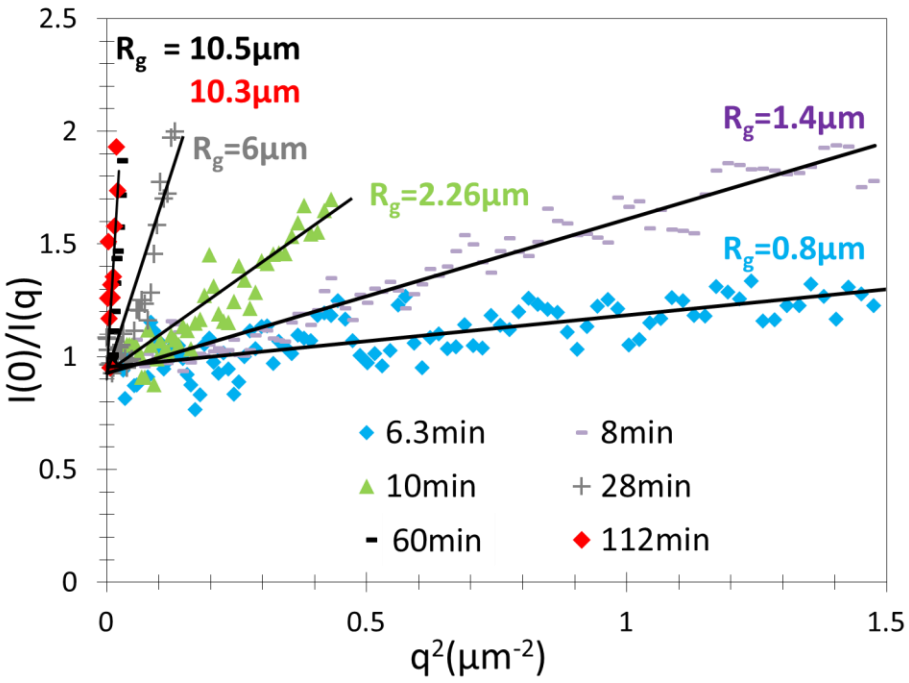

Figure 4.5 Guinier analysis of some of the waiting times for the gelling sample shown in Fig. 4.3

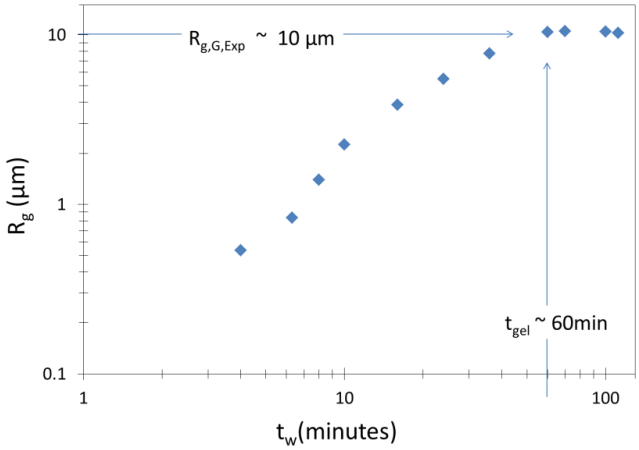

Figure 4.6 Rg vs. tw for the gel experiment shown in Fig. 4.4

4.3 Dynamic light scattering (DLS) set up and calibration

The Brownian motion of particles within the scattering volume causes fluctuation in the scattered intensity. The change of particle position with time is expressed by the intensity auto-correlation

function. The time average intensity correlation function $g_2(t)$, which is a measured quantity, is related to the normalized field correlation function, $f_1(t)$, through the Siegert relation

$$g_2(t) = 1 + \left| f_1(t) \right|^2 \tag{4.7}$$

For a dilute sample, one can write $f_1(t) = C\, e^{-t/\tau}$ where $\tau = 1/q^2 D$ and $D = K_B T/6\pi\eta a$. D is the diffusion coefficient of particles of radius a in a solution of viscosity η. The constant K_B is the Boltzmann constant and T is the temperature in Kelvin.

In any real experimental situation, however, $g_2(t)$ is always obtained as

$$g_2(t) = 1 + f_c \left| f_1(t) \right|^2 \tag{4.8}$$

where f_c is the coherence factor, which depends on the laser beam and instrumentation optics. f_c is an effect of the coherence of the intensity fluctuations. $f_c = 1$ represents the idealized condition of perfect coherence; i.e. the detector is assumed to be a "point detector". In reality detectors always have a finite detection area upon which the intensity fluctuation is collected. If two different points on the photo-detection area are distant, such that the intensity fluctuations from each point are not coherent with one another, the total fluctuation in the detected signal will be suppressed due to the mixing of the incoherent fluctuations. This causes the signal to noise ratio to be low, i.e. $f_c<1$. In practice f_c can approach 1, e.g. f_c can be bigger than 0.9 by using optical fibers. For many conventional DLS (without the use of optical fibers), f_c value of the order of 0.7 is considered fairly well.

What is coherence? Coherence is a measure of the correlation between the phases measured at different points on a wave. It can be defined as the degree of stability of a phase of a wave (light wave in our case) both in space and in time. There are two types of coherence: longitudinal and transverse coherence. The transverse coherence, often called the spatial coherence, is a measure of the correlation of a light wave's phase at different points transverse to the direction of propagation. The transverse coherence shows how uniform the phase of the wavefront is. On the other hand, the longitudinal coherence, often called temporal coherence, is a measure of the correlation of a light wave's phase at different points along the direction of propagation. The longitudinal coherence tells about how monochromatic the source is.

Let's first discuss the transverse coherence. Consider the light scattered from a source with an area (facing the detector) of $A_s = L_x L_y$ that is collected at a distance z from the source as illustrated in

Fig. 4.7. The coherence area (A_c) is the area of Fourier transform of the scattering source, i.e. $A_c = \Delta x\, \Delta y$. The scattering angles in the x-y plane, θ_x and θ_y, can be written as $\theta_x = \frac{\Delta x}{z}$ and $\theta_y = \frac{\Delta y}{z}$. Combining these with the general result for any scattering angle $\theta_{x\ or\ y} \approx \lambda / L_{x\ or\ y}$, A_c can be expressed as

$$A_c \approx \frac{z^2 \lambda^2}{L_x L_y} \tag{4.9}$$

Notice, the narrow dimension of the source corresponds to a wide dimension of the coherence area.

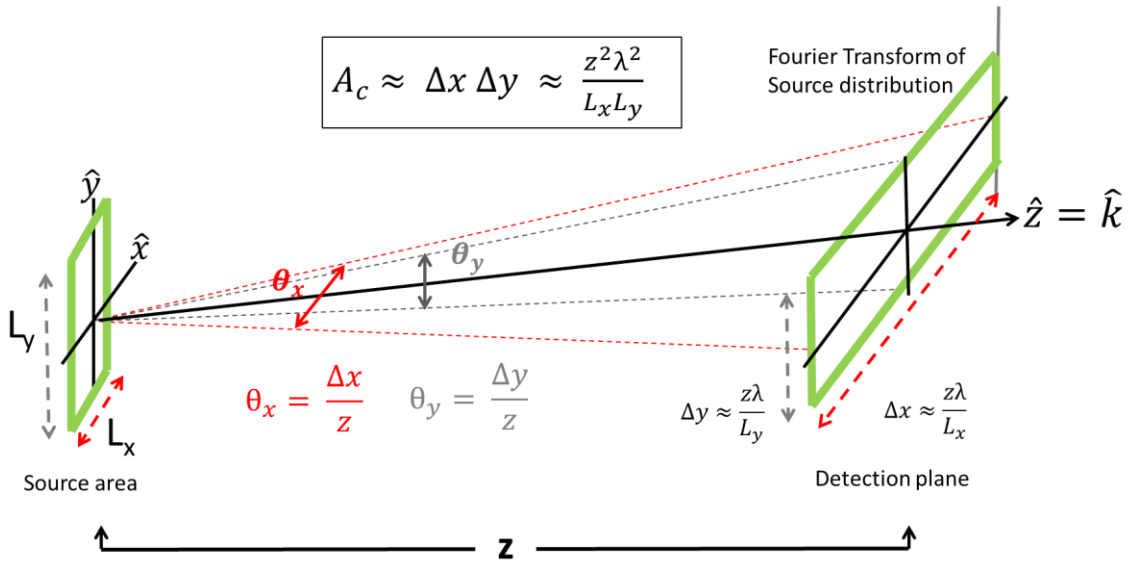

Figure 4.7 A schematic diagram to illustrate the spatial coherence.

Second, we discuss the longitudinal coherence (or temporal coherence). The longitudinal coherence concerns about the coherence along the wave propagation. In any light source, there exist phase noises or drifts that create spectral density. This will create a spectral line width Δf. The longitudinal coherence function and the spectral density are a Fourier transform pair. This means there exists a time, i.e a coherence time, t_c, that satisfies $t_c \Delta f \sim 1$. The narrower the spectral line width, the longer the coherence time.

Longitudinal coherence is often characterized by the coherence length L_c. L_c expresses the propagation distance over which the interference is still possible. If there are two light waves of slightly different frequencies, Δf, or wavelengths, $\Delta\lambda$, propagating in the $\vec{k}$ as shown in Fig. 4.8,

the coherence length $L_c = t_c\, c = c/\Delta f = \lambda^2/\Delta\lambda$, where the speed of light $c = \lambda f$ and the absolute value of $\Delta f = \Delta(c/\lambda) = c\,\Delta\lambda/\lambda^2$.

For example, for a sun light in the visible region, the wavelength ranges from 400nm-700nm (with an average wavelength of λ_{avg}=550nm and $\Delta\lambda$=300nm). The coherence length is $L_c \sim (550)^2/300$ ~1000nm ~2 λ_{avg}. For the laser beam used in this experiment the spectral line width is less than 0.2nm as indicated by the manufacturer (this corresponds to $\Delta f = c\lambda^2/\Delta\lambda$~400KHz). This yields L_c ~ 700m. One can see for laser technology Δf is very small, which creates large coherence length. This means the depth of the distance the light can travel and still be coherent is large.

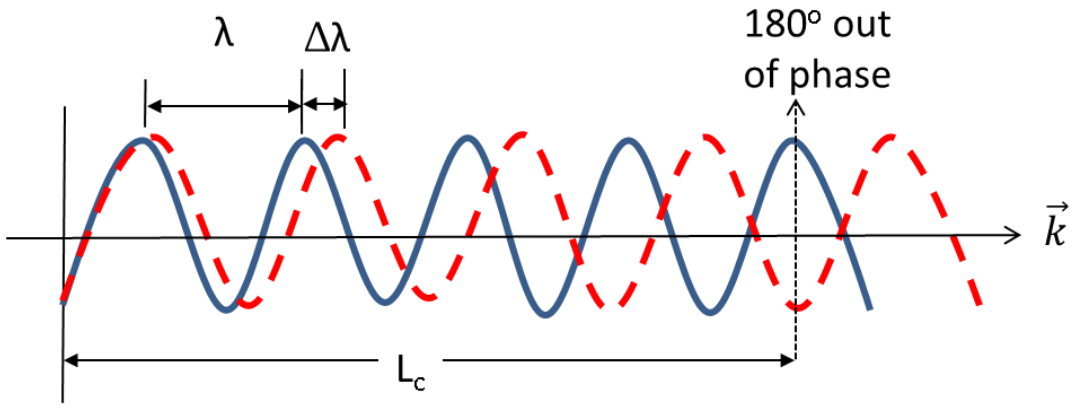

Figure 4.8 A schematic illustration of two waves propagating in the same direction with slight difference in wavelength.

Regardless, if it is the longitudinal or transverse coherence, the higher the coherence, the higher the visibility produced of the interference pattern. Visibility can be defined as $v = \frac{I_{max}-I_{min}}{I_{max}+I_{min}}$, where I_{max} and I_{min} are the maximum and minimum intensities (representing the bright and dark fringes respectively as shown in Fig. 4.9). In DLS the highest visibility can be achieved if the detection area $A_d << A_c$ as illustrated in Fig. 4.9.

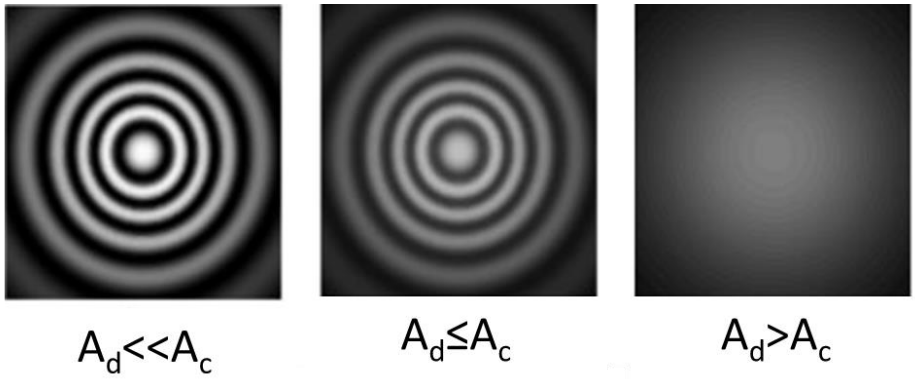

Figure 4.9 These figures demonstrate how visibility depends on the coherence area, A_c, and detection area A_d. These pictures are taken from google images.

A schematic diagram of DLS is shown in Fig. 4.10. A vertical polarized beam of λ=532nm in *vacuo* (Laserglow, model R533001GX) focused by a focusing lens (f_f=15cm) passed through the sample. The scattered light was collected via a photomultiplier tube (PMT) (Precision Instruments, model 3262RF). The PMT was placed on a movable arm to change the light scattering angle between 22° and 90° alternatively, which corresponds to q= 6μm^{-1} and 22.1μm^{-1}, respectively. The scattered light is imaged by an imaging lens (f_i = 12cm) into a small opening controlled by adjustable double slits. The signal was correlated using an ALV-5000 multiple-tau digital correlator.

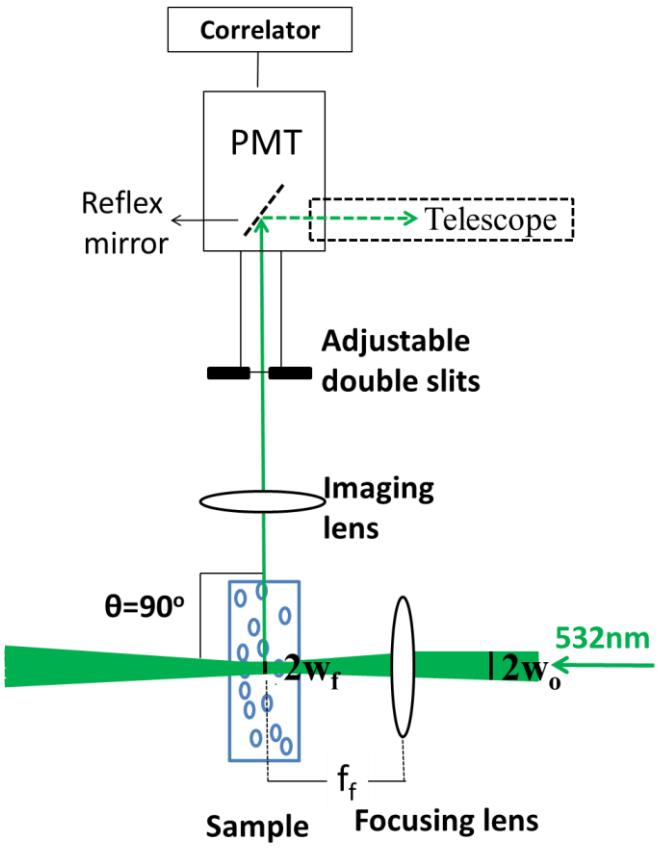

Figure 4.10 A schematic diagram of the DLS set up. The scattering angle is drawn to be 90°.

To obtain the best signal to noise ratio the spatial coherence needs to be considered. Equation (4.9) shows that the narrower the source dimensions, the wider the coherence area, A_c, in the detection plane. This allows for more experimental feasibility to choose $A_d << A_c$. The focusing lens is used to focus the original beam waist w_o = 1mm into the sample with a new beam waist $w_f = f_f\lambda/\pi w_o = 26\mu m$ for this setup. The scattering volume is 25cm from the detection plane. This gives $A_c \sim 3mm^2$ on the detection plane.

The imaging lens is used to image the scattering volume on the adjustable double slits. This allows for a focused image of the scattering volume to be seen by the experimentalist using the reflex mirror and telescope. The imaging lens is mounted on a translational stage to adjust the position of the scattering volume image. The detection area, A_d, is determined by the adjustable double slits opening. If the detector area contains one coherence area or less, then the scattered light will maintain the transverse coherence, which leads to a high signal to noise ratio. In this set up, $A_d \sim$

0.25mm x 0.25mm = 0.063mm^2. This makes A_c/A_d ~ 40 and gave a maximum signal to noise ratio, i.e maximum $g_2(t=0)$ =1.8. However, the larger the A_d is, the stronger the scattered intensity and the smaller the statistical noises are. Therefore, there is a trade-off in choosing a proper detection volume. To increase the scattered intensity one may do one or more of the following: increase A_d, increase the power of the laser, use higher concentration of sample, set up the detection at smaller scattering angle, or decrease the distance from the scattering volume to the detection area (z distance in Fig. 4.6). Another way to reduce the statistical noise is by choosing a longer duration time. Remember that $f_1(t) \sim \exp(-2t/\tau)$. If the total duration of the experiment is T, then the number of decay times during the experiment is T/τ. This should enhance the signal by $(T/\tau)^{1/2}$. Another factor that will counter-act the spatial coherence and lead to smaller $g_2(0)$ is the effect of unwanted scattered light. Like the scattered light or the flare from the cell walls, dust, air bubbles, and other forging matter in the solution. Preparing the sample in fume hood reduces the presence of dust. The method of injecting the sample will affect the bubble formation (see section 4.1).

To calibrate the DLS polystyrene spheres were used with 99nm diameter as reported by the manufacturer using TEM imaging technique. The DLS signal give $g_2(t)$ vs. t as shown in Fig. 4.10 (blue data). Equation (4.8) can be used to solve for $f_1(t) = ((g_2(t) - 1)/f_c)^{0.5}$. The value of f_c = $g_2(0)$-1= 0.8 for this case . Figure 4.11 shows the $f_1(t)$ vs. t. Finding the decay time $\tau = (q^2 D)^{-1}$ from $f_1(t)$ and using $q = (4\pi/\lambda) \sin(\theta/2)$ and the diffusion, $D = K_B T/6\pi\eta a$, one can find the radius of the particle. Figure 4.10 yielded a measured diameter 2a = 110nm. The difference between the measured size by DLS and the average size using TEM imaging is predictable. In any standard imaging techniques, like the TEM, the average size has to be smaller than the biggest size measured. In contrast, with light scattering techniques like DLS, the biggest size scatters the most, so the biggest size dominates the scattering functionality. This is supported by having the measured size using DLS bigger than the measured size using TEM imaging.

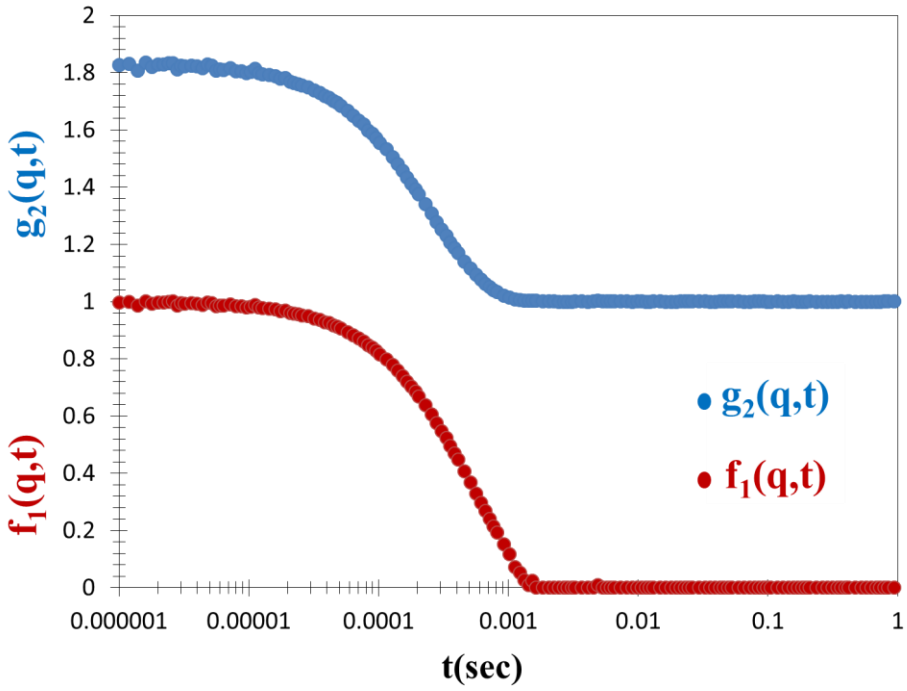

Figure 4.11 Intensity autocorrelation function $g_2(q,t)$ obtained from scattering of spherical polystyrene spheres and the corresponding dynamic structure factor $f_1(q,t)$.

Gel experiment

To initiate aggregation [$MgCl_2$] = 20mM was used for polystyrene spheres (pss) with radius a=20nm as measured by DLS. Data was collected after a waiting time t_w. Fig. 4.15 shows $f_1(t) = (\ (g_2(t) - 1\ )/f_c\ )^{0.5}$ for different t_w. Finding the decay time, τ, for each t_w, and using the analysis mentioned above, one can find the size of the aggregates at each t_w. It is found that this is the apparent size of the aggregates, R_{app}, not the true hydrodynamic size, R_h. This is because the aggregates'shape is not strictly a solid sphere. Lindsay et al. (Lindsay et al. 1988) showed that the apparent radius is the true hydrodynamic radius, R_h, if $qR_h<<1$. As $qR_h \rightarrow 1$, rotational diffusion can affect the decay rate of the dynamic correlation function, and the apparent radii R_{app} appears smaller than the true R_h. When $qR_h >>1$, R_{app} is smaller by a factor of ~ 2.25. However, we have noticed in the literature some experimental data deviates from this correction for $qR_h \geq 10$. (Manley et al. 2004; Lindsay et al. 1988; Lin et al. 1989a; Lin, Lindsay, Weitz, Klein, et al. 1990). Sandköhler et al. (Sandkühler et al. 2005) introduced a scattering model that accounts for the contribution of the internal dynamics of fractal clusters. Their model allows to describe the previously measured experimental data and correct for the deviation that was observed for qR_h

>10. We used the Lindsay et al. results for $qR_h \leq 10$ and the Sandköhler et al. results for $qR_h > 10$ to obtain the true R_h.

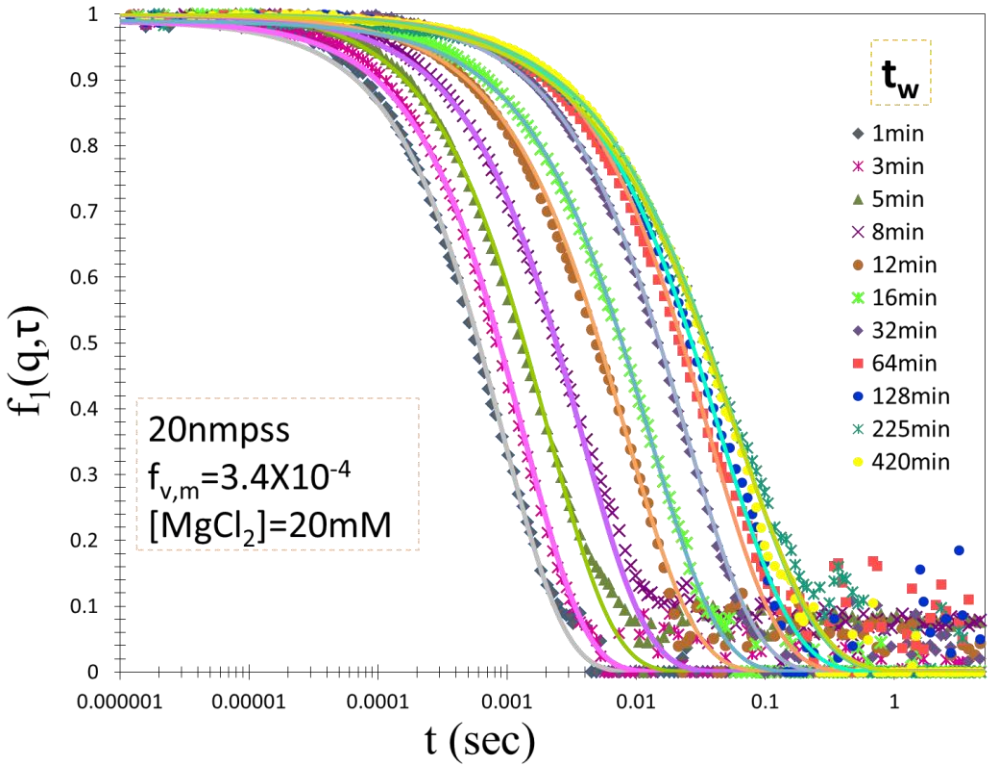

Figure 4.12 The dynamic structure factor f(q,t) vs. t for the gelling sample of f_{vm}=3.8 x 10^{-4} & [$MgCl_2$] = 10mM.

4.4 Transmitivity measurements and multiple scattering interpretations

Mokhtari et al. (Mokhtari, Sorensen, and Chakrabarti 2005) found that multiple scattering events were distributed by Poisson distribution. An expression for the average number of scattering events is reached when compared to Lambert-Peer law

$$< s > = nC_{ext}l \tag{4.10}$$

where n is the number of particles in the system, l is the optical path length of the sample, and C_{ext} is the total extension cross section of the particles, which can be expressed as the sum of the total scattering cross section and the total absorption cross section; $C_{ext} = C_{scat} + C_{abs}$. For the type of particles I used in this work the refractive index is real; $C_{abs} = 0$, and $C_{ext} = C_{scat}$.

The average number of scattering events, <s>, from a sample can be found from the ratio of the transmitted intensity to the incident intensity after and before passing through the sample. A schematic diagram is shown in Fig. 4.13.

The samples in this work are aggregating samples, and eventually, if aggregation is not interrupted, some will form gel. For these samples, the aggregates' sizes are increasing with the waiting time, t_w, which leads to changes in <s>. This is because <s> is proportional to C_{scat}, which increases with increasing size. To find the temporal evolution of <s> for such systems, a photo sensor (Thorlab) was used to measure the incident light I_o before starting the aggregation and the transmitted light after the onset of aggregation I_t at different waiting times t_w. This method relates $I_o(t_w=0)$, $I_t(t_w)$, and <s> (where <s> is a function of t_w) as follow:

$$I_t(t_w)/I_o(0) = Exp(-<s>) \quad (4.11)$$

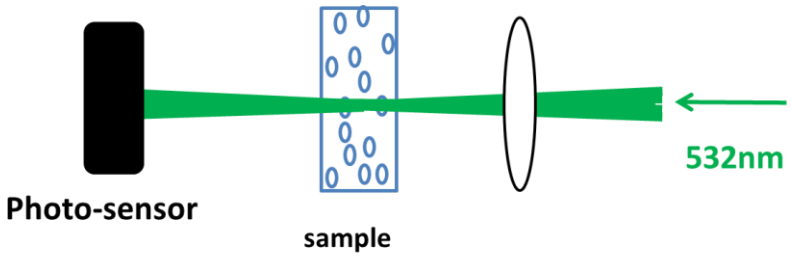

Figure 4.13 A schematic diagram of the transmitivity measurement.

MS measurements on different gel samples are illustrated in Fig. 4.13. Equal volumes of f_{vm} and [$MgCl_2$] are mixed into a 10mm x 5mm cuvette, with the shortest side of 5mm determining the optical path length. I_t/I_o is measured throughout the gelation process. This gave the temporal evolution of the <s> for each gel sample. The different volume fractions of monomers used are f_{vm} = 3, 3.8, 7.6, and 10 x 10^{-4}, and the corresponding [$MgCl_2$] = 10, 15, 16.8, and 17mM. Fig. 4.14 shows that <s> increases with time due to the aggregates growth. Eventually the <s> level off. The higher the volume fraction, the higher the <s> is reached before it levels off. This is due to the fact that higher f_{vm} corresponds to a higher number of monomers per volume, i.e higher n.

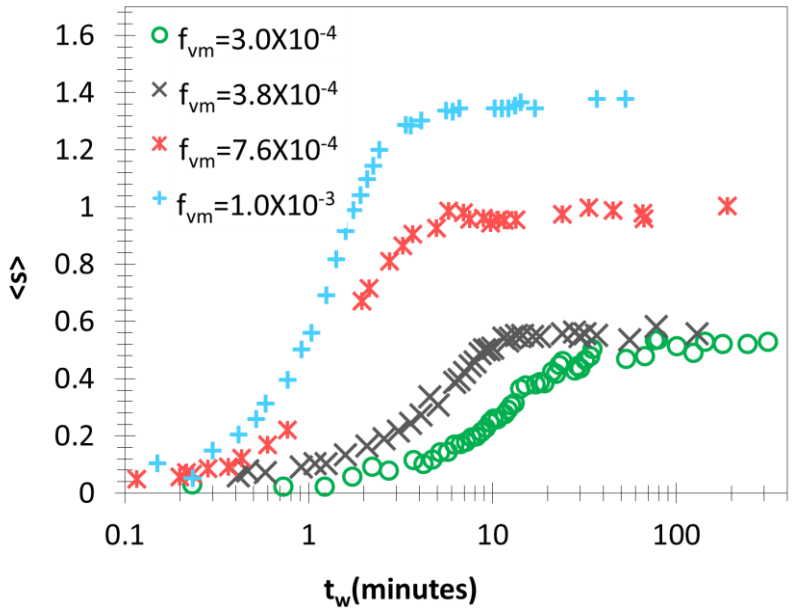

Figure 4.14 Temporal evolution of the <s> for different volume fractions f_{vm} = 3, 3.8, 7.6, and 10 x 10^{-4}, and the corresponding [$MgCl_2$] = 10, 15, 16.8, and 17mM.

4.5 Stability Ratio (W) measurements

In Chapter 3, we discussed the fast aggregates, which are the pure DLCA aggregates that occurred when the salt concentration used to induce aggregation was the critical coagulation concentration, ccc. This results in sticking probability, P = 1. On the other hand if the salt concentration used < ccc, then P < 1, for all P < 1 aggregates are called slow aggregates. Aggregation kinetics between the fast aggregates and slow aggregates are often quantified in terms of the stability ratio W. W is defined as the ratio between the kernel of doublet formation for the fast aggregation, K_{fast} (equivalently named the Smoluchowski kernel, K_{SE}) to the kernel of doublet formation for the slow aggregation K_{slow} i.e. $W = K_{fast\ or\ SE}/K_{slow}$. The fast kernel $K_{fast\ or\ SE}=8K_BT/3\eta$. The inverse of stability ratio 1/W can be understood as the collision efficiency, or the sticking probability between two colliding particles.

Holthoff et al. (Holthoff et al. 1996) showed that the aggregation kernel can be determined from the time it takes to form doublets. DLS can be used for this because the doublet hydrodynamic radius, $R_{h,2}$ is a factor of 1.35 to 1.38 bigger than the monomer radius a, depending upon the orientation of the doublet. We used the average factor of $R_{h,2}$ = 1.365a. Holthoff et al. provided a relation between the scattered intensity at t_w = 0, I(q,0), the scattered intensity at any waiting time

t_w, $I(q,t_w)$, the initial number concentration of the particles, N, the scattering wave vector, q, the monomer radius, a, and the aggregation kernel (fast or slow) for doublet formation, K, as follows

$$\frac{1}{I(q,0)}\frac{dI(q,tw)}{dt} = \frac{\sin(2aq)}{(2aq)} K N \quad (4.12)$$

Using the definition of $W=K_{fast}/K_{slow}$, then Eq.(4.12) can be written as:

$$\frac{1}{I(q,0)}\frac{dI(q,tw)}{dt} = \frac{\sin(2aq)}{(2aq)} W^{-1}K_{fast} N \quad (4.13)$$

W measurements were done for different volume fractions and salt concentrations for the same patch of particles with radius a = 20nm as measured by DLS. The scattering angle was fixed at 90°. DLS measurements provide a tool to measure R_h and the average intensity measured during data acquisition time I(θ).

The smallest f_{vm} we work with is ~ 100 more concentrated than what Holthoff et al. used. In addition the interest of this work is to study gelation which requires using relatively high salt concentrations to allow the samples to gel before they sediment. It is known that higher volume fraction and higher salt concentration mean faster kinetics. With the most dilute f_{vm}, at high salt concentrations doublet formation was either comparable to, and sometimes even faster than, the acquisition time required to take a DLS measurement to find $R_{h,2}$. To overcome this problem, small enough [$MgCl_2$] was used such that the doublet formation is significantly slower than the measurement time to find $R_{h,2}$. This enables the measurement of not only the $R_{h,2}$, but also the average intensity at the doublet size $I(q,t_d)$, where t_d is the time at which doublets are formed. The ratio of $I(q,t_d)/I(q,0)$ obtained from the lowest salt concentration was used as a reference for the time at which $R_{h,2}$ was reached for the higher salt concentration experiments. This procedure was repeated for each f_{vm} used.

Fig. 4.14(a) shows the $I(q,t_w)/I(q,0)$ vs. t_w for $f_{vm} = 1.9 \times 10^{-4}$ and different salt concentrations. The lowest [$MgCl_2$] used was 5mM which made the aggregation slow enough to enable a successful measurement of $R_{h,2}$. At $R_{h,2}$ we found $I(q,t_d)/I(q,0) = 1.9$. Taking this ratio worked as an alternative measure to find the time at which the doublets forms, t_d, at high salt concentrations. Additively, at high salt concentrations (starting from 20mM for $f_{vm} = 1.9 \times 10^{-4}$) t_d is comparable to the time of mixing. This creates a limited number of measurement of $I(q,t_d)/I(q,0)$. Figure 4.15 (a) shows the limited number of data starting at the 20mM salt concentration. Nevertheless, Fig.

2.15(b) (which is a zoomed in version of the x-axis of Fig. 4.14(a)) shows an increasing slope with increasing salt concentrations up to 40mM. This concentration may be recognized as the critical coagulation concentration, ccc, for this f_{vm}. The slope at 40mM can be used to experimentally find K_{fast}. To be careful in determining the ccc value and the associated slope, the $I(q,t_w)/I(q,0)$ vs. t_w is graphed beyond the doublet formation for all these runs as shown in Fig. 4.16. One can see that the kinetics of aggregation is clearly speeding up with increasing salt concentration up to about 40mM. Afterwards, there is no distinct change of the temporal evolution of $I(q,t_w)/I(q,0)$. This further concludes that for $f_{vm}=1.9x10^{-4}$, the ccc = 40mM. Due to the limited data points obtained for $[MgCl_2] \geq 40mM$, the data points for these concentrations were combined to give the slope of 1.04 as shown in Fig. 2.15 (b). This slope is used to find the experimental value of K_{fast}.

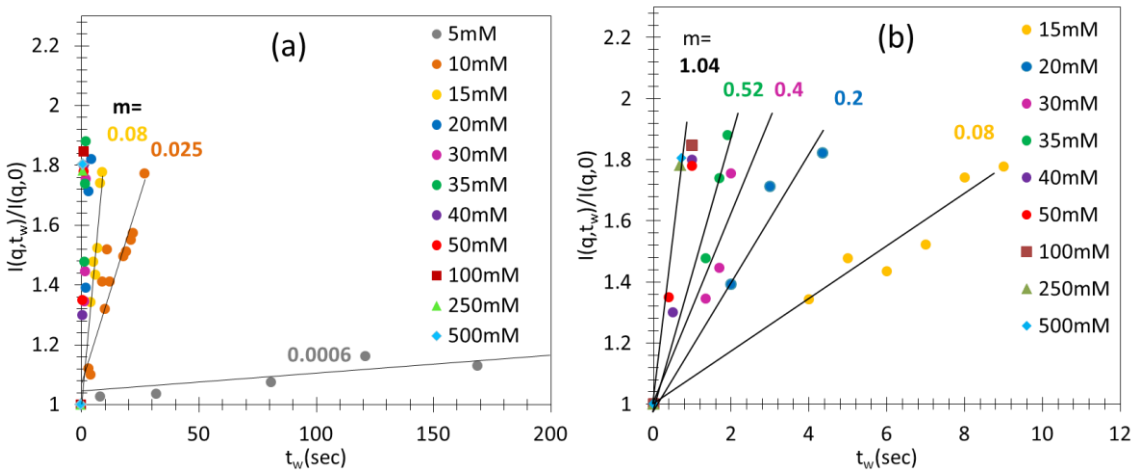

Figure 4.15 $I(q,t_w)/I(q,0)$ vs. t_w for 20nm particles with $f_{vm}=1.9x10^{-4}$ and different salt concentrations. The data are limited here to a waiting time at which the doublet are formed (~ $I(q,t_w)/I(q,0)$ ~1.9). (a) Shows all the salt concentrations used. (b) The same graph as in (a) but zoomed in for salt concentrations of 15mM and more.

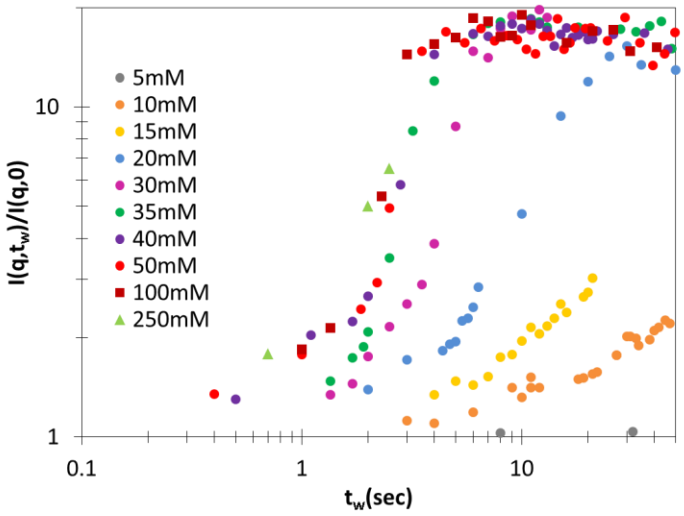

Figure 4.16 $I(q,t_w)/I(q,0)$ vs. t_w for the same runs showed in Fig. 4.14 but now the $I(q,t_w)/I(q,0)$ is graphed versus waiting time a way beyond the doublet formation time. Due to the limited number of data for $[MgCl_2] \geq 40mM$, I presented this graph to further check on when the critical coagulation concentration (ccc) is reached.

Now we obtain the slopes of $I(q,t_d)/I(q,0)$ vs t_w for all the salt concentrations including the ccc value. We use Eq. 4.12 to find K (slow and fast) and the corresponding W values. Fig. 4.17(a) shows K vs. $[MgCl_2]$. The experimental K_{fast} ($K_{fast,Exp}$) = 1.75 x $10^{-17}s^{-1}$ indicated by the red dashed line, whereas the theoretical K_{fast} ($K_{fast,Th.}$) = $K_{SE}=8K_BT/3\eta$ =1.36 x 10^{-17} s^{-1} indicated by the solid black line. This makes $K_{fast,Th}/K_{fast,Exp}$ = 0.78. Figure 4.17(b) shows W vs. $[MgCl_2]$ for f_{vm}=1.9 x 10^{-4}. Once W was calculated using $K_{fast,exp}/K_{slow}$ (red unfilled symbols) another time using $K_{fast,Th}/K_{slow}$ (black filled symbols). The salt concentration at which W reaches a constant value of ~1, is the critical concentration of coagolation, ccc.

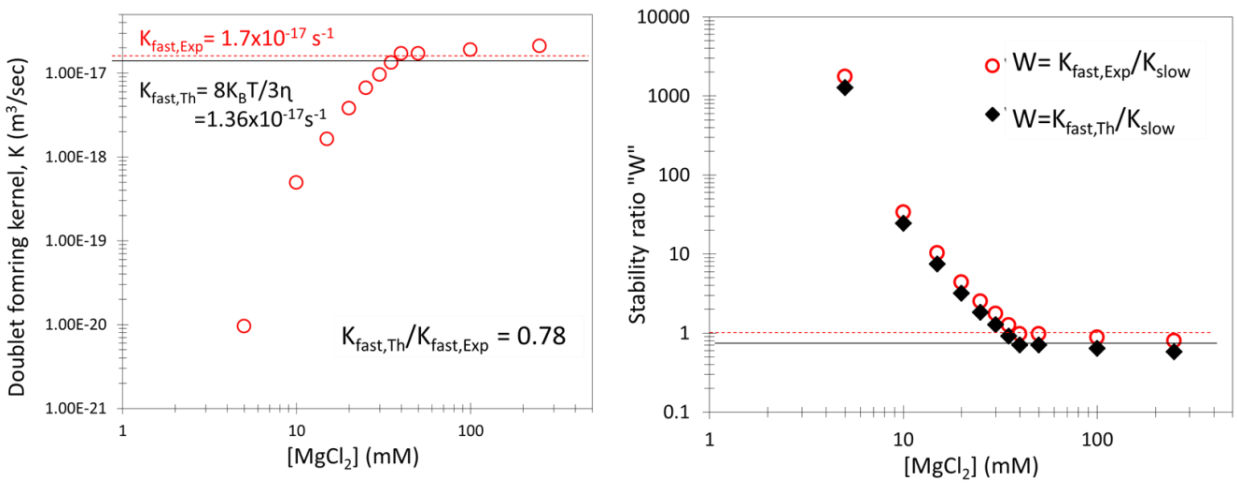

Figure 4.17 (a) doublet forming kernel K for different salt concentrations, (b) Stability ratio, W for different salt concentrations.

Figure 4.18 is a repeat of Fig. 4.17 except it shows different f_{vm}s. Again, the unfilled and filled symbols represent W = $K_{fast,Exp}/K_{slow}$ and $K_{fast,Th}/K_{slow}$, respectively. The red dashed line represents W = $K_{fast,Exp}/K_{slow}$ ~ 1, whereas the black solid line represents W = $K_{fast,Th}/K_{slow}$ ~ 0.7. This graph further confirms, experimentally, that for a good approximation one may consider $K_{fast,Th}$ ~ $K_{fast,Exp}$. To replace $K_{fast,Exp}$ with $K_{fast,Th}$ was an additional change to the Holthof et al. method. This change was inevitable due to the relatively high volume fractions we are interested in for the system to gel. This creates a very fast kinetics which makes finding the $K_{fast,Exp}$ unfeasable. This procedure is followed in finding W for all the gelling samples.

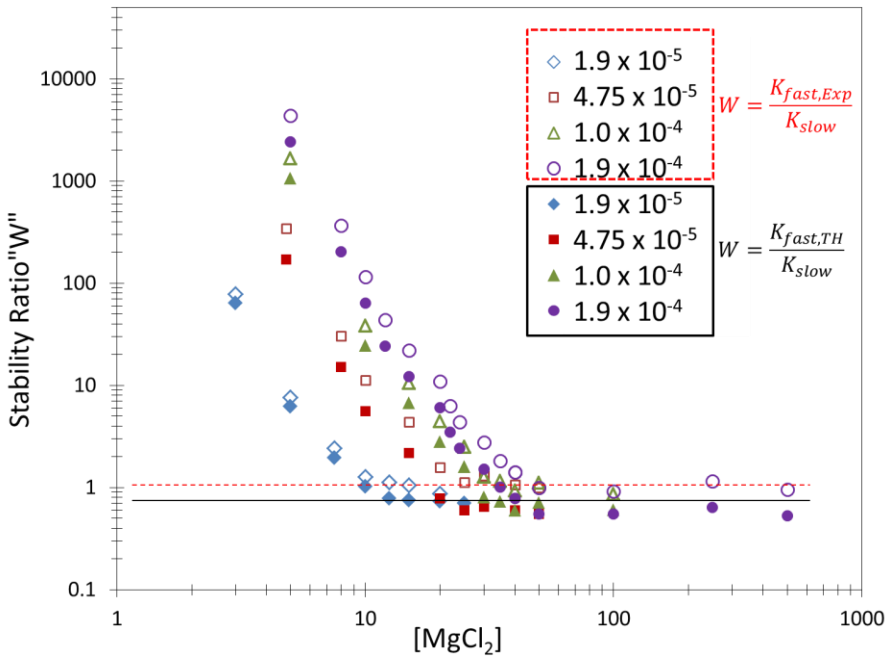

Figure 4.18 W vs. [$MgCl_2$] for different f_{vm}. The unfilled and filled symbols represent W = $K_{fast,Exp}/K_{slow}$ and $K_{fast,Th}/K_{slow}$, respectively. The dashed red line represent W = $K_{fast,Exp}/K_{slow}$ ~ 1, the black line represents W = $K_{fast,Th}/K_{slow}$ ~ 0.7.

Now we present W vs. [$MgCl_2$] graph for a wide range of initial monomer volume fractions ranging from 1.9 x 10^{-5} to 1 x 10^{-2} as shown in Fig. 4.19. The graph shows two slopes. One slope is represented by the black solid line(s) which, interestingly, takes a value of 3.1 ± 0.12 for all the different f_{vm}s. The second slope is represented by the color coded dashed lines and take values ranges from 4 to 6.5 for f_{vm} = 1.9 x 10^{-5} to 3.8 x10^{-4}, respectively. As discussed earlier, for low f_{vm}s, the ccc was determined experimentally when W ~ 1. For the higher f_{vm}s the kinetics was so fast that determining ccc was unfeasible. Nevertheless, I will consider the point at which the horizontal black dashed line crosses with the -3.1 slope of each f_{vm} represents the ccc for that f_{vm}. Figure 4.20 shows ccc vs. f_{vm}. The filled symbols represent the experimentally achieved ccc values (for lower f_{vm}s), meanwhile the unfilled symbols represent the ccc values obtained by crossing the -3.1 slope line with the horizontal dashed black line for the higher f_{vm}s. It is interesting that all the data fits in a slope of 0.5 ± 0.04. This provokes the idea of graphing W vs. [$MgCl_2$]/$f_{vm}^{0.5}$ as shown in Fig. 4.21. This graph creates "almost" a master curve for W < 100. These results are interesting and deserve further studies.

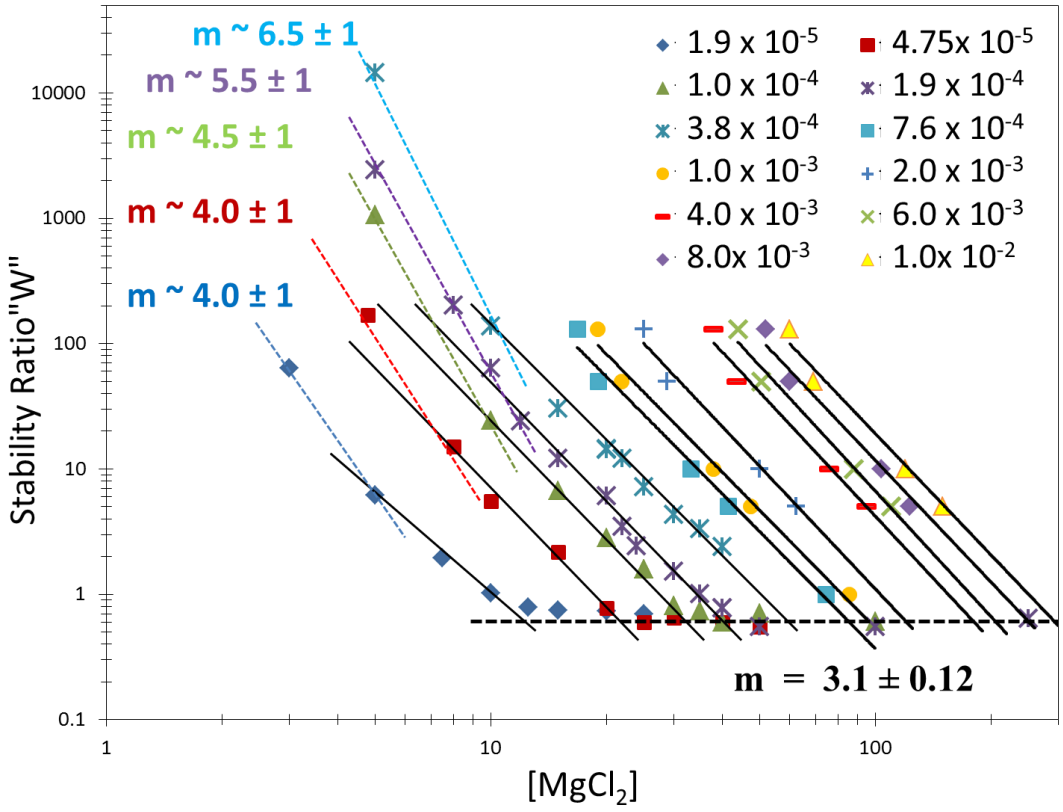

Figure 4.19 W vs. [$MgCl_2$] for a wide range of f_{vm} obtained as described above.

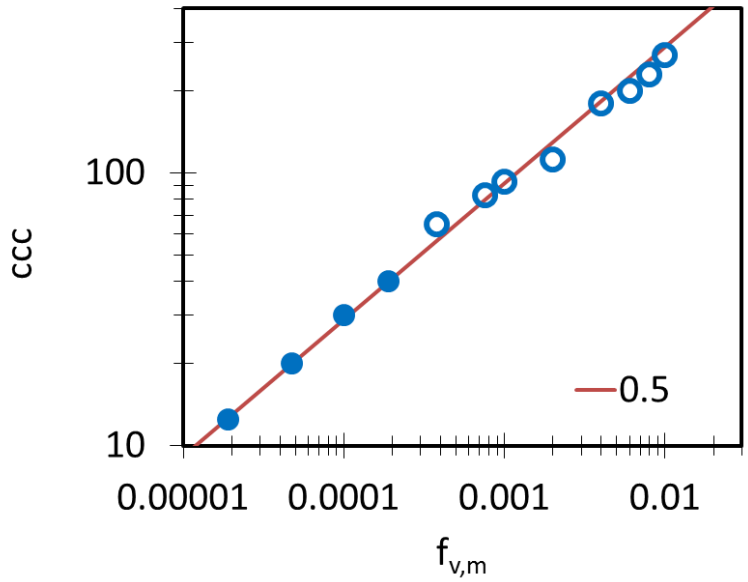

Figure 4.20 ccc vs. f_{vm} obtained from Fig. 4.19. Filled symbols represent the experimentally found ccc for f_{vm}s ranges from 1.9 x 10^{-5} to 1.9 x 10^{-4}. The unfilled symbols represent the ccc obtained from the solid lines of slope -3.1 crosses with the horizontal dashed lines for f_{vm}s ranges from 3.8 x 10^{-4} to 1 x 10^{-2}.

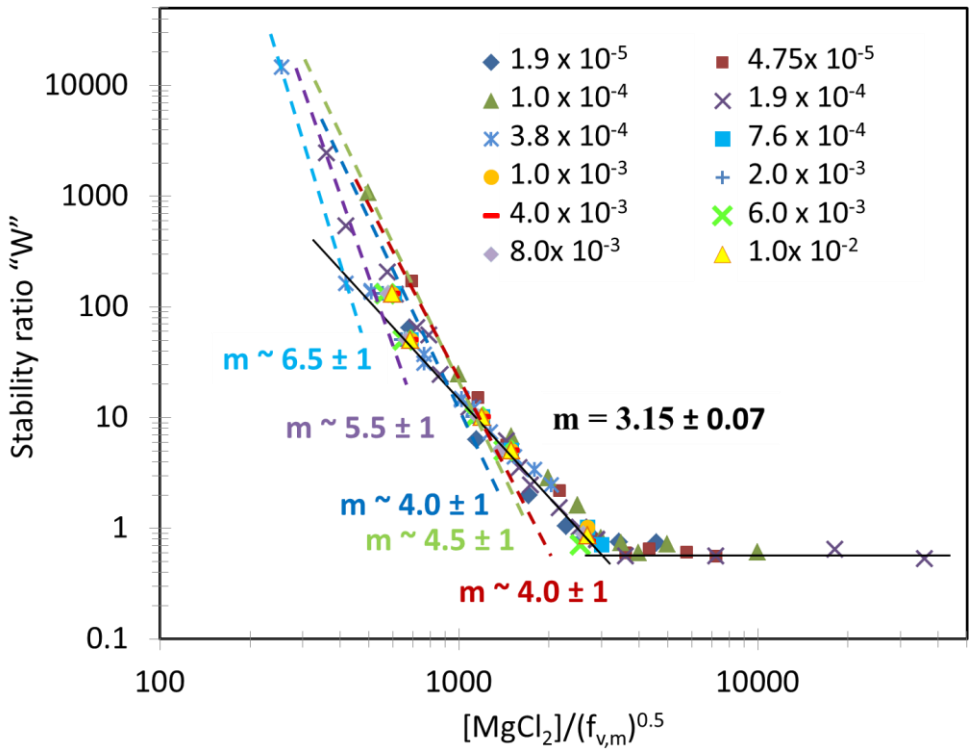

Figure 4.21 W vs. $[MgCl_2]/(f_{vm})^{0.5}$.

4.6 Combined setup

In Fig. 4.22 a schematic diagram for the combined SASLS and DLS with the transmitivity set up for probing the gel system. Figure 4.23 shows (a) the image of DLS and transmitivity setups, and (b) the image of SASLS setup.

These three combined setups allows for measuring, in real time and for a single sample, the following: the intensity $I(q,t_w)/I(q,0)$ growth rate, to eventually find the stability ratio W, the temporal evolution of $I(q\rightarrow 0)$, R_g, R_h and <s>, and to measure the fractal dimension, D_f.

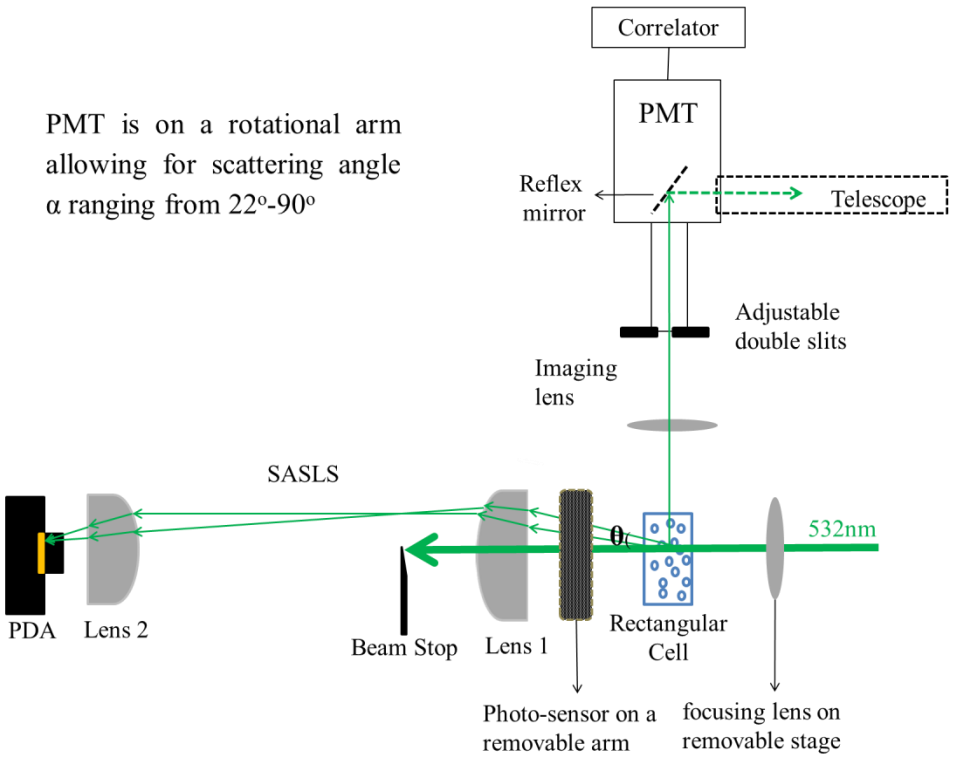

Figure 4.22 A schematic diagram for the three combined setups: SASLS, DLS, and transmitivity setup.

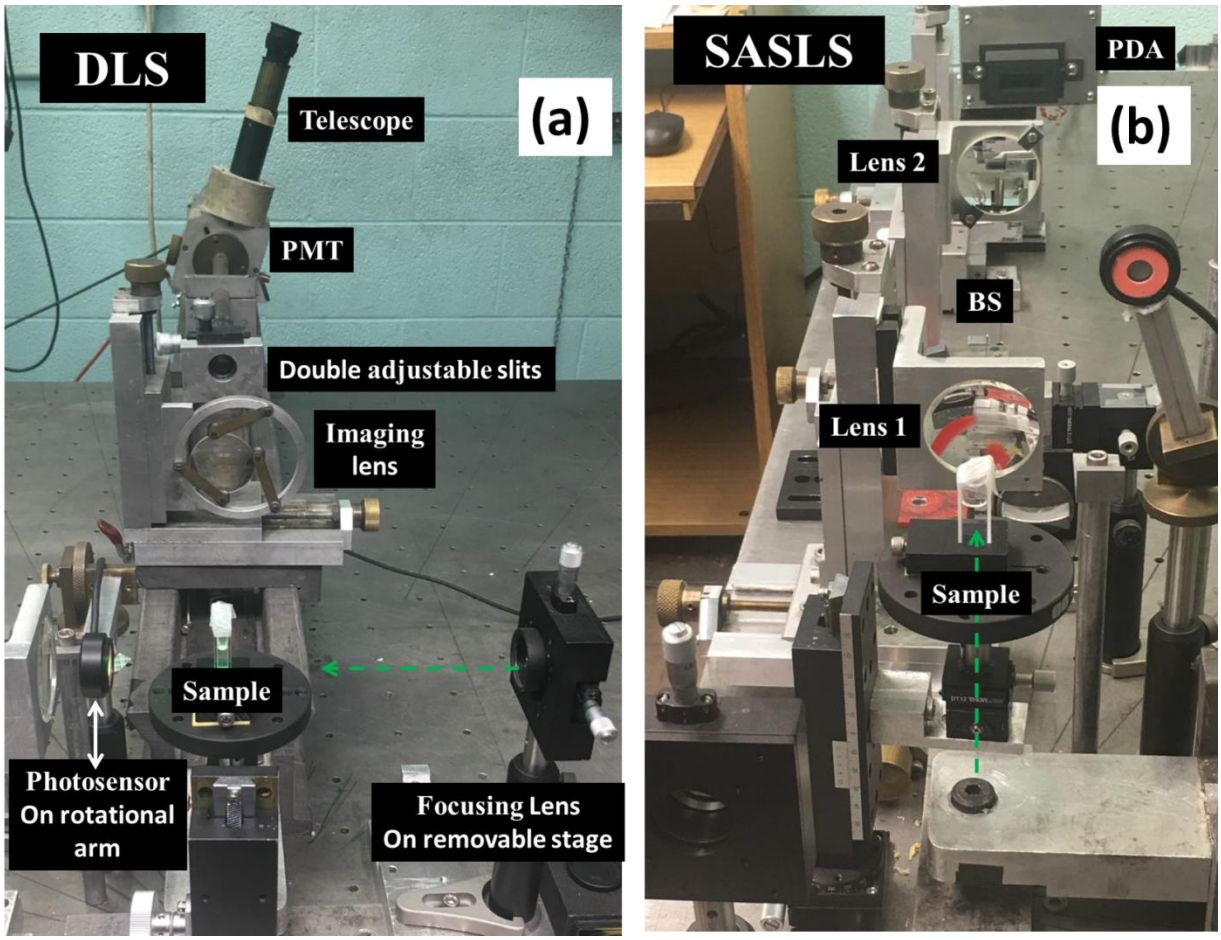

Figure 4.23 Images for DLS apparatus (a) and SASLS apparatus (b).

Chapter 5 - Experimental procedure

To successfully study the IGP theory, including the kinetics and the gel time perspectives, there are two main aspects that need to be considered. One is the integration between concepts and the variables in these experiments. For example, the fractal dimension and the monomer volume fraction both determine the size of the aggregate at the IGP and the gel time. At the same time the salt concentration and the monomer volume fraction determines the fractal dimension. Another aspect is the experimental challenges (or limitations) associated with this study, such as sedimentation and multiple scattering. This chapter is designed to give a road map of the procedure we followed to find the proper connection of the variables, and to a good extent overcome the challenges.

5.1 Design of experimental procedure

The range of f_{vm} used in this experiment was low bounded by sedimentation, and upper bounded by MS. Sedimentation was studied by Manley et al., who gave an expression to find the gravitational strain value on a cluster (Manley et al. 2004) despite using density matching medium. Gisler et al. (Gisler, Ball, and Weitz 1999) showed that colloidal aggregate gels break under external strain > 0.45. The strain value increases with increasing cluster size. At the same time the IGP theory predicts the aggregates' size to increase at the IGP with decreasing f_{vm} and increasing D_f. Following Manley et al. calculations for our system (where density difference between medium and particles $\Delta\rho \sim 10^{-3} g/cm^3$) indicate the cluster size at IGP where critical strain reaches ~80μm, which is higher than the measured R_g of our experiments. In addition, it was observed experimentally that sedimentation occurs for our system when $R_g \geq 18\mu m$. The $R_{g,G}$ value can be predicted from the IGP theory using the known f_{vm} and D_f, allowing us to avoid low volume fractions, which give $R_{g,G} > 18\mu m$ that would fail to gel due to sedimentation.

On the other hand, at large f_{vm}, MS perturbed the structure factor obtained from SASLS to yield a smaller slope, hence a smaller inferred D_f in the power law regime and smaller R_g measurements. It also affects the dynamic field correlation function obtained from DLS and eventually, yields a smaller R_h. We found that SASLS measurements are much more sensitive to MS than DLS ones. MS artifacts start to show on the SASLS structure factor for relatively high f_{vm} ($\sim 7.6X10^{-4}$ in our

experiment), but with increasing f_{vm} it becomes so severe (~f_{vm} ~$3x10^{-3}$ in our experiment) that the signal smears out and no aggregate growth can be detected in the forward scattering.

The experiments were designed to test the effect of the fractal dimension and the monomer volume fraction on the radius of gyration value at the IGP. In addition, it was meant to test the kinetics of sol-to-gel transition as described by the IGP theory. These relations were explained in Chapter 3. I found that having the correct fractal dimension is crucial to our data analysis. In addition, the multiple scattering, as mentioned earlier, will create artifacts in R_g and D_f measurements. The effect of MS artifacts on R_g was resolved by combining the DLS to extract R_h. Even though these two radii are not exactly equal, $R_h \sim 0.77\ R_g$ in the dilute regime, the assumption of $R_h \sim R_g$ can still be valid. In addition, our experimental values of R_h and R_g are comparable to each other as we will see this in Fig. 5.2 (a).

The effect of MS on D_f needed to be addressed as well. To do so, I found it very important for these experiments to measure the stability ratio W. Remember, W can be understood as the inverse of the probability of sticking, P, between particles. This probability is determined by the amount of salt added to the charged particles to screen the repulsive potential. If P = 1, the aggregates will form via the fast or pure DLCA aggregation. Otherwise, if P < 1, the aggregates will form via the slow aggregation.

I followed, for the most part, the procedure of Holthof et al. (Holthoff et al. 1996) to find the stability ratio. As a reminder, $W=K_{fast}/K_{slow}$, where K_{fast} is the fast aggregation kernel for doublet fomation, which is achieved at salt concentration defined as the critical coagulation concentration (ccc), and K_{slow} is the aggregation kernel for doublet formation for any salt concentration less than the ccc.

The experimental set up and data for W measurements was explained in section 4.5. Here I will summarize the method and talk about the procedure we followed to find D_f. The Holthof et al. method depends on finding the time at which doublet size is reached, t_d. The doublet size ~1.365 the initial monomers' size; R_h=1.36a. This defines the doublet time, t_d, which is involved in finding the doublet forming kernel, thus W. In my experiment, the challenge was the kinetics of forming the doublets on the order of the time scale of the measurements. This is because the initial monomer volume fractions I worked with are high enough to guarantee the system forms a gel. For example, the minimum volume fraction of monomers I used in my experiments was 100 times more

concentrated than the ones used by Holthof et al. In addition I used divalent salt with relatively high concentrations so that a gel may form. These choices make the kinetics very fast compared to Holthof et al. case.

To overcome this challenge, I used the ratio of the scattered intensity at doublet formation, I_d, to the scattered intensity of the monomers, I_o, before aggregation. This ratio was taken first with a very low salt concentration such that the kinetics is still slow enough to measure the doublet size. At the doublet size for each monomer volume fraction, I marked the ratio of I_d/I_o. This ratio value is now the reference value of finding t_d for the proper W calculations. It turned out that this ratio ranges experimentally from 1.7-1.9 for the different volume fractions I worked with.

This new twist we introduced to the Holthof et al. method to measure W was successful for gel experiments that are not in the pure DLCA regime. When dealing with the pure DLCA or fast aggregation, the kinetics are, again, too fast to find the I_d/I_o. This problem is even more severe when higher values of f_{vm} are used. The pure DLCA aggregates occur at the ccc point, which is different for each f_{vm}. At the ccc, the kinetics is the fastest for that specific f_{vm}. The doublets form for the gel samples so fast making it unfeasible to find the experimental fast aggregation kernerl, K_{fast}. In section 4.5 we found that the theoretical and experimental doublet forming kernels are about equal. Replacing the experimental value in the Holthof et al. method by the theoretical value of the doublet forming kernels overcomes the problem of fast doublets formation for gels.

Now that we can measure the stability ratio for the gelling system, we can continue in our procedure to overcome the MS artifacts on D_f values. To accomplish this, we grouped our experiments into groups. Each group consisted of different volume fractions and different salt concentrations such that the measured W values for all the volume fractions within one group were within ~20% or less of each other. We named the average value of the grouped W as W_{grp}. We did different SASLS measurements for different f_{vm} to determine the f_{vm} at which the structure factor contains no artifacts due to MS. Figure 5.1 (a) &(b) show I(q) vs. q at $t_w \sim t_{gel}$ for different gelling systems. The I(q) vs. q for $f_{vm} = 3$ & 3.8×10^{-4} correspond very well with each other to indicate that I(q) contains no MS artifacts for $f_{vm} \leq 3.8 \times 10^{-4}$. This experiment concluded that for $W_{grp} = 37 \pm 4$ the correct $D_f = 1.73 \pm 0.05$, and for $W_{grp} = 141 \pm 20$ the correct $D_f = 1.85 \pm 0.05$ as shown in Fig. 5.1 (a) and (b) respectively for the f_{vm} up to 3.8×10^{-4}.

However, notice for f_{vm}=7.6 X10^{-4} and 1 X10^{-3} the inferred D_f values were smaller due to MS artifacts. Simultaneously to SASLS measurements for each gel experiment, the transmitivity measurements were performed, and the <s> values near t_{gel} were recorded as insert tables in Fig. 5.1 (a) & (b). For f_{vm} = 3.8X10^{-4}, the average <s> ~ 0.5-0.55. From the Poisson distribution, this gives P(double scattering)/P(single scattering) = <s>/2 = 0.28. This is a significant fraction, but when comparing with Fig. 1 of Mokhtari et al. (Mokhtari, Sorensen, and Chakrabarti 2005), where <s> = 0.63, the I(q) vs q plot is still in good agreement with the Mie-scattering theory. Thus, it is reasonable to conclude that when <s> $\lesssim$ 0.55, there is no MS artifact to perturb the structure factor and harm the D_f measurement. We found that any gel experiments with the same W value will have the same D_f, regardless of their f_{vm} and salt concentrations. This is evident in Fig. 5.1(a) & (b), where the D_f was measured to be the same for f_{vm} = 3 x 10^{-4} and 3.8 x10^{-4} that had similar W.

To properly link W values to their corresponding D_f, we choose to work with f_{vm} = 3X10^{-4}, which satisfies the following conditions simultaneously: it can gel before it sediments, and no MS artifacts are present in the SASLS measurements. A series of experiments with this f_{vm} but different salt concentrations, which yielded different W values, were performed as shown in Fig. 5.2. Figure 5.2 (a) shows R_h and R_g vs. t_w for each W value, and (b) shows D_f vs. W. Note in Fig. 5.2(b) the black diamond corresponds to f_{vm} = 3 x 10^{-4}, but other points correspond to different f_{vm} that do not satisfy the first condition, but nevertheless still give a valid D_f measurement vs. W.

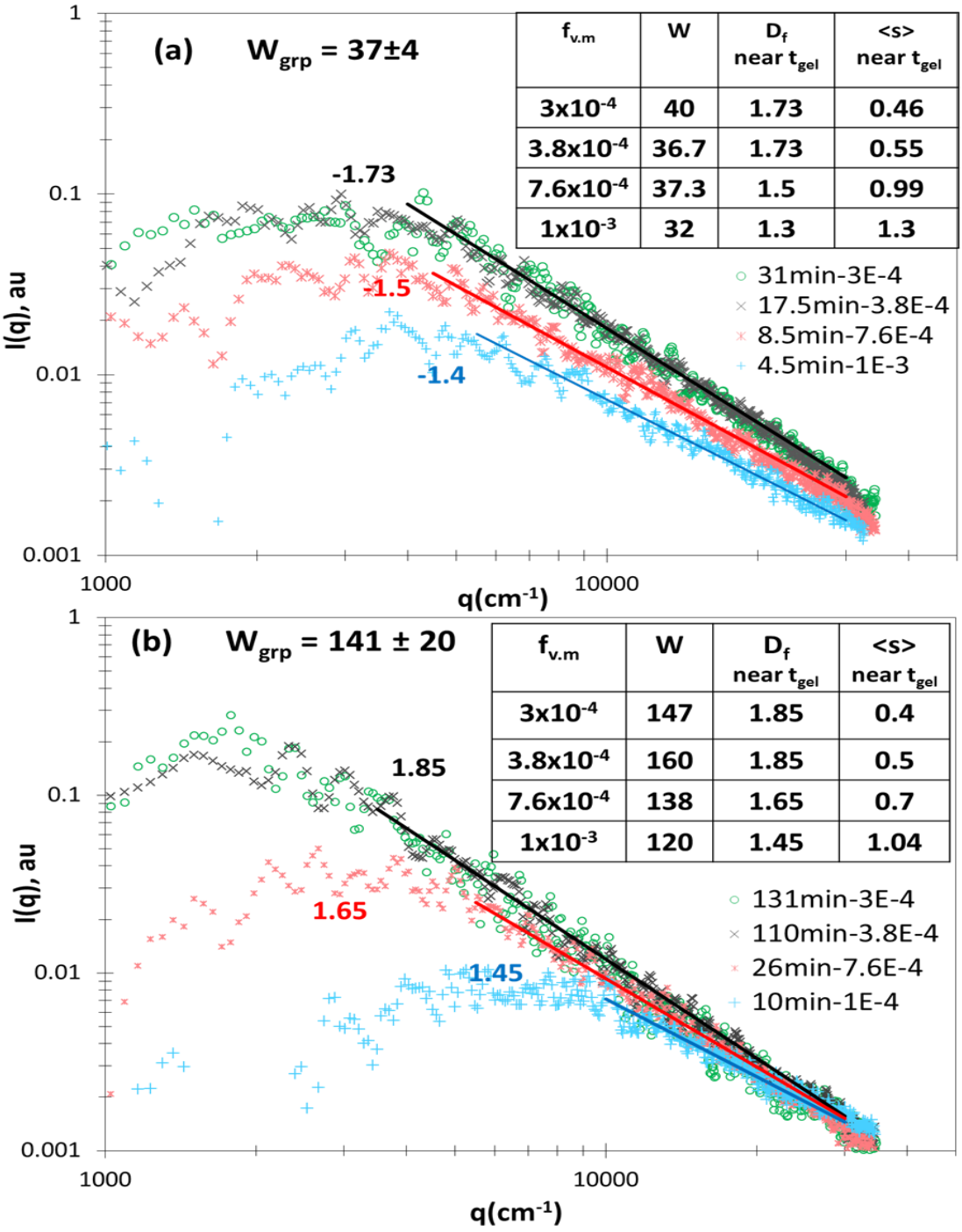

Figure 5.1 I(q) vs q at tw ~ tgel for different W_{grp} gelling systems with (a) W_{grp} =37±4 and (b) W_{grp} =141±20. Inserted tables show D_f, and <s> near tgel and W values for each individual gelling system. W values that are within 20% of each other are grouped together and averaged to give W_{grp} as shown in (a) &(b). Here we show that <s> up to 0.55 value shows no MS artifacts in the forward direction.

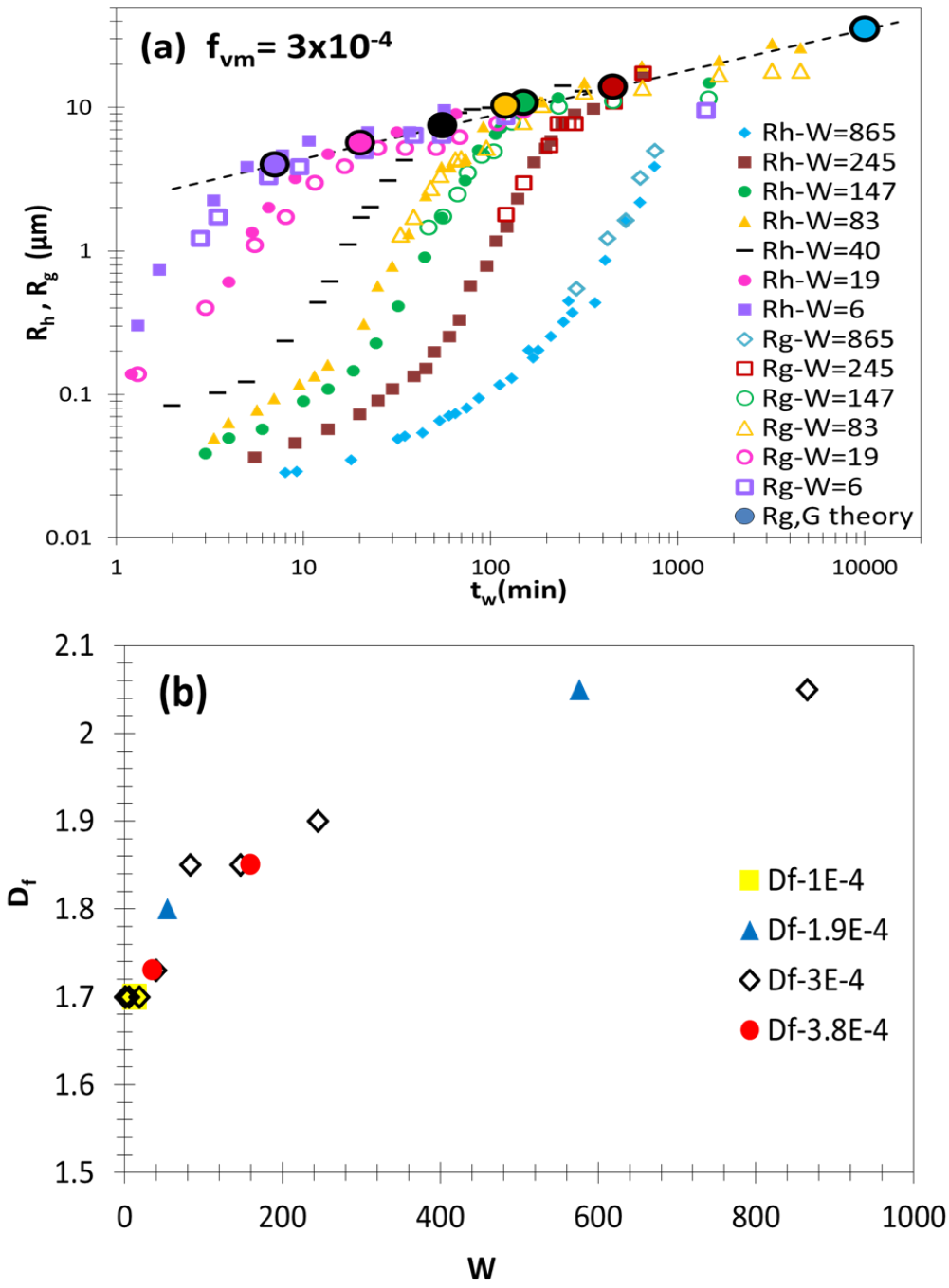

Figure 5.2 A series of gel experiments using f_{vm}=3X10^{-4} but different salt concentrations. (a) Rh, Rg vs tw with the measured W value of each experiment as indicated in the legend. (b) D_f vs. W graph. D_f was measured from the SASLS measurement near tgel.

Chapter 6 - The kinetics of the colloidal sol-to-gel transition

In this chapter we present investigations of the kinetics of the colloidal sol-to-gel transition by combining small angle static light scattering (SASLS) and dynamic light scattering (DLS) techniques. The light scattering theories, techniques, and calibration have been discussed in detail in Chapter 2 and 4. Two types of experiments were conducted. One is a non-gelling, aggregating experiment and the other is a gelling experiment. For the gel experiment dilute monomer volume fractions were used to allow for a full investigation of the gelation to obtain all possible kinetics regimes. The data verify the predictions of the ideal gel point (IGP) theory, where three regimes of kinetics are expected. This theory is fully discussed in sections 3.3.1.1 and 3.3.1.2. We observe the first regime, the well-known cluster-dilute regime, with a kinetic exponent of z = 1. The cluster-dilute regime followed by a cluster-dense regime with an enhanced kinetics and z ≃ 2. Finally, a gelation regime is observed where the aggregate growth slows and ceases to grow at the IGP predicted size, $R_{g,G}$. which takes the following expression

$$R_{g,G} = a[\, f_{v,m}^{-1} k_o (D_f / (2 + D_f))^{3/2}]^{1/(3-D_f)} \tag{6.1}$$

The results discussed in this chapter quantitatively verify the IGP theory. We conclude that the kinetics description provides a complete theory of the gelation process from sol to gel.

6.1 Results and discussion

6.1.1 Aggregating, non-gelling system

The aggregating, non-gelling system was very dilute, with a monomer volume fraction $f_{v,m}$ = 6.8×10^{-6}, and [$MgCl_2$] = 10mM. This very dilute system stayed in the cluster-dilute regime during the whole experiment (~ 18 hrs). Data was collected at different times after the onset of aggregation, a time that will be called the waiting time, t_w. DLS measurements were performed at scattering angles 22.1° and 90° for the same sample. These scattering angles correspond to q values of 6μm^{-1} to 22.2μm^{-1}, respectively. An example of the results are shown in Fig. 6.1, where the field correlation function $f_1(q,t)$ were graphed, for both scattering angles, at different t_w for the same aggregating, non-gelling sample. The solid lines are the fit lines to a stretched exponential $f_1(q,t) \sim exp(-t/\tau)^{\beta}$, where τ is the relaxation time and β is the stretching exponent. Initially, $f_1(q,t)$ starts as a single exponential representing a pure diffusive motion in the early

stages of aggregation (β=1), but later it starts to deviate from being exponential and becomes more stretched exponential in form. To illustrate this behavior, we graphed β vs. t_w for scattering angles 22.1° and 90° as shown in the insert of Fig. 6.1 (a) & (b). Initially, β takes a value of 1, then drops below that at $t_w \sim 20$ minutes and 4 minutes for scattering angles 22.1° and 90°, respectively. The $\beta < 1$ behavior indicates hindered motion of the diffusing aggregates (Ren et al. 1992; Roland Böhmer 1998). More of the stretched exponential discussions will be introduced in chapter 8. For such a dilute system, the scattered light in the forward direction was too weak to be detected by the SASLS.

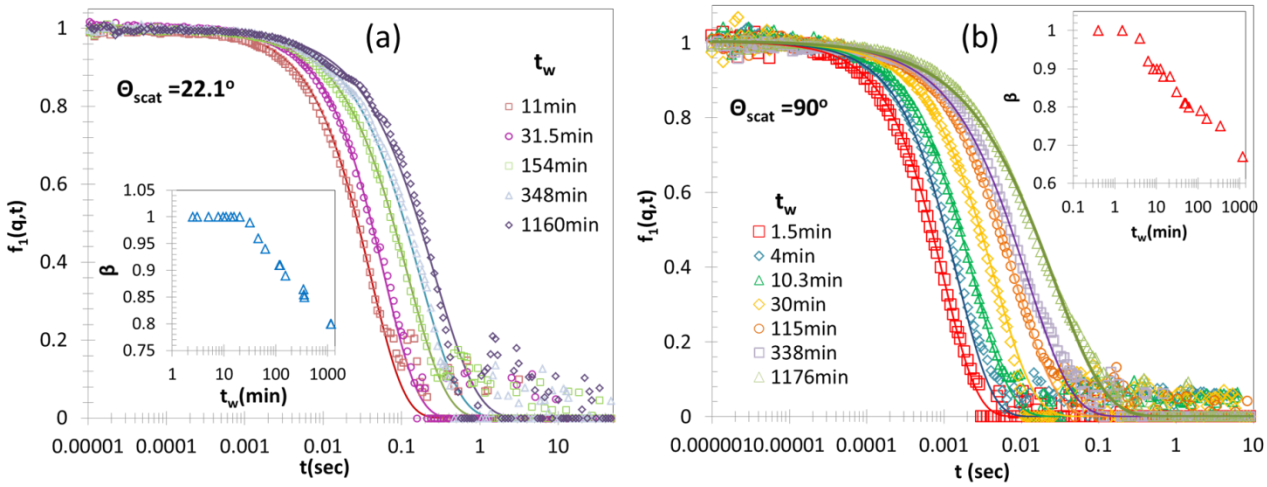

Figure 6.1 The field correlation function for the aggregating, non-gelling system of $f_{vm}=6.8\times10^{-6}$ and [$MgCl_2$] = 10mM measured simultaneously at two different scattering angles (a) 22.1° and (b) 90°. The solid lines are the fits for the stretched exponential $f_1(q,t) \sim exp(-t/\tau)^{\beta}$. The inserts represent the β vs. t_w graphs for each scattering angle.

The $f_1(q,t)$ yields an apparent radius, R_{app}. According to Lindsay et al. (Lindsay et al. 1988) the rotational diffusion of the aggregates affect the decay rate of the dynamic correlation function and yields smaller decay values if $qR_{app} > 1$. Lindsay's model showed a plateau value of 2.25 at about $qR_{app} \sim 10$. Experimental results did not show a plateau (Lin, Lindsay, Weitz, Klein, et al. 1990; Lin et al. 1989a; Lindsay et al. 1988; Manley et al. 2004). Sandköhler et al. (Sandkühler et al. 2005) introduced a model that accounts for the internal dynamics of the clusters. Their model nicely fits the experimental data for $qR_{app} > 10$. Lindsay et al. and Sandköhler et al. models were used for $qR_{app} \leq 10$ and $qR_{app} > 10$, respectively.

Figure 6.2 shows the R_h vs t_w for the non-gelling sample data shown in Fig. 6.1(a) and (b). Notice that R_h for both scattering angles of the same sample is in agreement with each other, and the slopes of these two independent measurements are yielding the same slope of 0.52 ± 0.06. This slope corresponds to z = 0.94 ± 0.05 and λ = 0.06 ± 0.05, which is a typical value for aggregates in the DLCA regime (Jullien 1987; Kolb, Botet, and Jullien 1983; J E Martin and Adolf 1991; Meakin 1987) with D_f = 1.8.

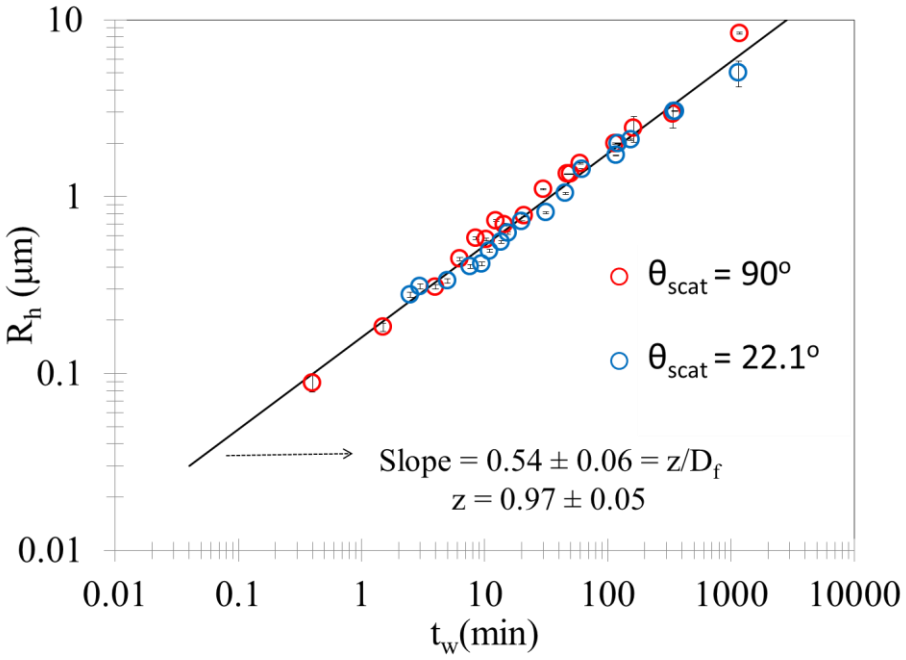

Figure 6.2 Temporal evolution of the true hydrodynamic radius, R_h, for both scattering angles 22.1° and 90°.

6.1.2 Gelling system

The gelling systems had monomer volume fractions of the order 10^{-4}. For these systems the kinetics was slow enough to allow for detecting all aggregation regimes from the onset of aggregation up to the gel formation within feasible experimental times.

Figure 6.3(a) shows the static scattered intensity I(q) vs. q for a gelling sample ($f_{v,m} = 3.8 \times 10^{-4}$ and salt concentration [$MgCl_2$] = 10mM). The power law slope is evidence of fractal aggregates with a fractal dimension D_f = 1.78 ± 0.05 formed via DLCA. The dynamic field correlation function $f_1(q,t)$ vs t in Fig. 6.3(b) shows complete relaxations over all times to indicate that the gelling

system remains ergodic. This indicates that the excursions of the segments within the gel is greater than q^{-1}, so the scattering appears ergodic (A. Krall and Weitz 1998). The insert represents the β vs. t_w graph for this sample.

The SASLS provides I(q) vs. q graph at different t_w. Each I(q) vs. q provides a measure of the intensity at small q values at that t_w. The hump at smaller q values is due to cluster-cluster anti-correlation (Oh and Sorensen 1999) which occurs when in the cluster-dense regime (Huang, Oh, and Sorensen 1998). It will be further established below that all the SASLS measurements were taken when the system was in the cluster-dense regime. It is reasonable to assume that the value of I(q) at the peak of each hump is the value of the intensity at small q. We will call it I(0). SASLS can also be used to find R_g from Guinier analysis. $f_1(q,t)$ vs. t can be used to find R_h assuming Stokes-Einstein Brownian motion of the aggregates. It is known that $R_h \sim 0.77\ R_g$ for aggregates in the dilute regime (C. M. Sorensen 2011). For the purpose of identifying a general trend of kinetics one may assume $R_h \sim R_g$. Then, each of R_h, R_g, & I(0) can probe the kinetics because $I(0) \sim t^z$ and $R_h \sim R_g \sim t^{z/D_f}$.

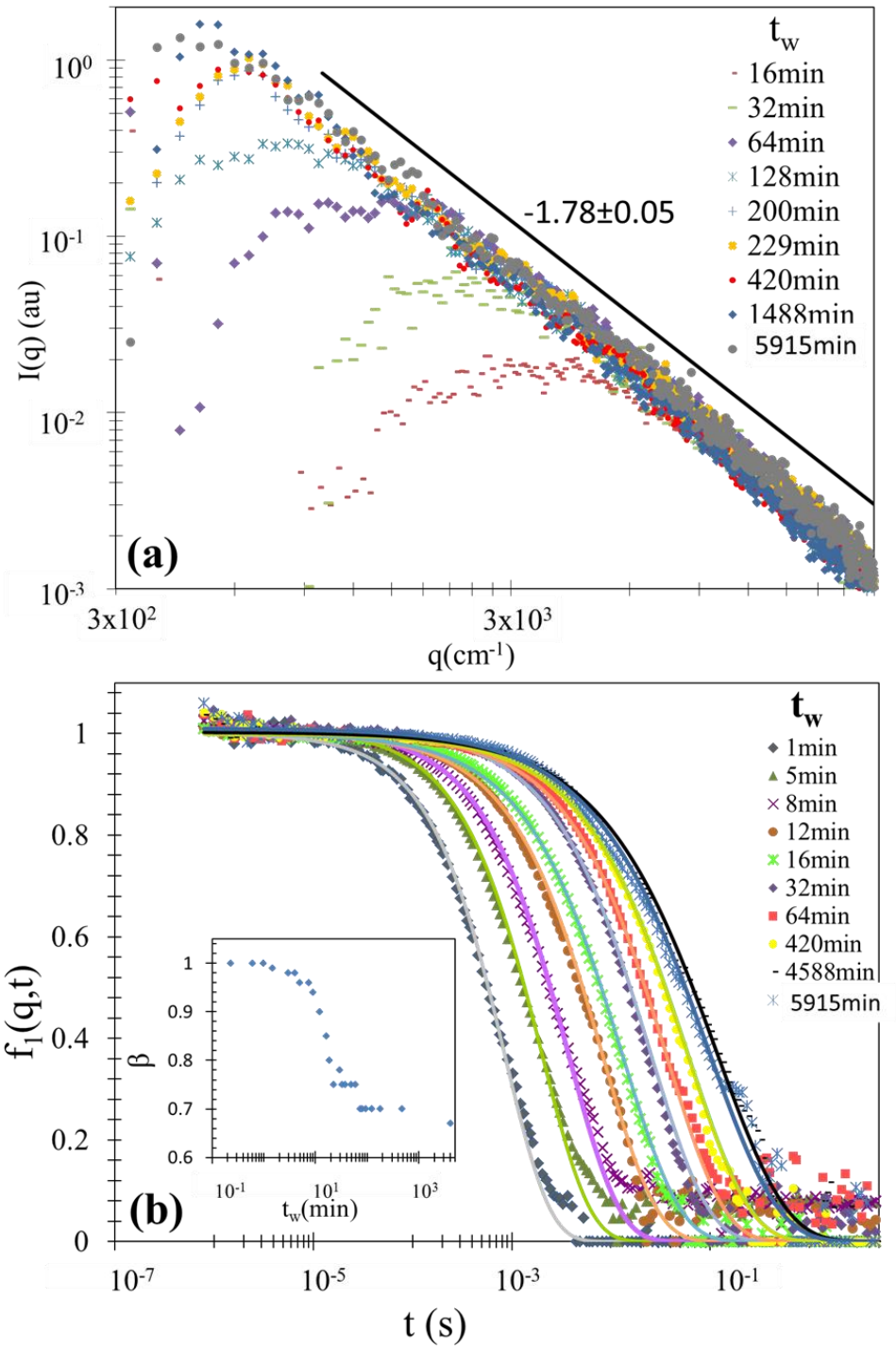

Figure 6.3 Light scattering results for the gelling sample ($f_{v,m}$ = 3.8x10^{-4} & [$MgCl_2$] = 10mM) at various waiting times (t_w) after aggregation initiation. (a) SASLS measured I(q) vs q. The slopes at large q imply D_f = 1.78 ± 0.05. (b) DLS measured dynamic structure factor $f_1(q,t)$ vs t for the same gelling sample shown in (a). The insert shows the stretching exponent β vs t_w.

Figure 6.4 plots R_g, R_h and I(0) versus the waiting time t_w for the gelling colloid with $f_{v,m}$ = 3.8 x 10^{-4} and salt concentration of 10mM. The three different kinetic regimes are demonstrated. The first regime is immediately after the onset of aggregation and continues up to a time we will call it a transition time t_{trans} ~ 5 minutes. After that, there is enhanced aggregation representing the second regime. Finally, the kinetics slows down drastically at the "rounding off time" where t_w ~ 80 minutes. R_g, I(0), and R_h vs. t_w graphs obtained from SASLS and DLS were in support of the second and the third regime. The first regime was detected only by the DLS because the aggregate sizes were below the range of the SASLS setup.

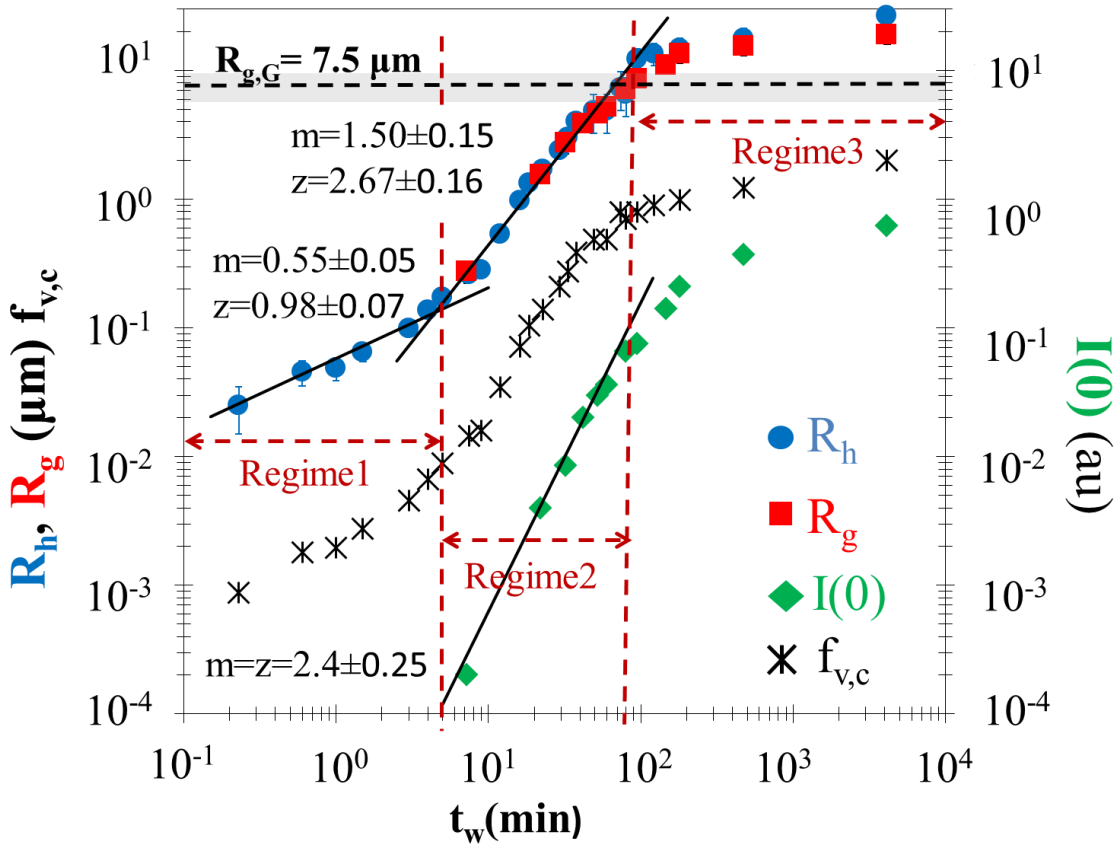

Figure 6.4 Temporal evolution of R_h, R_g, I(0), and $f_{v,c}$ for the gelling sample ($f_{v,m}$ = 3.8x10^{-4} and salt concentration [$MgCl_2$]=10mM). R_h vs. t_w shows the three different regimes, R_g and I(0) vs t_w further support the 2nd and 3rd regimes. Solid lines are fits to these symbols and their slopes, m, and corresponding dynamic scaling exponents, z = mD_f for $R_{g\ or\ h}$ vs. t_w and m = z for I(0) vs. t_w, respectively. The D_f value used is 1.78 as measured in Fig. 3 (a) and $R_{g,G}$ was calculated using Eq. (6.1) and marked with black dashed line. The experimental error in D_f gives a range of $R_{g,G}$ values as indicated by the highlighted area in the graph. The star symbols represent the evolution of the volume fraction of the clusters, $f_{v,c}$, calculated using Eq.(6.2)

The first regime obtained from the R_h vs. t_w plot (Fig. 6.4) gives a kinetic exponent z=0.98±0.07 hence $\lambda \simeq 0$ as expected for a cluster-dilute case (Meakin 1987; R. Jullien 1987; Kolb, Botet, and Jullien 1983; J E Martin and Adolf 1991). At the second regime, which begins at $t_{trans} \sim 5$ minutes, the data (R_h, R_g and I(0)) indicate a kinetic exponent $z > 2$, as shown on the graph, a value that is higher than the expected $z = 2$ by the IGP theory. However, a correction of the time scale is appropriate. The correction involves recognizing that the second temporal regime did not start at $t_w = 0$ but rather near the transition time $t_{trans} \sim 5$ minutes as indicated by the data. When we plot R_h, R_g & I(0) vs. the t_w-t_{trans} as indicated by the unfilled symbols in Fig. 6.5, we find that both radii give an exponent $z = 1.87 \pm 0.14$ to imply $\lambda = 0.47 \pm 0.04$, and I(0) gives $z = 1.80 \pm 0.2$ to imply $\lambda = 0.44 \pm 0.06$. These three measurements are in good agreement with IGP predictions for the cluster-dense regime to have $1< z < 2$ before the IGP is reached. In Figs. 6.4 & 6.5 the growth of both R_h and R_g starts to drastically slow down and rounds off near the cluster size of 9 ± 3 μm. The fractal colloidal gels are fragile, such that any gentle shaking can cause the gel to collapse. Thus tests of rigidity or measurement of the shear modulus cannot be used to determine the gel point. Nevertheless, the sol-to-gel transition is over when the transition ceases, i.e. when temporal evolution of key parameters stops. That is why we define the region of rounding off in the R_g, R_h vs. t_w graph to indicate the time at which the system starts to gel. The cluster size obtained at rounding off is $\sim 9 \pm 3$ μm is in good agreement with the theoretical value of the radius of gyration at the IGP calculated to be $R_{g,G} = 7.5 \pm 1.8$ μm using Eq. (6.1) and indicated by the highlighted area in Fig. 6.4. After the rounding off time, R_g and R_h start to take slightly different values. This difference might be due to a couple of factors. One might be due to the correction that was made to the DLS apparent radius in an attempt to obtain the true hydrodynamic radius, R_h as described earlier. Another reason could be the cluster-cluster anti-correlation affecting the R_g SASLS measurement. On top of that, gelation adds to the complexity of the scattering system as the clusters are no longer individual and interdigitation might be taking place.

Computer simulations (Fry et al. 2002) show that the enhancement of the kinetics is due to the crowding in the cluster-dense regime, where crowding was measured by the normalized cluster free volume Ω. The data can be represented in terms of the cluster volume fraction, $f_{v,c}$, which is defined as the ratio of the volume occupied by the clusters to the total volume of the system, V_{sys}, in other words $f_{v,c} = 1-\Omega$. With the assumption that $R_g \simeq R_h$, the measured R_h value can be used to find the number of monomers per cluster, i.e $N \sim k_o(R_g/a)^{D_f}$. Knowing the total number of

monomers in the system N_m, the number of clusters $N_c = N_m/N$ can be found under the assumption of same size, spherical aggregates (the IGP assumptions). To find the $f_{v,c}$ we need to find the total volume of the clusters. Each cluster occupies a volume that is contained within its perimeter. For the assumption of spherically symmetric aggregate one may write the perimeter radius $R_p=[(D_f+2)/D_f]^{1/2}R_g$. Then the $f_{v,c}$ can be calculated as:

$$f_{v,c}(t) = (4\pi/3)[(D_f + 2)/D_f]^{3/2} N_c(t) R_g^3(t)/V_{sys} \tag{6.2}$$

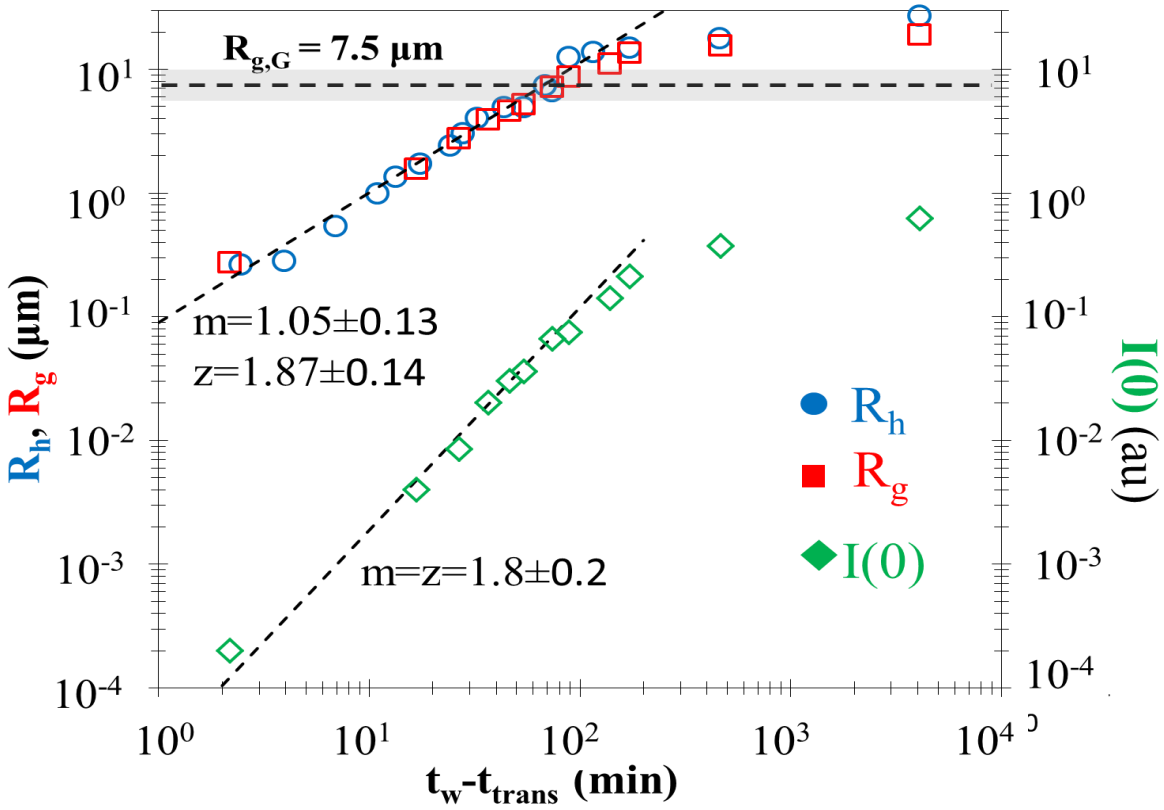

Figure 6.5 Temporal evolution of R_g, R_h & I(0) vs. t_w–t_{trans} with their slopes (dashed lines) and corresponding z values. t_{trans} is the time at which cluster-dilute transitions to cluster-dense (t_{trans}~5min in Fig. 2). The D_f used is 1.78 as measured in Fig. 3 (a) and $R_{g,G}$ was calculated using Eq. (6.1) and marked with dashed line. The experimental error in D_f gives a range of $R_{g,G}$ values as indicated by the highlighted area.

When $f_{v,c}$ vs. t_w is graphed as shown in Fig. 6.4, the volume fraction of clusters starts to increase from $f_{v,c} = f_{v,m} = 3x10^{-4}$ at t_w=0 to about 1% when the kinetics is transitioning from that expected

for cluster-dilute to cluster-dense at t_{trans}. This explicitly demonstrates that crowding enhances aggregation. The third regime is when R_h, R_g, and I(0) are all rounding off showing a drastic slowing down in kinetics. The rounding off indicates the IGP. This rounding correlates well with the $f_{v,c}$ approaching unity. Afterward the $f_{v,c}$ slowly increases above unity to indicate cluster interdigitation.

Figure 6.6 shows R_h & R_g vs t_w for a series of gel experiments with fixed $f_{v,m} = 3x10^{-4}$ but different $MgCl_2$ concentrations (5mM, 7mM, 8mM, 9mM, 10mM, 15mM, and 20mM). This is in contrast to Fig. 6.4 which displays a detailed discussion of one experiment. The salt concentration and D_f values are summarized in Table 6.1. The higher values of salt concentrations led to fractal

Table 6.1 Summary of the experimental results presented in Fig. 4. The fractal dimension D_f, the slope of regime1 and regime2 ($m_{regime1}$ & $m_{regime2}$) with their corresponding kinetic exponents values ($z_{regime1}$ & $z_{regime2}$).

$[MgCl_2]$ mM	D_f	$m_{regime1}$	$z_{regime1}$	$m_{regime2}$	$z_{regime2}$
5	2.05±0.05	0.5±0.1	1.0±0.2	1.7±0.15	3.5±0.3
7	1.9±0.05	0.56±0.1	1.1±0.2	1.3±0.05	2.5±0.1
8	1.85±0.05	0.6±0.1	1.1±0.2	1.1±0.05	2.0±0.1
9	1.85±0.05	0.62±0.1	1.15±0.2	1.05±0.1	1.9±0.2
10	1.8±0.05	0.6±0.1	1.1±0.3	1.05±0.1	1.9±0.1
15	1.73±0.05			1.0±0.15	1.73±0.3
20	1.73±0.05			1.0±0.2	1.73±0.3

dimensions of 1.73 and 1.8 to imply the DLCA regime. On the other hand, for the smaller salt concentrations the fractal dimensions were larger to imply the diffusion limited regime is giving way to the reaction limited regime. At extreme RLCA, we expect $D_f \sim 2.1$ (Lin et al. 1989c). Nevertheless, both of these fractal dimensions are significantly different than the spatial dimension, and that difference is the primary reason why the gel is formed.

Figure 6.6 displays the growth kinetics for a wide range of $MgCl_2$ concentrations. The same three regimes of kinetics as demonstrated in Fig. 6.4 are found. The only exceptions are with the fastest kinetics where cluster-dilute occurred too fast to be detected (the 15mM and 20mM cases), and for the slow kinetics where sedimentation occurred before gelation (as the 5mM case where sedimentation was observed at $t_w \sim 1000$min), or probably in a compatible time scale with gelation

(as the 7mM case where sedimentation was observed at t_w ~1300min). Sedimentation occurred for the 5mM &7mM runs due to the cluster size to which the system can grow becoming comparable to the size at which the critical strain is reached. This will affect the z values measured for these two experiments as will be shown below. It is worth mentioning that for the rest of the experiments sedimentation was either never observed or observed at least up to the point t_w was more than 10 fold larger than the time where the third regime started, i.e. IGP is reached.

The first regime slopes in Fig. 6.6 ($m_{regime1}$) and z values ($z_{regime1}$) are summarized in Table 6.1. The experimental z values are slightly higher than, but within uncertainty of, the expected value of 1 for the cluster-dilute regime. Nevertheless, all dilute regimes are followed by the enhanced kinetics of the dense regime which continues up to the rounding off regime where IGP occurs.

Another feature shown in Fig. 6.6 is the large color coded circles which designate the predicted $R_{g,G}$ values by the IGP theory. These large circles were placed in the following manner: at each gel experiment the waiting time at which the third regime the "rounding off" regime occurred is determined from R_h & R_g rounding off. This is the time at which gelation starts i.e. the IGP is reached. Then Eq. (6.1) is used to calculate the theoretical R_g at the IGP i.e. $R_{g,G}$ using the measured D_f values summarized in Table 6.1. The figure shows that the third regime the "rounding off" regime occurred at smaller R_g and R_h with higher salt concentrations. The higher salt concentration yields smaller D_f; see Table 6.1. The IGP theory predicts a strong dependence of $R_{g,G}$ on D_f, Eq. (6.1). The smaller D_f yields smaller $R_{g,G}$ for a fixed $f_{v,m}$ and monomer size. This behavior is mapped very well with the theoretical $R_{g,G}$ values calculated from the IGP theory for each experiment. The black dashed line is used to guide the eye through these points.

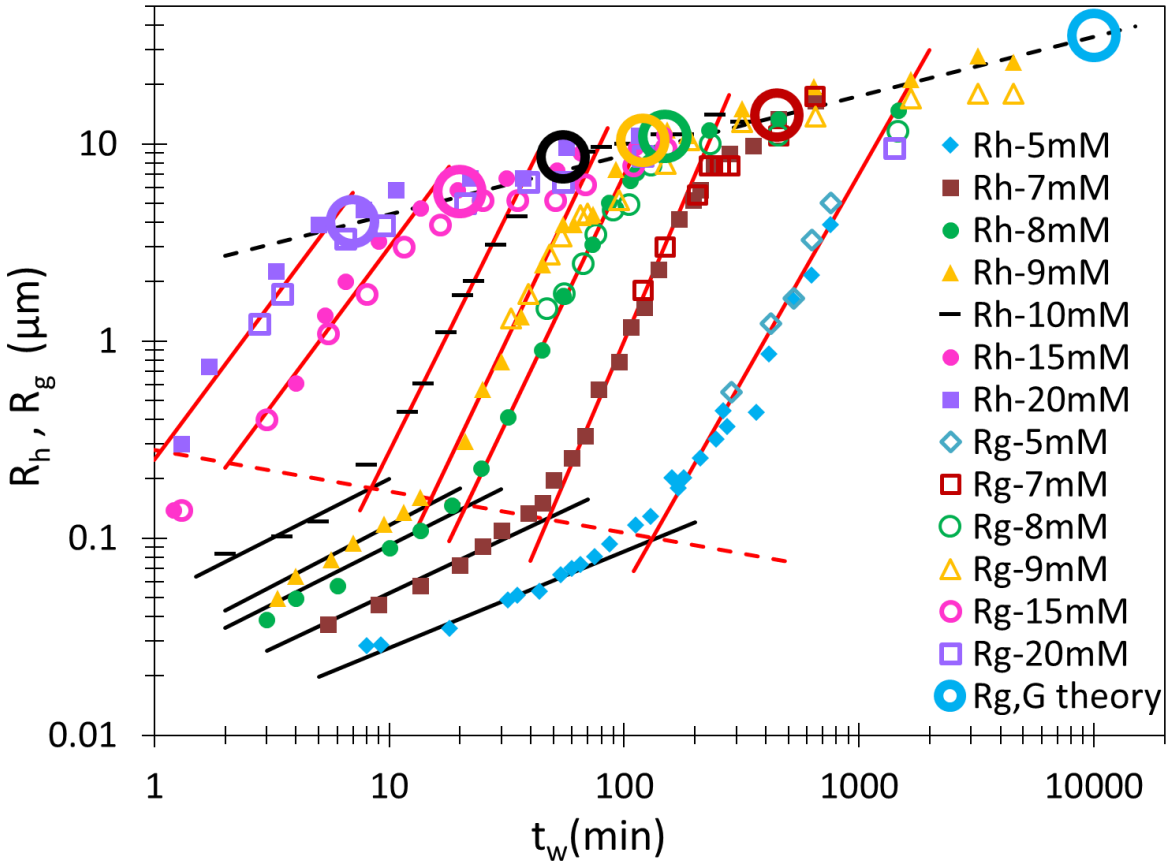

Figure 6.6 Temporal evolution of R_h, R_g for the gelling sample ($f_{v,m} = 3x10^{-4}$) destabilized with different amounts of $MgCl_2$. R_h vs. t_w shows the three different regimes, R_g vs t_w further supports the 2nd and 3rd regimes. Solid lines are fits to these symbols. The red dashed line is to guide the eye when regime1 transitions to regime2. $R_{g,G}$ was calculated using D_f values, summarized in Table 1, & Eq. (6.1), then graphed vs t_w at which "rounding off" i.e. IGP occurs as big color coded circles. The black dashed line is used to guide the eye. Summary of the D_f, slopes in regime1 and corresponding z values are found in Table1.

To explore the second regime R_h and R_g vs. $t_w - t_{trans}$ must be plotted; hence the transition time t_{trans} for all the experiments must be determined. Figure 6.6 shows t_{trans} for all runs except for the 15mM and 20mM experiments. To find t_{trans} for these experiments we did the following: from Fig. 6.6 we observed that the first regime transitions to the second regime in a linear fashion in log-log scale indicated by the dotted red line. By extrapolating this line one can estimate t_{trans} ~ 2min and ~ 1min for 15mM and 20mM, respectively. Figure 6.7 shows R_h and R_g vs t_w-t_{trans} and slopes for the second regime ($m_{regime2}$) and the corresponding z values ($z_{regime2}$) are summarized in Table 6.1. The kinetics during the second regime is enhanced i.e. $1 < z < 2$ as indicated by the IGP theory for

all the experiments except for the 5mM & 7mM. As mentioned above, the 5mM and to less extend the 7mM experimental z values in the second regime are affected by sedimentation.

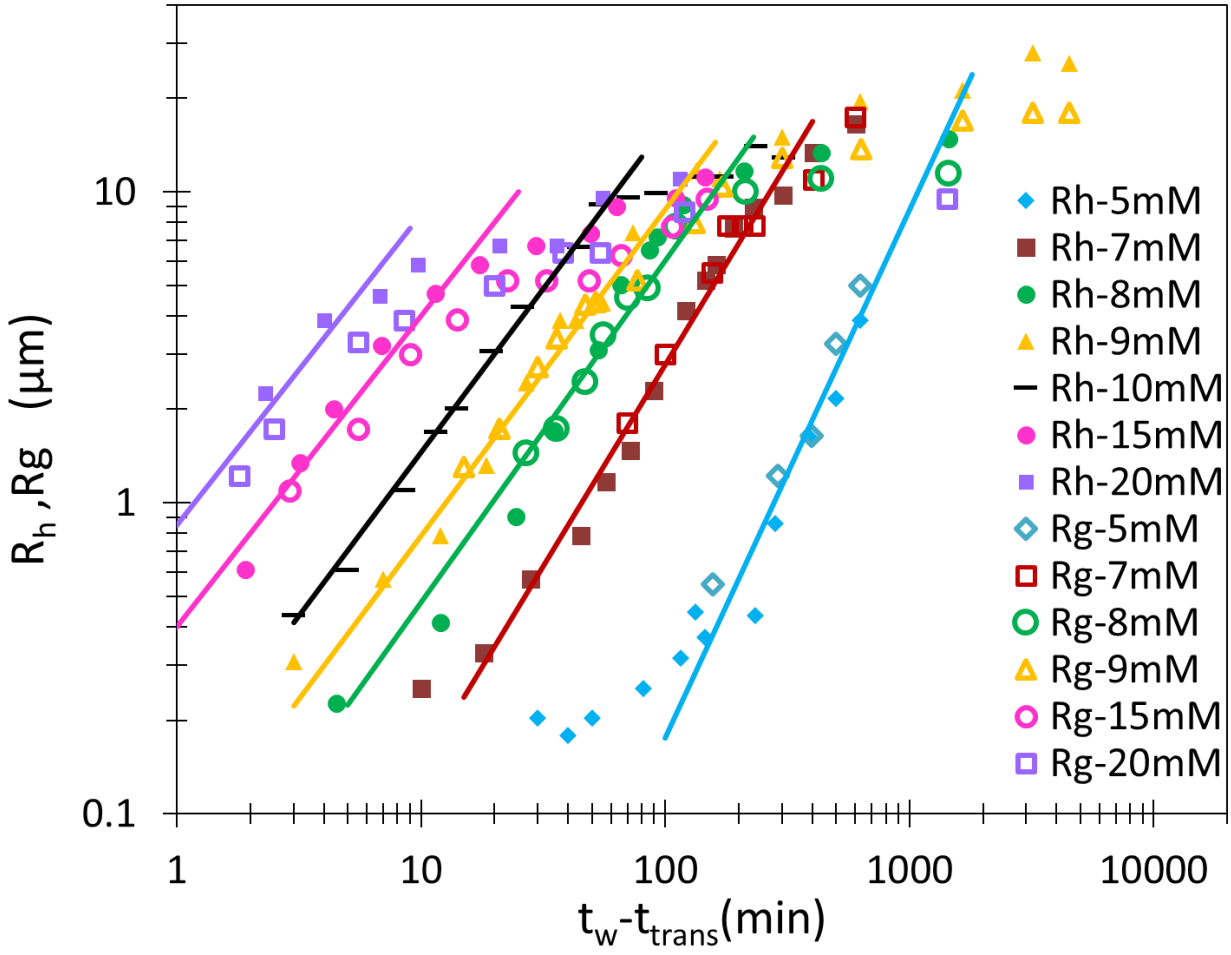

Figure 6.7 Temporal evolution of R_h, R_g vs. t_w–t_{trans} for the gelling samples ($f_{v,m}$ = 3x10^{-4}) destabilized with different amounts of $MgCl_2$. t_{trans} is the time at which the cluster-dilute regime transitions to cluster-dense. t_{trans} values are determined experimentally for each run from Fig. 6. The solid lines are the fits to the data points. Summary of the D_f, slopes in regime2 and corresponding z values are found in Table1.

An important concept that the IGP theory advocates is the existence of the two fundamental length scales, the average aggregate size, $R_h \sim R_g$, and average mean nearest neighbor separation R_{nn}. These two length scales grow with different functionalities with the number of monomers per aggregate, $R_g \sim N^{1/D_f}$ and $R_{nn} \sim N^{1/d}$, which causes the system to gel. To follow the evolution of these two length scales we first define a general size $R \simeq R_h \simeq R_g$. This is reasonable given that our data support the fact that $R_h \simeq R_g$. The mean aggregate nearest neighbor separation is R_{nn} =

$(V_{sys}/N_c)^{1/3}$, where $N_c \sim N_m/N$. Figure 6.8 compares these two fundamental length scales of the system by plotting the ratio R/R_{nn} vs. t_w. It shows that the clusters grow relatively closer to each other with time. Notice that at the transition time, t_{trans}, $R/R_{nn} \sim 0.08$ - 0.1 for all the runs, marked by the grey highlight. This is consistent with the reported value based on the IGP theory (C. Sorensen and Chakrabarti 2011) of $R_{nn} \simeq 10\ R$ where the system begins the cluster-dense regime. In addition, Fig. 6.8 shows that the ratio R/R_{nn} stops increasing in the range ~ 0.34 – 0.43 when the kinetics slow drastically at the rounding off point (except for 5mM where sedimentation occurred). This range has been highlighted in red and it is in an excellent agreement with IGP prediction of $R_{nn} \sim 2.3\ R_g$ for fractal clusters with $D_f = 1.8$ to start touching (C. Sorensen and Chakrabarti 2011). The question remaining: what is the meaning of the points that occur beyond the IGP? Can these data represent the degree of interdigitation? Recall, in Fig. 6.4 the cluster volume fraction in the system grows beyond unity at later stages of gelation to indicate interdigitation.

To test the volume fraction dependence, experiments with two different monomer volume fractions, $f_{v,m} = 3.0\text{x}10^{-4}$ and $7.6\text{x}10^{-4}$ were conducted keeping D_f the same. The $7.6\text{x}10^{-4}$ data contained multiple scattering (MS) artifacts that affect the Porod regime in the static structure factor. This inhibited the ability to measure the correct D_f value for this f_{vm} by SASLS.To overcome the MS artifact in the D_f measurement for the higher volume fractions but maintain the same D_f among the different volume fractions, we followed the procedure described in chapter 5. In summary, the D_f value was maintained the same by changing the salt concentrations such that the measured stability ratio, W, was almost the same. The W measurement was made following, for the most part, Holthoff et al. method (Holthoff et al. 1996).

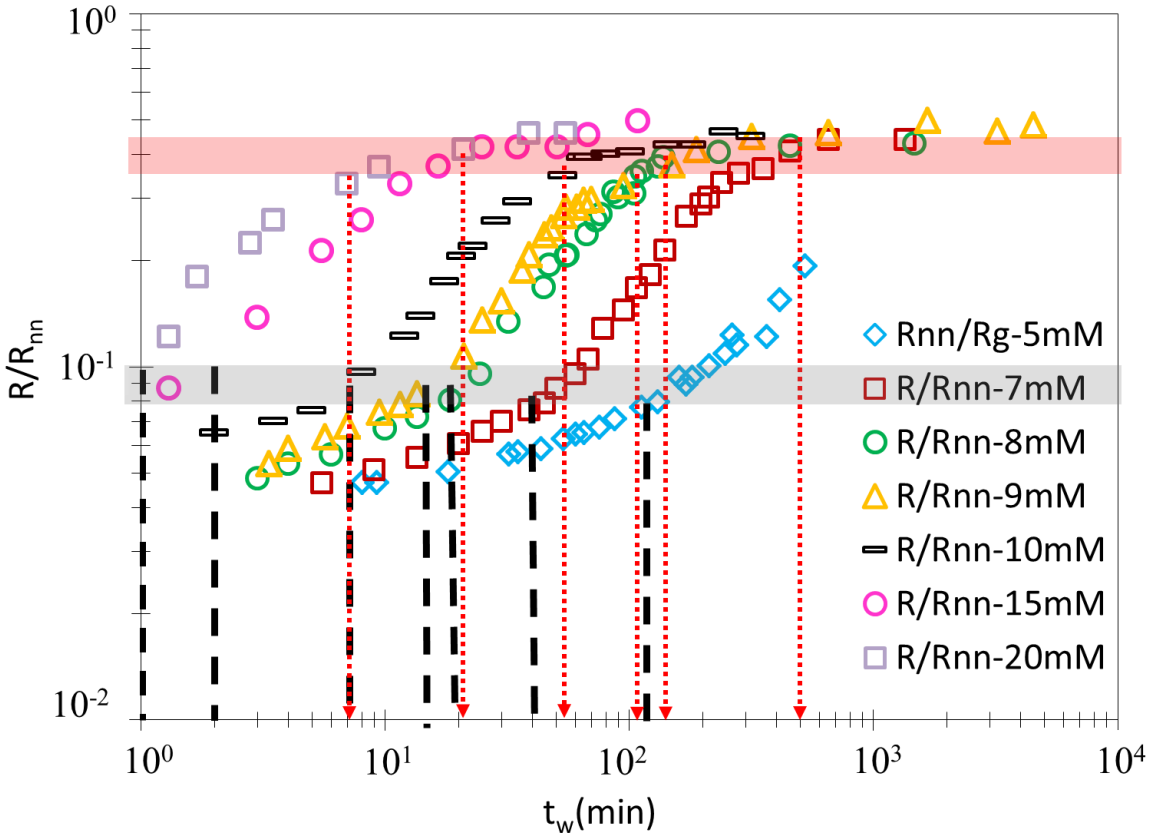

Figure 6.8 The temporal evolution of the ratio of the two fundamental length scales in the system; aggregate size divided by the mean nearest neighbor distance, R/R_{nn} vs. t_w. The vertical dashed black lines represent the transition time t_{trans} for each run as determined from Fig. 6. The horizontal grey highlight represents the corresponding range of R/R_{nn} at which t_{trans} occurs for all the runs. The color red pointing down arrows represents the time at which the "rounding off" occurs as determined from Fig. 6 for each run. The red highlight shows the corresponding range of R/R_{nn} at which the "rounding off" i.e. the IGP occurs for all the runs.

For $f_{v,m}$=3.0x10^{-4} and 7.6x10^{-4} the salt concentrations used were 9mM and 12mM to yield similar W values of 94 and 105, respectively. Figure 5.2(b) in chapter 5 shows that W ~ 100 yields a D_f ~ 1.85. This is in an excellent agreement with the measured D_f = 1.85 ± 0.05 by SASLS for the f_{vm} = 3 x 10^{-4}, which has no MS artifacts. Using this value of D_f for both runs, the IGP predicted $R_{g,G}$ to be ~ 5.7 μm and 12.3 μm for $f_{v,m}$ = 3 x 10^{-4} and 7.6 x 10^{-4}, respectively. The corresponding errors in $R_{g,G}$ are shown in a color coded highlight in the figure.

Figure 9 shows the temporal evolution of R_h for f_{vm} = 3 x 10^{-4} and 7.6 x 10^{-4}. This figure does not show a definite support of the $R_{g,G}$ dependence on the $f_{v,m}$. This might indicate a breakdown of the $f_{v,m}$ dependence, however, all the other aspects of the IGP theory are demonstrated experimentally

in this chapter like the three regimes of kinetics and the fractal dimension dependence. An equally valid argument is that the $f_{v,m}$ dependence rather weak compared to the strong dependence on D_f. That makes the uncertainty in measuring D_f hinder the $f_{v,m}$ functionality. In addition, experimentally we were confined between sedimentation and multiple scattering leaving less than a factor of 3 range of $f_{v,m}$ to work with. Fortunately, Wu et al. studied colloidal gels using fluorinated polymer colloids, which have a very low optical contrast with respect to water. The formed gels were transparent. This allows them to study dense colloidal systems with no MS artefacts. After extracting and analyzing their experimental data, it was found that $R_{g,G} \sim f_{vm}^{1/(3-D_f)}$, exactly as predicted by the IGP theory. Detailed discussion of the analysis of their data will be introduced in chapter 9.

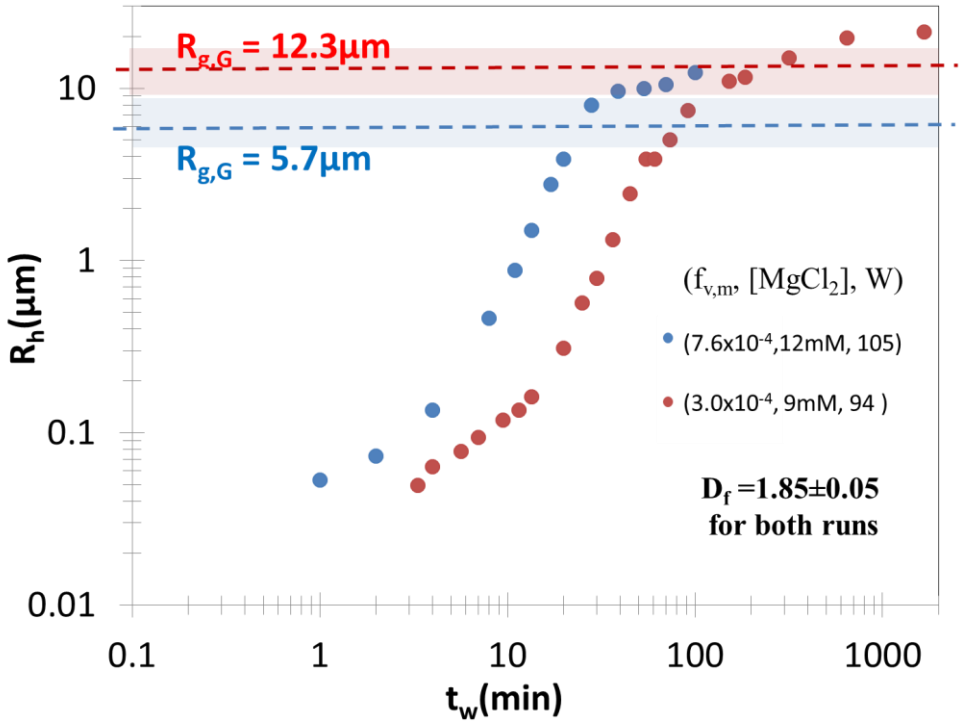

Figure 6.9 Experimental verifications of $R_{g,G}$ dependence on $f_{v,m}$ and D_f. R_h vs t_w/t_{IGP} for two different monomer volume fractions ($7.6x10^{-4}$ and $3x10^{-4}$) but with same measured D_f. The dashed lines represent the calculated values of $R_{g,G}$ and the highlights are the corresponding range of $R_{g,G}$ due to the experimental error in D_f measurements.

6.2 Conclusions

The studies presented here with low volume fraction colloids allow enough time for the kinetics aspects of the sol-to-gel transition to be observed in their entirety. We find that the gelation of a dilute ensemble of spherical particles with isotropic attractive forces evolves through three successive growth regimes to yield a kinetically arrested gel. These results are in quantitative agreement with the IGP theory and previous theoretical and simulation studies (Fry et al. 2004; C. Sorensen and Chakrabarti 2011; R. Dhaubhadel et al. 2006; W. Kim, Sorensen, and Chakrabarti 2004; Wongyo Kim et al. 2006; Christopher M. Sorensen et al. 2003; Fry et al. 2002). This experiment also unifies gelation in aerosols and colloids through the IGP theory. Here we stress the evolution from sol to gel is best described by the kinetics theory. In the literature there are other descriptions of gelation: gelation is viewed as a thermodynamic phase transition and a percolation phenomenon. In summary, this work leads us to conclude that the sol-to-gel transition (gelation) is a kinetic phenomenon well described by the Ideal Gel Point theory. Our unique perspective regarding how systems gel will be discussed further in chapter 9 where we explore the literature and show how our understanding fits the other descriptions of gelation.

Chapter 7 - Fractal colloidal gel time

In Chapter 6 the IGP theory was tested for the colloidal sol-to-gel transition to verify the kinetics description of gelation. Question remains: how fast does a sol, when destabilized, form a gel? And how does the gel time, t_{gel}, depend on the parameters such as fractal dimension, D_f, stability ratio, W, and initial monomer volume fraction f_{vm}?

In Chapter 3 two attempts where discussed to find the gel time. Both started with the Smoluchowski equation (SE) and assumed all aggregates are of the same size and have a constant kernel. These assumptions simplify the SE and yielded Eq. (3.32) which takes the following expression

$$t_{gel} = \frac{4\pi}{3} k_o^{3/(3-D_f)} \left(\frac{D_f}{2+D_f}\right)^{D_f/(3-D_f)} {K_{fast}}^{-1}\, a^3\, f_{vm}^{-3/(3-D_f)} \tag{7.1}$$

This expression is derived for the pure DLCA model, where $K_{fast} = 8k_BT/3\eta$. The most general expression is shown in Eq. (3.24) and is written in terms of the stability ratio, $W = K_{fast}/K_{slow,}$ for any aggregation kernel as

$$t_{gel} = W.\ \frac{4\pi}{3} k_o^{3/(3-D_f)} \left(\frac{D_f}{2+D_f}\right)^{D_f/(3-D_f)} {K_{fast}}^{-1}\, a^3\, f_{vm}^{-3/(3-D_f)} \tag{7.2}$$

The second attempt, introduced by Bremer et al. (L. G. B. Bremer, Walstra, and van Vliet 1995), applied the excluded volume concept to correct for the aggregate rate calculated by the SE. This entailed comparing the distance over which particles with excluded volume have to diffuse ($R_{nn} \sim n^{-1/3}$) and the actual distance between the peripheries, X. Bremer's attempt leads to Eq. (3.31) which gives the following expression for the gel time

$$t_{gel} = \left(1 - \left(\frac{6D_f}{2D_f+3}\right) + \left(\frac{3D_f}{D_f+6}\right)\right) K_{Bremer}^{-1}\, a^3\, {f_{vm}}^{-3/(3-D_f)} \tag{7.3}$$

Where K_{Bremer} is given in Eq. (3.25) as

$$K_{Bremer} = \frac{8\,A\,K_BT}{3\eta} = A\,K_{fast} \tag{7.4}$$

A is a constant described by Bremer in Eq. (3.26) to be

$$A = \frac{BP}{4W} \tag{7.5}$$

Where P is the polydispersity index and B is the ratio of the collision radius of aggregates, R_c, to their hydrodynamic radius, R_h, i.e. $B = R_c/R_h$. In both attempts the gel time scales with the monomer size, a, the stability ratio, W, and monomer volume fraction, f_{vm}, in the following manner

$$t_{gel} \sim W\, K_{fast}^{-1}\, a^3 {f_{v,m}}^{-3/(3-D_f)} \tag{7.6}$$

This scaling behavior was introduced by Sorensen and Chakrabarti (C. M. Sorensen and Chakrabarti 2011).

The kinetics picture of t_{gel} scaling with W and f_{vm} summarized above, and represented in details in Chapter 3, was validated experimentally to further confirm the role played by the kinetic description of the sol-to-gel transition. It worth alerting the reader that our interpretation of the results in this chapter relies heavily on the experimental procedure we developed and discussed in Chapter 5. It is known that using the same salt concentration for different f_{vm} might yield different W, and that D_f depends on W. Nevertheless, when it comes to t_{gel} measurements, the relation between D_f, W, and salt concentration is sometimes underestimated or misrepresented by researchers (Mokhtari 2007; van der Linden et al. 2015; Zhang et al. 2016).

7.1 Results and discussions

For each gel experiment the three techniques of SASLS, DLS and transmitivity measurement were combined to simultaneously probe the temporal evolution of R_g, I(0), R_h, and <s> while the system is transitioning from sol to gel. In addition, the stability ratio measurement was conducted for each gel experiment at the initial stages of aggregation. The different gel experiment then grouped together such that they have the same W value (within ~ 20% of each other). This new group of W is named W_{grp}.

Determination of the gel time for a fragile colloidal gel is difficult because there is no distinct change in any of the measurable quantities. The gel time, t_{gel}, in this work is defined as the time at which a drastic slowdown in kinetics, a "rounding off", is observed in the R_h, R_g, I(0), and <s> vs. t_w graphs. These gel times are named as $t_{gel\text{-}Rh}$, $t_{gel\text{-}Rg}$, $t_{gel\text{-}I(0)}$, and $t_{gel\text{-}<s>}$, respectively.

The gel times could vary between the different definitions in the same gel experiment. Figure 7.1 is an example of R_h, R_g, I(0) and <s> vs. t_w for (a) $f_{vm} = 3 \times 10^{-4}$, $[MgCl_2] = 8mM$, $W = 147 \pm 30$ and (b) $f_{vm} = 1 \times 10^{-3}$, $[MgCl_2] = 13.3mM$, $W = 120 \pm 27$. Notice for $f_{vm} = 3 \times 10^{-4}$ the <s> = 0.4, which satisfies the conclusion discussed in Chapter 5 that for <s> $\lesssim 0.55$ there is no multiple scattering (MS) artifacts to perturb the structure factor. Therefore, Fig. 7.1(a) shows $t_{gel\text{-}Rh} \approx t_{gel\text{-}Rg} \approx t_{gel\text{-}I(0)}$. However, $t_{gel\text{-}<s>}$, occurs sooner than the others. In addition, the radii R_g and R_h experimental values are in agreement with each other. On the other hand, for $f_{vm} = 1 \times 10^{-3}$, the average number of scattering events <s> ~ 1, so MS is much greater, which results in artifacts in the measurements of R_g, and to less extend in R_h. This is evident in Fig. 7.1(b) where these two measurements have clear discrepancies. In addition, $t_{gel\text{-}Rh}$, $t_{gel\text{-}Rg}$, & $t_{gel\text{-}I(0)}$ are now different due to MS. Nevertheless, the drastic slowdown in kinetics still holds whether MS artifacts are present or not. Thus, for each of these rounding off times they represent a time related to t_{gel}.

Regardless of the different functionalities of the coefficients in t_{gel} expressions obtained by our group and Bremer, Eq. (7.6) shows that both approaches produce the same scaling behavior of t_{gel} with f_{vm}, W and a^3. Figure 7.2 tests the scaling of t_{gel} on W by plotting experimental $t_{gel\text{-}Rh,\ Rg,\ I(0),\ \&\ <s>}$ vs. W for a) $f_{vm} = 3 \times 10^{-4}$, and b) 7.6×10^{-4}, with slopes of 1.05 ± 0.1 and 1.0 ± 0.1, respectively. The plot shows an excellent agreement with the scaling behavior predicted in Eq. (7.6).

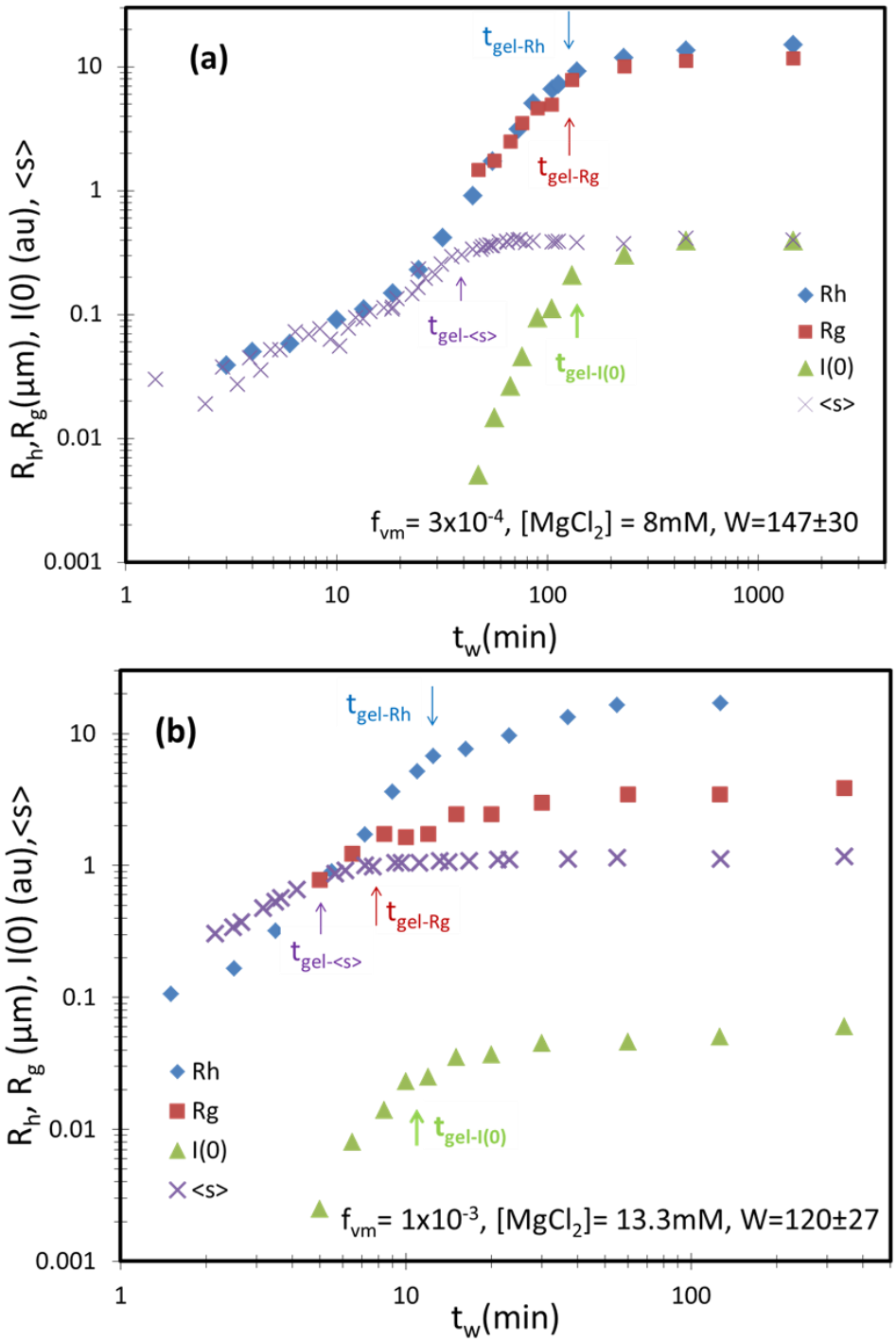

Figure 7.1 R_h, R_g, I(0) and <s> vs t_w for (a) f_{vm} = 3 x 10^{-4}, [$MgCl_2$] = 8mM, W=147 ± 30 and (b) f_{vm}=1x10^{-3}, [$MgCl_2$] = 13.3mM, W = 120 ± 20. The arrows indicate t_{gel} for each definision. Note that the average number of scattering events <s> is about a factor of 3 larger for f_{vm} = 1 x 10^{-3} compared to f_{vm} = 3 x 10^{-4}.

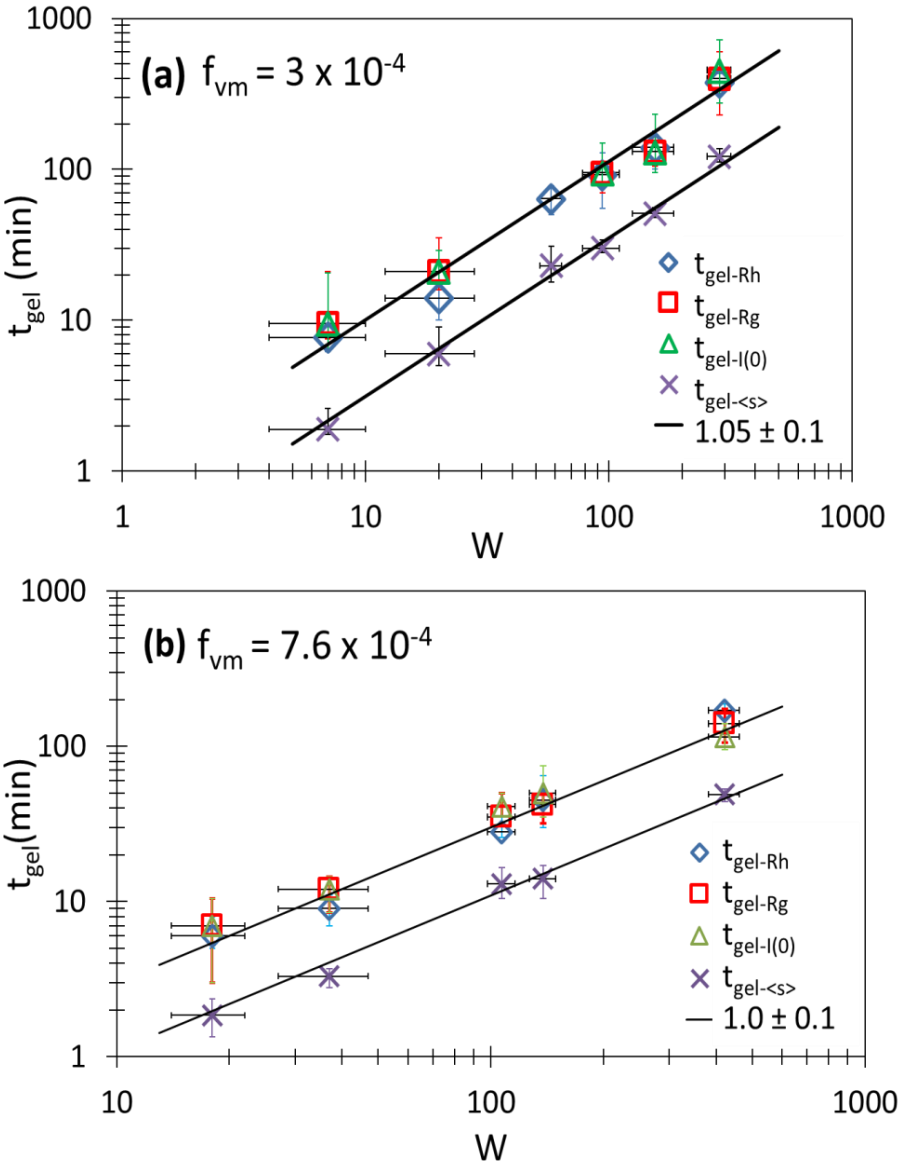

Figure 7.2 $t_{gel-Rh, Rg, I(0), \& <s>}$ vs. W for f_{vm} = (a) 3 x 10^{-4} and (b) 7.6 x10^{-4}. All gel times (regardless of the definition) for both f_{vm} yielded t_{gel} ~ W, which is in agreement with Eq. (7.6).

To test for the dependence of t_{gel} with f_{vm}, one must account for the fact that D_f is a function of W. Thus the wide range of W values explored in this work was grouped into four different W_{grp} with their corresponding D_f values. Table 7.1 summarizes all the different gel experiments. Figure 7.3 shows an example of a group, consisting of graphs of different gel experiments with different f_{vm}

and [$MgCl_2$] all in the same group, W_{grp} = 37 ± 4. The corresponding D_f = 1.73 ± 0.05 for this group as shown in Fig. 5.2(b).

Figure 7.4 (a) shows a log-log plot of the $t_{gel\text{-}Rh}$, $t_{gel\text{-}Rg}$, $t_{gel\text{-}I(0)}$ & $t_{gel\text{-}<s>}$ vs f_{vm} inferred from Fig. 7.3 (a) – (d). The absolute values of the slopes of lines in the graph are 2.2 ± 0.2, for $t_{gel\text{-}Rh}$, $t_{gel\text{-}Rg}$, $t_{gel\text{-}I(0)}$, and 2.1 ± 0.2, for $t_{gel\text{-}<s>}$. These values are in agreement with the absolute value of the theoretical exponent in Eq. (7.6) of 3/(3-1.73) = 2.36 ± 0.09. These plots have been repeated for the rest of W_{grp} and shown in Fig. 7.4 (b) – (d). Again, the slopes of $t_{gel\text{-}Rh,\ Rg,\ I(0),\ and\ <s>}$ vs. f_{vm} are all in agreement with the theoretical exponents when the corresponding D_f is used for that W_{grp}.

Table 7.1 Summary of all the experimental data (f_{vm}, C_s, and measured W) that make up the four different W_{grp} and the corresponding D_f value for each W_{grp}.

(a) W_{grp} = 37 ± 4 D_f = 1.73 ± 0.05			(b) W_{grp} = 141 ± 20 D_f = 1.83 ± 0.05			(c) W_{grp} =285 ± 16 D_f = 1.9 ± 0.05			(d) W_{grp} =438 ± 75 D_f = 2.05 ± 0.1		
f_{vm}	C_s (mM)	W	f_{vm}	C_s (mM)	W	f_{vm}	C_s (mM)	W	f_{vm}	C_s (mM)	W
3×10^{-4}	10	40	3×10^{-4}	8	147	1×10^{-3}	8	271	7.6×10^{-4}	8.3	422
3.8×10^{-4}	15	36.7	3.8×10^{-4}	8.2	160	1.5×10^{-3}	8.7	303	1×10^{-3}	9	540
7.6×10^{-4}	16.8	37.3	7.6×10^{-4}	11.6	138	1.9×10^{-3}	10	282	1.5×10^{-3}	8.6	390
1×10^{-3}	17	32	1×10^{-3}	13.3	120				1.9×10^{-3}	8.8	400

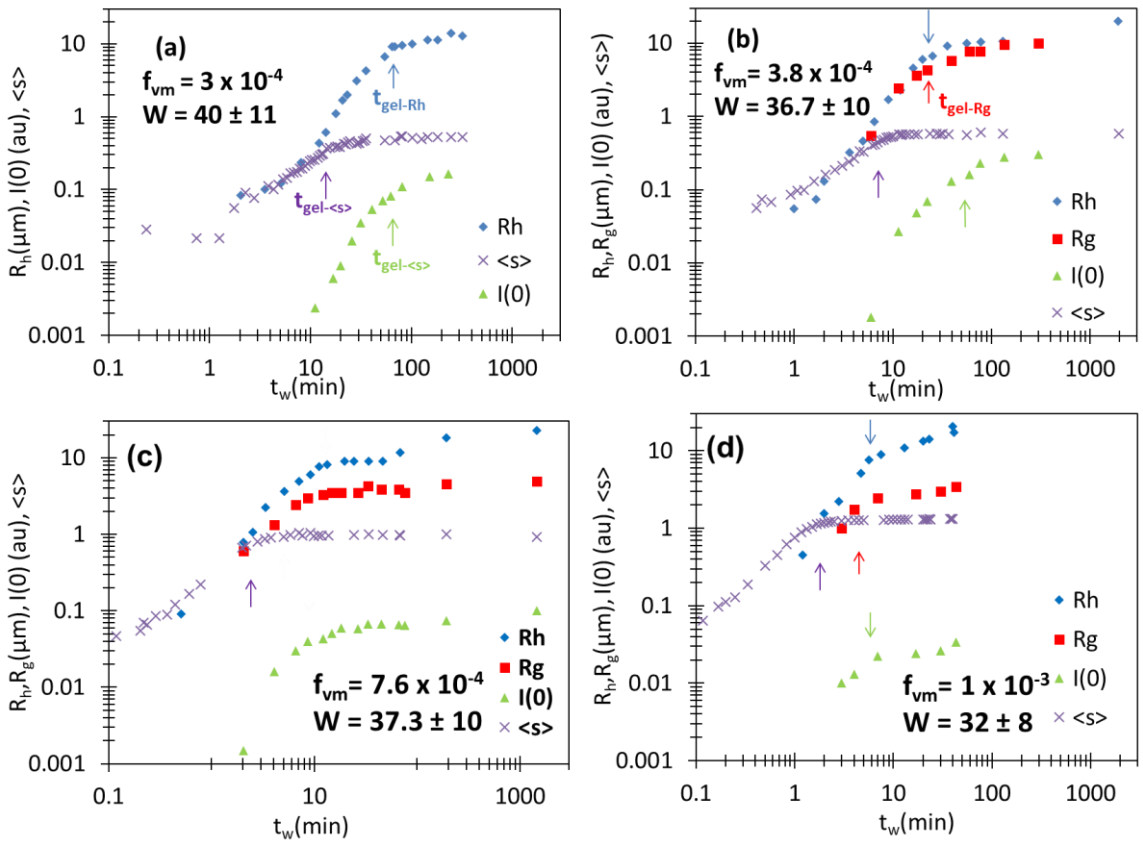

Figure 7.3 R_h, R_g, I(0) &<s> vs t_w for four different gelling experiments of different f_{vm} and salt concentration but the same average W_{grp} = 37 ± 4. Arrows indicte t_{gel} for each difinistion.

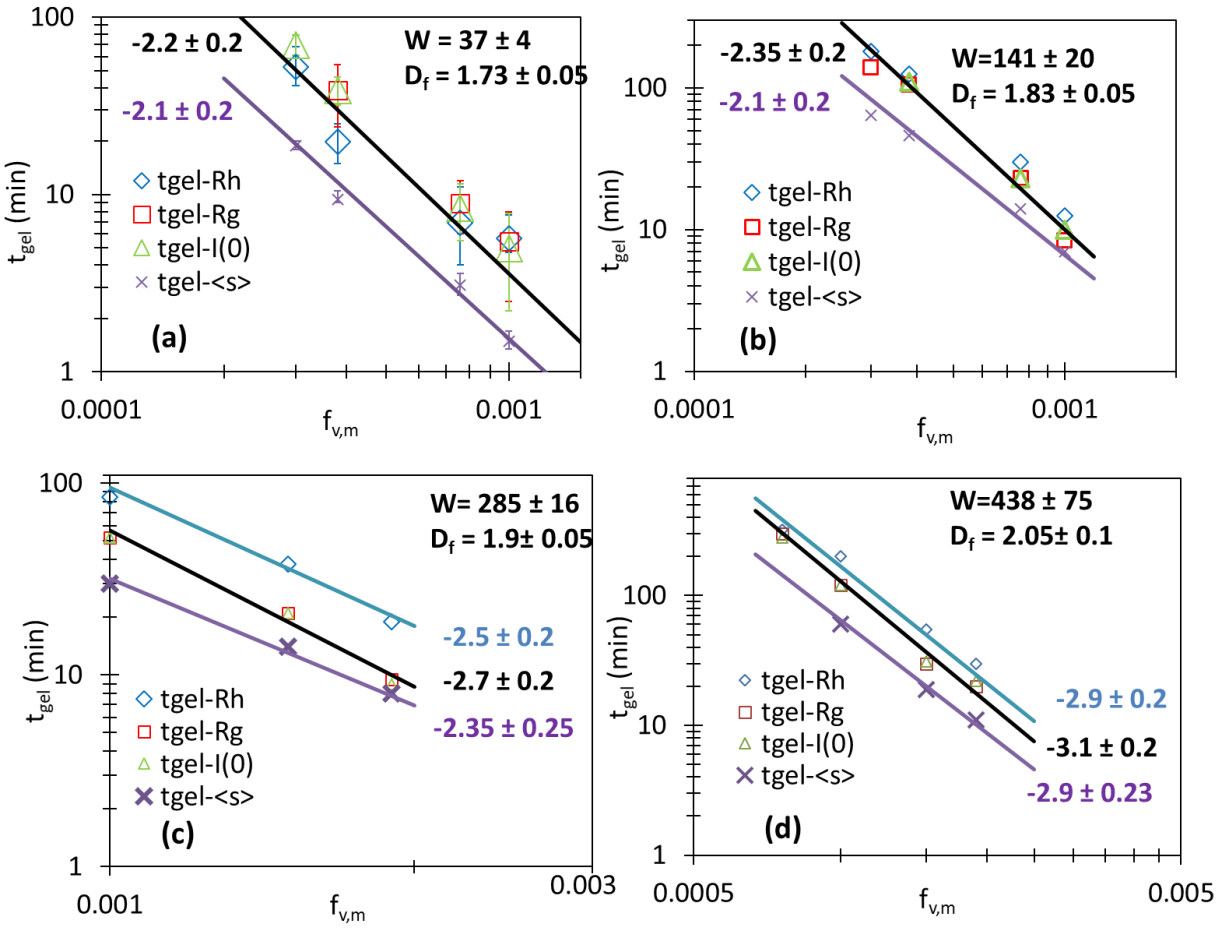

Figure 7.4 $t_{gel\text{-}Rh,\ Rg,\ I(0),\ \&<s>}$ vs. f_{vm} for four different average W_{grp} sets (a) W_{grp} = 37 ± 4, (b) W_{grp} = 141 ± 20, (c) W_{grp}=285±16, and (d) W_{grp} = 438 ± 75. The absolute values of the measured exponents are shown in the figures. The comparison to the theoretical values are summarized in Table. 7.2.

While each plot in Fig. 7.4 shows t_{gel} (from all definitions) vs. f_{vm} for each W_{grp}, Fig. 7.5 uses the same data but plots t_{gel} (for each definition) vs f_{vm} for all W_{grp} in separate plots. Figure 7.5 makes it clear that for smaller W_{grp} but the same f_{vm} t_{gel} is reached quicker. In addition, the slope for t_{gel} vs. f_{vm} increases with increasing W, consistent with increasing D_f, see Fig. 5.2(b). The values of the slopes are shown in the graphs. Table 7.2 summarizes the results and shows for each W_{grp} the corresponding measured D_f using SASLS, the absolute value of the experimental exponents of t_{gel} vs. f_{vm} for all different definitions, $m_{tgel\text{-}Rh}$, $m_{tgel\text{-}Rg}$, $m_{tgel\text{-}I(0)}$ & $m_{tgel\text{-}<s>}$, the average values of these experimental exponents, and the absolute value of the theoretical exponent for each D_f, i.e.(3/(3-D_f)).

It's worth noting from Fig. 7.5 that the W_{grp} influence on t_{gel} is decreased with increasing f_{vm} as indicated by the different slopes. The extrapolated f_{vm} at which W_{grp} is no more a factor in t_{gel} ranges between 0.05 - 0.13. This extrapolated range is done by extending the best line fits for the lowest and highest W_{grp} in Fig. 7.5 (a) – (d). The question one may ask: Is t_{gel} dependent on W, f_{vm}, and D_f for dilute gels differ than t_{gel} dependence for dense gels?

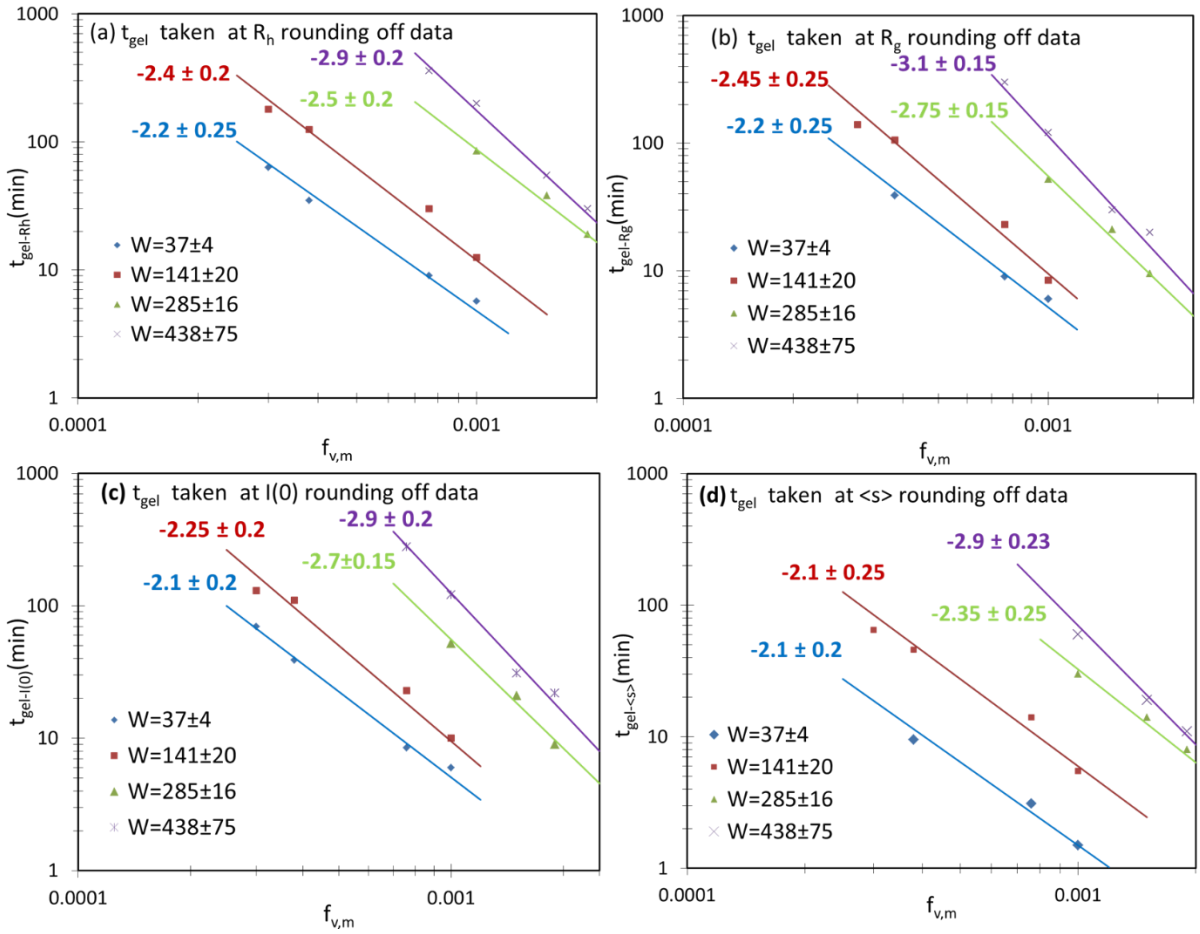

Figure 7.5 t_{gel} vs. f_{vm} for the same data presented in Fig. 7.6 but graphed for each (a) t_{gel-Rh}, (b) t_{gel-Rg}, (c) $t_{gel-I(0)}$, and (d) $t_{gel-<s>}$ separately for all four W_{grp}. Table 7.2 summarized the experimental measured exponent to the theoretical one after using the proper D_f.

Table 7.2 Summary of the W_{grp}, measured D_f value for each W_{grp}, the measured exponent from t_{gel} vs. f_{vm} for the different difinisions, $m_{tgel\text{-}Rh,\ Rg,\ I(0),\ \&\ <s>}$, the average experimental value of the exponent for all t_{gel} definition, theoretical exponent (for that particular W_{grp}).

		The absolute value of the exponents obtained from Fig. 7.5 for different t_{gel} definitions					
W_{grp}	D_f (from I(q) vs. q)	$m_{tgel\text{-}Rh}$	$m_{tgel\text{-}Rg}$	$m_{tgel\text{-}I(0)}$	$m_{tgel\text{-}<s>}$	Average exponent	Theoretical exponent
37 ± 4	1.73 ± 0.05	2.2 ± 0.25	2.2 ± 0.25	2.1 ± 0.2	2.1 ± 0.2	2.15 ± 0.23	2.36 ± 0.1
141 ± 20	1.83 ± 0.05	2.4 ± 0.2	2.45 ± 0.25	2.25 ± 0.2	2.1 ± 0.25	2.3 ± 0.23	2.56 ± 0.11
285 ± 16	1.9 ± 0.05	2.5± 0.2	2.75 ± 0.15	2.7 ± 0.15	2.35 ± 0.25	2.6 ± 0.19	2.73 ± 0.12
438 ± 75	2.05 ± 0.1	2.9 ± 0.2	3.1 ± 0.15	2.9 ± 0.2	2.9 ± 0.23	2.95 ± 0.2	3.16 ± 0.17

Furthermore, knowing any of the $t_{gel\text{-}Rh,Rg,I(0),\ and\ <s>}$ vs. f_{vm} enables the researcher to use the best line fit of these graphs to predict the value of D_f. Table 7.3 compares the measured D_f from SASLS with the predicted D_f values from the slopes of the different t_{gel} vs. f_{vm}. The measured D_f values are in agreement with the predicted ones from $t_{gel\text{-}Rh,\ Rg,\ I(0)\ \&<s>}$.

Table 7.3 Summary of the D_f value using the best fit of t_{gel} from table 2 above and compare it to the D_f measured from S(q).

W_{grp}	D_f (from I(q) vs. q)	D_f (best fit of $t_{gel\text{-}Rh}$)	D_f (best fit of $t_{gel\text{-}Rg}$)	D_f (best fit of $t_{gel\text{-}I(0)}$)	D_f (best fit of $t_{gel\text{-}<s>}$)
37 ± 4	1.73 ± 0.05	1.64 ± 0.16	1.64 ± 0.16	1.57 ± 0.15	1.57 ± 0.14
141 ± 20	1.83 ± 0.05	1.75 ± 0.1	1.78 ± 0.13	1.67 ± 0.12	1.57 ± 0.17
285 ± 16	1.9 ± 0.05	1.8 ± 0.12	1.91 ± 0.06	1.89 ± 0.06	1.72 ± 0.14
438 ± 75	2.05 ± 0.1	1.97 ± 0.08	2.03 ± 0.05	1.97 ± 0.07	1.97 ± 0.08

The functionality of t_{gel} on W and f_{vm} has now been tested experimentally. The results we discussed so far were in support of the functionality of t_{gel} on W and f_{vm} as predicted by KSU and Bremer approaches. Now we wish to compare the coefficients that are obtained experimentally with the predicted ones obtained by our group and Bremer.

The coefficients are a function of D_f in both KSU's and Bremer's approaches. We will call the coefficients $C_{t_{gel-KSU}}(D_f)$ and $C_{t_{gel-Bremer}}(D_f)$ which are expressed in Eq.s (7.7) and (7.8), respectively.

$$C_{t_{gel-KSU}}(D_f) = \frac{4\pi}{3} k_o^{3/(3-D_f)} \left(\frac{D_f}{2+D_f}\right)^{3D_f/2(3-D_f)} \quad (7.7)$$

$$C_{t_{gel-Bremer}}(D_f) = \frac{1}{3A'}\left(1 - \left(\frac{6D_f}{2D_f+3}\right) + \left(\frac{3D_f}{D_f+6}\right)\right) \quad (7.8)$$

Where A' = WA.

To compare these theoretical coefficients with the experimental coefficient, $C_{t_{gel-Exp}}$, replace the ~ sign in Eq. (7.6), and rewrite it as

$$t_{gel} = C_{t_{gel-Exp}}(D_f)\ W\ K_{fast}^{-1}\ a^3 {f_{v,m}}^{-3/(3-D_f)} \quad (7.9)$$

Then solve for $C_{t_{gel-Exp}}(D_f)$ in Eq. (7.9). The experimental coefficients were calculated for each f_{vm} with the measured monomer size, a = 20nm, measured W value, and D_f for each gel experiment. In Chapter 4, we discussed the fast kinetics for the gelling experiments make it unfeasible to find K_{fast} experimentally. To overcome this difficulty we used $K_{fast} = K_{fast,Th} = K_{fast,SE} = 8K_BT/3\eta$. We did the same for the K_{fast} in Eq.(7.9) to solve for $C_{t_{gel-Exp}}$.

Figure 7.6 shows the three coefficients as described in Eq. (7.7), (7.8) and (7.9). The black dotted-dashed line represents $C_{t_{gel-KSU}}$. The red dotted-dashed line represents $C_{t_{tgel-Bremer}}$. The points represent the experimental coefficients in this work. The errors associated with the experimental coefficients are calculated in reference to the errors in D_f measurements. The experimental gel time used in Fig. 7.6 graphs is taken from the t_{gel-Rh} definition.

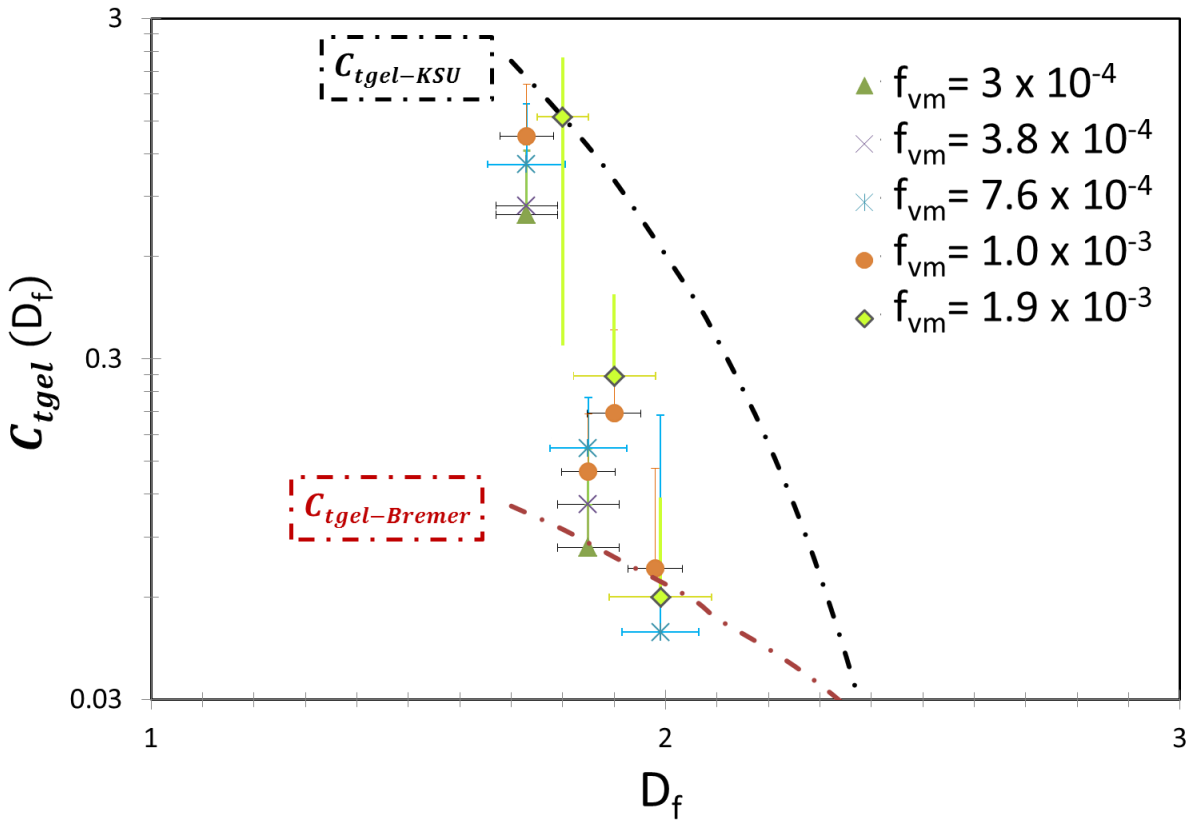

Figure 7.6 The gelation coefficient vs. D_f for the experimental data points, the KSU t_{gel} coefficient (dash-dot black line), and the Bremer t_{gel} coefficient (dash-dot red line) obtained from Eq. (7.7), (7.8), and (7.9), respectively.

Figure 7.6 suggests that the data is upper bounded by the KSU coefficient and lower bounded by the Bremer coefficient. A correction can be made to the KSU approach by considering polydispersity. The polydispersity can affect the structure factor as discussed in Chapter 2. Equation (2.20c) shows that the polydispersity factor C_p affects the structure factor in the following manner (C. M. Sorensen and Wang 1999)

$$S(q) = C\, C_p (\, qR_g \,)^{-D_f} \;\; ; \;\; qR_g > 1 \qquad (7.10)$$

Where C =1. Following the method of Sorensen and Wang, the C_p value was obtained from the structure factor measurement at the gel time. Figure 7.7 shows two different gel experiments each of f_{vm} = 3 x 10^{-4} but with different salt concentrations such that W = 22 and W = 143. The corresponding C_p values were found to be 1.5 and 2.2, respectively. The gel experiments that contain MS artifacts will results in wrong values of C_p. Figure 7.8 shows the measured C_p values

obtained around the gel times vs. D_f for different gel experiments from our work (blue points), that exhibit no MS artifacts. In addition, it shows the C_p values vs D_f reported by Sorensen and Wang (C. M. Sorensen and Wang 1999) (red points). Both data sets correspond well with each other. Despite this agreement, it is clear from Fig. 7.8 that it does not give evidence of the functionality of C_p on higher D_f values. At high D_f values does C_p reach a certain value and then plateau, or does it keep increasing with D_f?

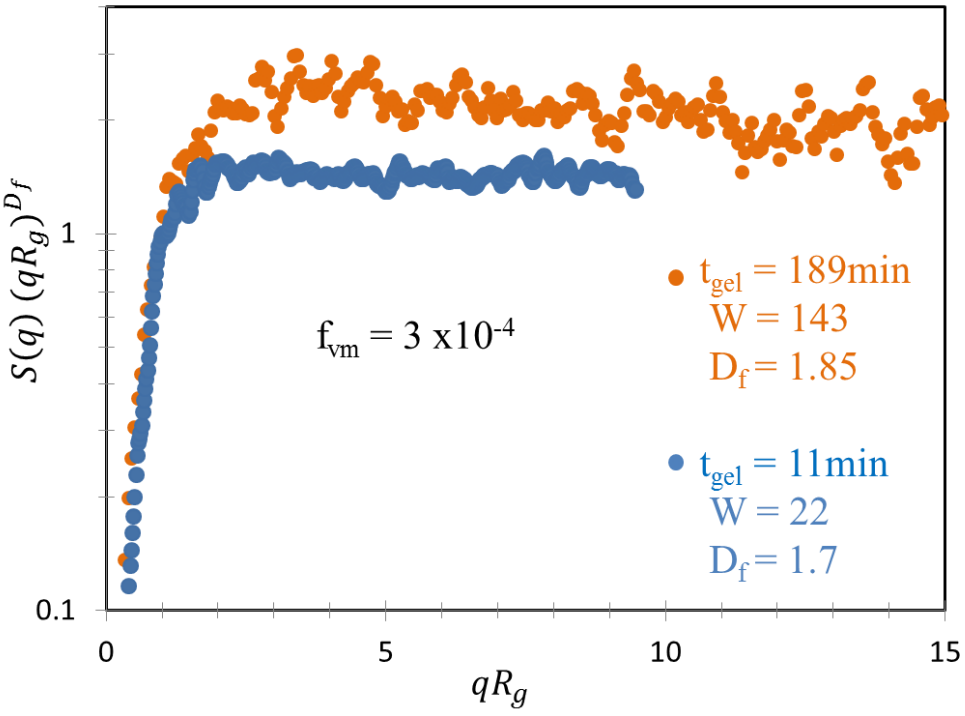

Figure 7.7 $S(q)(qR_g)^{Df}$ vs. qR_g for the same f_{vm}=3x10^{-4} but different salt concentrations to yield different W values with different D_f=1.85 and 1.7 as indicated in the graph as orange and blue data, respectively. The constant value at large qR_g is CC_p in Eq. (7.10).

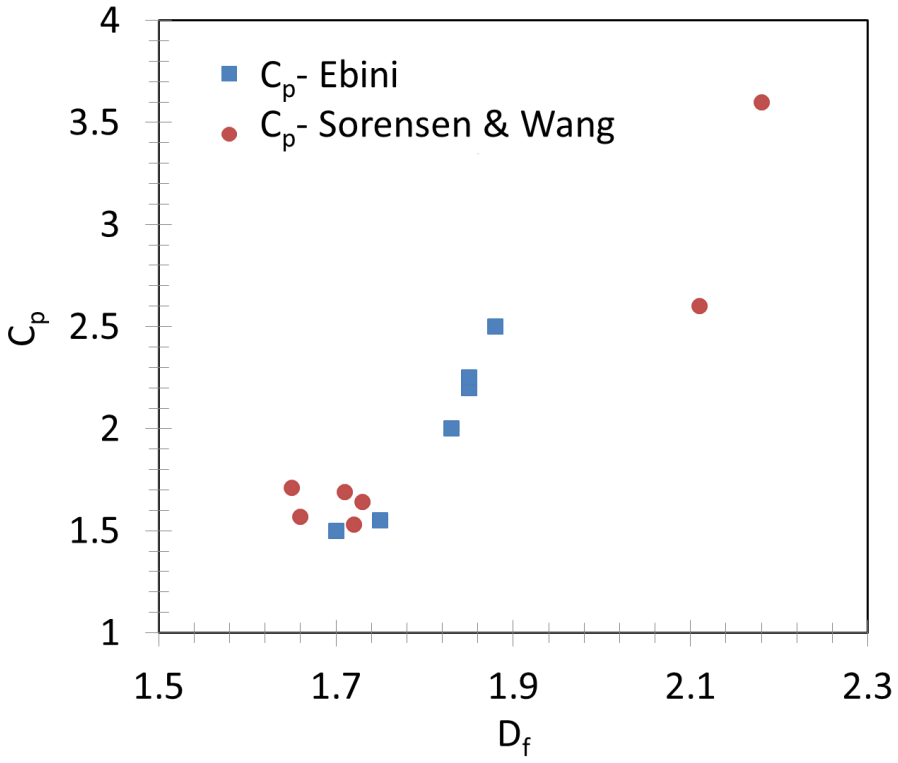

Figure 7.8 shows C_p vs. D_f. Blue points are the values obtained from the experimental data from this work following Sorensen and Wang method (C. M. Sorensen and Wang 1999). The red points are the values reported by Sorensen and Wang.

Nevertheless, one can still use the C_p graph and correct for the polydispersity in the C_{tgel} vs D_f graph. Although the polydispersity factor C_p appears in the structure factor, as shown in Eq. (7.10), it does not necessarily take the same functionality of the polydispersity index P, as shown in Bremer's A factor. Both C_p and P originate from the same source: the polydispersity in aggregates' size distribution. As an *ad hoc* correction to the C_{tgel} vs D_f, I will consider C_p equal to P. Then, the correction will be to divide $C_{tgel\text{-}KSU}$ by C_p. As discussed above, there are two different possible behaviors of C_p on D_f at higher D_f values, hence two different possible corrections. The first correction can be done by considering C_p eventually plateaus with higher values of D_f at a C_p value of ~ 3.5, then the corrected $C_{tgel\text{-}KSU1}$ vs. D_f takes the form of the solid blue line in as shown in Fig. 7.9. The second correction can be done by considering C_p increases with increasing D_f, then the corrected $C_{tgel\text{-}KSU2}$ vs. D_f takes the form of the solid purple line as shown in Fig. 7.9. The subscripts 1 & 2 in $C_{tgel\text{-}KSU}$ indicate the first and second corrections used for $C_{tgel\text{-}KSU}$. This correction,

although need to be further investigated, shows a better fit of the KSU theory to the experimental data.

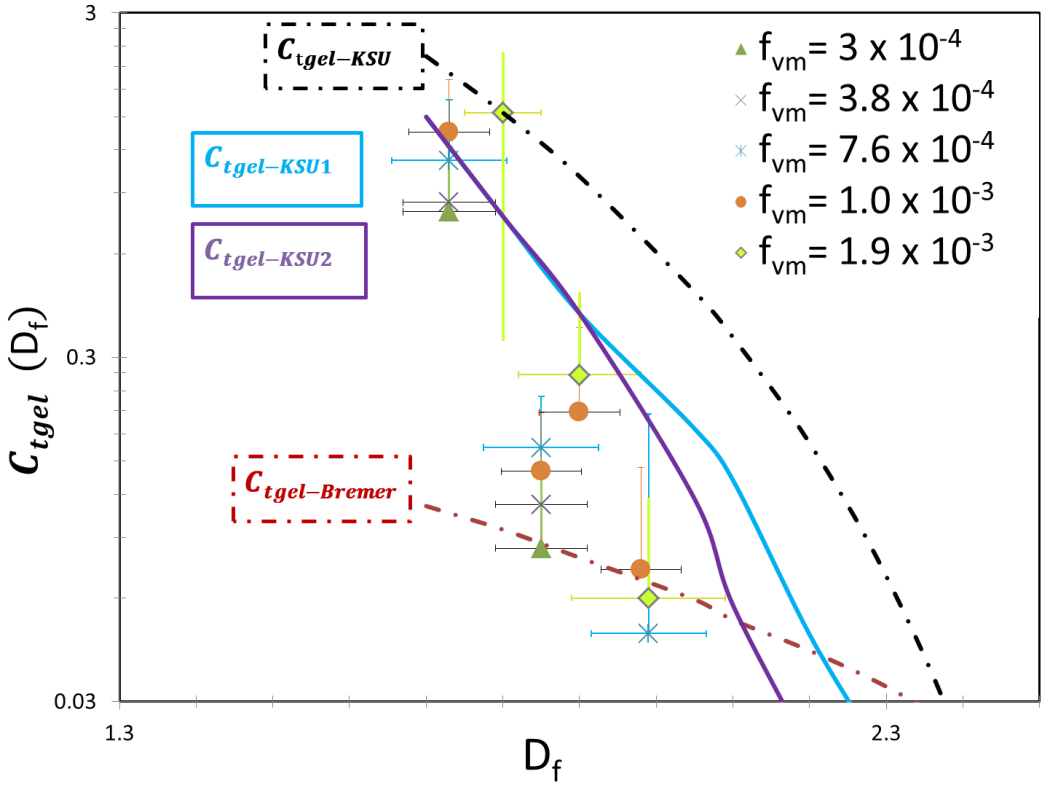

Figure 7.9 A replicate of Fig. 7.6 except the two possible polydispersity corrections at high values of D_f are made to the KSU theory and shown in solid lines. The blue line represents the first correction where C_p eventually plateaus with D_f. The purple line represents the second correction where C_p increases with D_f.

It is important to note that the gel time as described by KSU initiated with the solution of SE with the assumptions of constant kernel and equal sized aggregates, as described in Eq. (3.20)

$$\frac{dn}{dt} = -k\, n^2 \tag{7.11}$$

Which yielded a solution, as in Eq. (3.21), of

$$n = (K\, t)^{-1} \tag{7.12}$$

This solution implies a kinetic exponent z =1 as the case of cluster-dilute case. In Chapter 6 we provided evidence to the IGP predictions of increasing z in the cluster-dense regime due to crowding. As an ad hock, one might write the solution as

$$n = (K\,t)^{-z} \tag{7.13}$$

Then the t_{gel} scales with f_{vm} as

$$t_{gel} \sim f_{vm}^{-3/z(3-D_f)} \tag{7.14}$$

Where $1 \leq z < 2$. The discussion above was done with z = 1.

7.2 Conclusion

The t_{gel} scaling with W and f_{vm} was validated as described in Eqs. (7.2) and (7.3). This was done by introducing the experimental procedure that account for the crucial importance of D_f, which is sometimes overlooked in the literature. These equations are derived from the kinetic description of gelation, making the kinetics description overrule the thermodynamic and percolation descriptions, which are often used to describe the sol-to-gel transition. If the procedure presented in this study is followed, the D_f value can be predicted from the best fit of t_{gel} vs. f_{vm} graph.

Even though the gel time scaling with W and f_{vm} worked in an agreement with the predicted exponents by Eq. (7.6), the coefficients did not. The polydispersity correction seems to give promising results. Another correction I can pursue is the relation between the collision to the hydrodynamic radii, R_c/R_h. In our theory we consider them equal, in real cases they are not.

Chapter 8 - Anomalous diffusion in the cluster-dilute regime

The priciples of dynamic light scattering (DLS) were introduced in Chapter 2. In DLS the fluctuations in the scatterered intensities, due to the relative motion between the probed entities in the sample, are monitored. The entities can be a wide range of colloids or aerosols. DLS provides a measure of the field correlation function $f_1(q,t)$, where q is the scattering wavevector, $q = 4\pi/\lambda \sin(\theta/2)$. The general form of the field correlation function is $f_1(q,t) \sim exp(-t/\tau)^{\beta}$, where τ is the relaxation time and β is an exponent indicative of the type of motion. If $\beta = 1$, then the probed entities are going through normal diffusion characterized by the Brownian motion. If $\beta \neq 1$, in some cases it was found that an anomalous diffusion is occurring (R. Böhmer 1998; Roland Böhmer et al. 1998; 1998; Bouchaud and Pitard 2001; Chamberlin 1998; Cipelletti et al. 2000b; Klafter and Sokolov 2005; A. H. Krall and Weitz 1998). If $\beta < 1$ then β refers to a stretched exponential and the motion is said to be sub-diffusive, Meanwhile if $\beta > 1$ then it refers to a compressed exponential and the motion is referred to as a super-diffusive.

Anomalous diffusion is commonly reported in the literature when the entities probed were in crowded states. For colloidal gels, for example, the observations of $\beta < 1$ occur while the system is going through the sol-to-gel transition (Di Biasio 1998; A. H. Krall and Weitz 1998; Mattsson et al. 2009) and for $\beta > 1$ it was reported in aging gelling systems (Bouchaud and Pitard 2001; Cipelletti et al. 2000b; Ruta et al. 2014).

What determines the observation of a stretched exponential or a compressed exponential is the choice of q used in the light scattering experiment. q has an inverse unit of length. Thus the size the experimental set up can probe is of the order of q^{-1}. We will call a region with size q^{-1} a q^{-1}-region. When the q^{-1}-region is smaller than the aggregates size, then a stretched exponential is observed, whereas if the q^{-1}-region is larger than the largest aggregate size, then a compressed exponential is observed. A simulation study done by Del Gado and Kob (Del Gado and Kob 2007) show that when the q^{-1}-region is smaller than the cluster size, the stretched exponential appears due to the internal dynamics of the aggregates. If on the other hand the q^{-1}-region is larger than the largest aggregate size, the compressed exponential appears due to the restructuring of the gel.

8.1 Results and discussions

Two types of experiments were performed in this work with the polystyrene particles: one type were the non-gelling experiments and the other type were the gelling experiments. For the non-gelling experiments two initial monomer volume fractions were used, f_{vm} = 6.8 x 10^{-6} and 3.4 x 10^{-5} but the same [$MgCl_2$] = 10mM. Each non-gelling experiment was perfomed almost simultanously between two different scattering angles. One scattering angle was fixed at 90^o and the other angle takes either 49.4^o or 22.1^o. For the gelling experiments the initial volume fraction used was either 3.4 x 10^{-4} or 4 x 10^{-4} and the [$MgCl_2$]= 8mM, 10mM, and 20mM. The scattering angle for the gelling experiments were fixed at 90^o.

An example of the temporal evolution of the field correlation function $f_1(q,t)$ for an aggregating, non-gelling experiment was shown in Chapter 6, Fig. 6.1. The solid lines are the fit lines to a stretched exponential $f_1(q,t) \sim exp(-t/\tau)^{\beta}$. From these fit lines β vs. t_w is obtained.

For the non-gelling experiments the aggregates remained in the cluster-dilute regime as indicated by the kinetic exponent z = 0.95 ± 0.08 throughout the experimental time. This is shown in Fig. 8.1 for the different non-gelling samples when D_f=1.75 is used.

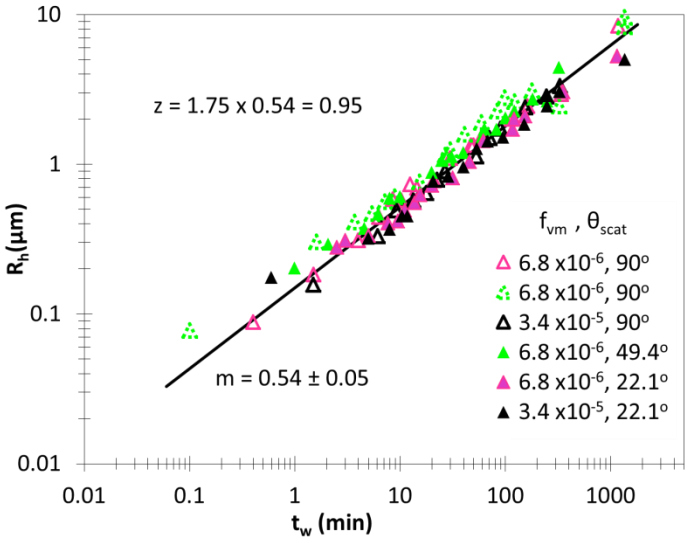

Figure 8.1 R_h vs. t_w for the different non-gelling experiments. [$MgCl_2$]=10mM for all samples. The slope is m.

Figure 8.2 shows β vs. t_w for all the different non-gelling samples with different scattering angles. Initially, β takes a value of 1, and then drops below that at certain t_w depending on the scattering

angle for each experiment. At 90° scattering angle (unfilled triangles), β drops below 1 sooner than at smaller scattering angles (filled triangles). Our report of a stretched exponential for aggregates in the cluster-dilute regime for the non-gelling samples is unique. In literature, the stretched exponential is usually reported when the system of study is in the dense state.

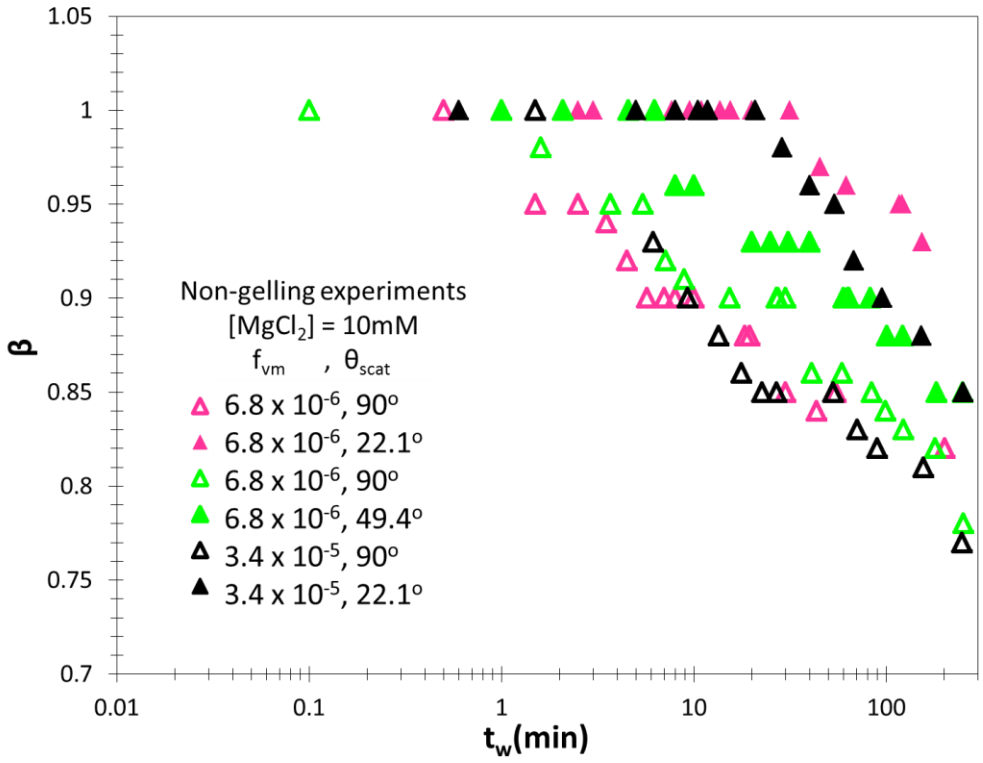

Figure 8.2 β vs. t_w for the different aggregating, non-gelling samples.

For the gelling samples the scattering angle was fixed at 90°. In Chapter 6 an example of the field correlation function, $f_1(q,t)$, for gelling sample was shown in Fig. 6.3(b). β was obtained from the solid fit lines to $f_1(q,t)$. Figure 8.3 shows β vs. t_w for all the experiments, gelling and non-gelling. The gelling samples are represented by unfilled squares.

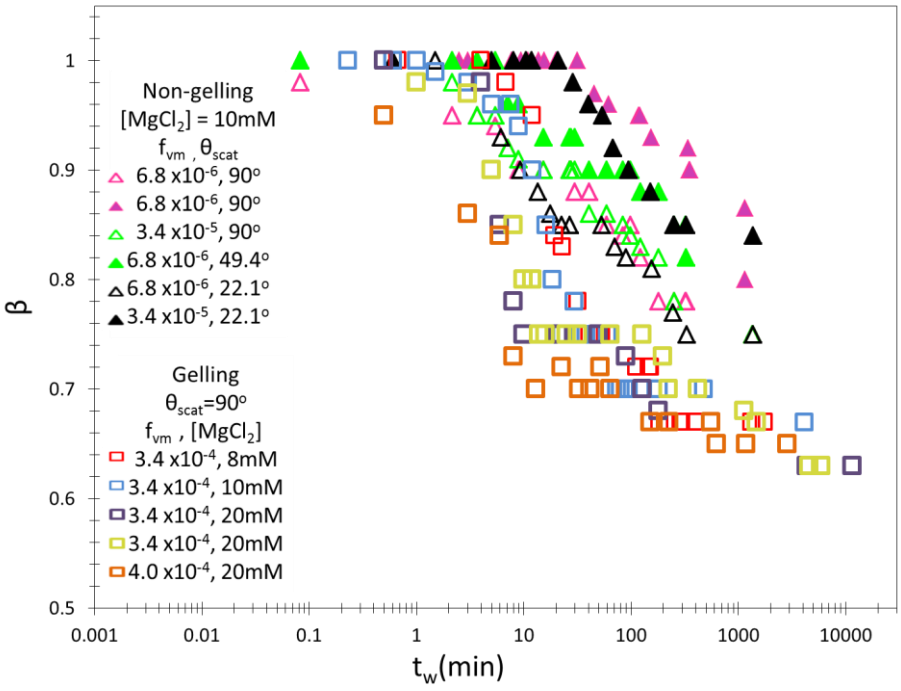

Figure 8.3 β vs. t_w for the different gelling and non-gelling samples.

It is interesting here to note that even for gelling samples, β starts to deviate from 1 when the aggregates are in the cluster-dilute regime. For example, the blue square data points are corresponding to $f_{vm} = 3 \times 10^{-4}$ and $[MgCl_2] = 10mM$. β starts to deviate from 1 at $t_w \sim 1min$. Figure 8.4 shows the temporal evolution of R_h vs. t_w for this run. At $t_w \sim 1min$, the system is still in the cluster-dilute regime as indicated by the dashed up-right arrow.

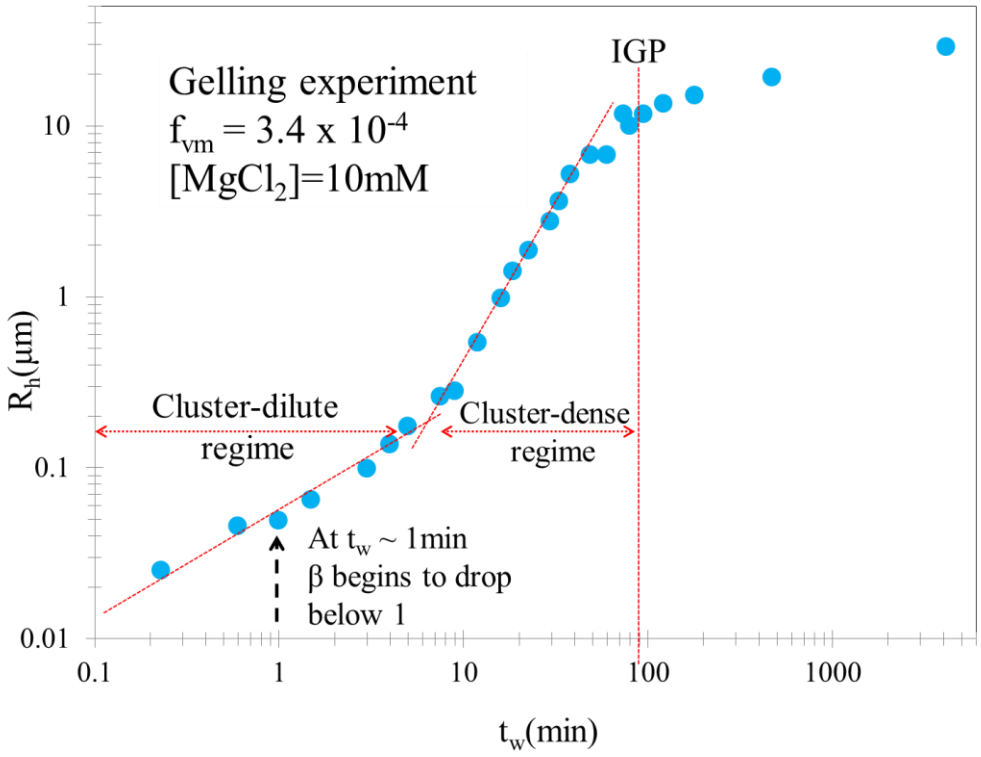

Figure 8.4 R_h vs. t_w for a gelling sample made with f_{vm} = 3.4 x 10^{-4} and [$MgCl_2$] = 10mM.

Table 8.1 summarizes the scattering angles used and the size of the corresponding q^{-1}-region. Notice the length scales probed in our experiments are very short. This is consistent with the literature in observing a stretched exponential for such short length scales.

To test whether the observation of a stretched exponential is due to probing the internal dynamics of an aggregate, we plot β vs. qR_h for both the gelling and the non-gelling experiments. As a reminder, the non-gelling experiments were done with two different monomer volume fractions, 6.8x10^{-6} and 3.4x10^{-5}, but for the gelling experiments the monomer volume fractions were very comparable to each other: 3.4 x 10^{-4} and 4 x 10^{-4}. I will treat these two monomer volume fractions as if they are equal in the coming discussion and refer to them as f_{vm} = (3.4 & 4) x10^{-4}.

Table 8.1 Summarizes the scattering angles and the corresponding q^{-1}-regions.

Scattering angle (θ_{scat})	q^{-1}-region (nm)
22.1°	167
35.2°	105
49.4°	77
90°	45

Figure 8.5 shows β vs. qR_h for (a) $f_{vm} = 6.8 \times 10^{-6}$, scattering angles of 90°, 49.4°, & 22.1°, $[MgCl_2]$ = 10mM; (b) $f_{vm}=3.4 \times 10^{-5}$, scattering angles 90° and 22.1°, $[MgCl_2]$ = 10mM; and (c) $f_{vm} = (3.4 \text{ \& } 4) \times 10^{-4}$, scattering angle of 90°, $[MgCl_2]$ = 8mM, 10mM, 20mM.

All the graphs in Fig. 8.5(a), (b), & (c) show all the data of the same f_{vm} fall onto one curve. Regardless of the scattering angles used like the cases in Fig. 8.5(a) & (b), or the different kinetics due to different $[MgCl_2]$ used, like the case of Fig. 8.5 (c). In addition, these figures show that initially β takes the value of 1 and then deviates from that when $qR_h > 1$; hence $q^{-1} < R_h$. This is consistent with Del Gado's picture of probing the internal dynamics of an aggregates yields a stretched exponential.

A unique observation Fig. 8.5 provides is the minimum qR_h value at which β starts to drop below 1 for the different f_{vm} used. We will distinguish this specific qR_h value with the symbol $(qR_h)_{min}$. For $f_{vm} = 6.8 \times 10^{-6}$, $(qR_h)_{min} \sim 6 \sim 2\pi$. Whereas for $f_{vm} = 3.4 \times 10^{-5}$, $(qR_h)_{min} \sim 4$, and finally for $f_{vm} = (3.4 \text{ \& } 4) \times 10^{-4}$ $(qR_h)_{min} \sim 1.3$. In other words, for the field correlation function to starte showing a stretched exponential form, the average aggregate size needs to grow up to ~ $6q^{-1}$, $4q^{-1}$, and $1.3q^{-1}$ for the $f_{vm} = 6.8 \times 10^{-6}$, 3.4×10^{-5}, and $(3.4 \text{ \& } 4) \times 10^{-4}$ respectively. This strongly indicates that $(qR_h)_{min}$ is a function of f_{vm}. Figure 8.6 (a) illustrates this point by graphing $(qR_h)_{min}$ vs. f_{vm}. The slope obtained is m = - 0.37 ± 0.06 to empirically suggests the scaling relation $(qR_h)_{min} \sim f_{vm}^{-0.37}$. For each monomer volume fraction there is an average monomer nearest neighbor separation, $R_{nn,m}$ which can be calculated from $R_{nn,m} = (particle\ volume/f_{vm})^{1/3}$. Combining this expression for $R_{nn,m}$ with the scaling $(qR_h)_{min} \sim f_{vm}^{-0.37}$, we expect $(qR_h)_{min} \sim R_{nn,m}^{1.1}$. Figure 8.6 (b) shows $(qR_h)_{min}$ vs. $R_{nn,m}$ with a slope of m = 1.15 ± 0.13, consistent with what we expected.

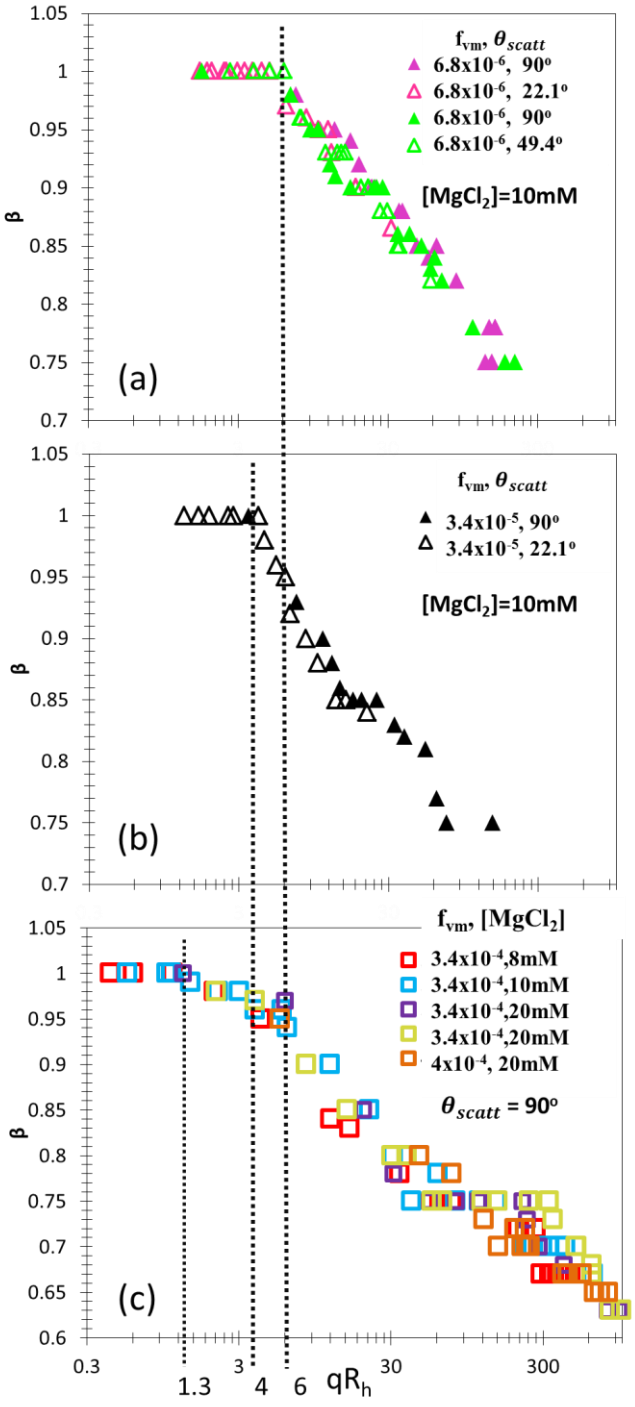

Figure 8.5 β vs. qR_h for non-gelling samples with (a) fvm = 6.8 x 10^{-6}, (b) fvm = 3.4 x 10^{-5}, and for the gelling samples with (c) f_{vm} = (3.4 & 4) x 10^{-4}. The vertical dotted lines indicate the minimum qRh values at which the stretched exponential appears for the different f_{vm}.

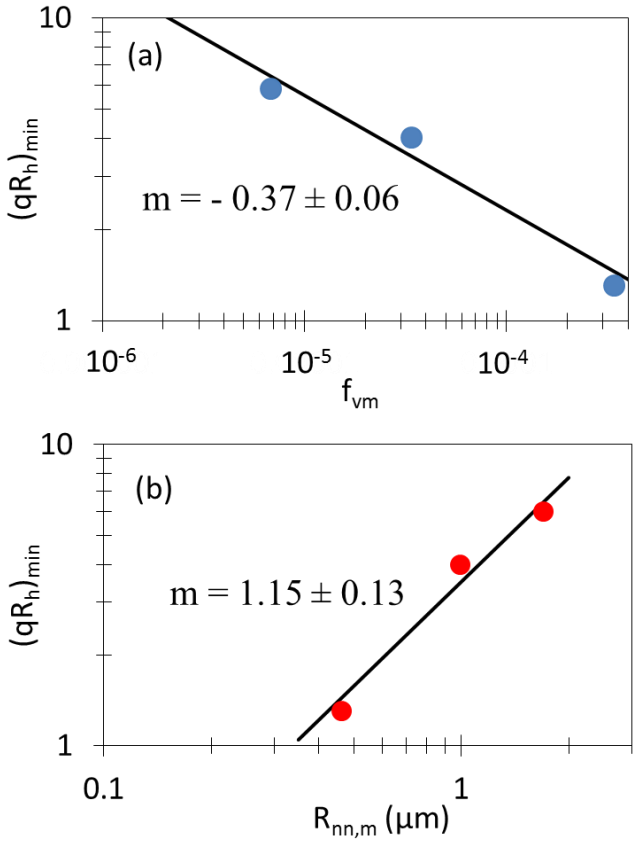

Figure 8.6 $(qR_h)_{min}$ vs. (a) f_{vm} (b) $R_{nn,m}$. The slope is m.

One may wonder whether β relate to the kinetics of the system. In an attempt to relate to this point we plot β vs. t_w/t_{gel} as shown in Fig. 8.7, where t_{gel} is the gel time defined at which the kinetics of the system drastically slows down. Combining our knowledge from Chapter 6 & 7, t_{gel} occurs for systems with no multiple scattering artifacts at the ideal gel point (IGP). The IGP corresponds to an aggregate size of $R_{g,G}$. For the gelling experiments t_{gel} was obtained experimentally from the temporal evolution of R_h. For example, Fig. 8.4 shows R_h vs. t_w and provides a t_{gel} ~ 90 minutes. On the other hand, for the non-gelling experiments, the gel time was extrapolated from Fig. 8.1 after calculating the size of the aggregates at the IGP using Eq. 3.19. For the non-gelling experiments with $f_{vm} = 6.8 \times 10^{-6}$ the calculated $R_{g,G} \sim 95\mu m$ and the extrapolated $t_{gel} \sim 2 \times 10^5$ minutes, and for the $f_{vm} = 3.4 \times 10^{-5}$ the calculated $R_{g,G} \sim 36\mu m$ and the extrapolated $t_{gel} \sim 3 \times 10^4$ minutes. In contrast to the non-gelling experiments where the system remained in the cluster-dilute regime, the system in the gelling experiments evolved from cluster-dilute to cluster-dense and

eventually the IGP is reached, where the gel starts forming. These evolving regimes for the gelling samples were indicated with blue dotted lines in Fig. 8.7.

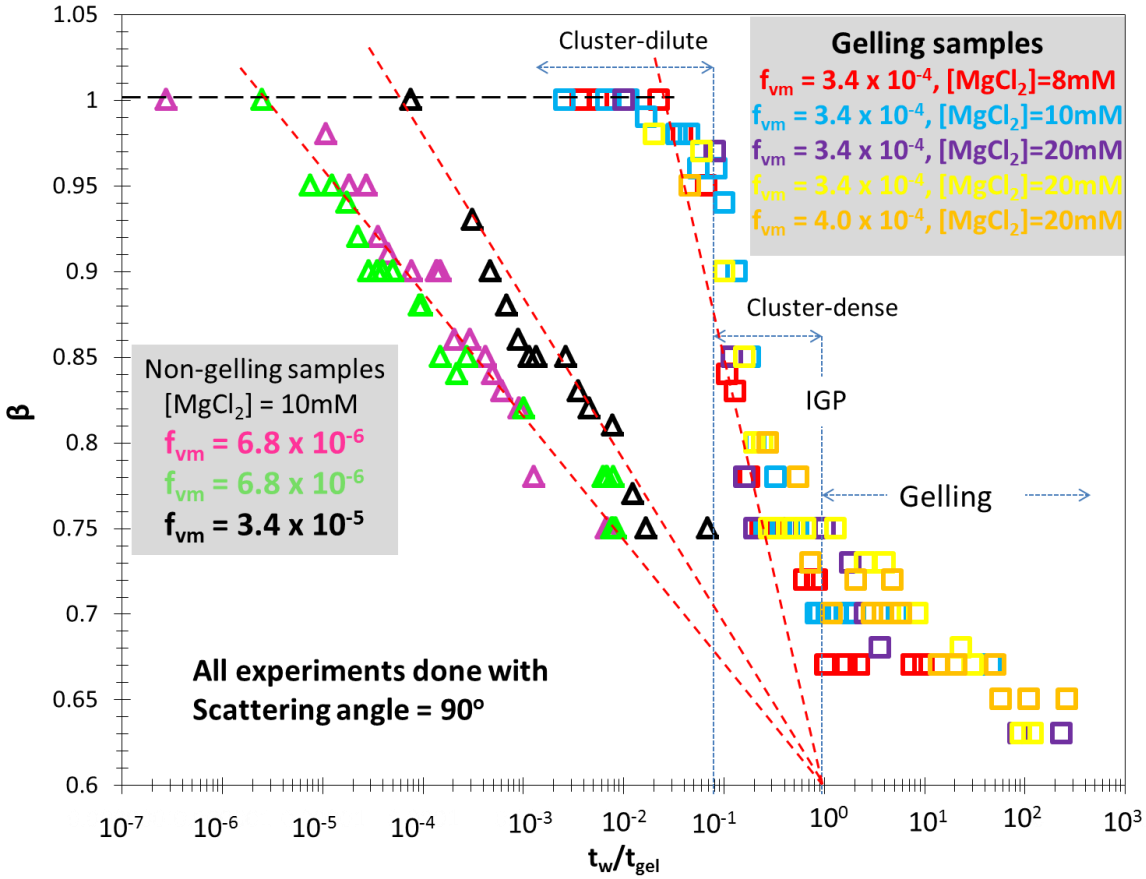

Figure 8.7 β vs. t_w/t_{gel} for the gelling and non-gelling experiments.

Figure 8.7 shows three data groups. One for each volume fraction used in this experiment: 6.8 x 10^{-6}, 3.4 x 10^{-5}, and (3.4 &4) x 10^{-4}. For these three sets β starts from value of 1, as indicated by the horizontal dashed line, before it begins to drop below 1. The three data sets suggest if we start a line for each set from the t_w/t_{gel} at which β value starts to drop below 1 and draw these lines along the data points for each set, all the lines will end up at $t_w/t_{gel} \sim 1$ and $\beta \sim 0.6$. These lines are represented by the red dashed lines in Fig. 8.7. One may ask: What is special about β =0.6? In addition, for the gelling experiments, the data strongly suggests the decrement of β slows down as the system reached the IGP. Why is that? And how does this relate to the elasticity of a gel? Does β reach a final value then plateau? Or does it keep decreasing with the aging of the gel?

8.2 Conclusion

This chapter shows the behavior of an anomalous diffusion in the form of a stretched exponential. Our results show that the field correlation function can be fitted to a stretched exponential function while the system is still in the cluster-dilute regime, regardless if the system will eventually gel or not. This is in contrast to the common results in literature that show the stretched exponential exponent β drops below unity only when the system is in a dense state. Our results are in support of the picture of probing the internal dynamics of the aggregates for small q values even for systems in the cluster-dilute regime.

This Chapter shows two unique observations. One is that for the field correlation function to start taking the form of a stretched exponential ($\beta < 1$) the average aggregate size needs to grow bigger than the probed q^{-1}-region. Empirically we found $(qR_h)_{min}$ scales with f_{vm} as $(qR_h)_{min} \sim f_{vm}^{-0.37}$. This yielded the scaling of the nearest neighbor separation of monomers, $R_{nn,m}$, to $(qR_h)_{min}$ to takes the form $(qR_h)_{min} \sim R_{nn,m}^{1.15}$. The second observation is when we force a line from the point at which β starts to drop below 1 on a β vs. t_w/t_{gel} graph, for the different monomer volume fractions, and allow these lines to pass through the data, all the lines are ending at one point, $t_w/t_{gel} \sim 1$ and $\beta \sim 0.6$. These two major observations lead a curious mind to pursue the work to understand how $(qR_h)_{min}$ depends on f_{vm}, what $\beta = 0.6$ signifies, and how β relates to the kinetics of a gel, aging of a gel, and the elasticity of a gel.

Chapter 9 - Unified description of the sol-to-gel transition

The IGP theory is a simple development of the kinetic description of the sol-to-gel transition. However, there are two other main descriptions of the same process. One is a thermodynamic phase transition description and the other is a percolation description. We discussed these descriptions in Chapter 3.

This chapter has two goals. First is to extend the application of the IGP into different data that already exists in the literature with the emphasis on the importance of following the experimental procedure described in Chapter 5. A second goal is to unify the description of the sol-to-gel transition. We will do that by briefly summarizing the key points of the other descriptions and try to explain the discrepancies that appear between these descriptions from the perspective of the IGP theory.

9.1 Applying the IGP theory to the literature

In the literature there are lots of data that I can use to test for the IGP prediction of $R_{g,G}$ and the t_{gel}. I will combine these data with my own to extend the application of the IGP to different ranges of: particle types, sizes, initial monomer volume fractions, salt concentrations, and salt types.

9.1.1 IGP theory predition of the radius of gyration at the IGP

Here I wish to apply the IGP prediction of the radius of gyration at the IGP, $R_{g,G}$ given in Eq. (3.19) to a collection of experimental data presented in the literature. The IGP predicted the following format of the $R_{g,G}$

$$R_{g,G} = a[\, f_{v,m}^{-1} k_o (D_f / (2+D_f))^{3/2}\,]^{1/(3-D_f)} \tag{9.1}$$

To be able to find $R_{g,G,}$ the initial monomer size, a, monomer volume fraction, f_{vm}, and the fractal dimension D_f need to be known.

In the literature some work presented the evolution of the scattered intensity and the measured value of D_f (Asnaghi, Carpineti, and Giglio 1994a; Carpineti and Giglio 1992; Cipelletti et al. 2000c; Ebini and Sorensen 2019; Lu et al. 2008; Tanaka, Nishikawa, and Koyama 2005; Mokhtari et al. 2008; Wu et al. 2011). The temporal evolution of the scattered intensity enabled the use of Guinier analysis to obtain the temporal evolution of R_g during the gelation process. On the other

hand, other work required careful analysis by taking the data and represent it in our newly designed procedure, explained in Chapter 5, to compensate for the lack of measuring D_f (Wu, Xie, and Morbidelli 2013).

An example of the temporal evolution of the scattered intensity was given by Cipelletti et al. (Cipelletti et al. 2000c). They worked with polystyrene spheres with radius a = 10.5nm, [$MgCl_2$] = 16mM, and $f_{vm} = 4.8 \times 10^{-4}$. They provided I(q) vs. q data as shown in Fig. 9.1(a), with an insert of the measured D_f values. This figure is the original figure from their work. The temporal evolution of the scattered intensity gave me the access to find R_g. The calculated $R_{g,G}$ was 8 ± 2.5 μm as indicated in the shaded area of R_g vs. t_w in Fig. 9.1(b). There is an excellent agreement between the calculated $R_{g,G}$ and the experimental $R_{g,G}$. As a reminder, we defined the experimental $R_{g,G}$ throughout this work as the cluster size at which the IGP is reached. The IGP is defined when the kinetics starts drastically slowing down. Figure 9.1 shows the system starts to gel at t_{gel} ~ 1.4hrs. Additionally, Fig. 9.1(a) shows an interesting feature at later stages of gelation, 4.1 & 137 days. The intensity at small q values, hence large length scales, starts to increase. The authors did not explain this behavior, but one may wonder might this indicate the superaggregates that have been seen in soot aerogels and in sheared colloidal gels? The data in Fig. 9.1(a) has no applied shear beyond the initial mixing process of the colloid and salt.

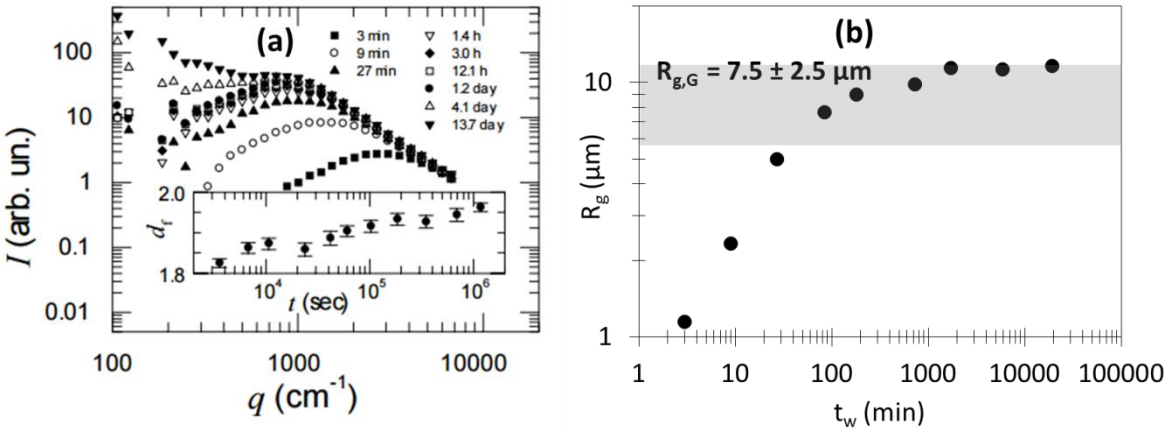

Figure 9.1 (a) I(q) vs. q for fractal colloidal system made of 10.5nm radii particles and destabilized by 16mM $MgCl_2$. The insert shows the evolution of D_f. This image is taken from (Cipelletti et al. 2000c), (b) R_g vs. t_w extracted from Fig. 9.1(a) with a calculated $R_{g,G}$ using Eq. (9.1) obtained to be 7.5 ± 2.5μm. The shaded area represents the error range in calculated $R_{g,G}$.

An example of a detailed analysis of the data was the case of Wu et al. data (Wu, Xie, and Morbidelli 2013). They worked on colloidal gels using fluorinated polymer colloids, which have

a very low optical contrast with respect to water. The formed gels were transparent. This allowed them to study dense colloidal systems with no multiple scattering (MS) artifacts. They used two different monomer radii a = 21nm and 37.5nm. The aggregation was initiated by adding different concentrations of NaCl. They monitor the evolution of the scattering structure using small angle light scattering (SALS) which provided the temporal evolution of the aggregates as shown in Fig. 9.2 for monomer sizes (a) 21nm and (b) 37.5nm. The data shown in Fig. 9.2 are the original data provided by Wu et al. except we relabeled the axis and legends.

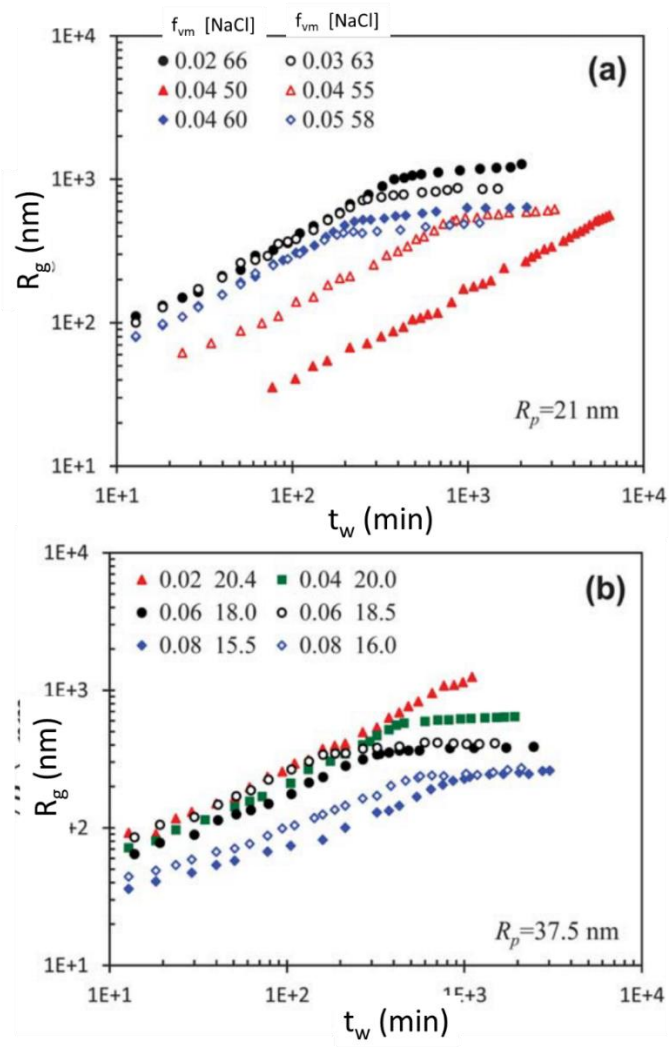

Figure 9.2 R_g vs. t_w for different fvm and salt concentrations for monomer radii of (a) 21nm and (b) 37.5nm. These are the original graphs (Wu, Xie, and Morbidelli 2013) we just relabeled legend and axis.

Wu et al. support the kinetic description of gelation and proposed $R_{g,G} \sim f_{vm}^{-1/(3-D_f)}$, same proportionality introduced by the IGP theory as described in Eq. (9.1). They presented the

aggregate size at gelation $R_{g,G}$ for the two different radii as shown in Fig. 9.3. The slope they got is -1.05. This let them to conclude that $D_f = 2.05$. D_f was not measured in their work.

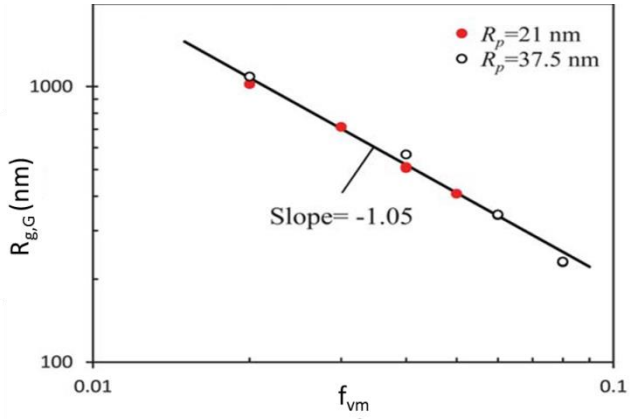

Figure 9.3 $R_{g,G}$ vs f_{vm} for 21nm particles (red points) and 37.5nm particles (unfilled black points). This is the original graph from (Wu, Xie, and Morbidelli 2013) with axis relabeled.

Figure 9.3 shows for different monomer radii, 21nm & 37.5nm, $R_{g,G}$ vs. f_{vm} collapses onto one curve. The authors concluded that the cluster volume fraction, f_{vc}, at gelation is higher for the smaller radii. From $R_{g,G}$ values, they estimated the f_{vc} = 0.8 and 0.5 for 21nm and 37.5nm, respectively. In our attempt of deriving $R_{g,G}$ we assumed $f_{vc} \sim 1$, regardless of the different sizes of monomers. I puzzle with this picture, because fractal aggregates scaling occurs in a similar manner for different sized particles under the same initial conditions. Instead, I suggest an alternative explanation for the observation in Fig. 9.3. It is possible that the D_f for the 21nm particles was slightly higher than the D_f for the 37.5nm particles at the same f_{vm}. This slightly higher D_f compensates for the smaller monomer size and resulted in the same $R_{g,G}$.

Wu et al. measured W values ranges from 3 x 10^5 to 3 x 10^7. The smallest W value measured by Wu et al. is ~ 100 times higher than the highest W value I worked with. The highest value I worked with was W ~ 900 and gave a measured D_f =2.05 as shown in Fig. 5.2(b). Nevertheless, Wu et al. made their analysis with the estimation of D_f = 2.05. This made me wonder whether D_f = 2.05 truly represents the fractal dimension in their work or not. I will utilize the results obtained in my work to re-estimate the D_f value in two different ways. One way is to utilize the results in Chapter 6, where the scaling relation $R_{g,G} \sim f_{vm}^{-1/(3-D_f)}$ proved correct. The second way is to utilize the work done in Chapter 7 where $t_{gel} \sim f_{vm}^{-3/(3-D_f)}$ seems to work as well. Clearly both $R_{g,G}$ and t_{gel}

are sensitive to the true D_f value. That is why I developed the procedure, in my work, of finding W values for each run and grouping these W values within a range that gave the same D_f value. Wu et al. did not measure D_f, nevertheless I created two different W groups out of their data, W_{grp1} and W_{grp2}. W_{grp1} contains W values ranges from 7 x 10^6 to 3 x 10^7, meanwhile W_{grp2} contains W values ranges from 3 x 10^5 to 4 x 10^6.

A side note worth mentioning here is sedimentation starts to inhibit gelation at a critical size, as indicated by Wu et al., of ~ 1200nm and 2000nm for monomer sizes of 21nm and 37.5nm, respectively. A close look at Fig. 9.2 shows the size at which the kinetics is rounding off is almost at the critical aggregate size at which the sedimentation will occur for the case of 21nm monomer at f_{vm} = 0.02 and [NaCl] = 66mM, or very close to the critical sedimentation size like the case of 37.5nm at f_{vm} = 0.02 and [NaCl] = 20.4mM . Wu et al. did not exclude these two points from their analysis, but I will.

The first attempt to estimate D_f was using the scaling relation $R_{g,G} \sim f_{vm}^{-1/(3-D_f)}$. I did that by extracting the experimental cluster size at gelation, $R_{g,G,Exp}$, for each experiment they provided in Fig. 9.2(a) & (b), except the near sedimentation ones. Figure 9.4 (a) shows $R_{g,G,Exp}$ vs. f_{vm} for $W_{grp1\&2}$. The green & black data points represent W_{grp1} and W_{grp2}, respectively. Note that Fig. 9.4 differs than Wu et al. original figure shown in Fig. 9.3 by four data points. Two are the data points I excluded due to sedimentation might inhibit the aggregation. The other two points where at f_{vm} = 0.06 & 0.08 for the 37.5nm that Wu et al. did not include in his $R_{g,G}$ vs. f_{vm} plot, without mentioning any reason for excluding them. This comparison is made easier when I replicate their $R_{g,G}$ vs. f_{vm} by extracting $R_{g,G}$ from Fig. 9.3 (a) and (b) except for the near sedimentation ones. This is shown in Fig. 9.4(b).

For W_{grp1} we have only three data points for only two different monomer volume fractions. Possibly they might fit into a different slope than the black points, W_{grp2}, but for such a short range on a log-log scale and small number of data, I will not claim a separate slope for W_{grp1}. For W_{grp2} the situation is better in terms of the number of data but not in the range of data. Hence, I will consider one slope for both W groups. The solid black line in Fig. 9.4 represent a slope of m = -1.3 ± 0.2, this corresponds to D_f = 2.25 ± 0.1. The dashed blue line in the same figure is the -1.05 slope Wu et al. claimed, which might be taken as a lower bound limit of the best line fit, but not

the best line fit itself. In conclusion, this procedure provided an estimation of $D_f = 2.25 \pm 0.1$ which is higher than the 2.05 value they estimated.

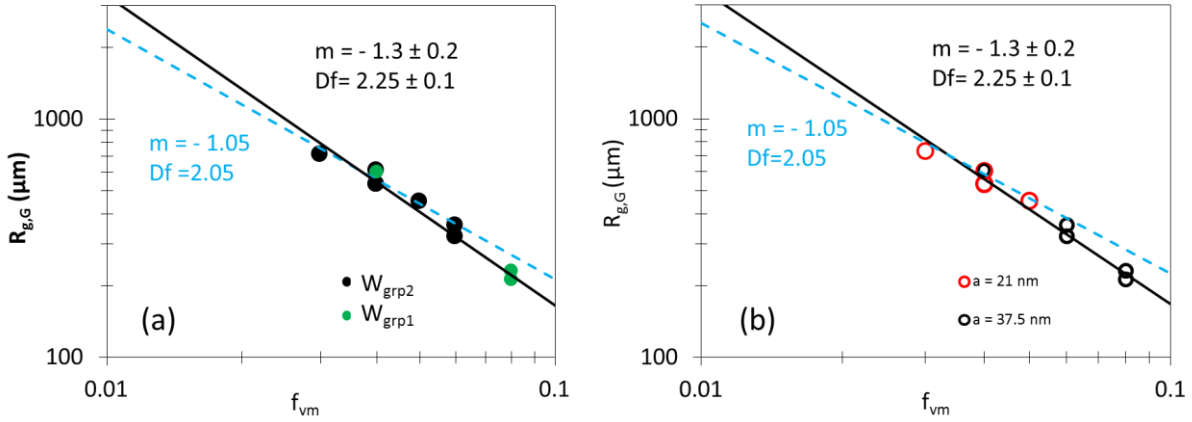

Figure 9.4 (a) and (b) plot $R_{g,G}/a$ vs f_{vm} then both radii should have the same slope if they have the same D_f.

The second way to test for the D_f value is by using the scaling relation $t_{gel} \sim f_{vm}^{-3/(3-D_f)}$. Again, I want to check for the D_f value, this time from the point of view of t_{gel}. Back to the original data shown in Fig. 9.2(a) & (b) I obtained the t_{gel} for the different f_{vm}s except the excluded ones due to sedimentation. Figure 9.5(a) shows t_{gel} vs. f_{vm} for the two different monomer sizes. Figure 9.5(b) shows $t_{gel}/(a^3W)$ vs. f_{vm} for the same data shown in Fig. 9.5(a). The best line fit for these data, regardless whether it belongs to $W_{grp1 \text{ or } 2,}$ is - 4 ± 0.5 as indicated by the black line. When this slope compared with the exponent in the relation $t_{gel} \sim f_{vm}^{-3/(3-D_f)}$ a $D_f = 2.25 \pm 0.1$ is obtained. This D_f value is consistent with the value obtained in the previous method. I will conclude, that the best estimation of the fractal dimension in Wu et al. data is $D_f = 2.25 \pm 0.1$.

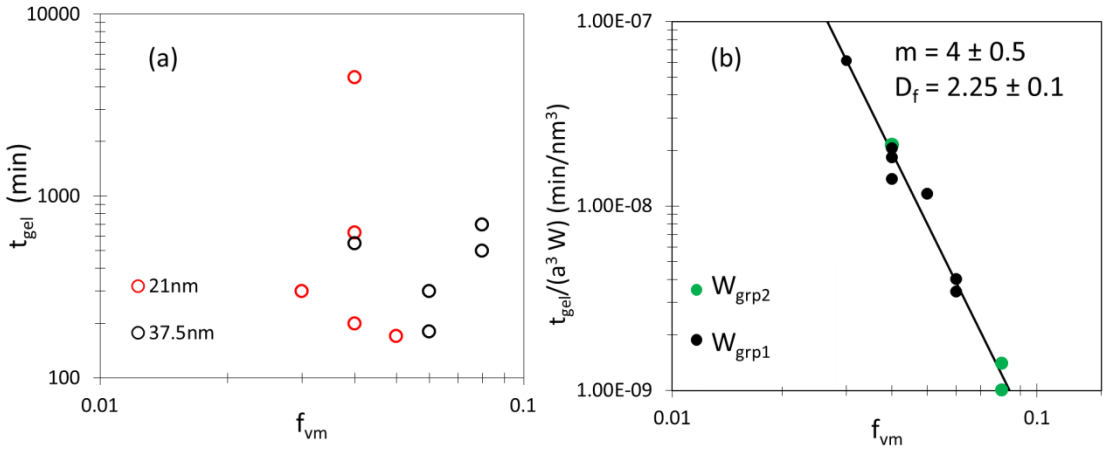

Figure 9.5 (a) t_{gel} vs. f_{vm} extracted from Fig. 9.2 (a) &(b), (b) $t_{gel}/(a^3 W)$ vs. f_{vm} for $W_{grp1\ \&2}$ for the same data shown in (a).

Now I am ready to apply the IGP prediction of $R_{g,G}$, using Eq. (9.1), to the set of data provided by Wu et al. in Fig. 9.2 (a) and (b). I will start with the analysis with Fig. 9.2 (b) for a = 37.5nm because they are easier to discuss. Figure 9.6 is a replicate of Fig. 9.2(b) except now I added the horizontal lines to indicate the $R_{g,G}$ values as calculated using Eq.(9.1).

For each f_{vm}-[NaCl] combination two $R_{g,G}$s are calculated. One is by using D_f = 2.25 represented by the solid lines. The other $R_{g,G}$ is calculated using D_f =2.05 represented by the dashed lines. For clarity, the solid lines shifted to the right and the dashed lines shifted to the left. In addition, the lines are color coded with the data. If more than one data set represented by the same color, then the symbols associated with the data the line represents are provided at the end of the line for the solid lines, or at the beginning of the line for the dashed lines. It is clear that, when D_f = 2.25 is used, the IGP works very well with Wu et al. data. Note that the data represented by the solid red triangles does not match the theoretical value. This is the data set that I excluded in my estimation of D_f because I suspect sedimentation is occurring.

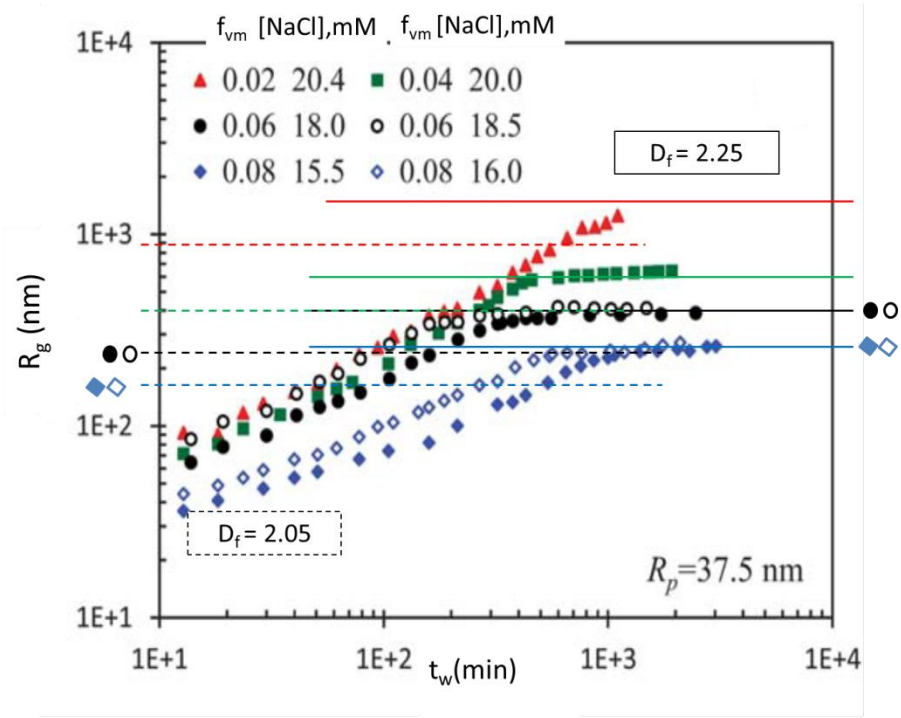

Figure 9.6 A replicate of R_g vs. f_{vm} original graph presented by Wu et al. in Fig. 9.2(b). The horizontal lines are to represent the calculated $R_{g,G}$ values using Eq.(9.1). The solid lines represent the calculated $R_{g,G}$ using D_f = 2.25, and shifted to the right. The dashed lines represent the calculated $R_{g,G}$ with D_f = 2.05 and shifted to the left. The lines are color coded and the associated symbols are identified at the edge of the lines if more than one symbol represents the same color.

Similar to Fig. 9.6, Fig. 9.7 is a replicate of Fig. 9.2(a) except now we added the horizontal lines to indicate the $R_{g,G}$ values as calculated using Eq.(9.1). In Fig. 9.7(a), the solid lines, slightly shifted to the right, represent the calculated $R_{g,G}$ for each f_{vm} using D_f = 2.25. The dotted lines, slightly shifted to the left, represent the calculated $R_{g,G}$ using D_f = 2.05. Again, the calculated $R_{g,G}$ values using D_f =2.25 better represent the experimental $R_{g,G}$ at round off than using D_f = 2.05. At the same time, it is clear that D_f = 2.25 is not in an excellent agreement like the previous case of 37.5nm particles illustrated in Fig. 9.6. If I use the upper limit of the estimated D_f = 2.25 ± 0.1, i.e. D_f =2.35, in calculating $R_{g,G}$, a good agreement with the experimental values are reached. This is shown in the color coded horizontal lines in Fig. 9.7(b). This step can be justified after considering the two following observations: 1) recall in Fig. 9.3, $R_{g,G}$ for the 21nm is equivalent to the $R_{g,G}$ for the 37.5nm for the same f_{vm}. This suggests the D_f for 21nm data sets are slightly higher than the D_f for the 37.5nm sets. 2) a close look at the W values for 21nm in W_{grp2} shows that the average

W values for 21nm particles is ~ 3 times higher than the average W values for 37.5nm particles in the same group.

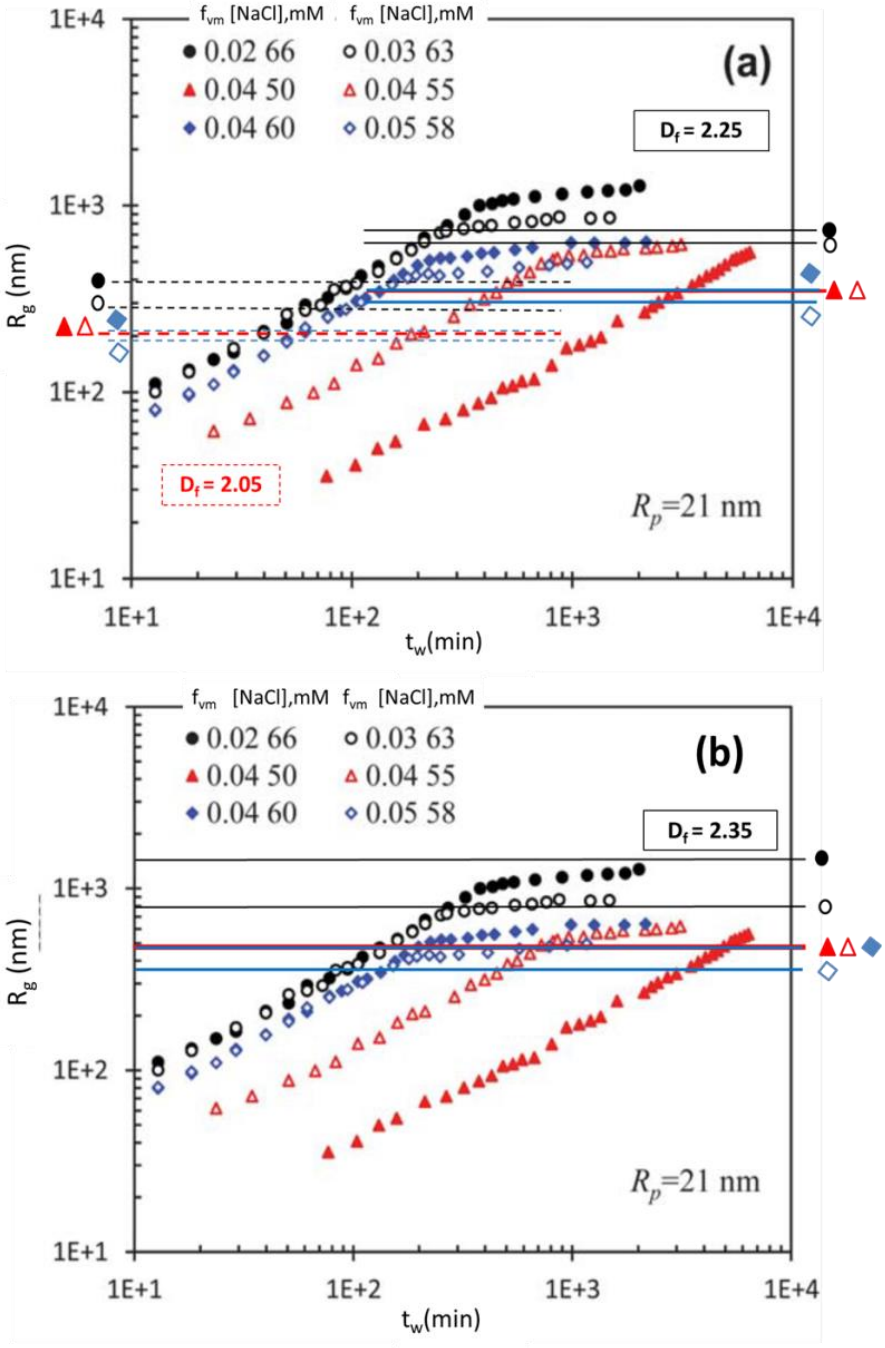

Figure 9.7 A replicate of R_g vs. f_{vm} original graph presented by Wu et al. in Fig. 9.2(a). The horizontal lines are to represent the calculated $R_{g,G}$ values using Eq.(9.1). (a) The solid lines represent the calculated $R_{g,G}$ using D_f = 2.25, and shifted to the right. The dashed lines represent the calculated $R_{g,G}$ with D_f = 2.05 and shifted to the left. (b) The horizontal solid lines represent the calculated $R_{g,G}$ using D_f = 2.35. The lines are color coded and the associated symbols are identified at the edge of the lines if one color represents more than one symbol.

To put the IGP theory in its final test, I constructed Fig. 9.8 that shows $R_{g,G}/a$ vs. f_{vm}. This figure represents combination of my own data and the different experimental data in literature. The solid blue lines are the theoretical $R_{g,G}$ calculated using Eq. (9.1) when D_f used ranges between 1.7 and 1.95. This range of D_f is determined by the lowest and highest D_f values the experimental $R_{g,G}$ data between the blue lines represent. Similarly, the solid red lines are the theoretical $R_{g,G}$ when D_f used ranges between 2.05 and 2.35, which is also determined by the range of D_f the data represent. Figure 9.8 summarizes the success of the IGP theory in finding the $R_{g,G}$.

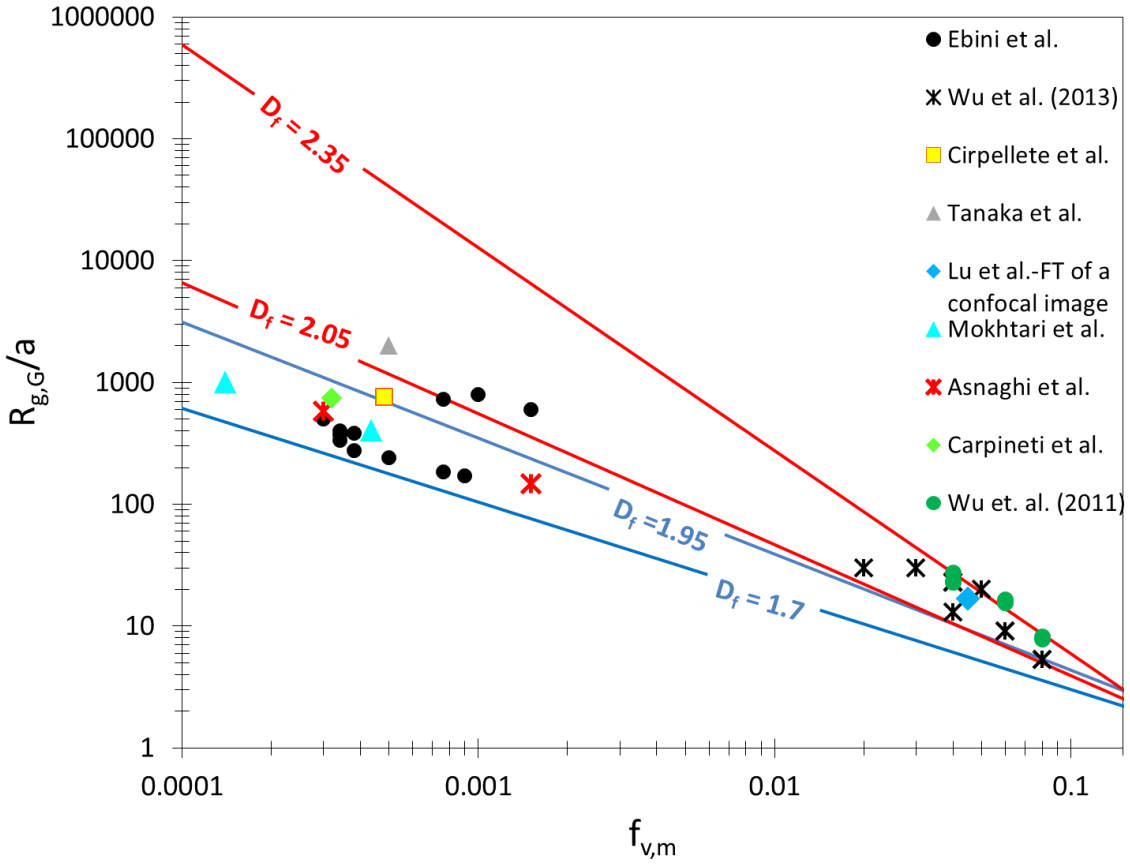

Figure 9.8 $R_{g,G}/a$ vs. f_{vm} for different data in the literature combined with my data. The blue solid lines are the theoretical $R_{g,G}$ calculated using Eq. (9.1) for D_f values ranges between 1.7 and 1.95, which is the range of D_f for the experimental data points between these two lines. Similarly, the red lines are the theoretical $R_{g,G}$ calculated using D_f values between 2.05 and 2.35, which is the range of the experimental D_f values associated with the data points between these two lines. The data in this graph are taken from (Asnaghi, Carpineti, and Giglio 1994a; Carpineti and Giglio 1992; Cipelletti et al. 2000c; Ebini and Sorensen 2019; Lu et al. 2008; Tanaka, Nishikawa, and Koyama 2005; Mokhtari et al. 2008; Wu et al. 2011; Wu, Xie, and Morbidelli 2013).

9.1.2 IGP theory prediction of the gel time

Here I present empirical results from literature regarding the gel time and how it scales with f_{vm}. The results are yet to be further understood. In our work, knowing D_f is essential as well as W. Some experiments provided f_{vm} and W but not D_f, others provided series of data for different f_{vm} but with no D_f nor W measurements.

I will go back to Wu et al. (Wu, Xie, and Morbidelli 2013) data, as they studied scaling of the gelation time. They introduced a dimensionless aggregation time τ, defined as $\tau = K_{fast}\, n_o\, t_w/W$, n_o is the initial number concentration of the monomers. Wu et al. constructed R_g/a vs. τ plots as shown in Fig. 9.9(a) & (b) from the origioanl data they presented in their work and shown in Fig. 9.2.

The slope in these figures implies $R_g/a \sim \tau^{2/3}$. They propose this relation should hold true at the gel points (τ_g, $R_{g,G}$) as well. Note, τ_g, is the dimensionless gel time. Combining this with the scaling $R_{g,G} \sim f_{vm}^{-1/(3-D_f)}$ allows for $\tau_g \sim f_{vm}^{-3/2(3-D_f)}$. Figure 9.10 shows τ_g vs. f_{vm} for all the 21nm and 37.5nm monomers. This results in a slope of -1.6. Comparing the slope of -1.6 with the exponent of -3/2(3-D_f), Wu et al. estimated a D_f = 2.05.

It is important to remind the reader that even though the results in Chapter 7 show a good agreement between the experimental and the theoretical exponents in the t_{gel}-f_{vm} relation; $t_{gel} \sim f_{vm}^{-3/(3-D_f)}$, an exact formalism for t_{gel} is yet to be achieved. In addition, the f_{vm} I used in my work ranges from ~ 1 x 10^{-4} to 2 x 10^{-3} whereas Wu et al. f_{vm} ranges from 0.02 to 0.08.

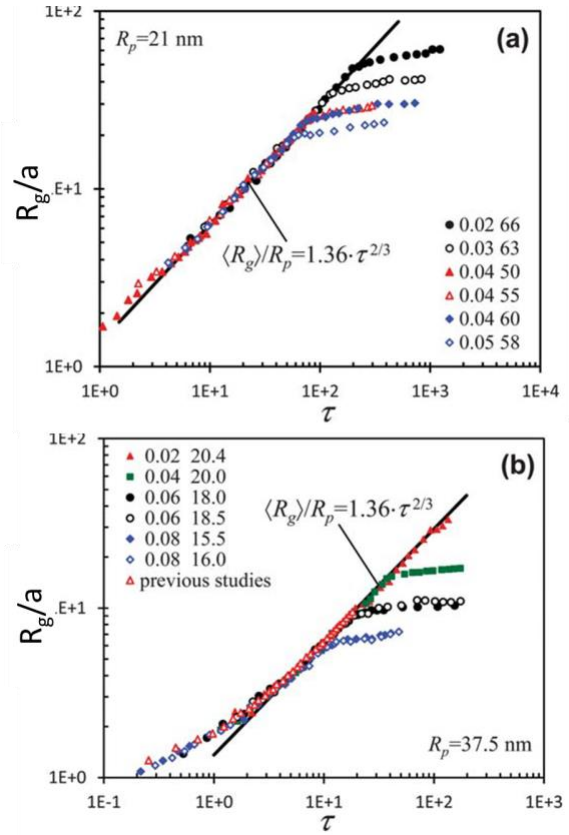

Figure 9.9 R_g/a vs. τ for 21 and 37nm. Graphs taken from Wu et al.(Wu, Xie, and Morbidelli 2013).

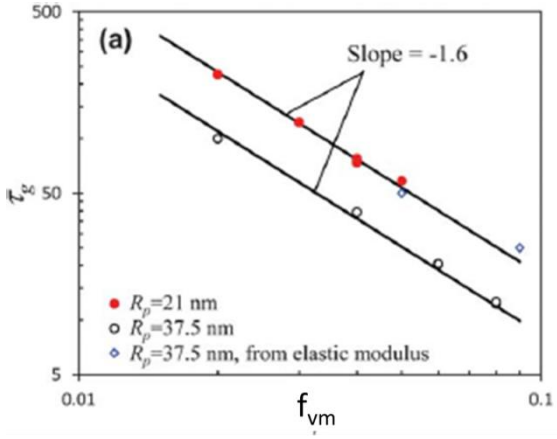

Figure 9.10 τ_g vs. f_{vm}. Graph taken from Wu et al. (Wu, Xie, and Morbidelli 2013).

In Chapter 7, I presented Fig. 7.9 where the gelation coefficient vs. D_f for the experimental data points, the KSU t_{gel} coefficient, and the Bremer t_{gel} coefficient obtained from Eq. (7.7), (7.8), and (7.9), respectively was graphed vs. D_f. Here I present Fig. 9.11 combined the t_{gel} coefficient of my data with Wu's data. The data of Wu et al.was presented twice, once with $D_f = 2.05$ and the second with $D_f = 2.25 \pm 0.1$. The figure shows Wu et al. data works in consistent with my data when $D_f = 2.25 \pm 0.1$ is used.

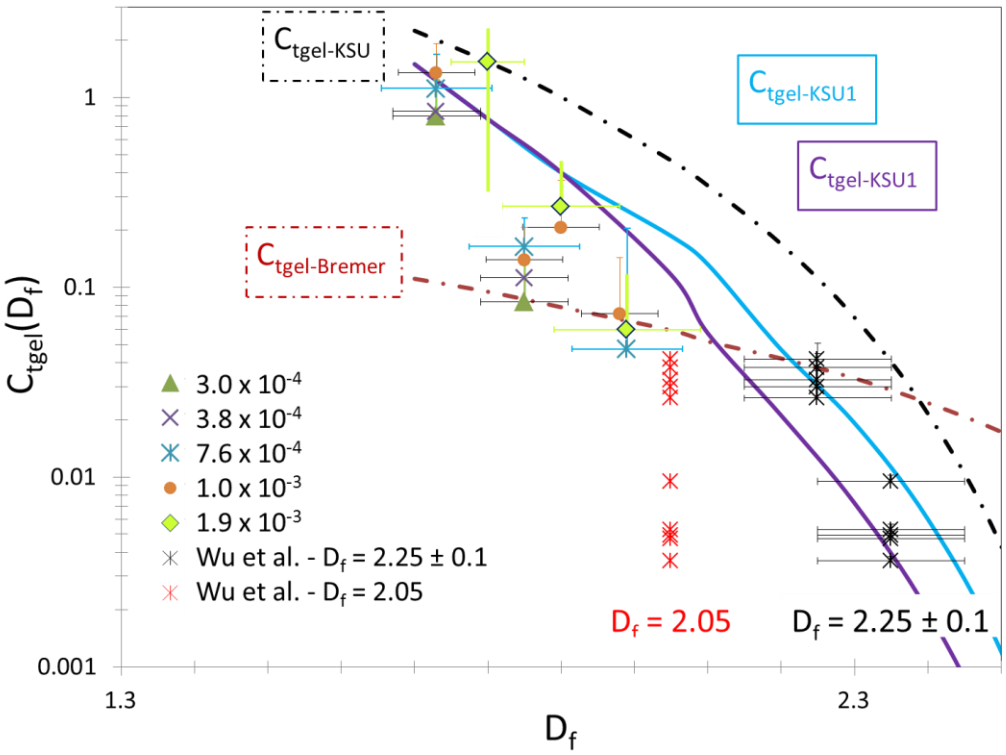

Figure 9.11 The gelation coefficient vs. D_f for the experimental data points, the KSU t_{gel} coefficient, Wu et al. data with $D_f = 2.05$ & 2.25 ± 0.1, and the Bremer t_{gel} coefficient obtained from Eq. (7.7), (7.8), and (7.9), respectively.

Another nice set of t_{gel} data was presented by van der Linden et al.(van der Linden et al. 2015). They investigated the Hofmeister effect in gelation kinetics of colloidal silica using two types of salts; [NaCl] and [KCl].They introduced a hydration potential, V_h, to the general DLVO potential such that: $V_{tot} = V_{vdW}+V_R+V_h$. They found $t_{gel} \sim f_{vm}^{-(3+Df)/3}$. Figure 9.12(a) and (b) show the original graphs provided by the researchers of t_{gel} vs. f_{vm} of Ludox particles. The reported slope of the solid line is -1.7. According to the authors this slope is in a good agreement with the all the data sets. When they compare this slope to the exponent $-(3+D_f)/3$, they estimated $D_f = 2.1$. Linden et al.

did not measure either W or D_f. A quick check of the exponent – $(3+D_f)/3$ with my data shows this exponent fails tremendously. For example, take the experimental exponent of -2.1 obtained in my data for a measured W of 37 ± 4 as shown in Fig. 7.4(a), that corresponds to a measured D_f of 1.73 ± 0.05. Apply the van der Linden et al. proposed exponent to the experimentally obtained -2.1 will give a D_f = 3.3, much greater than the measured 1.73.

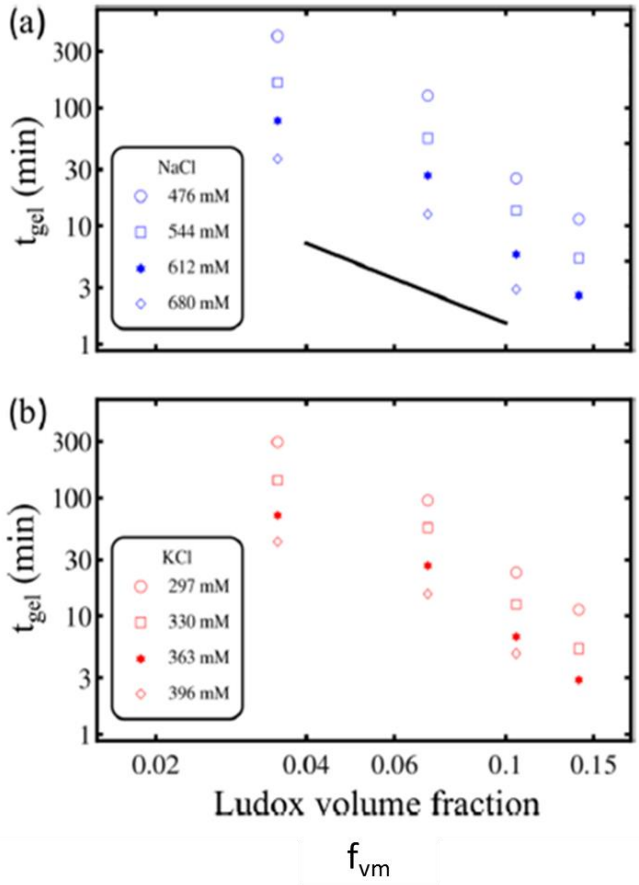

Figure 9.12 t_{gel} vs f_{vm} for Ludox particles. These graphs are taken form van der Linden et al. (van der Linden et al. 2015).

Another example of t_{gel} data that provide no D_f measurements and no W measurements are the data presented by Zhang et al. (Zhang et al. 2016).The authors studied the influence of changing the counter ions on colloidal gels. They concluded that changing the counter ions changes the kinetics of the gel but not the final structure of the gel. I think this statement should be constraint to be true only if the stability ratio was kept constant. The authors did not explicitly mention this constraint. Regardless, they present nice data of the gel time, t_{gel}, defined as the time at which the

sample supports its own weight after being turned upside down. Figure 9.13 presents their original graph, but I relabeled the axis. Notice in the x-axis they have the % f_{vm} and not the f_{vm}. These authors followed the steps of van der Linden et al. and claim a slope of -1.7 to fit all the data provided in the figure and estimated D_f to be 2.1. They further supported their conclusion with Wu et al. of -1.6 slope shown in Fig. 9.10, between τ_g vs. f_{vm}. Zhang et al. wrongly mix between t_{gel} and τ_g. And that τ_g is a function of f_{vm}. Using the definition of $f_{vm} = (4\pi/3)n_o a^3$ one can rewrite $\tau = K_{fast}\, f_{vm}\, t_w/(4\pi/3)Wa^3$.

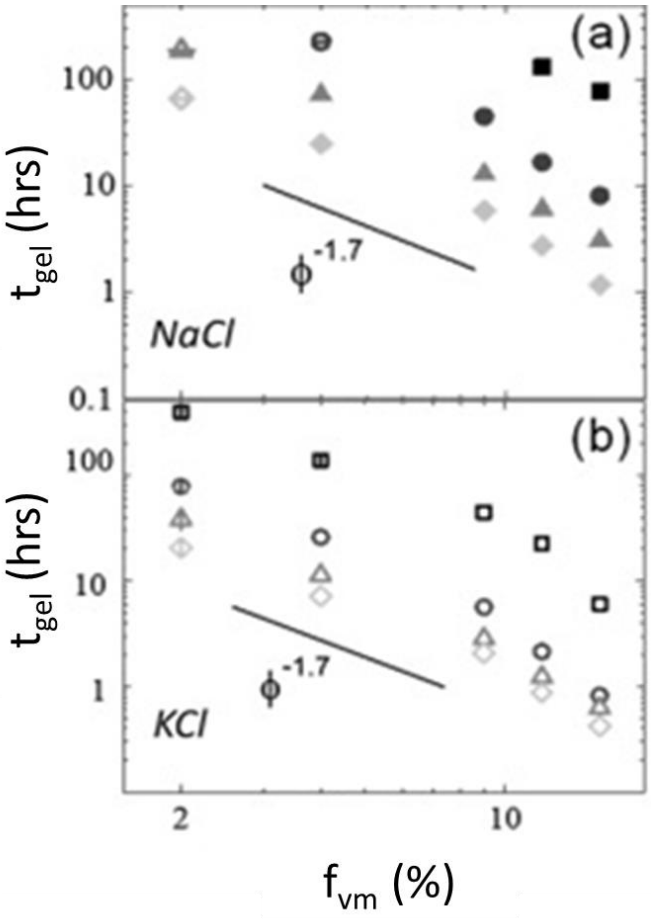

Figure 9.13 t_{gel} vs. % f_{vm} . These graphs are taken from Zhang et al.(Zhang et al. 2016).

Both van der Linden et al. and Zhang et al. provided nice sets of data of t_{gel} vs. f_{vm}. Both groups used monovalent salts NaCl and KCl to destabilize the particles. Both claimed a slope of -1.7 fits all of their data. I disagree with both. Figure 9.14 (a) & (b) shows a replicate of van der Linden et

al. data, and (c) & (d) is a replicate of Zhang et al. data, with a best line fit for each set of data. It is clear best fit is not -1.7.

van der Linden et al. used a maximum of the salt concentration of only 1.4 the minimum. Whereas Zhang et al. used a maximum salt concentration of 5 times the smallest. For monovalent salt it is reasonable to assume that the required difference in salt concentrations to yield a significant difference in W is higher than what is required for higher-valent salt.

For van der Linden data the narrow range of using monovalent salt concentrations worked to my advantage of reasonably assuming that each set of data is already within a close proximity of D_f values. Another assumption I can make, justified by our results, that if t_{gel} vs. f_{vm} can fit on a straight line, this indicates that the data for different values of f_{vm} have similar W, hence similar D_f. As an example, let's remember Wu et al. t_{gel} vs. f_{vm} data shown in Fig. 9.5(a), the data were all over the place. In constrast, when I replot this data but this time normalize tgel to W and monomer volume, in other words plot t_{gel}/a^3W vs. f_{vm}, as shown in Fig. 9.5(b), the data collapses into a straight line. This is why, with caution, I will assume for Zhang et al. that each set of data has almost the same D_f. This overcomes the lack of not knowing W nor D_f for these data.

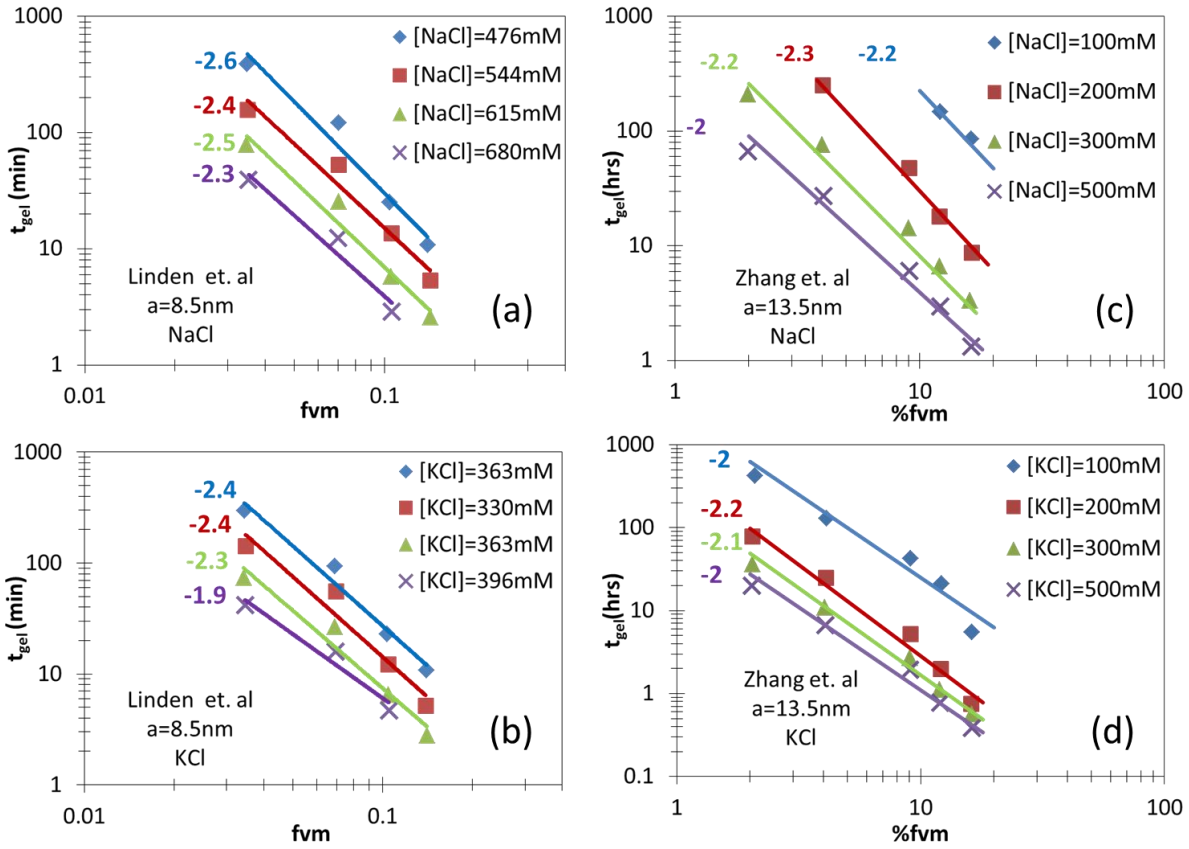

Figure 9.14 t_{gel} vs. f_{vm} for (a) and (b), tgel vs. % fvm for (c) and (d). This data is a duplicate of the original data in Fig. 9.11 and 9.12 with adding the best line fit for each set of data.

Now we combine all the data for t_{gel} vs. f_{vm} we discussed above with my data. This is shown in Fig. 9.15. Each data set represents a strong linear behaviour on a log-log scale to indicate that the assumptions we made for Linden's and Zhang's data were reasonable, and that a power law dependence of t_{gel} vs. f_{vm} exists. I like to bring the readers' attention to the great correspondence between the unfilled dark-red diamond points with the filled bright-red circle at the low f_{vm} in the graph. The red diamonds are data obtained by Lattuda et al. (Lattuada et al. 2004) who worked on 35nm particles and they indicate their W = 1-2. The red circle is one of my data, and I measured W ~2. The only data that does not exibit a straight line in this graph is the data of Wu et al. (yellow diamonds). But we have seen in Fig. 9.5 that when we normalize t_{gel} to a^3W and graph it vs. f_{vm} a linear behaviour is obtained.

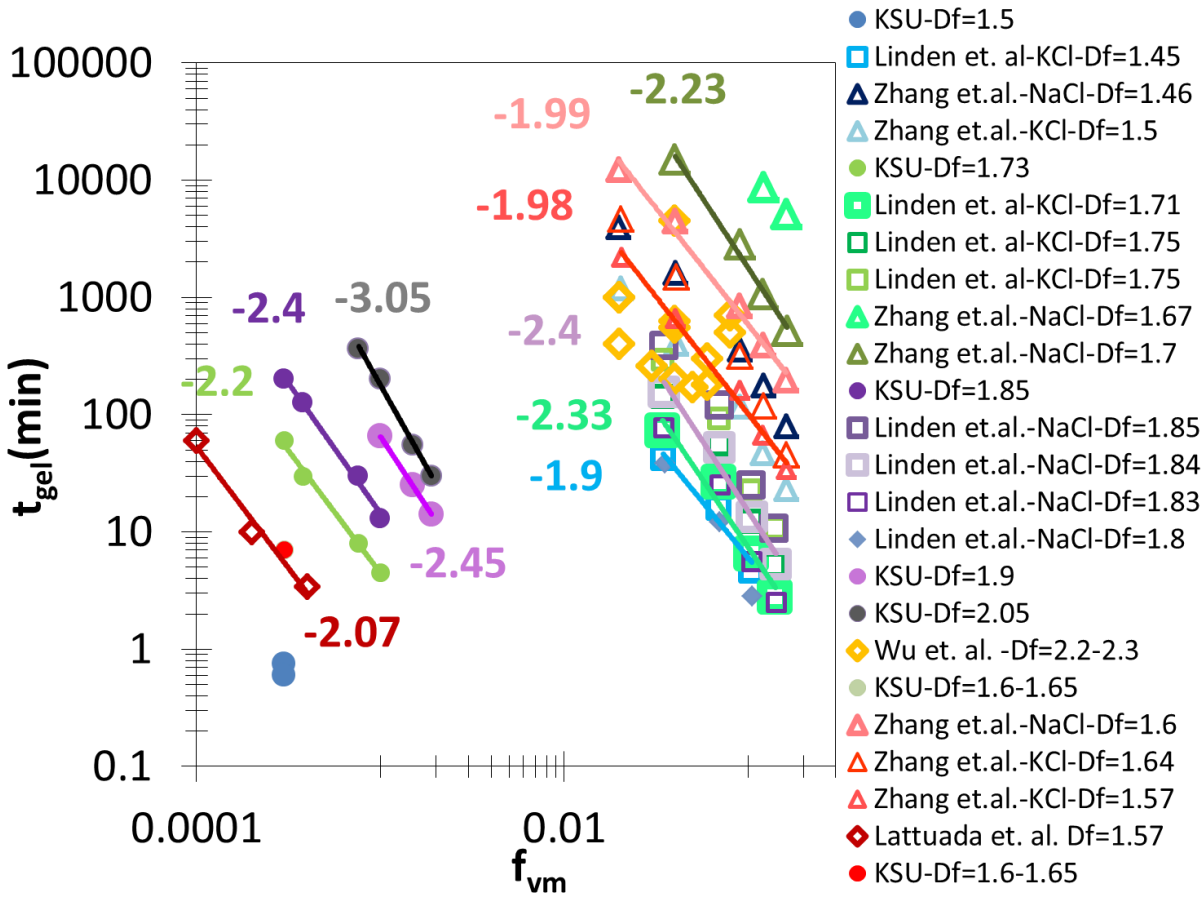

Figure 9.15 t_{gel} vs. f_{vm} for different groups combined as discussed in the text. These data are gathered from: our work, Wu et al. (Wu, Xie, and Morbidelli 2013), Lattuada et al. (Lattuada et al. 2004), vad der Linden et al. (van der Linden et al. 2015), and Zhang et al. (Zhang et al. 2016).

I aim to create a graph that unites all these data. Graphing t_{gel}/a^3W vs. f_{vm} make sense because these samples are of different monomers sizes and different W. We learnt in Chapter 7 that for each W group will yield a certain exponent that reasonably represents D_f for the system. Working in reverse, I grouped different sets of data in Fig. 9.14 that have the same exponent together. Same exponent means similar W and D_f. For example the data that have exponent between 1.95 to 2.15 I grouped them together.

To obtain t_{gel}/a^3W vs. f_{vm} graph I need to know W, which is not provided for all the data. However, one might come to the realization that the W value is simply a scaling factor that will connect all the data of the same exponent in a linear fashion keeping the exponent, or the slope, the same. Figure 9.16 shows many plots. Each plot is a result of grouping the data with the same exponent in Fig. 9.15. Then divide by the monomer volume presented by a^3, and a constant so we can rescale the data in a linear fashion, maintaining their exponent. This constant I name it W*, because it is not the stability ratio, W, but it is related to W.

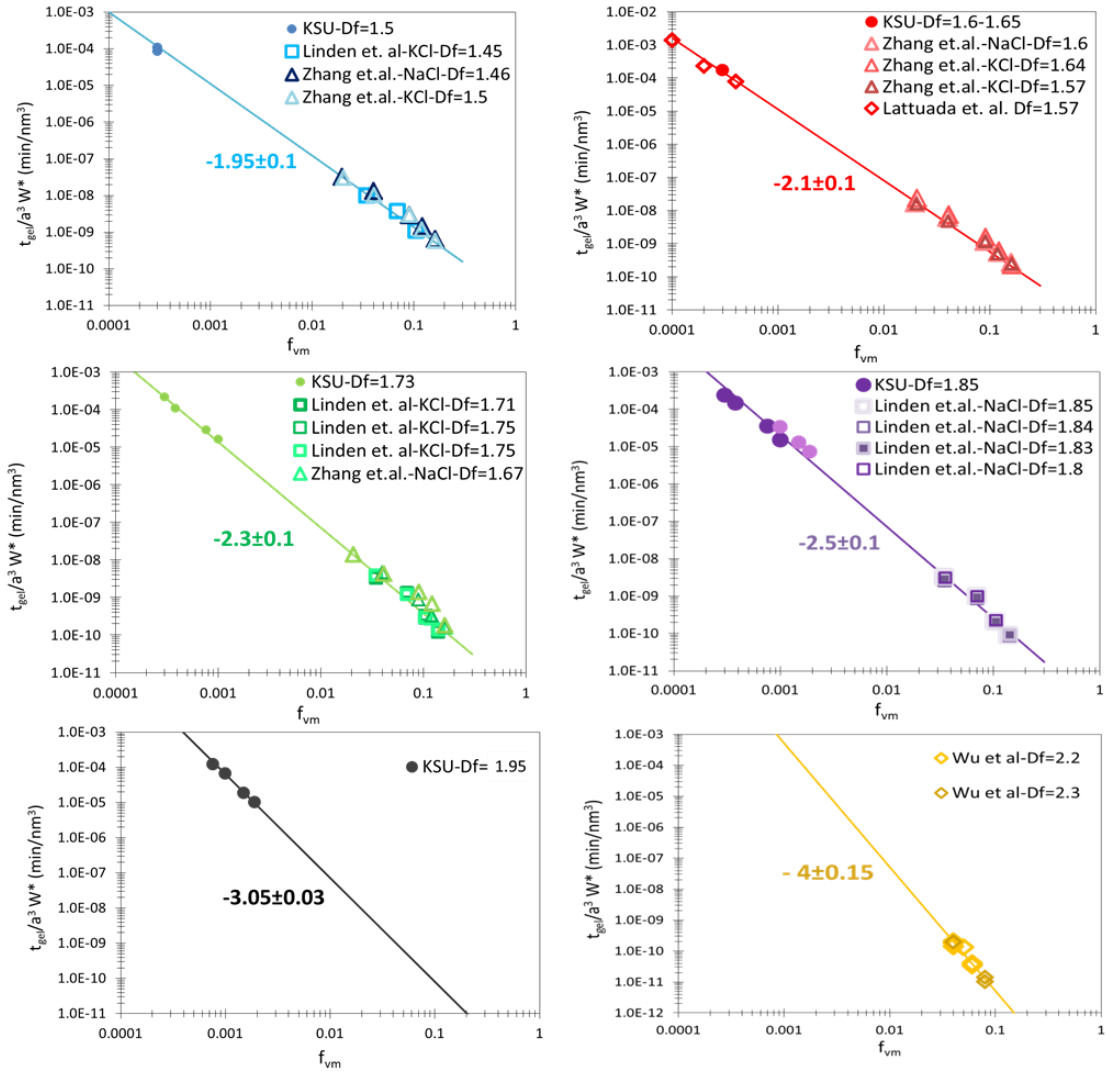

Figure 9.16 t_{gel}/a^3W^* vs. f_{vm}. These data are taken from Fig. 9.14 with the grouping procedure discussed in the text. Please note W* is not the stability ratio W.

Combining the different groups of data represented in Fig. 9.15 (a) - (d) results in Fig. 9.16. Interestingly, this figure show the data are crossing at f_{vm} ~ 0.007 - 0.01. The meaning of this corssing is yet to be determined.

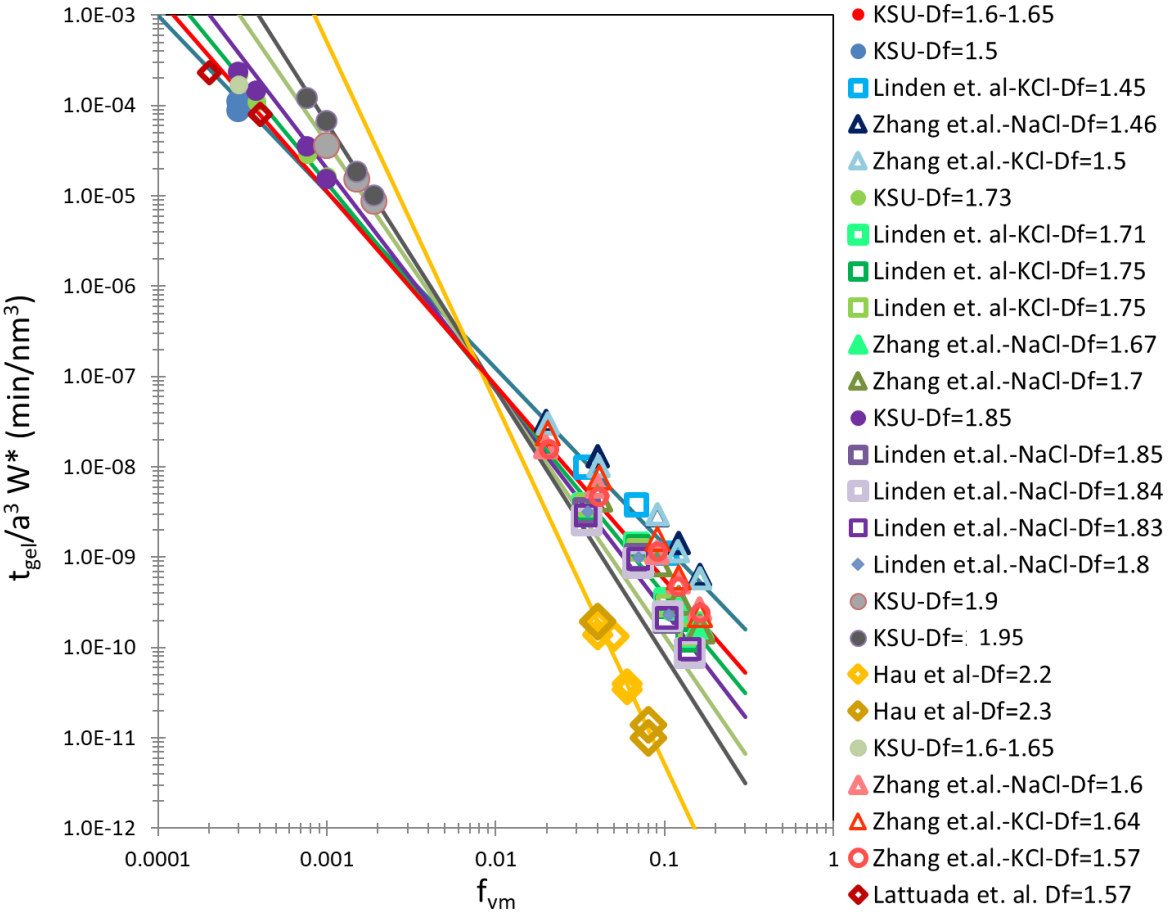

Figure 9.17 t_{gel}/a^3W^* vs. f_{vm} for all the data presented in Fig. 9.15(a) – (d).

Another way to represent the data is by graphing t_{gel}/a^3W vs. $f_{vm}^{-3/(3-Df)}$. The theory predicts a slope of value 1. This is shown if Fig. 9.18, with an average slope of all the runs of 0.98 ± 0.02. The D_f values were obtained from the exponents in Fig. 9.16 for each group.

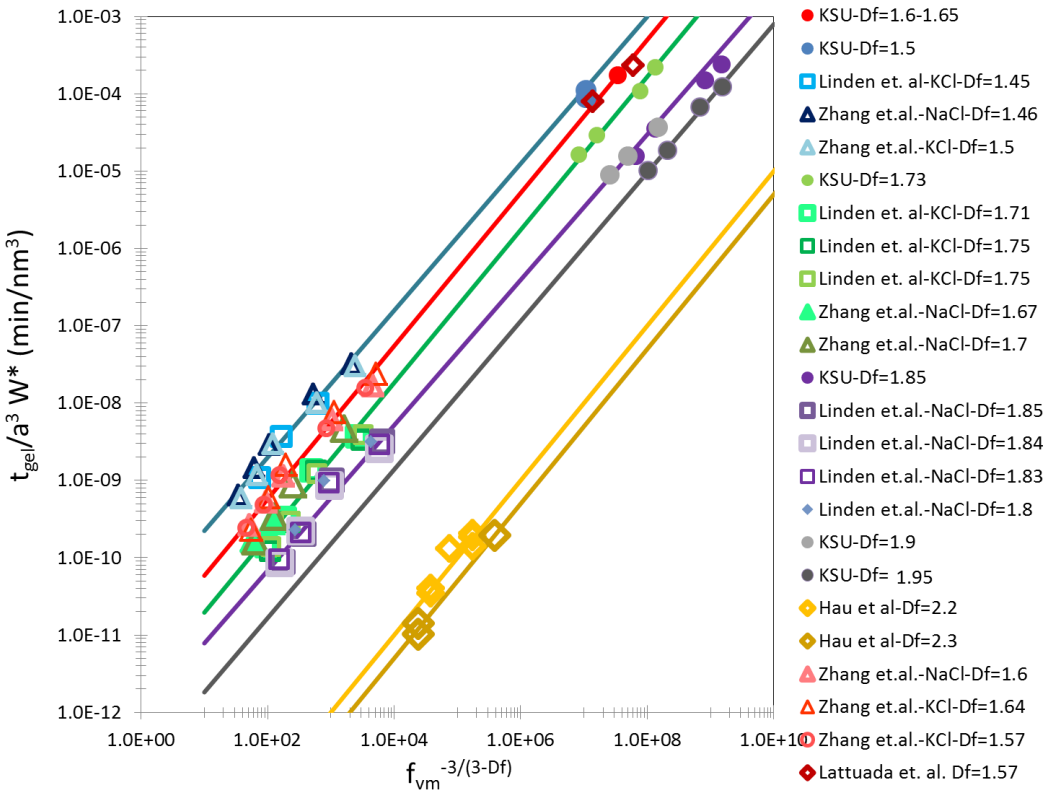

Figure 9.18 t_{gel}/a^3W^* vs. $f_{vm}^{-3/(3-Df)}$ for all the data presented in Fig. 9.16.

9.2 Unified picture of the sol-to–gel transition: what does the IGP offer?

In this section, I will gather the knowledge I gained in my dissertational work, and from our group, to come up with explanations of the observations and predictions that made the success of phase separation and percolation descriptions of gelation from the perspective of IGP theory, which is a kinetic theory. I hope to convince the reader that gelation is a kinetic process, and that the IGP theory can account for all the other observations and predictions made by the other descriptions.

In Chapter 3 we saw the close resemblance of the structure factor for light scattering observations done on binary liquids going through spinodal decomposition (SD) with the structure factor for fractal aggregate suspensions. The first similarity is the existence of a peak at a finite q value in the structure factor that increases with time. This q value at the peak (or max) is defined as q_m. The q_m position shifted to smaller q values with time as shown in Fig. 3.16. The second similarity

is the scaling behavior of the optical structure factor exhibits with q/q_m if plot according to Eq. 3.32 that takes the form (Bates and Wiltzius, 1989; Carpineti and Giglio, 1992)

$$S(q/q_m, t) = q_m^{-d}(t)\, F(q/q_m) \tag{9.2}$$

where $F(q/q_m)$ is a time independent scaling function and d is a scaling exponent which for fluid systems is the spatial dimension, d = 3. By replacing d with D_f in Eq. (9.2), the scaling behavior was achieved for colloidal aggregates at later stages of aggregation but not at the early stages as shown in Fig. 3.15(a) & (b) respectively. The scaling behavior in the structure factor during late stages of colloidal aggregation led to the conclusion that particulate gelation is a phase separation (Carpineti and Giglio 1992; Lu et al. 2008).

It is known that when a fluid is quenched inside the coexistence line to a two-phase state from an initially thermodynamic stable, one-phase state, it undergoes phase separation and eventually separates into two phases. This separation shows an increasing peak in the structure factor and a shift of the peak position to smaller q_m values. On the other hand, if we consider light of wavelength λ scatters from particles of radius, a, the structure factor will show the Guinier regime at a q value of ~ a^{-1}. If the sample is replaced by bigger particles, the structure factor will increase and the Guinier regime will shift to smaller q. For an aggregating system, the starting point is the monomer radius, a, that is usually < λ. With time, these monomers will form k-mers and their size will grow showing not only an increase in the structure factor but also a Guinier regime shift toward smaller and smaller q values. If the aggregates are in the cluster-dense regime, i.e. $R_{nn} \leq 10R_g$, a peak on the structure factor will appear at q_m. The peak is due to the anticorrelation in a dense system. The anticorrelation function may occur to any dense system regardless if it is binary liquid going through SD or colloidal aggregates (Oh, and Sorensen 1998). It has been shown (Cerdà et al. 2004; Huang, Oh, and Sorensen 1998) that Eq. (9.2) is a specific case of a more general situation.

Any two-phase system, such as an aggregating particulate system or an un-mixing binary liquid, will have two length scales, one for each component. Thus, for an aggregating system of particles there will be the mean cluster size, R_g, and the mean nearest neighbor distance R_{nn}. The structure factor will reflect these two lengths in q-space with a peak, perhaps broad, between these two lengths, inverted into q-space. If the clusters are compact with D_f = d, like the case of an un-mixing binary liquid, these two length scales are proportional ($R_g \sim R_{nn} \sim N^{1/d}$) and structure factor scaling will occur early on in the phase separation process because there is only one length scale. On the

other hand, if the clusters are fractals and $D_f < d$, these two lengths are independent ($R_g \sim N^{1/Df}$ and $R_{nn} \sim N^{1/d}$) and the average cluster size grows faster than the average cluster–cluster separation with aggregation. Hence, the structure factor cannot be scaled early in the aggregation when the system is cluster-dilute, i.e. when $R_{nn} >> R_g$. This is consistent with observations by Carpineti at early stages of aggregation. On the other hand, an apparent scaling peak will occur in the cluster-dense regime when $R_{nn} \sim R_g$ for non-compact clusters as an artifact to yield a structure factor equivalent to Eq. (9.2). This is observed in late stages of aggregation when the system is cluster-dense.

To emphasize the importance of the two length scales, R_g and R_{nn}, for the system of fractal clusters, and how the scaling as described in Eq. (9.2) is an artifact of R_{nn} approaching R_g at late stages of aggregation (Cerdà et al. 2004; Huang, Oh, and Sorensen 1998), we present the initial data of I(q) vs. q for different waiting times as shown in Fig. 9.19(a), which is then graphed according to Eq. (9.2), replacing d with D_f as shown in Fig. 9.19(b). It is clear, no scaling occurs early in the aggregation process all the way up to 109min. It is only at t_w = 200min scaling starts to work (scaling possibly occurred earlier than 200min but difiantly later than 109min). This is consistent with Carpineti's observation that scaling occurs only at late stages of aggregation. Note that the 200min and 420min are similar pair of data, as well as 1488min and 5905min is another similar pair. The system might be near saturation. Nevertheless, Fig. 9.19(b) shows scaling is taking place between these two pairs. It worth noting for this system the IGP occurs at $t_w = t_{gel} \sim$ 200min as shown in the insert of I(0) vs. t_w and R_g vs. t_w in Fig. 9.19(b) as a vertical dotted line.

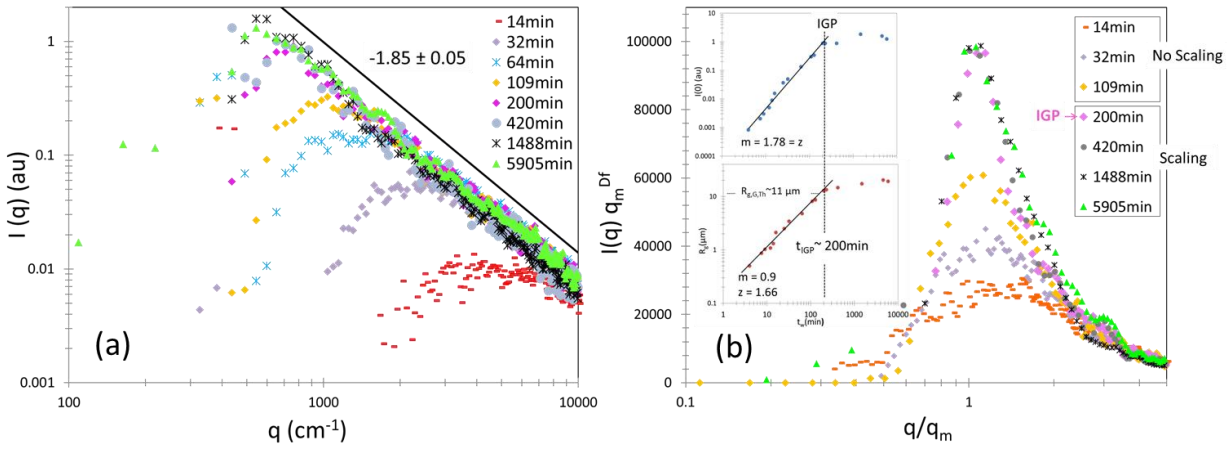

Figure 9.19 (a) I(q) vs. q with $D_f = 1.85 \pm 0.05$ and (b) $I(q)q_m^{Df}$ vs. q/q_m. The inserts in (b) are I(0) & R_g vs. t_w. Both inserts show the IGP ~ 200min. The slope in I(0) vs. t_w graph represents the kinetic exponent z = 1.78. The slope in R_g vs. t_w graph represents $z/D_f = 0.9$ which yields z = 1.66.

Lets' go back to our simple picture of why a system gels. In Chapter 3 we discussed how $R_{nn} \sim N^{1/d}$ and $R_g \sim N^{1/Df}$. For fractal aggregates, $D_f < d$, then R_g will grow with N faster than R_{nn}. A schematic diagram for this picture was shown in Fig. 3.3. The point at which $2R_g$ and R_{nn} cross defines the IGP.

From the experimentally measured R_g for each t_w, I calcuated the average number of monomers per cluster size using $N = k_o\,(R_g/a)^{D_f}$, and the R_{nn} using $R_{nn} = (N_m/(N.V_{sys}))^{-1/d}$. N vs. t_w is shown in the insert of Fig. 9.20. At the IGP, $t_{gel} \sim 200$min, the average number of monomers in the aggregate is N_{IGP} =100,000. Figure 9.20 shows R_g, $2.3R_g$, and R_{nn} vs. N. The slope of R_g vs. N indicates $R_g \sim N^{0.55}$,which gives a fractal dimension of D_f =1.82. This D_f value is consistent with the measured D_f value from the structur factor, $D_f = 1.85 \pm 0.05$ as shown in Fig. 9.19(a). In addition, R_{nn} vs. N shows $R_{nn} \sim N^{0.33}$, which exactly a d = 3. On top of that, R_{nn} and $2.3R_g$ are equal, where their corrosponding lines cross, at N value of 100,000 which is the N_{IGP}. This figure summarizes the importance of having two length scales, each with different dpendence on N, such that the sysetm will eventually gel. In contrast, for a non fractal aggregate, like water droplet in a cloud, both R_g and $R_{nn} \sim N^{1/d}$. For the water droplet aggregates, the green and red lines in Fig. 9.20 will never meet, hence the system will never gel. For this particluar system, scaling will occur at early stages because the system has the length scales $R_g \sim R_{nn}, \sim N^{1/d}$.

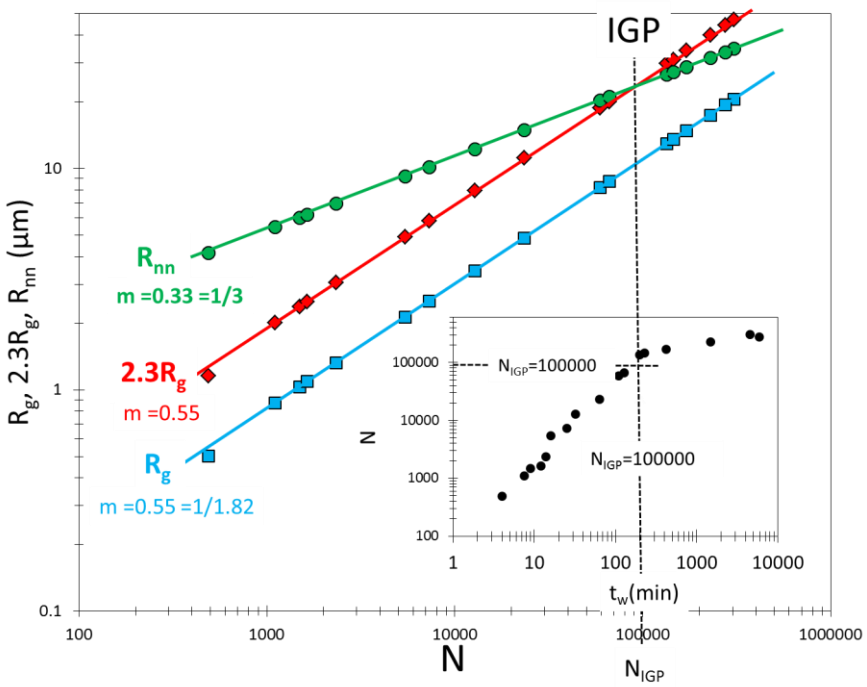

Figure 9.20 R_g, $2.3R_g$, and R_{nn} vs. N. The insert is N vs. t_w. The insert shows that N_{IGP} =100,000. R_{nn} crosses with $2.3R_g$ at N =N_{IGP} =100,000 represented by the vertical dotted line.

To put Fig. 9.19(b) and 9.20 in respect with the initial SASLS data, I present Fig. 9.21. This is a complex figure, but will present our argument of the artifact in SASLS that leads to what appears as scaling in a new perspective. We start with replicating Fig. 9.19(a), where it represents I(q) vs. q for different waiting times, except for t_w = 420min and 1488min. Additionally, it shows color coded points with I(q) vs. q for each t_w. These points represent the following: the big squares are ($R_g^{-1}, I(0)$), the big diamonds are ($(2.3R_g)^{-1}, I(0)$), and the big circles are ($R_{nn}^{-1}, I(0)$), for each t_w. I(0) is the intensity at small q values before the dip occurs.

Recall that the I(q) vs. q, shows a Rayleigh regime at small q values, the power law regime at big q values, and a Guinier regime in the transition between Rayleigh to power law regimes. Figure 9.19(a) gives a D_f = 1.85 ± 0.05 and the Guinier analysis for each t_w gives the temporal evolution of R_g. Our data shows a dip in the very small q values in Rayleigh regime. The dip occurs due to cluster-cluster anticorrelation function which occurs when the system is in the cluster-dense regime, i.e. $R_{nn} \leq 10R_g$ (Oh and Sorensen 1999). Originally, if clusters are in the cluster-dilute regime, the dip will not occur and an undisturbed Rayleigh regime will appear.

Figure 9.21 shows at t_w = 14min, there exists a dip, to indicate the clusters are in the cluster-dense regime. In Chapter 6 all the SASLS were detected in the cluster-dense regime, with the kinetic exponent, z > 1. As a quick check, the z value obtained from I(0) vs. t_w and R_g vs. t_w, as shown in the inserts of Fig. 9.19(b), are 1.78 and 1.66, respectively. This further confirms the clusters are in the dense regime. Despite the system is in the cluster-dense regime, t_w = 14 min still can show some of the Rayleigh regime, between 3000cm^{-1} ≤ q ≤ 7000 cm^{-1}. A portion of Rayleigh regime continues up to t_w = 109min. The appearance of some of the Rayleigh regimes indicates there are two different length scales that are distinguishable for the SASLS, R_g & R_{nn}. In contrast, at the IGP, $t_w = t_{gel}$ ~ 200min, the Rayleigh regime has completely disappeared due to inability to distinguish between R_{nn} and R_g at such close proximity. This is why the apparatus starts to see one length scale, probably a combination of R_g and R_{nn}. It is this inability to distinguish R_g from R_{nn} creates the artifact that leads to scaling.

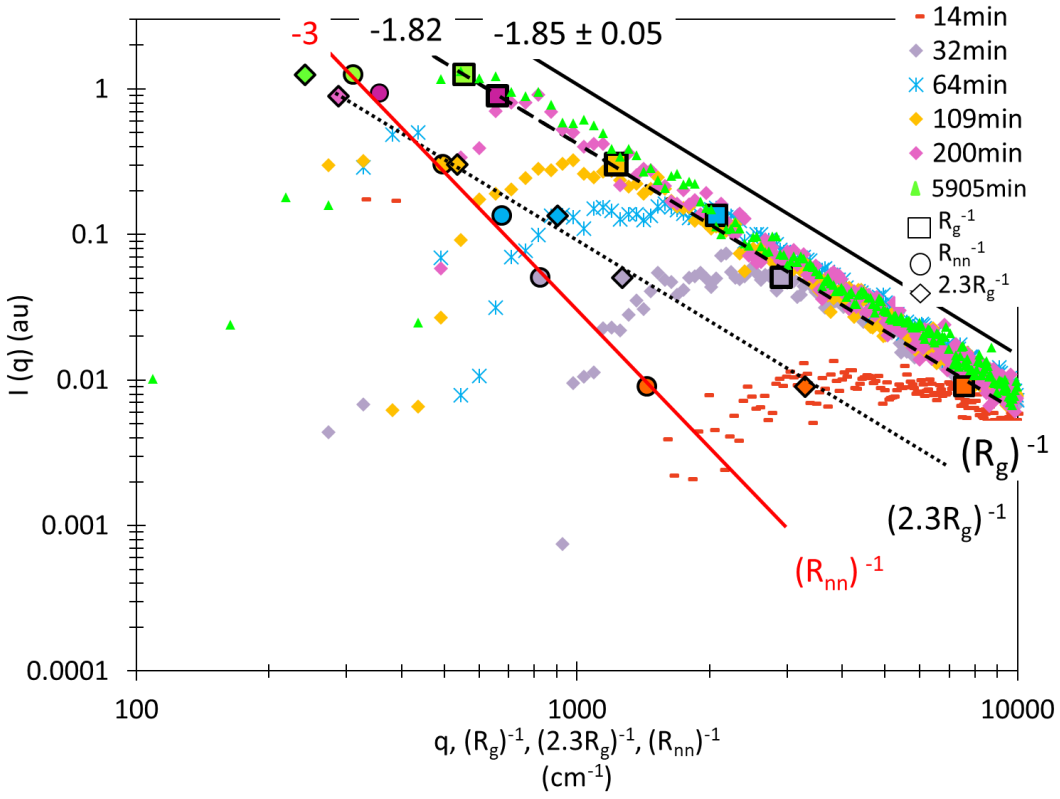

Figure 9.21 This figure shows four graphs: (1) The temporal evolution of I(q) vs. q for gelling experiment. The solid black line represents the power law regime with D_f = 1.85 ± 0.05. (2) ($R_g^{-1}, I(0)$). (3) ($(2.3R_g)^{-1}, I(0)$). Both the black dashed & dotted black lines represents a slope of -1.82. (4) ($R_{nn}^{-1}, I(0)$), the solid red line gives a slope of -3.

As mentioned earlier, the solid black line represents the slope of the usual power law regime for I(q) vs. q with a $D_f = 1.85 \pm 0.05$. The black dashed line fits $((R_g)^{-1}, I(0))$ data points, and the slope of this line represents the exponent of I(0) scaling with $(R_g)^{-1}$. $I(0) \sim N \sim R_g^{Df}$, hence, $I(0) \sim ((Rg)^{-1})^{-Df}$. The slope of the dashed black line gives a value of $D_f = 1.82$, consistent with what is measured from the power law regime of $D_f = 1.85 \pm 0.05$. The dotted black line is nothing but a shift of the dashed black line to fit the $((2.3R_g)^{-1}, I(0))$ data points. The solid red line fits $((R_{nn})^{-1}, I(0))$ data points, and the slope of this line represents the exponent of I(0) scales with $(R_{nn})^{-1}$. $I(0) \sim N \sim (R_{nn})^d$, hence, $I(0) \sim ((R_{nn})^{-1})^{-d}$. The slope for the red solid line is $-3 = d$ as predicted. Again, the dashed line and the solid red line cross at t_w close to 200min, consistent of the $t_{gel} \sim 200$min we found earlier.

The thermodynamic description of gelation was strongly supported by Lu et al. who studied a dense colloidal system of particles made attractive via a polymer depletion interaction (Lu et al. 2008). The polymer concentration controlled the inter-particle interaction potential range and strength, U, relative to the thermal energy, U/kT. This ratio, which is thermodynamic in nature, determined when the gelation was initiated, after which an evolving spinodal-decomposition-like peak in the structure factor appeared. Lu et al. concluded that gelation of spherical particles with isotropic, short-range attractions is initiated by a thermodynamic instability that triggers gel formation via spinodal decomposition. These observations can be easily explained by the high initial volume fraction of monomers used in the experiment. The aggregating sol finds the cluster-dense and subsequent gel regimes very soon after destabilization, the thermodynamic instability. Due to the high monomer volume fraction, there is no time to see the two aggregation growth regimes clearly visible like the case of our diluter system; their system simply appears to gel immediately after when the depletion interaction is strengthened. In fact, for any sol, all the thermodynamics really does is initiate the aggregation, after that the whole evolution is kinetic. In light of their work we would conclude that thermodynamics triggers gel formation and gelation boundaries are thermodynamic, but the sol-to-gel mechanism is kinetic.

A more recent theoretical approach to the sol-to-gel transition was achieved with the connection to statistical thermodynamic for irreversible binary aggregates (Matsoukas 2015; 2014). Initially, in a system of N_c clusters there exists a single mode size distribution. With time, the average number of N_c clusters is reduced with increasing in their size. Up to a point, where a second moment of size distribution starts to appear. This bimodal size distribution form due to the creation

of a giant cluster, i.e. the system starts gelling. Interestingly, similar observation was obtained via a recent simulation work done by Liu et al. (P. Liu et al. 2019) on colloidal aggregates in the DLCA regime using the kinetic description. The simulation showed the existence of one size distribution for the clusters in the system, but at later stages of aggregation a bimodal distribution starts to appear after the IGP is reached. This bimodal distribution is justified by the creating of the giant cluster that fills the entire system volume. Hence, the gel began to form. This picture, which is purely kinetics, produced the same results as the statistical approach.

The percolation theory is another description of the sol-to-gel transition. The evolution of sol to gel is modeled by adding sites or bonds at random to a volume until the connectivity percolates, i.e. a volume spanning cluster appears with a fractal dimension of $D_f = 2.5$ (D. Stauffer 1976; Dietrich Stauffer, Coniglio, and Adam 1982; De Gennes 1976). This implies that the structure of a gel is that of a percolation aggregate with $D_f = 2.5$, not that of, for example, a diffusion limited cluster-cluster aggregation (DLCA) aggregate formed kinetically with $D_f = 1.8$. The question is how can the kinetic model, which successfully describes the sol's approach to the gel, yield percolated aggregates which successfully span the system volume and have a $D_f = 2.5$ near the gel point? Our group worked with soot aerosols and colloidal aggregates that extended the viability of the kinetic description of the sol-gel transition (C. Sorensen and Chakrabarti 2011; R. Dhaubhadel et al. 2006; Fry et al. 2002; Wongyo Kim et al. 2006; Mokhtari et al. 2008; Christopher M. Sorensen et al. 2003).

Experiments involving both light scattering and electron microscope studies of soot aerosol aggregates at late stages of aggregation explicitly demonstrated superaggregates with a fractal dimension of $D_f = 2.5$ (R. Dhaubhadel et al. 2006; W. Kim, Sorensen, and Chakrabarti 2004; Christopher M. Sorensen et al. 2003). Similar results was obtained on a sheared colloidal aggregates, showing a superaggregates morphology beyond the IGP (Mokhtari et al. 2008). Aerosol aggregation and colloidal aggregation showed the same fractal dimension for a percolated gel. The term "superaggregate" was introduced because superaggregates are hybrids composed of smaller aggregates with a fractal dimension of $D_f = 1.8$. Thus the aggregates have a different morphology than the entire gel. Parallel to the experimental work, simulation work (Fry et al. 2004) supported these results and concluded that superaggregates form via DLCA will pass from aggregate dilute regime (when $R_{nn} >> R_g$), where the $D_f = 1.8$ are formed, to the aggregate dense

regime ($R_{nn} \leq 10R_g$) leading to gelation. At a special point where volume fraction of the DLCA aggregates is unity, the system is at the ideal gel point (IGP).

Additionally, earlier studies by Martin and Adolf (J E Martin and Adolf 1991; James E. Martin and Wilcoxon 1989) indicated that the kinetic and percolation approaches can merge at the "critical growth stage" that occurs late in the aggregation process where the aggregate volume fraction approaches unity. There the aggregates become a "huge monomer" with radius at the IGP of $R_{g,G}$ that percolate to form a gel of $D_f = 2.5$. The equivalent fractal dimension of $D_f = 2.5$ for both the static percolation aggregate and the kinetically grown superaggregate is very suggestive of structural equivalence. Furthermore, comprehensive simulations work by Heinson et al. showed that there exist three parameters that completely specify the structure of a gel. One is the fractal dimension, second is the prefactor that appears in the mass-radius scaling k_o, and the third one is the monomer packing fraction within the aggregate (W. R. Heinson, Sorensen, and Chakrabarti 2012). It was shown that the canonical DLCA yields superaggregates with fractal dimension, prefactor and monomer packing fraction identical to the static bond percolation aggregates (W. R. Heinson, Chakrabarti, and Sorensen 2017). Furthermore, recent simulations from our lab have demonstrated that aggregation kinetics leads to a separate phase of superaggregates with structure isomorphic with percolation clusters (W. R. Heinson, Chakrabarti, and Sorensen 2017; P. Liu et al. 2019). Hence in a gelling sol, percolation is a consequence of aggregation kinetics.

In conclusion, a complete description of gelation should incorporate any description presented for modelling the gel. The relatively new IGP theory, which is a kinetic theory, provides the insights to unify the three different descriptions. Hence, the sol-to-gel transition is, indeed, a kinetic process.

References

Asakura, Sho, and Fumio Oosawa. 1958. “Interaction between Particles Suspended in Solutions of Macromolecules.” *Journal of Polymer Science* 33 (126): 183–192.

Asnaghi, D., M. Carpineti, and M. Giglio. 1994a. “Recent Developments in Aggregation Kinetics.” *MRS Bulletin* 19 (5): 14–18.

Asnaghi, D., Marina Carpineti, and Marzio Giglio. 1994b. “Recent Developments in Aggregation Kinetics” 19 (5): 14–18.

Ball, R. C., D. A. Weitz, T. A. Witten, and F. Leyvraz. 1987. “Universal Kinetics in Reaction-Limited Aggregation.” *Physical Review Letters* 58 (3): 274.

Bates, Frank S., and Pierre Wiltzius. 1989. “Spinodal Decomposition of a Symmetric Critical Mixture of Deuterated and Protonated Polymer.” *The Journal of Chemical Physics* 91 (5): 3258–3274.

Berne, Bruce J., and Robert Pecora. 2000. *Dynamic Light Scattering: With Applications to Chemistry, Biology, and Physics*. Courier Corporation.

Böhmer, R. 1998. “Non-Exponential Relaxation in Disordered Materials: Phenomenological Correlations and Spectrally Selective Experiments.” *Phase Transitions: A Multinational Journal* 65 (1–4): 211–231.

Böhmer, Roland. 1998. “Non-Exponential Relaxation in Disordered Materials: Phenomenological Correlations and Spectrally Selective Experiments.” *Phase Transitions: A Multinational Journal* 65 (1–4): 211–31.

Böhmer, Roland, R. V. Chamberlin, G. Diezemann, B. Geil, Andreas Heuer, G. Hinze, S. C. Kuebler, Ranko Richert, B. Schiener, and H. Sillescu. 1998. “Nature of the Non-Exponential Primary Relaxation in Structural Glass-Formers Probed by Dynamically Selective Experiments.” *Journal of Non-Crystalline Solids* 235: 1–9.

Bouchaud, J.-P., and E. Pitard. 2001. “Anomalous Dynamical Light Scattering in Soft Glassy Gels.” *The European Physical Journal E* 6 (3): 231–236.

Bremer, Leon GB. 1992. “Fractal Aggregation in Relation to Formation and Properties of Particle Gels.” PhD Thesis, Bremer.

Bremer, Leon G.B, Pieter Walstra, and Ton van Vliet. 1995. “Estimations of the Aggregation Time of Various Colloidal Systems.” *Colloids and Surfaces A: Physicochemical and Engineering Aspects* 99 (2–3): 121–27. https://doi.org/10.1016/0927-7757(95)03159-B.

Brinker, C. Jeffrey, and George W. Scherer. 2013. *Sol-Gel Science: The Physics and Chemistry of Sol-Gel Processing*. Academic press.

Broide, Michael L., and Richard J. Cohen. 1990. “Experimental Evidence of Dynamic Scaling in Colloidal Aggregation.” *Physical Review Letters* 64 (17): 2026.

Carpineti, Marina, and Marzio Giglio. 1992. “Spinodal-Type Dynamics in Fractal Aggregation of Colloidal Clusters.” *Physical Review Letters* 68 (22): 3327–30. https://doi.org/10.1103/PhysRevLett.68.3327.

Cerdà, Juan J., Tomás Sintes, C. M. Sorensen, and A. Chakrabarti. 2004. “Structure Factor Scaling in Colloidal Phase Separation.” *Physical Review. E, Statistical, Nonlinear, and Soft Matter Physics* 70 (5 Pt 1): 051405.

Chamberlin, Ralph V. 1998. “Experiments and Theory of the Nonexponential Relaxation in Liquids, Glasses, Polymers and Crystals.” *Phase Transitions: A Multinational Journal* 65 (1–4): 169–209.

Cipelletti, Luca, S. Manley, R. C. Ball, and D. A. Weitz. 2000a. “Universal Aging Features in the Restructuring of Fractal Colloidal Gels.” *Physical Review Letters* 84 (10): 2275–78. https://doi.org/10.1103/PhysRevLett.84.2275.

Cipelletti, Luca, Suliana Manley, R. C. Ball, and D. A. Weitz. 2000b. “Universal Aging Features in the Restructuring of Fractal Colloidal Gels.” *Physical Review Letters* 84 (10): 2275.

Cipelletti, Luca, Suliana Manley, RC Ball, and DA Weitz. 2000c. “Universal Aging Features in the Restructuring of Fractal Colloidal Gels.” *Physical Review Letters* 84 (10): 2275.

De Gennes, P.G. 1975. “Critical Dimensionality for a Special Percolation Problem.” *Journal de Physique* 36 (11): 1049–54. https://doi.org/10.1051/jphys:0197500360110104900.

———. 1976. “On a Relation between Percolation Theory and the Elasticity of Gels.” *Journal de Physique Lettres* 37 (1): 1–2. https://doi.org/10.1051/jphyslet:019760037010100.

Del Gado, Emanuela, and Walter Kob. 2007. “Length-Scale-Dependent Relaxation in Colloidal Gels.” *Physical Review Letters* 98 (2): 028303.

Derjaguin, B. v, and L. Landau. 1941. “Theory of the Stability of Strongly Charged Lyophobic Sols and of the Adhesion of Strongly Charged Particles in Solutions of Electrolytes.” *Progress in Surface Science* 43 (1–4): 30–59.

Dhaubhadel, R., A. Chakrabarti, and C. M. Sorensen. 2009. “Light Scattering Study of Aggregation Kinetics in Dense, Gelling Aerosols.” *Aerosol Science and Technology* 43 (11): 1053–1063.

Dhaubhadel, R., F. Pierce, A. Chakrabarti, and C. M. Sorensen. 2006. “Hybrid Superaggregate Morphology as a Result of Aggregation in a Cluster-Dense Aerosol.” *Physical Review E* 73 (1): 011404.

Dhaubhadel, Rajan, Corey S. Gerving, Amitabha Chakrabarti, and Christopher M. Sorensen. 2007. “Aerosol Gelation: Synthesis of a Novel, Lightweight, High Specific Surface Area Material.” *Aerosol Science and Technology* 41 (8): 804–10. https://doi.org/10.1080/02786820701466291.

Di Biasio, A. 1998. “Relaxation Phenomena in Sol–Gel Transition.” *Colloids and Surfaces A: Physicochemical and Engineering Aspects* 140 (1–3): 279–287.

Dongen, P. G. J. van, and M. H. Ernst. 1985. “Dynamic Scaling in the Kinetics of Clustering.” *Physical Review Letters* 54 (13): 1396–99. https://doi.org/10.1103/PhysRevLett.54.1396.

Ebini, Raiya Husein, and Christopher Michael Sorensen. 2019. “Light Scattering Studies of the Sol-to-Gel Transition in Particulate Systems.” *Journal of Colloid and Interface Science* 556: 577–583.

Family, Fereydoon, Paul Meakin, and Tamás Vicsek. 1985. “Cluster Size Distribution in Chemically Controlled Cluster–Cluster Aggregation.” *The Journal of Chemical Physics* 83 (8): 4144–4150.

Ferri, Fabio. 1997. “Use of a Charge Coupled Device Camera for Low-Angle Elastic Light Scattering.” *Review of Scientific Instruments* 68 (6): 2265–74. https://doi.org/10.1063/1.1148135.

Fry, D., A. Chakrabarti, W. Kim, and C. Sorensen. 2004. “Structural Crossover in Dense Irreversibly Aggregating Particulate Systems.” *Physical Review E* 69 (6). https://doi.org/10.1103/PhysRevE.69.061401.

Fry, D., Tomàs Sintes, A. Chakrabarti, and C. M. Sorensen. 2002. “Enhanced Kinetics and Free-Volume Universality in Dense Aggregating Systems.” *Physical Review Letters* 89 (14): 148301.

Gimel, Jean Christophe, Dominique Durand, and Taco Nicolai. 1995. “Transition between Flocculation and Percolation of a Diffusion-Limited Cluster-Cluster Aggregation Process Using Three-Dimensional Monte Carlo Simulation.” *Physical Review B* 51 (17): 11348.

Gimel, Jean Christophe, Taco Nicolai, and Dominique Durand. 1999. “3d Monte Carlo Simulations of Diffusion Limited Cluster Aggregation up to the Sol-Gel Transition: Structure and Kinetics.” *Journal of Sol-Gel Science and Technology* 15 (2): 129–136.

Gisler, Thomas, Robin C. Ball, and David A. Weitz. 1999. “Strain Hardening of Fractal Colloidal Gels.” *Physical Review Letters* 82 (5): 1064.

Guinier, André, Gérard Fournet, and Kenneth L. Yudowitch. 1955. “Small-Angle Scattering of X-Rays.”

Hasmy, Anwar, and Rémi Jullien. 1995. “Sol-Gel Process Simulation by Cluster-Cluster Aggregation.” *Journal of Non-Crystalline Solids* 186: 342–348.

———. 1996. “Percolation in Cluster-Cluster Aggregation Processes.” *Physical Review E* 53 (2): 1789.

Heine, M. C., and Sotiris E. Pratsinis. 2007. “Brownian Coagulation at High Concentration.” *Langmuir* 23 (19): 9882–9890.

Heinson, W. R., Amitabha Chakrabarti, and Christopher M. Sorensen. 2017. “Kinetic Percolation.” *Physical Review E* 95 (5): 052109.

Heinson, W. R., C. M. Sorensen, and A. Chakrabarti. 2012. “A Three Parameter Description of the Structure of Diffusion Limited Cluster Fractal Aggregates.” *Journal of Colloid and Interface Science* 375 (1): 65–69.

Heinson, William R., Yuli W. Heinson, Pai Liu, and Rajan K. Chakrabarty. 2018. “Breakdown of Fractal Dimension Invariance in High Monomer-Volume-Fraction Aerosol Gels.” *Aerosol Science and Technology* 52 (9): 953–956.

Holthoff, Helmut, Stefan U. Egelhaaf, Michal Borkovec, Peter Schurtenberger, and Hans Sticher. 1996. “Coagulation Rate Measurements of Colloidal Particles by Simultaneous Static and Dynamic Light Scattering.” *Langmuir* 12 (23): 5541–49. https://doi.org/10.1021/la960326e.

Huang, H., C. Oh, and C. M. Sorensen. 1998. “Structure Factor Scaling in Aggregating Systems.” *Phys. Rev. E* 57 (1): 875–880. https://doi.org/10.1103/PhysRevE.57.875.

Isaev, S. A., P. A. Baranov, N. A. Kudryavtsev, D. A. Lysenko, and A. E. Usachov. 2006. “Complex Analysis of Turbulence Models, Algorithms, and Grid Structures at the Computation of Recirculating Flow in a Cavity by Means of VP2/3 and FLUENT Packages. Part 2. Estimation of Models Adequacy.” *Thermophysics and Aeromechanics* 13 (1): 55–65.

Israelachvili, Jacob N. 2011. *Intermolecular and Surface Forces*. Academic press.

Jullien, R. 1987. “Aggregation Phenomena and Fractal Aggregates.” *Contemporary Physics* 28 (September): 477–93. https://doi.org/10.1080/00107518708213736.

Jung, S. J., Rose Amal, and Judy A. Raper. 1996. “Monitoring Effects of Shearing on Floc Structure Using Small-Angle Light Scattering.” *Powder Technology* 88 (1): 51–54.

Kikuchi, Yosuke, Hirotsugu Yamada, Hiromi Kunimori, Takao Tsukada, Mitsunori Hozawa, Chiaki Yokoyama, and Masaki Kubo. 2005. “Aggregation Behavior of Latex Particles in Shear Flow Confined between Two Parallel Plates.” *Langmuir* 21 (8): 3273–3278.

Kim, W., C. M. Sorensen, and A. Chakrabarti. 2004. “Universal Occurrence of Soot Superaggregates with a Fractal Dimension of 2.6 in Heavily Sooting Laminar Diffusion Flames.” *Langmuir* 20 (10): 3969–3973.

Kim, Wongyo, Christopher M. Sorensen, Danny Fry, and Amitabha Chakrabarti. 2006. “Soot Aggregates, Superaggregates and Gel-like Networks in Laminar Diffusion Flames.” *Journal of Aerosol Science* 37 (3): 386–401.

Klafter, Joseph, and Igor M Sokolov. 2005. “Anomalous Diffusion Spreads Its Wings.” *Physics World* 18 (8): 29–32. https://doi.org/10.1088/2058-7058/18/8/33.

Kolb, M. 1984. “Unified Description of Static and Dynamic Scaling for Kinetic Cluster Formation.” *Physical Review Letters* 53 (17): 1653.

Kolb, M., R. Botet, and R. Jullien. 1983. “Scaling of Kinetically Growing Clusters.” *Physical Review Letters* 51 (13): 1123–26. https://doi.org/10.1103/PhysRevLett.51.1123.

Kolb, M., and R. Jullien. 1984. “Chemically Limited versus Diffusion Limited Aggregation.” *Journal de Physique Lettres* 45 (20): 977–81. https://doi.org/10.1051/jphyslet:019840045020097700.

Krall, A. H., and D. A. Weitz. 1998. “Internal Dynamics and Elasticity of Fractal Colloidal Gels.” *Physical Review Letters* 80 (4): 778.

Krall, AH, and DA Weitz. 1998. “Internal Dynamics and Elasticity of Fractal Colloidal Gels.” *Physical Review Letters* 80 (4): 778.

Lattuada, Marco, Peter Sandkühler, Hua Wu, Jan Sefcik, and Massimo Morbidelli. 2003. “Aggregation Kinetics of Polymer Colloids in Reaction Limited Regime: Experiments and Simulations.” *Advances in Colloid and Interface Science* 103 (1): 33–56. https://doi.org/10.1016/S0001-8686(02)00082-9.

Lattuada, Marco, Hua Wu, Peter Sandkühler, Jan Sefcik, and Massimo Morbidelli. 2004. “Modelling of Aggregation Kinetics of Colloidal Systems and Its Validation by Light Scattering Measurements.” *Chemical Engineering Science* 59 (8–9): 1783–98. https://doi.org/10.1016/j.ces.2004.01.033.

Leyvraz, F, and H R Tschudi. 1982. “Critical Kinetics near Gelation.” *Journal of Physics A: Mathematical and General* 15 (6): 1951–64. https://doi.org/10.1088/0305-4470/15/6/033.

Lin, M. Y., RUDOLF Klein, H. M. Lindsay, DAVID A. Weitz, ROBIN C. Ball, and PAUL Meakin. 1990. “The Structure of Fractal Colloidal Aggregates of Finite Extent.” *Journal of Colloid and Interface Science* 137 (1): 263–280.

Lin, M. Y., H. M. Lindsay, D. A. Weitz, R. C. Ball, R. Klein, and P. Meakin. 1989a. “Fractals in the Natural Sciences-Universality of Fractal Aggregates as Probed by Light Scattering.” In *Proc. R. Soc. Lond. A*, 423:71–87. The Royal Society.

———. 1989b. “Universality of Fractal Aggregates as Probed by Light Scattering.” *Proceedings of the Royal Society of London. A. Mathematical and Physical Sciences* 423 (1864): 71–87.

———. 1989c. “Universality in Colloid Aggregation.” *Nature* 339 (6223): 360–62. https://doi.org/10.1038/339360a0.

Lin, M. Y., H. M. Lindsay, D. A. Weitz, R. C. Ball, R. Klein, and Paul Meakin. 1990. “Universal Reaction-Limited Colloid Aggregation.” *Physical Review A* 41 (4): 2005.

Lin, M. Y., H. M. Lindsay, D. A. Weitz, RCBR Klein, R. C. Ball, and Paul Meakin. 1990. “Universal Diffusion-Limited Colloid Aggregation.” *Journal of Physics: Condensed Matter* 2 (13): 3093.

Linden, Marte van der, Breanndán O. Conchúir, Elisabetta Spigone, Arun Niranjan, Alessio Zaccone, and Pietro Cicuta. 2015. “Microscopic Origin of the Hofmeister Effect in Gelation Kinetics of Colloidal Silica.” *The Journal of Physical Chemistry Letters* 6 (15): 2881–2887.

Lindsay, H. M., R. Klein, D. A. Weitz, M. Y. Lin, and P. Meakin. 1988. “Effect of Rotational Diffusion on Quasielastic Light Scattering from Fractal Colloid Aggregates.” *Physical Review A* 38 (5): 2614.

Liu, Haifeng, Jinshu Mao, Kangde Yao, Guanghui Yang, Lei Cui, and Yilin Cao. 2004. “A Study on a Chitosan-Gelatin-Hyaluronic Acid Scaffold as Artificial Skin in Vitro and Its Tissue Engineering Applications.” *Journal of Biomaterials Science, Polymer Edition* 15 (1): 25–40. https://doi.org/10.1163/156856204322752219.

Liu, Pai, William R. Heinson, Christopher M. Sorensen, and Rajan K. Chakrabarty. 2019. “Kinetics of Sol-to-Gel Transition in Irreversible Particulate Systems.” *Journal of Colloid and Interface Science* 550 (August): 57–63. https://doi.org/10.1016/j.jcis.2019.04.067.

Lu, Peter J., Emanuela Zaccarelli, Fabio Ciulla, Andrew B. Schofield, Francesco Sciortino, and David A. Weitz. 2008. “Gelation of Particles with Short-Range Attraction.” *Nature* 453 (7194): 499–503.

M. von Smoluchowski. 1916. *Phys., Z.* 23: 585.

Mandelbrot, Benoit B. 1977. *Fractals: Form, Chance, and Dimension*. Vol. 706. WH Freeman San Francisco.

Manley, Suliana, L. Cipelletti, V. Trappe, AE Bailey, Rebecca J. Christianson, U. Gasser, V. Prasad, PN Segre, MP Doherty, and S. Sankaran. 2004. “Limits to Gelation in Colloidal Aggregation.” *Physical Review Letters* 93 (10): 108302.

Martin, J E, and D Adolf. 1991. “The Sol-Gel Transition in Chemical Gels.” *Annual Review of Physical Chemistry* 42 (1): 311–39. https://doi.org/10.1146/annurev.pc.42.100191.001523.

Martin, James E., and Jess P. Wilcoxon. 1989. “Spatial Correlations and Growth in Dilute Gels.” *Physical Review A* 39 (1): 252.

Matsoukas, Themis. 2014. “Statistical Thermodynamics of Clustered Populations.” *Physical Review E* 90 (2): 022113.

———. 2015. “Statistical Thermodynamics of Irreversible Aggregation: The Sol-Gel Transition.” *Scientific Reports* 5: 8855.

Mattsson, Johan, Hans M. Wyss, Alberto Fernandez-Nieves, Kunimasa Miyazaki, Zhibing Hu, David R. Reichman, and David A. Weitz. 2009. “Soft Colloids Make Strong Glasses.” *Nature* 462 (7269): 83.

Meakin, Paul. 1987. “Fractal Aggregates.” *Advances in Colloid and Interface Science* 28: 249–331. https://doi.org/10.1016/0001-8686(87)80016-7.

Melis, Stefano, Marcel Verduyn, Giuseppe Storti, Massimo Morbidelli, and Jerzy Ba\ldyga. 1999. “Effect of Fluid Motion on the Aggregation of Small Particles Subject to Interaction Forces.” *AIChE Journal* 45 (7): 1383–1393.

Mokhtari, Tahereh. 2007. “Studies of the Effects of Shear on Colloidal Aggregation and Gelation Using Small Angle Light Scattering.” PhD Thesis, Kansas State University.

Mokhtari, Tahereh, A. Chakrabarti, Christopher M. Sorensen, Chung-yin Cheng, and Dennis Vigil. 2008. “The Effect of Shear on Colloidal Aggregation and Gelation Studied Using Small-Angle Light Scattering.” *Journal of Colloid and Interface Science* 327 (1): 216–223.

Mokhtari, Tahereh, Christopher M. Sorensen, and Amit Chakrabarti. 2005. “Multiple-Scattering Effects on Static Light-Scattering Optical Structure Factor Measurements.” *Applied Optics* 44 (36): 7858–7861.

Odriozola, G, A Moncho-Jordá, A Schmitt, J Callejas-Fernández, R Martínez-García, and R Hidalgo-Álvarez. 2001. “A Probabilistic Aggregation Kernel for the Computer-Simulated

Transition from DLCA to RLCA." *Europhysics Letters (EPL)* 53 (6): 797–803. https://doi.org/10.1209/epl/i2001-00210-x.

Oh, C., and C. M. Sorensen. 1999. "Scaling Approach for the Structure Factor of a Generalized System of Scatterers." *Journal of Nanoparticle Research* 1 (3): 369–377.

Olivier, B. J., and C. M. Sorensen. 1990. "Variable Aggregation Rates in Colloidal Gold: Kernel Homogeneity Dependence on Aggregant Concentration." *Physical Review A* 41 (4): 2093.

Pusey, Peter N., and W. Van Megen. 1989. "Dynamic Light Scattering by Non-Ergodic Media." *Physica A: Statistical Mechanics and Its Applications* 157 (2): 705–741.

R. Jullien. 1987. *Aggregation and Fractal Aggregates*. Singapore: World Scientific.

Ren, S. Z., W. F. Shi, W. B. Zhang, and C. M. Sorensen. 1992. "Anomalous Diffusion in Aqueous Solutions of Gelatin." *Physical Review A* 45 (4): 2416–22. https://doi.org/10.1103/PhysRevA.45.2416.

Rottereau, Manuel, Jean Christophe Gimel, Taco Nicolai, and Dominique Durand. 2004a. "Monte Carlo Simulation of Particle Aggregation and Gelation: I. Growth, Structure and Size Distribution of the Clusters." *The European Physical Journal E* 15 (2): 133–140.

———. 2004b. "Monte Carlo Simulation of Particle Aggregation and Gelation: II. Pair Correlation Function and Structure Factor." *The European Physical Journal E* 15 (2): 141–148.

Russel, William Bailey, W. B. Russel, Dudley A. Saville, and William Raymond Schowalter. 1991. *Colloidal Dispersions*. Cambridge university press.

Ruta, B., O. Czakkel, Y. Chushkin, F. Pignon, R. Nervo, F. Zontone, and M. Rinaudo. 2014. "Silica Nanoparticles as Tracers of the Gelation Dynamics of a Natural Biopolymer Physical Gel." *Soft Matter* 10 (25): 4547–4554.

Sandkühler, Peter, Marco Lattuada, Hua Wu, Jan Sefcik, and Massimo Morbidelli. 2005. "Further Insights into the Universality of Colloidal Aggregation." *Advances in Colloid and Interface Science* 113 (2–3): 65–83. https://doi.org/10.1016/j.cis.2004.12.001.

Sandkühler, Peter, Jan Sefcik, Marco Lattuada, Hua Wu, and Massimo Morbidelli. 2003. "Modeling Structure Effects on Aggregation Kinetics in Colloidal Dispersions." *AIChE Journal* 49 (6): 1542–1555.

Selomulya, Cordelia, Graeme Bushell, Rose Amal, and T. D. Waite. 2002. "Aggregation Mechanisms of Latex of Different Particle Sizes in a Controlled Shear Environment." *Langmuir* 18 (6): 1974–1984.

Serra, Teresa, Jordi Colomer, and Xavier Casamitjana. 1997. "Aggregation and Breakup of Particles in a Shear Flow." *Journal of Colloid and Interface Science* 187 (2): 466–473.

Smoluchowski, M. Von. 1916. "Three Discourses on Diffusion, Brownian Movements, and the Coagulation of Colloid Particles." *Phys. Z. Sowjet.* 17: 557–571.

Soos, Miroslav, Amgad S. Moussa, Lyonel Ehrl, Jan Sefcik, Hua Wu, and Massimo Morbidelli. 2008. "Effect of Shear Rate on Aggregate Size and Morphology Investigated under Turbulent Conditions in Stirred Tank." *Journal of Colloid and Interface Science* 319 (2): 577–589.

Sorensen, C. M. 2001. "Light Scattering by Fractal Aggregates: A Review." *Aerosol Science and Technology* 35 (2): 648–87. https://doi.org/10.1080/02786820117868.

———. 2011. "The Mobility of Fractal Aggregates: A Review." *Aerosol Science and Technology* 45 (7): 765–79. https://doi.org/10.1080/02786826.2011.560909.

Sorensen, C. M., J. Cai, and N. Lu. 1992. “Light-Scattering Measurements of Monomer Size, Monomers per Aggregate, and Fractal Dimension for Soot Aggregates in Flames.” *Applied Optics* 31 (30): 6547–6557.

Sorensen, C. M., and A. Chakrabarti. 2011. “The Sol to Gel Transition in Irreversible Particulate Systems.” *Soft Matter* 7 (6): 2284–2296.

Sorensen, C. M., W. B. Hageman, T. J. Rush, H. Huang, and C. Oh. 1998. “Aerogelation in a Flame Soot Aerosol.” *Physical Review Letters* 80 (8): 1782.

Sorensen, C. M., and G. M. Wang. 1999. “Size Distribution Effect on the Power Law Regime of the Structure Factor of Fractal Aggregates.” *Physical Review E* 60 (6): 7143–48. https://doi.org/10.1103/PhysRevE.60.7143.

Sorensen, Christopher M., Wongyo Kim, Dan Fry, Dan Shi, and Amitabha Chakrabarti. 2003. “Observation of Soot Superaggregates with a Fractal Dimension of 2.6 in Laminar Acetylene/Air Diffusion Flames.” *Langmuir* 19 (18): 7560–7563.

Sorensen, CM, and A. Chakrabarti. 2011. “The Sol to Gel Transition in Irreversible Particulate Systems.” *Soft Matter* 7 (6): 2284–96.

Stauffer, D. 1976. “Gelation in Concentrated Critically Branched Polymer Solutions. Percolation Scaling Theory of Intramolecular Bond Cycles.” *Journal of the Chemical Society, Faraday Transactions 2* 72: 1354. https://doi.org/10.1039/f29767201354.

Stauffer, Dietrich, Antonio Coniglio, and Mireille Adam. 1982. “Gelation and Critical Phenomena.” In *Polymer Networks*, edited by Karel Dušek, 44:103–58. Berlin, Heidelberg: Springer Berlin Heidelberg. https://doi.org/10.1007/3-540-11471-8_4.

Swift, David L., and S_K_ Friedlander. 1964. “The Coagulation of Hydrosols by Brownian Motion and Laminar Shear Flow.” *Journal of Colloid Science* 19 (7): 621–647.

Tanaka, Hajime, Yuya Nishikawa, and Takehito Koyama. 2005. “Network-Forming Phase Separation of Colloidal Suspensions.” *Journal of Physics: Condensed Matter* 17 (15): L143.

Torres, Francisco E., William B. Russel, and William R. Schowalter. 1991. “Floc Structure and Growth Kinetics for Rapid Shear Coagulation of Polystyrene Colloids.” *Journal of Colloid and Interface Science* 142 (2): 554–574.

Verwey, Evert Johannes Willem, Jan Theodoor Gerard Overbeek, and K. Van Nes. 1948. *Theory of the Stability of Lyophobic Colloids: The Interaction of Sol Particles Having an Electric Double Layer*. Elsevier Publishing Company.

Vicsek, Tamás. 1989. “Fractal Growth Phenomena.” *Computers in Physics* 3 (5): 108–108.

Victor, J. M., and J. P. Hansen. 1984. “«Liquid-Gas» Transition in Charged Colloidal Dispersions.” *Journal de Physique Lettres* 45 (7): 307–312.

Weitz, D. A., J. S. Huang, M. Y. Lin, and J. Sung. 1985. “Limits of the Fractal Dimension for Irreversible Kinetic Aggregation of Gold Colloids.” *Physical Review Letters* 54 (13): 1416–19. https://doi.org/10.1103/PhysRevLett.54.1416.

Wong, Po-zen, and Qi-zhong Cao. 1992. “Correlation Function and Structure Factor for a Mass Fractal Bounded by a Surface Fractal.” *Physical Review B* 45 (14): 7627.

Wu, Hua, Paolo Arosio, Olga Gennadievna Podolskaya, Dan Wei, and Massimo Morbidelli. 2012. “Stability and Gelation Behavior of Bovine Serum Albumin Pre-Aggregates in the Presence of Calcium Chloride.” *Physical Chemistry Chemical Physics* 14: 4906. https://doi.org/10.1039/c2cp40125h.

Wu, Hua, Jianjun Xie, Marco Lattuada, Joachim Kohlbrecher, and Massimo Morbidelli. 2011. "Effect of Primary Particle Size and Salt Concentration on the Structure of Colloidal Gels." *The Journal of Physical Chemistry C* 115 (4): 931–36. https://doi.org/10.1021/jp103100k.

Wu, Hua, Jianjun Xie, Marco Lattuada, and Massimo Morbidelli. 2005. "Scattering Structure Factor of Colloidal Gels Characterized by Static Light Scattering, Small-Angle Light Scattering, and Small-Angle Neutron Scattering Measurements." *Langmuir* 21 (8): 3291–95. https://doi.org/10.1021/la047403n.

Wu, Hua, Jianjun Xie, and Massimo Morbidelli. 2005. "Kinetics of Cold-Set Diffusion-Limited Aggregations of Denatured Whey Protein Isolate Colloids." *Biomacromolecules* 6 (6): 3189–97. https://doi.org/10.1021/bm050532d.

Wu, Hua, Jian-jun Xie, and Massimo Morbidelli. 2013. "Kinetics of Colloidal Gelation and Scaling of the Gelation Point." *Soft Matter* 9: 4437-. https://doi.org/10.1039/c3sm00117b.

Zhang, Li, Alesya Mikhailovskaya, Doru Constantin, Giuseppe Foffi, Joseph Tavacoli, Julien Schmitt, François Muller, Cyrille Rochas, Nan Wang, and Dominique Langevin. 2016. "Varying the Counter Ion Changes the Kinetics, but Not the Final Structure of Colloidal Gels." *Journal of Colloid and Interface Science* 463: 137–144.